Development of a Low-Field ^{3}He MRI System to Study Posture-Dependence of Pulmonary Function

A dissertation presented

by

Leo Lee Tsai

to

The Committee on Higher Degrees in Biophysics

in partial fulfillment of the requirements

for the degree of

Doctor of Philosophy

in the subject of

Biophysics

Harvard University

Cambridge, Massachusetts

July 2006

Thesis advisor
Ronald Lee Walsworth

Author
Leo Lee Tsai

Development of a Low-Field ^{3}He MRI System to Study Posture-Dependence of Pulmonary Function

Abstract

This thesis describes the design and construction of a low-field, open-access magnetic resonance imaging (MRI) system for *in vivo* ^{3}He imaging of the human lungs. Our system permits the study of lung function in both horizontal and upright postures, a subject with important implications in pulmonary physiology and clinical medicine. We constructed a custom polarizer that uses spin exchange optical pumping (SEOP) to hyperpolarize ^{3}He to 10–15%. The low-field imager (LFI) uses a bi-planar B_0 coil design that produces an optimized 65 G (6.5 mT) magnetic field for ^{3}He and ^{1}H MRI at 210 kHz and 275 kHz, respectively. Bi-planar coils produce the x, y, and z magnetic field gradients and provide up to 79-cm inter-coil gap for the imaging subject. We use solenoidal Q-spoiled RF coils for operation at low frequencies, and are able to exploit the lack of significant sample loading effects to allow for pre-tuning/matching schemes and for accurate pre-calibration of flip angles.

We use several noise filtering techniques and modified several electronic components to be compatible at 200–300 kHz. This allows sufficient SNR to perform thermal ^{1}H imaging at 65 G. We have produced images of water phantoms as well as slice-selected images of a human head. We have also produced ^{3}He images of sealed glass cells and plastic bags at resolutions and SNR similar to those on conventional high-field systems. We have also exploited a well-known ^{3}He relaxation dependency on oxygen concentration to obtain NMR and image-based measurements of pO_2 in known gas mixtures inside of plastic bags. Finally, we present initial ^{3}He MR images of human lungs obtained with the LFI.

Contents

List of Figures

List of Tables

Acknowledgments

First I would like to thank my advisor, Ron Walsworth, for all of his support and guidance throughout these past few years. He is as energetic and enthusiastic about his work now as he was the first time I met him nearly ten years ago, when he gave a visiting lecture during my sophomore year at college and first inspired me to learn more about MRI. I hope to carry a similar spirit and attitude throughout my own career and life.

I am deeply grateful to Matt Rosen for his help and work on the polarizer and the imager. He has taught me to be a better designer, engineer, machinist, and physicist, all while being a great colleague and friend. He has constantly reminded me to maintain an optimistic view and, most of all, to just have fun. My PhD experience would not have been quite as colorful without our various side-lessons/discussions about lock-picking, graphic design, typography, music, glassblowing, power tools, home improvement, and cycling.

My research experience would have been impossible without Ross Mair, who has helped me with everything from experimental planning and pulse sequence programming to navigation through the nightmarish travel reimbursement process at the CFA. I have learned invaluable writing skills from him, for everything from grant applications to scientific papers to the everyday lab book. He has also been the ideal traveling companion to the numerous conferences we have attended. I am most thankful for his extraordinary and unwavering kindness and patience throughout my time here, even through the most challenging times.

I benefited greatly from working with Tina Pavlin on various projects related to high-field ^{3}He imaging. I was inspired by her level of perseverance and dedication to her work, a trait that I have since tried to emulate.

Jim Maddox provided invaluable assistance in getting the B_0 power supply working and stabilized. I am also grateful to Mirko Hrovat for sharing his expertise of the Techron gradient amplifiers while I was battling the various stability and noise

issues on the LFI.

I am deeply indebted to the CFA machine shop personnel—Larry, Ken, Joe, and Kevin—for all of their help and assistance in constructing a myriad of components for the LFI.

I would like to thank several of the other senior scientists at the CFA, including David Phillips, Irina Novikova, Yanhong Xiao, Cindy Hancox, Ed Mattison, and Bob Vessot, who have assisted me at various moments throughout my time here, and who have made the laboratory an enjoyable and stimulating place to work.

I have had the pleasure of working with and amongst a wonderful group of graduate students. Glenn Wong, Marc Humphrey, Federico Cané, and Ruopeng Wang welcomed me to the group and made my transition from medical school a pleasant one. Mason Klein and I joined the group at the same time and worked on the granular segregation project together. He was fantastic to work with and remains a close colleague. John Ng worked with me on the UNH imaging project and the early stages of the LFI project. I am extraordinarily fortunate to have had John as one of my best friends since high school, and I am thrilled to be joining him back in medical school next year. Alex Glenday, Mike Hohensee, and Christine Wang have been a lot of fun to work with. Special credit goes to Alex for sacrificing three days of his life winding the outer B_0 coils with Matt and myself. I have also had the privilege of working with an excellent group of undergraduates. Chris Smallwood helped with some of the early LDA performance tests, and Rachel Burke did an outstanding job with B_0 field mapping, coil shimming, and polarization calibration measurements.

We collaborated with Bill Hersman's group at the University of New Hampshire for the early low-field lung imaging experiments. I would like to thank him and his group for many useful discussions throughout the years, both at his laboratory and at various conferences. In particular I would like to thank Iulian Ruset for many insightful discussions while we coauthored a paper on the UNH system, and for his continued

support and encouragement towards my thesis work.

I would also like to thank Sam Patz, George Topulos, and Jim Butler, with whom I worked on the early RBV experiments during my second year of medical school; they have provided much mentoring, advice and encouragement throughout my graduate school career.

I have had a wonderful graduate school experience as part of the Biophysics Program at Harvard, thanks to Jim Hogle and Michele Jakoulov as well as my fellow Biophysics classmates. I would also like to thank past and present members of the MD/PhD Office—Tara Smith, Janelle McCluskey, Linda Burnley, Robin Lichtenstein, and Yi Shen—for their support since my first days as a medical student.

My PQE was one of the most rewarding and valuable experiences of my academic career, and I would like to thank my examiners, Ragu Kalluri, Donald Ingber, and Michael Gimbrone, for inspiring me to think more critically and effectively when incorporating new technological ideas into hypothesis-driven biological science. My thesis committee, Jim Butler, Dan Shannon, Dan Sodickson, and Jim Hogle, have continued to provide invaluable advice and encouragement throughout my PhD years.

I would not be here without the inspiration I have received from my past research supervisors and mentors: Miriam Rivas and Martin Carter at the Rockefeller University, Enrique Peacock-Lopez and Protik (Tiku) Majumder at Williams College, and Laurie Hall at Cambridge University. Along the way I have had the pleasure of working with two amazing colleagues at Tiku's lab: Balakrishna Narasimhan and Peter Nicholas.

I have received generous funding from several sources: The Goldwater Foundation, The Herchel Smith Foundation, NASA Graduate Student Research Program, and the Medical Scientist Training Program. Special thanks to Dean Peter Grudin and Lynn Chick at Williams College who took great care of me during my time in England.

I would like to thank all of my friends for all their support through these

years. I am especially grateful to Glenn Yiu, Bob Ohgami, Brian Hafler, John Ng, John Greenland, Amy Lee, Jenny Chang, and Savita Dandapani for many wonderful memories during my time at Harvard. And thanks to Dan Velez, Patrick Wang, and Altay Israfel, who have stood by me since the old days back in Queens, New York.

There are a few members of my extended family that deserve special mention. Thomas and Katrina Huang, Pao-Hsia Yeh, Ken Yeh, and Jorge Lopez have cared for me in innumerable ways, and I am forever grateful. My parents-in-law, Hsin-cheng and Gloria Chuang, and my brother-in-law, Les, have welcomed me into their family with open arms.

I would not be here without the steadfast support and boundless love from my mother and father. Throughout my life I have given them plenty to worry about—I was a "special" child, to say the least—but they never lost faith. Mom and Dad, I love you both, always.

My brother Ken has been my best friend and greatest inspiration for all my life. I am grateful for all of his love and support, and for the many laughs we've shared over the years. I am also appreciative for the support of my sister-in-law, Elsa, who is both an accomplished scientist and a wonderful addition to our family.

Finally, I thank my wife, Barbara. There is nobody else I would rather have by my side. She recently declared that my best trait is "being goofy." We have much in common. I look forward to the many adventures that await us.

Dedication

To my love, Barbara.

Our best years are yet to come!

Chapter 1

Introduction

For centuries the art and practice of diagnostic medicine has improved not only through experience and accumulated knowledge of human physiology and disease, but also through a series of technological advancements that have allowed us to measure or visualize disease processes and their effects on the body with capabilities far exceeding those of the basic physical exam. One of the most striking examples of medical advancement is the field of radiology, which began with Wilhem Röentgen's first X-ray films of his wife's hand in 1896. This demonstrated the possibility of visualizing internal disease processes and trauma in a non-invasive fashion. Other modalities such as positron emission tomography (PET), X-ray computer tomography (CT), and magnetic resonance imaging (MRI) have since emerged to become essential clinical tools in modern clinical centers. Although these imaging methods differ significantly in their methods and capabilities, they are very closely related to one another through an elegant combination of decades- and centuries-old principles in mathematics, chemistry, and physics.

This thesis explores the use of ^{3}He MRI in studies of the human lung, an organ that has been extraordinarily difficult to study *in vivo* even with the most modern imaging tools available. We begin with an overview of currently available lung function

measurements and discuss the need to obtain more quantitative information about local pulmonary dynamics and orientation-dependence. A brief overview of different lung imaging methods are compared, concluding with our case for hyperpolarized noble gas MRI and its use in orientation-dependent studies of lung function.

1.1 Lung Anatomy and Gas Exchange

The lungs provide the primary interface for gas exchange between atmospheric air and blood. The human lungs are divided into the right and left parts via the left and right bronchi, which in turn branch into ever smaller bronchioles. The lung is divided into distinct lobes, with three major ones on the right lung and two on the left. The initial fifteen or sixteen bronchial branches serve only to deliver gas to the periphery of the lungs and constitute the conducting zone of the lung. The remaining seven branches, which are part of the respiratory zone, include acinar units [1]. Each acinar unit contains clusters of alveolar sacs, where the bulk of gas exchange occurs.

Most of the volume of a typical human lung is comprised of approximately 300 million alveoli. A typical alveolus spans approximately 250 microns in diameter and possesses a wall thickness as little as 0.3 microns. Surrounding vasculature can often support only one row of erythrocytes. The remaining volume is occupied by gas. The result is an enormous total surface area—$\sim$ 260 m^2, approximately equal to the area of a tennis court—optimized for gas exchange between blood and the external atmosphere. Adult lungs hold a maximum of approximately 7 L of gas at atmospheric pressure, known as total lung capacity (TLC). Typical breathing patterns at rest, however, contain a tidal volume (V_T) of about 0.5 L, at 10–15 breaths per minute (bpm). At the end of a typical exhalation, the volume of air remaining inside the lungs, known as the functional residual capacity (FRC) is approximately 1.5 L. If necessary, a person can force out approximately 1.0 L more air beyond FRC, with the remaining air known

as the residual volume (RV). Therefore the maximum volume of air a person is able to inhale or exhale is between RV to TLC ($\sim$ 6.5 L), known as the vital capacity (VC). Figure 1.1 summarizes the lung volume definitions. RV cannot be decreased further

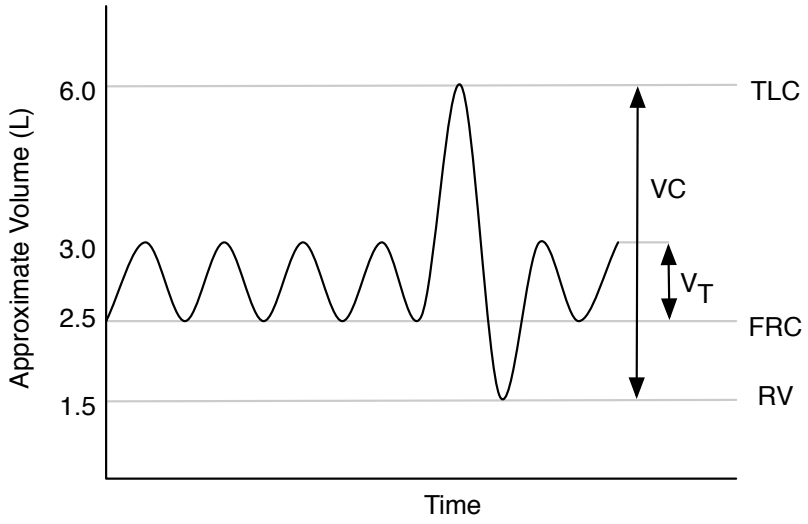

Figure 1.1: A diagram of typical adult human lung volumes. TLC–Total Lung Capacity, RV–residual volume, FRC–Functional Residual Capacity, V_T–Tidal Volume, VC–Vital Capacity.

due to rebounding forces provided by the chest wall. This is necessary, to keep the respiratory zones from collapsing from the surface tension of the water lining the walls, even in the presence of lung surfactants.

Gas exchange in the lung is driven by diffusion across concentration gradients (Figure 1.2). Pulmonary arteries carry deoxygenated blood ($pO_2 \sim 40$ mm Hg) rich in carbon dioxide ($pCO_2 \sim 46$ mm Hg). Fresh atmospheric gas contains approximately 160 mm Hg of O_2 and virtually no carbon dioxide. Within the humid environment of the airway and alveolar space $pO_2 \sim 150$ mm Hg. As erythrocytes travel through the alveolar walls oxygen diffuses into and binds the hemoglobin complex and carbon dioxide is released. Chemical equilibrium is usually established by the time a red blood cell travels only a third of its path. The final equilibrium pressures established are pO_2

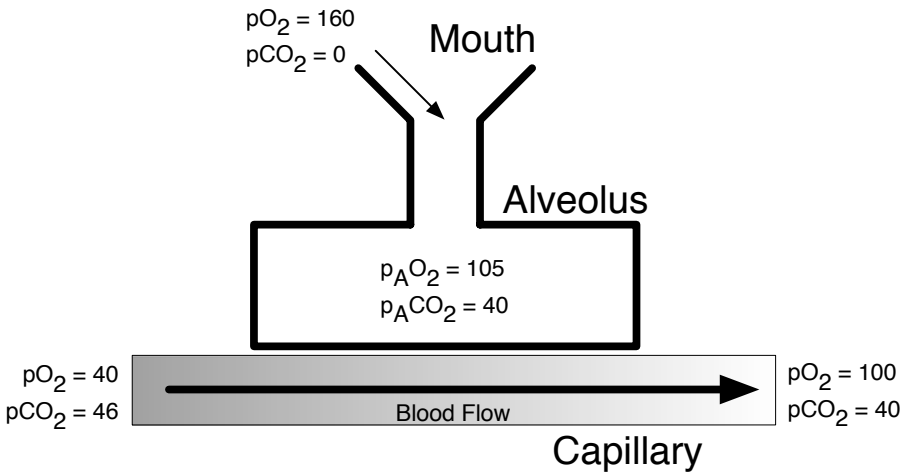

Figure 1.2: A diagram of approximate pO_2 and pCO_2 values during normal gas exchange as described in typical physiology textbooks [2]. All values are in mm Hg.

of 100 mm Hg and $\mathrm{pCO_2} \sim 40$ mm Hg.

The total alveolar ventiltion, $\dot{V}_A$ for the resting human lungs is ~ 5 L/min, based on typical breathing rates and tidal volumes. The blood perfusion rate, $\dot{Q}$ is also roughly 5 L/min, as determined by the cardiac rate and stroke volume. The commonly-used ratio $\dot{V}_A/\dot{Q}$ is thus roughly unity in a normal lung, but deviates—or becomes "mismatched"—if either gas or blood flow is disrupted and gas exchange is compromised. This process can be sudden, such as an aspirated object or an embolism, or one that worsens over time, as in the case of many restrictive and obstructive diseases, and can be homo- or heterogeneous. The clinical challenge is to localize the source of disruption and to understand the mechanism that causes the mismatch.

1.2 Measuring Pulmonary Function

The term "pulmonary function" is vague; the data obtained from such tests can refer to a wide variety of lung characteristics such as gas ventilation, blood perfusion, or $\dot{V}_A/\dot{Q}$. All these methods focus on the same problem: to determine how well the

lung is achieving its primary goal of efficient gas exchange between the blood and the atmosphere.

The majority of clinical techniques must rely on indirect methods of measurement. This is necessary because despite the lung's enormous degree of interaction with the external world, the organ itself is highly inaccessible to non-invasive observation, since air is moved back and forth through a single, small airway. The diaphragm lies directly beneath the lungs and the lateral and posterio-anterior aspects of the thorax are surrounded by the ribcage. The lungs themselves are sealed inside an airtight pleural sac that—in concert with the semi-rigid thoracic wall—provides a negative pressure necessary to maintain a minimal expansion; any disruption of this boundary can lead to the collapse of the tissue. Pressure transducers and sensors can provide local information a few branches deeper than the bronchus but cannot penetrate the smaller respiratory zones. Blood gas sampling from the pulmonary vasculature is possible only from the major vessels and is highly impractical and reserved only as an extreme measure.

1.2.1 Clinical Methods

A significant amount of information about the lungs can be gathered using indirect methods. Since the lungs are significantly less dense than the surrounding anatomical structures in the thorax, the organ's physical boundary within the thorax can be determined through percussion. Changes in the lung tissue density can also be determined, e.g., a localized streptococcal pneumonia. Airflow can also be assessed by auscultation; pathology can alter flow dynamics, resulting in changes in generated sound, such as wheezing in asthma. A more quantitative method of airflow dynamics, however, relies on measuring gas volumes and contents moving in and out of the airway opening, i.e., the mouth.

Spirometry is the most common pulmonary function test performed in the clinic. This cost-effective and non-invasive technique measures the volume and flow of

inspired and expired gas at the mouth. Patients are asked to take a breath to TLC, then to exhale as hard as possible into a closed tube to the instrument, until RV is reached. This volume is known as the forced vital capacity (FVC), which is the same volume as VC. Two typical data types are measured: forced expiratory flow (FEF) and forced expiratory volume (FEV). Certain values, such as the FEV at one second after the start of exhalation (FEV_1), are compared to average values from the general population. The ratio FEV_1/FVC, usually expressed as a percentage, is especially popular. In general, a healthy subject has a FEV_1/FVC ratio of $\sim 80\%$. Obstructive lung diseases such as asthma result in lower values, while restrictive lung diseases yield greater values.

RV and TLC can also be clinically important, but cannot be measured using spirometry. Measurements of these values can be obtained using several methods, the most common being helium dilution and body plethysmography. In helium dilution, the patient's mouth is connected to an apparatus with a known initial volume and concentration of helium gas. The subject then breaths from RV and the helium mixes inside the lung. Eventually the helium establishes a concentration equilibrium across the volume of the instrument and the lung volume. The new helium concentration can then be used to obtain the lung at RV, and TLC = RV + VC, the latter being obtainable with spirometry. Body plethysmography uses Boyle's gas law to obtain a measurement of FRC, which can then be used to calculated RV and TLC. The subject is housed inside an airtight chamber, and expires and inhales against a closed shutter from FRC. Pressure transducers measure airway and box pressures during this process. Changes in lung volume are reflected by changes in the box pressure, and the absolute FRC can then be calculated.

Quantitative measurements of inhomogeneous lung $\dot{V}_A$ or $\dot{V}_A/\dot{Q}$ can be obtained via the airway, through use of gas elimination techniques. The most frequently used clinical tool for $\dot{V}_A/\dot{Q}$ determination is the multiple inert gas elimination technique (MIGET) [3]. The subject is first injected with a saline solution with multiple

dissolved gases. After equilibrium is established in the vasculature, gas washout is sampled by mass spectrometry at exhalation. The multiple nitrogen washout (MBNW) [4] is similar to MIGET but much simpler and can be used only to measure ventilation dynamics, or lung volume; here the subject inhales from a pure oxygen source and a mass spectrometer records the nitrogen washout for each exhalation. Both MIGET and MBNW rely on a model of the lung consisting of multiple parallel "compartments" with different ventilation or $\dot{V}_A/\dot{Q}$ characteristics. Should all compartments behave in a similar, homogeneous fashion, the gas elimination fraction would be a linear function with breath number. Non-linearities come from compartments with different behavior (e.g., a shunt or embolus). Although gas elimination techniques cannot pinpoint the exact location of a lesion causing a ventilation disruption or $\dot{V}_A/\dot{Q}$ mismatch, they can characterize the extent of mismatch or ventilation defects in complex clinical cases. MBNW can also be used to measure FRC in ventilated patients that are excluded from plethysmography [5].

1.2.2 Non-Clinical Methods

The above tests constitute the typical clinical techniques used to assess pulmonary function. The data obtained from these methods provide limited information; those from auscultation and percussion is local but purely qualitative, and those from spirometry, dilution, and plethysmography are quantitative but global. Much of our fundamental understanding of pulmonary dynamics has come from studies using more invasive methods to acquire both quantitative and localized data from animal models. Studies of regional lung dynamics in the past half-century have employed techniques falling under three general categories: *ex vivo* studies, invasive measurements using catheterization techniques, and imaging. The first two methods have been employed since the mid-20th century but have been largely restricted to animal models. Floures-cent microspheres have been favored for *ex vivo* studies of both perfusion and ventila-

tion in the periphery of the lung since multiple markers can be used [6]. This technique allows for very high-resolution mapping of ventilation and perfusion data, but suffers from systematic errors associated with rapid sacrificing, freezing, and sectioning of lung samples. Catheterization with pressure and flow sensors provides real-time *in vivo* data and has provided much insight into gas conductance mechanics, but this is limited to non-respiratory branchioles larger than the size of the catheter. Lastly, although canine and porcine lungs (the most popular animal models) possess a similar alveolar structure to human lungs, many aspects of gross anatomy and physiology are considerably different.

1.3 Pulmonary Imaging

Lung imaging has had a long history, beginning with the adoption of chest X-ray as a routine clinical tool in the mid-20th century. Since then, technological advances have allowed the measurement of both regional *and* quantitative data in a non-invasive manner. The first methods to allow such measurements *in vivo* used scintillography of radioactive tracers such as ^{133}Xe, $^{13}N_2$, and $^{15}O_2$ to quantify regional ventilation and/or perfusion [7–9]. Even though detector technology has progressed considerably, such imaging is rarely performed on humans due to dosage limitations, limitations associated with isotope production, and poor resolution.

Chest X-ray imaging remains by far the most cost-effective non-invasive way to image the lungs, and it remains the most popular method. Although many pathological processes in X-ray radiographs can be detected by the trained eye, it is a purely qualitative tool that does not resolve lung tissue well, and only as 2D projections. More recently, PET, CT, and MRI have been used in clinical research for non-invasive quantitative imaging of the lungs. As discussed below, these methods have different strengths and weaknesses that yield complementary data on pulmonary function and anatomy.

1.3.1 CT

Computer tomography (CT) was demonstrated clinically in 1973 [10–13] and rapidly adopted into clinical use by 1980. The technology combined the knowledge of X-ray penetration and interaction with living tissue with multi-projection image reconstruction techniques to produce true two-dimensional slices of anatomy, rather than simple projection radiographs. Modern instruments utilize the same core principles, but greater detector sensitivity and increased computational power have lead to faster imaging at a fraction of the radiation dosage. Single-slice acquisition was restricted to the axial plane, but multi-slice and spiral CT techniques have extended the imaging plane along the orthogonal (typically inferio-superior) axis so that sagittal, coronal, and oblique slices can be obtained.

CT has two major advantages over other 3D imaging tools: speed and resolution. Current systems employ multiple-detector arrays that offer as many as 64 slices per projection rotation, which can be completed in under one second. Clinical systems now offer sub-millimeter resolution, making CT by far the best modality for most anatomical imaging applications. The use of "high-resolution" CT, or HRCT, has proven especially effective in diagnosing diffuse lung diseases, bronchiectasis, and small airway diseases such as obliterative bronchiolitis [14].

CT has been used to quantitatively measure changes in lung tissue density, but it has largely been relegated for anatomical use. Perfusion studies have been performed using radio-opaque contrast agents, but use has been limited only to studies of embolism or lung nodules [15]. Quantitative perfusion or ventilation imaging is difficult with CT due to a lack of contrast between healthy and pathological areas using X-rays. Increasing restrictions on radiation dosage has also limited the use of CT as a method to probe local gas exchange in humans, since perfusion/ventilation data require multiple images to be obtained during wash-in or wash-out of contrast agents.

1.3.2 PET

Positron emission tomography (PET) was developed in 1972 and first used clinically in 1975 [16]. While CT uses an external X-ray source as the probe, PET utilizes positron-emitting radiotracers that can be incorporated into metabolically-active agents. Positron annihilation leads to pairs of photons that are emitted in opposite directions; detectors isolate only these photon pairs, allowing truly quantitative localization of the radiation sources, although resolution is limited to the centimeter scale. Modern PET systems now contain integrated CT units so that quantitative data from the former can be co-registered with detailed anatomy offered by the latter.

PET has the ability to obtain both tomographic and quantitative data from a wide variety of metabolic tracers. $^{13}N_2$ has been used to obtain true quantitative and regional measurements of $\dot{V}_A/\dot{Q}$ and alveolar ventilation in the lungs [17, 18]. These studies use a bolus injection of $^{13}N_2$; due to the negligible solubility of nitrogen in blood, virtually all of the tracer diffuses into the pulmonary alveolar space during an initial pass through the pulmonary vasculature. An initial PET scan of the lungs is thus reflective of the regional perfusion within the lungs, and consequent scans obtained during ventilation show decreasing signal due to elimination of the tracer from the alveoli. Disruptions in perfusion are seen as variations in the initial signal amplitude, while ventilation defects can be visualized by changes in the elimination rate within the sampling region. This technique has been used recently to study sudden heterogeneous ventilation instabilities arising from initially uniform small-airway constriction patterns in asthmatics [19]. Most importantly, the quantitative $\dot{V}_A/\dot{Q}$ data from PET has been shown to accurately predict global gas measurements from MIGET. No other imaging modality has been able to show such an agreement in $\dot{V}_A/\dot{Q}$ data; for this reason, PET is currently regarded as the gold standard in regional $\dot{V}_A/\dot{Q}$ *in vivo* mapping of the lung.

1.3.3 ^{1}H MRI

Magnetic resonance imaging (MRI) has provided the medical and scientific community with a powerful technique to non-invasively visualize and contrast soft tissue structures *in vivo*. Although the first MR image was demonstrated in 1973, the principles of magnetic resonance were demonstrated experimentally by Bloch and Purcell in 1946 [20,21]. This technique was rapidly adopted by chemists and named nuclear magnetic resonance (NMR). Imaging was made possible by Lauterbur and Mansfield, who used magnetic field gradients to obtain spatial information [22, 23].

MRI has two distinct advantages over PET and CT: it uses no ionizing radiation and provides greatly improved soft-tissue contrast. One major drawback, however, is its relatively poor signal-to-noise ratio (SNR). In order to boost MR signals, ^{1}H MRI requires the use of very large magnetic fields and relies on the high water-density of the region of interest. The latter restriction has largely prevented MRI from being a popular diagnostic tool in lung imaging because lung tissue is comprised mainly of gas space. Lung MRI is made more difficult by local magnetic field gradients across tissue-air boundaries, known as magnetic susceptibility-induced background (or internal) gradients, which degrade SNR even further. Lastly, like CT, ^{1}H MRI samples from the lung tissue only, not from the gas spaces.

Despite these difficulties, functional lung studies with ^{1}H MRI have been performed using molecular oxygen as a contrast-enhancing agent [24–26]. The ^{1}H source comes from the lung tissue but is affected by the presence of oxygen, which is a paramagnetic substance. The oxygen diffuses readily into lung tissue and shortens the T_1 relaxation properties of the nearby ^{1}H spins, a quantifiable process. The alveolar partial pressure, p_AO_2, can be indirectly calculated from such measurements. This technique, however, does not directly sample from the gas space in the alveoli, and requires accurate respiratory gating and image co-registration techniques.

MR angiography (MRA) is used to image vasculature and has been adapted

for use in visualizing pulmonary vessel disorders [27]. Contrast-enhanced MRA, or cMRA, employs blood-pool agents such as gadolinium-GTPA to highlight MR signals from blood only. This has been exploited to provide qualitative measurements of pulmonary perfusion [28, 29]. However, quantitative information is difficult to obtain because a highly non-linear relationship exists between contrast agent concentration and MR signal.

1.4 Lung MRI with ^{3}He and ^{129}Xe

^{3}He and ^{129}Xe are two noble gases widely used in lung MRI. Hyperpolarized ^{3}He was first produced in the early 1960's using spin-exchange optical pumping (SEOP) with Rb [30] or metability-exchange optical pumping (MEOP) [31]. For three decades the use of polarized ^{3}He lay exclusively in the field of high-energy physics as a target for nuclear scattering experiments [32]. Then in the early 1990's hyperpolarized ^{129}Xe was used as a gas NMR probe for studies of porous media [33]. Shortly afterwards the first MRI image (a pair of rat lungs inflated with ^{129}Xe) was made in 1994 [34]. Since then hyperpolarized noble gas MRI has developed into a distinct field with an emphasis on lung imaging. ^{3}He and ^{129}Xe are currently both used in the pulmonary research community, and each has distinct advantages.

^{3}He is well suited for lung imaging for several reasons. It is an inert gas that can be safely inhaled, and because it is essentially insoluble in blood the detected MR signals originate exclusively from gas spaces (Figure 1.3). The gyromagnetic ratio of ^{3}He is high and polarization techniques have steadily improved over the past decade [36–38], allowing MRI with high SNR despite the relatively low density of helium at room temperature. ^{3}He MRI was first demonstrated in sealed cells and rat lungs in 1996 [39]. Since then ^{3}He has been used to assess ventilation dynamics in healthy and diseased human lungs [40]. ^{3}He T_1 relaxation (defined in Appendix A) is also sensitive to the

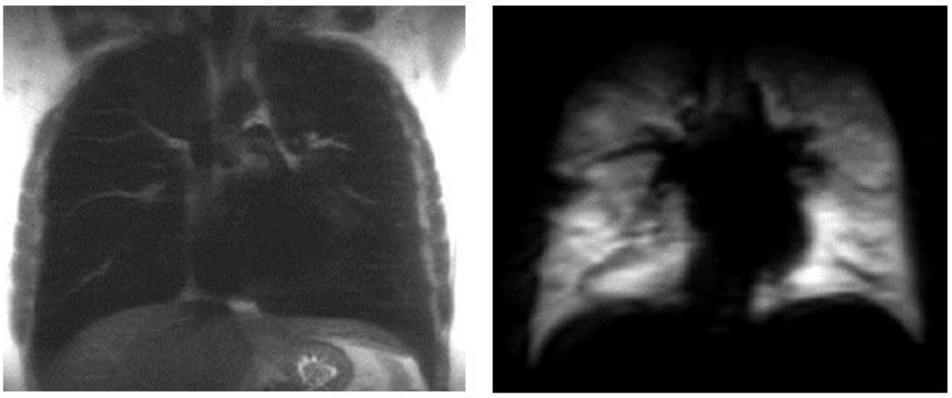

Figure 1.3: A comparison of ^{1}H and ^{3}He chest images of the same human subject on a 1.5 T clinical MRI system. The lungs produce poor MR signals on the ^{1}H image to the left, whereas the ^{3}He image on the right reveals only the lung gas space. Images are from [35].

paramagnetic properties of molecular oxygen [41], a property that has been used to measure regional partial pressure of oxygen (pO_2) [42]. Lastly, the degree of restricted diffusion of ^{3}He inside the alveolar sacs can be measured as the apparent diffusion coefficient (ADC) using MR. This has enabled the detection of disease-driven alterations of alveolar dimensions, e.g. in emphysema [43, 44].

^{129}Xe is polarized using SEOP with Rb, in a similar fashion to ^{3}He. Although the spin exchange process is not as efficient for ^{129}Xe, newer polarization techniques in the past year have been developed to produce output levels acceptable for initial human studies [45]. Although ^{129}Xe is an inert gas, it is partially soluble in blood and lipids, and as a result, exhibits an anaesthetic effect in humans when it reaches brain tissue. ^{129}Xe also exhibits a significant NMR chemical shift when moving from the gas to dissolved phase, a process that can be isolated *in vivo* [46]. This shift has recently been used to measure surface/volume ratios within human lungs [47]. Studies of ADC and pO_2 are also under development.

^{129}Xe has a major advantage in that it has a natural abundance of 26%. This is in contrast to ^{3}He, which is produced by tritium decay and is extremely rare ($\sim 10^{-4}$

abundance relative to ^{4}He). Most of the world's supply of ^{3}He has been produced as a by-product of nuclear weapons manufacturing, which has been curtailed over the past decade and a half. It is estimated that the total amount of ^{3}He on Earth is $\sim$ 400 kg. Thus, ^{3}He lacks the cost-effectiveness to become a routine clinical tool, but its superior MR characteristics and bio-compatibility enable it to be used as a powerful tool for the study of pulmonary physiology.

1.5 Thesis Goal: Multi-Postural Human Lung Imaging

With the exception of chest X-rays, all of the conventional imaging systems listed above share one trait: the requirement to image the subject in a horizontal position. This is a result of convenience to both the instrument designer and the imaging subject; it is easier to keep the subject still in a supine or prone orientation, plus many patients cannot tolerate being imaged in the upright position. It is also much easier to design an imaging instrument that requires only one subject orientation. This thesis project involves the construction of an open-access, low-magnetic-field MRI system optimized for both horizontal and upright ^{3}He imaging of human lungs so that comparisons of lung structure and function can be made across different subject orientations.

We draw from lessons learned from previous studies in our laboratory and with our collaborators. Earlier members of our group tested the concept of low-field MRI of ^{3}He [48] on a solenoidal magnet, showing that a large magnetic field is not necessary to obtain ^{3}He images with the same quality as those from conventional scanners. Since then we have developed novel magnet designs for human imaging that relied on simple resistive coil elements rather than cumbersome superconductors. More recently we demonstrated the feasibility of this type of open-access ^{3}He lung MRI on a prototype system [49].

1.6 Posture-Dependence in Lung Function

Regional heterogeneity of pulmonary ventilation and perfusion is well-known to be influenced by gravity [1, 50, 51], but is also affected by the lung parenchyma and surrounding organs and stroma, leading to some controversy over which effect is more physiologically relevant [52–54]. This has important clinical implications in mechanical ventilation, for example, where patients who are ventilated in a prone position tend to have improved gas exchange compared to those lying supine [55, 56], and perfusion and ventilation changes are evident [57]. FRC and gas elimination has been shown to be gravity-dependent [58], suggesting local differences in local airway resistance.

Of particular interest is the change in gas exchange dynamics when a subject is moved from a supine to an upright position. This change in orientation forces thoracic and abdominal contents downwards, lowering the diaphragm and distending the lungs. Ribcage motion during the breathing cycle is also increased as a result of the altered load as well as changes in respiratory muscle tone [59]. Total FRC and conductance is known to significantly decrease in normal individuals undergoing such a postural change [60, 61], but regional dynamics have not been measured. Although this has a small net effect on the overall respiratory mechanics of normal individuals, it can have a profound impact in disease. For example, in obese patients TLC and FRC are markedly decreased in either posture, while baseline airway resistance is increased and maximized in the supine state [62]. Although it is generally understood that global lung mechanics are altered due to the increased load from surrounding abdominal contents and subcutaneous fat in such individuals, this provides an inadequate explanation for the observed changes in pulmonary function [63].

Regional measurements reflecting local gas dynamics would reveal areas where the most significant physiological changes occur within the lung following a change in subject posture. Such data would be useful for a wide variety of clinical problems such as

aerosol drug delivery to mechanical ventilation techniques. Posture-depedence may also be revealed in a variety of pathophysiological processes, with potential implications for novel treatments. For example, PET imaging has suggested that gas exchange defects in asthmatic lungs possess gravitational-dependence, but so far the data are restricted to axial slices across supine lungs [19].

To date, all pulmonary function tests performed on upright individuals have been via spirometry, with global resistance/conductance measurements limited to forced oscillation techniques performed at the mouth. $\dot{V}_A/\dot{Q}$, pO_2, and ADC maps of the lung as obtained via PET or MRI are capable of reliably resolving regional dynamics and anatomical features, but these have all been performed on supine or prone individuals only.

1.7 Dissertation Overview

The goal of this project was to design, construct, and optimize an open-access MRI system that would allow quantitative ^{3}He studies of human lung function as a function of subject orientation. Chapter 2 details the ^{3}He hyperpolarizing process and the apparatuses built and used to produce and monitor hyper-polarized ^{3}He in our experiments, as well as basic NMR experiments and tests performed. Chapter 3 describes the motivation and advantages of imaging at low-fields, and describes the design, construction, and optimization of the low-field MRI system. Chapter 4 details ^{1}H and ^{3}He NMR and imaging experiments used to optimize the MRI system for qualitative imaging as well as quantitative measurements of pO_2. Chapter 5 provides a description of ^{3}He lung experiments performed thus far, and outlines future projects that would take full advantage of the unique features of the imaging system.

Chapter 2

Hyperpolarized ^{3}He NMR and MRI

This chapter begins with a comparison between thermally polarized ^{1}H and hyperpolarized ^{3}He NMR, followed by an overview of the spin-exchange optical pumping technique (SEOP) used to produce hyperpolarized ^{3}He. We then provide details of the ^{3}He polarizer and the polarimeter system. Flip angle and polarization calibrations are then described, followed by a general description of imaging pulse sequences used in our ^{1}H and ^{3}He experiments.

2.1 Thermally Polarized ^{1}H vs Hyperpolarized ^{3}He

A basic overview of the principles of NMR is given in Appendix A. This summary includes a very brief description of the principles of nuclear magnetic resonance. Included are definitions and discussion of T_1 and T_2 relaxation and flip angle (θ), which will be used repeatedly throughout the remainder of this dissertation.

NMR is possible because atoms possessing a non-zero nuclear spin have a net magnetic moment. For nuclear spin-$\frac{1}{2}$ systems such as ^{1}H and ^{3}He, the net polarization

P of an ensemble of spins can be defined as:

$$P \equiv \frac{N_+ - N_-}{N_+ + N_-}, \tag{2.1}$$

where N_+ and N_- refer to the number of spins in the nuclear spin sublevel (m_I) $+\frac{1}{2}$ or $-\frac{1}{2}$, respectively. The bulk magnetization M_0 of a collection of spins is:

$$M_0 = \frac{1}{2} N \gamma \hbar P, \tag{2.2}$$

where N is the total number of spins and γ is their gyromagnetic ratio. At a given temperature T and an external magnetic field B_0, P follows a thermal equilibrium:

$$P = \tanh(\frac{\gamma \hbar B_0}{2 k T}) \approx \frac{\gamma \hbar B_0}{2 k T}, \tag{2.3}$$

where k is the Boltzmann constant. The approximation is valid for all practical cases because the magnitude of the nuclear magnetic moment is extremely small. At 300 K and 1 T, $P = 3.4 \times 10^{-6}$ for protons in water. This small polarization factor, in combination with the small proton magnetic moment, is the reason why a large B_0 is desirable for conventional ^{1}H NMR and MRI, as $M_0 \propto B_0$.

When ^{3}He is placed in a static magnetic field it too will achieve a Boltzmann polarization. However, for all practical purposes the net magnetization of a 1 L sample of ^{3}He at atmospheric pressure is miniscule in comparison to the equivalent sample volume of water, owing primarily to the smaller density of ^{3}He. A comparison of the two species is summarized in Table 2.1. The net result is a total ^{3}He magnetization that is 2.3×10^{-4} smaller than water for an equivalent volume at a given B_0. This makes conventional MRI with thermally polarized ^{3}He impractical even with the most sensitive detectors.

Hyperpolarization refers to a process whereby nuclear moments are polarized to a level greater than the Boltzmann level. SEOP, MEOP, and direct nuclear polarization (DNP) are all examples of hyperpolarization schemes. For ^{3}He, P can be increased to 0.1–0.6 using the hyperpolarizing technique described in the following section. This

	^{1}H	^{3}He
Gyromagnetic Ratio (kHz/G)	4.26	3.24
Magnetic moment (μ_N)	-2.79	-2.13
Spin density at 300 K, 1 atm (L^{-1})	6.69×10^{25}	2.69×10^{22}
P at 1 T (thermal equilibrium)	3.4×10^{-6}	2.6×10^{-6}
Total magnetic moment for 1 L sample (μ_N)	6.35×10^{20}	1.49×10^{17}

Table 2.1: Table comparing NMR characteristics for ^{1}H and ^{3}He. ^{1}H density for a human subject is roughly similar to that of pure water, which was used for these calculations.

$\sim 10^5$ improvement over thermal polarization results in a net magnetization that equals or exceeds that of an equivalent volume of water, and thus makes ^{3}He MRI a practical imaging modality.

2.2 Spin-Exchange Optical Pumping of ^{3}He

Spin-exchange optical pumping (SEOP) of ^{3}He is a two-step process: Rb valence electrons are optically pumped to a single ground-state spin state and then collisional spin-exchange between the polarized Rb electron and ^{3}He nuclear spin transfers the polarization [36, 64].

2.2.1 Optical Pumping of Rb

Optical pumping of alkali metals was first demonstrated by Kastler in 1950 [65], a discovery which later earned him a Nobel Prize. SEOP with ^{3}He uses rubidium (Rb, Z = 37), a soft, silver-colored metal with a melting point of 312 K.

Figure 2.1 summarizes the Rb optical pumping scheme, also known as depopulation optical pumping. The Rb is typically heated so that there is an appreciable amount of Rb vapor present. Circularly-polarized laser light is tuned to the 794.7 nm D1 line to drive transitions from the $5^2S_{\frac{1}{2}}$ ground state to the $6^2P_{\frac{1}{2}}$ excited state. $\sigma+$ polarized light is drives only a $m = -\frac{1}{2}$ to $m = +\frac{1}{2}$ transition. Electrons can decay

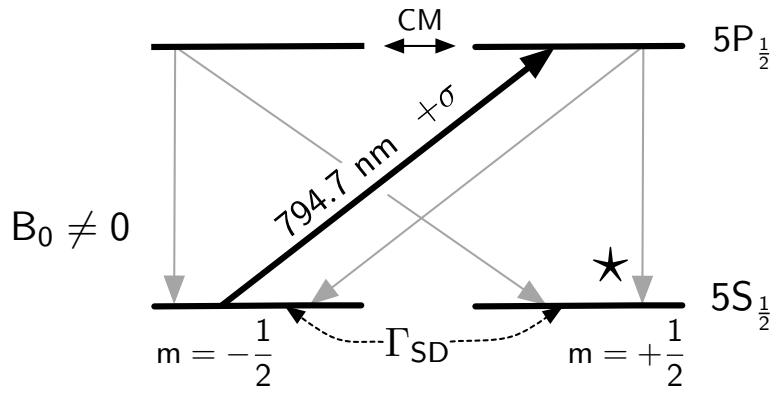

Figure 2.1: A diagram of the Rb optical pumping process. A non-zero magnetic field B_0 causes splitting of the spin angular momentum to $\mathsf{m} = \pm\frac{1}{2}$. $+\sigma$ 794.7 nm light drives a $\Delta\mathsf{m} = +1$ transition only (black arrow). Collisional mixing (CM) occurs between the spin sublevels in the $5\mathsf{P}_{\frac{1}{2}}$ state. Light gray lines show Rb decay dominated by N_2 quenching. This process results in a net polarization of the Rb to the $\mathsf{m} = +\frac{1}{2}$ ground state ($\star$), counteracted by spin destruction factors (Γ_{SD}).

back to the $m = -\frac{1}{2}$ or $m = +\frac{1}{2}$ ground state, with probabilities $\frac{2}{3}$ and $\frac{1}{3}$, respectively, as given by the Clebsh-Gorden coefficients. However, randomly-polarized fluorescence from this decay can re-excite ground-level Rb electrons back to either the $m = -\frac{1}{2}$ or $m = +\frac{1}{2}$, effectively destroying the desired electron polarization, a process known as radiative trapping. To limit this effect, nitrogen is added as a buffer gas. Excited electrons can then decay without any photon emission, instead transferring their energy to the rotational and vibrational motion of the nitrogen. A few hundred Torr of N_2 is enough to quench radiation trapping by reducing the lifetime of the Rb in the excited state [66]. The buffer gas and nearby ^{3}He also induces collisional mixing in Rb between $m = \pm\frac{1}{2}$ within the $6^2\mathrm{P}_{\frac{1}{2}}$ state. This results in an equal re-population of the ground states. However, any electrons returning to $m = -\frac{1}{2}$ are re-excited by the $+\sigma$ laser light. Eventually the Rb electrons are pumped into the $m = +\frac{1}{2}$ ground state with a typical re-pumping time of order milliseconds.

This description has thus far ignored the hyperfine interaction. The ground-

state Hamiltonian operator of Rb in a static magnetic field $\boldsymbol{B} = B_0\hat{\boldsymbol{z}}$ is

$$H = a\boldsymbol{I}\cdot\boldsymbol{S} + g_e\mu_B S_Z B_Z + \frac{\mu_I}{I} I_Z B_Z, \tag{2.4}$$

where $\boldsymbol{S}$ is the electron spin angular momentum, $\boldsymbol{I}$ is the nuclear spin ($I = \frac{5}{2}$ for ^{85}Rb and $\frac{3}{2}$ for ^{87}Rb), $g_e = 2.002$ is the electron g value, μ_B is the Bohr magneton, and μ_I is the nuclear magnetic moment. The first term describes the hyperfine interaction with a as the magnetic dipole coupling coefficient, and the second and third terms describe the nuclear and electron spin interactions with the applied magnetic field, respectively. At low fields typically used for the polarization process, the hyperfine interaction *dominates* over the Zeeman one. The total angular momentum is $F = I + S$, but $+\sigma$ light drives only $\Delta m_F = +1$ transitions, so there still remains a sublevel that cannot be optically driven and polarization can proceed. Angular momentum can be transferred to nuclear sublevels, slowing the the overall polarization process [67]. However, in practice this can be ignored because the steady-state polarization is achieved very quickly. Also, under typical operating conditions, the hyperfine levels are all equally excited by the laser light. This is because pumping cells are typically run well above 1 bar and the resulting pressure-broadened D1 linewidth is roughly an order of magnitude or greater than the hyperfine splitting. Thus the simplified description of Rb optical pumping above suffices.

The steady-state polarization of Rb is achieved through a balance of optical pumping rate γ_{opt} and the depolarizing spin destruction rate Γ_{SD}:

$$P_{Rb} = \frac{\gamma_{opt}}{\gamma_{opt} + \Gamma_{SD}}. \tag{2.5}$$

The position-dependent optical pumping rate depends on the laser intensity profile $\Phi(\boldsymbol{r}, \nu)$ and the Rb absorption cross-section $\sigma(\nu)$, both a function of the laser frequency ν:

$$\gamma_{opt}(\boldsymbol{r}) = \int \Phi(\boldsymbol{r}, \nu)\, \sigma(\nu)\, \mathrm{d}\nu \tag{2.6}$$

Several factors contribute to Γ_{SD}, including radiation trapping, Rb–wall interactions, and Rb–^{3}He, Rb–N_2, and Rb–Rb interactions. Of these, Rb–wall interactions dominate. Rb can collide against a cell wall (usually made of glass) and depolarize, but this effect is limited because the presence of other gases (N_2 and ^{3}He) at high pressures restricts the diffusion of the Rb atoms within the cell volume. Thus a thin layer of depolarized Rb coats the inner cell wall, except at the side where laser light enters; it is here that a large portion of photon absorption occurs, as there is constantly a large population of depolarized Rb atoms.

Collisional interactions between Rb and other gas atoms, including a second Rb atom, fall under two general categories. The first is the spin-rotation interaction, whereby the Rb electron spin angular momentum $\boldsymbol{S}$ is conferred to the rotational momentum $\boldsymbol{N}$ of the colliding pair. The second is spin exchange, which involves transfer of the Rb electron spin angular momentum to some external spin system. Both these processes contribute to Γ_{SD} but are relatively minor in the case of ^{3}He, and can be ignored for our purposes. In these cells, if there is enough laser power to match the optical thickness of the Rb vapor in the cell, the Rb polarization is typically near 100%. This is in great contrast to SEOP with ^{129}Xe, where particularly strong Rb–Xe spin rotation interactions dominate in Γ_{SD} and can significantly reduce Rb polarization [68, 69].

2.2.2 Rb–^{3}He Spin Exchange and ^{3}He Hyperpolarization

The collisional interaction between ^{3}He and Rb is a combination of both spin rotation and spin exchange terms:

$$\boldsymbol{H}_{Rb-He} = \gamma\, \boldsymbol{N} \cdot \boldsymbol{S} + \alpha\, \boldsymbol{K} \cdot \boldsymbol{S}. \tag{2.7}$$

The first term is the spin rotation interaction as discussed in the previous section. The second term refers to spin exchange, a Fermi-contact interaction where $\boldsymbol{K}$ is the nuclear spin of ^{3}He. γ and α are coupling constants that are strongly dependent on inter-atomic

separation. Both terms result in a net depolarization of Rb, but the second process is responsible for transferring the polarized Rb spin state to ^{3}He. It is by this transfer that ^{3}He becomes hyperpolarized. Recently, the spin exchange coefficients for Rb–^{3}He were measured to be $\sim 7 \times 10^{-20}$ cm^3/s [70].

While the steady-state of Rb polarization in a ^{3}He cell is achieved in several milliseconds, ^{3}He polarization occurs on the order of hours. The relatively slow ^{3}He hyperpolarization rate is due primarily to the tight overlap required between the Rb electronic wave function and the ^{3}He nucleus for spin exchange to occur; α is strongly exponential with inter-atomic distance, so only a small fraction of collisions can produce enough of this overlap [71].

^{3}He hyperpolarization via SEOP can be described by a simple exponential:

$$P_{^3\mathrm{He}}(t) = P_{\mathrm{Rb}}\frac{\gamma_{SE}}{\gamma_{SE}+\Gamma}[1 - e^{-(\gamma_{SE}+\Gamma)t}], \tag{2.8}$$

where the Rb polarization assumes a steady state as described by Equation 2.5, and γ_{SE} and Γ represent the Rb–^{3}He spin exchange and total ^{3}He spin depolarization rates, respectively.

Since a small fraction of Rb–^{3}He collisions lead to spin exchange, it is proportional to the Rb density inside a cell, assuming enough laser power is provided [72]. This favors the use of heated cells for ^{3}He SEOP because the Rb vapor pressure is highly sensitive to temperature:

$$\log_{10} p = 10.55 - \frac{4132}{T}, \tag{2.9}$$

where T is expressed in Kelvin, and p is in bar [73].

2.2.3 ^{3}He Relaxation

^{3}He depolarization can occur through multiple mechanisms, of which the most important are ^{3}He–^{3}He and ^{3}He–wall interactions, and ^{3}He interactions with magnetic

field inhomogeneities. In practice, ^{3}He depolarization is synonymous with T_1 relaxation because the thermal polarization of ^{3}He is essentially zero; the Γ term in Equation 2.8 can therefore be substituted with $1/T_1$.

^{3}He polarization is performed in glass cells because they are transparent to laser light and are resistant to alkali metals. They can also withstand high heat and pressure, have low out-gassing rates, and are relatively impermeable to ^{3}He. In practice most high-volume-delivery ^{3}He polarizer cells possess T_1 of several tens of hours [72]. It has been theorized that wall relaxation occurs due to ferromagnetic impurities in the glass [74]. ^{3}He gas can dissolve in glass long enough to become depolarized. Recent studies by Jacob et. al. have shown that the relaxation mechanism in Pyrex$^{\text{TM}}$(borosilicate) glass stems from dissolved ^{3}He interacting with $^{+3}$Fe ions, with the corresponding activation energy dominated by ^{3}He diffusion within the cell [75]. Non-stick wall coatings have prolonged relaxation times [76] but are often incompatible for gas delivery or for Rb containment. Functional polarizers require the ^{3}He/Rb cell to contain valves for gas delivery; relaxation is accelerated at o-rings and vacuum grease where ^{3}He can more easily be adsorbed, so cells are often designed with long capillaries to prolong ^{3}He diffusion times to those areas.

Magnetic field inhomogeneity depolarizes ^{3}He because atoms diffusing through local field gradients can experience a non-adiabatic change in magnetic field direction, leading to spin flips. The contribution to T_1 is described by the following relationship:

$$\frac{1}{T_1} \sim D\left(\frac{\nabla B}{B}\right)^2, \tag{2.10}$$

where D is the diffusion constant of ^{3}He, B_0 is the average magnetic field and ∇B is the magnetic field gradient [77, 78]. It has been recently revealed that wall relaxation may be in part due to local magnetic field in homogeneities from impurities in the glass or even Rb itself, and degaussing such cells can lead to significant increases in T_1 time [79].

^{3}He self-relaxation is the last major mechanism of depolarization within a cell,

and is achieved through magnetic-dipole to magnetic-dipole interactions, first studied in detail at low temperatures [80]. Newbury et. al. determined that, at room temperature, the dipolar relaxation rate is:

$$\frac{1}{\tau} = \frac{[^3\mathrm{He}]}{744}\mathrm{h}^{-1}, \tag{2.11}$$

where $[^3\mathrm{He}]$ is the density of the gas in amagats [81]. This represents the practical limit of ^{3}He T_1 for a given pressure. With careful preparation it is possible to create ^{3}He cells whereby this dipolar relaxation dominates over wall relaxation and magnetic field inhomogeneity effects [36], but this is difficult to do in practice, especially for cells designed for gas delivery.

2.3 ^{3}He Polarizer

We produce highly polarized ^{3}He using the SEOP method described above. For human imaging studies which require large volumes of hyperpolarized ^{3}He, we designed and built a modular ^{3}He polarizer with gas storage, transport, and delivery stages similar to other noble gas polarization systems [72, 82]. Photographs of the polarizer can be seen in Figure 2.2. Our system also needed to be transportable for ^{3}He experiments performed at multiple sites, so we constructed our system to have a minimal footprint and a frame with built-in casters for easy transport. The chassis was built using an aluminum framing system [Bosch Industries] that we could modify and assemble to our specifications. The polarizer itself can be divided into five general sections: the B_0 coils, the ^{3}He cell and oven, the laser and optics, the gas filling and vacuum station, and the gas delivery system. A schematic diagram can be seen in Figure 2.3.

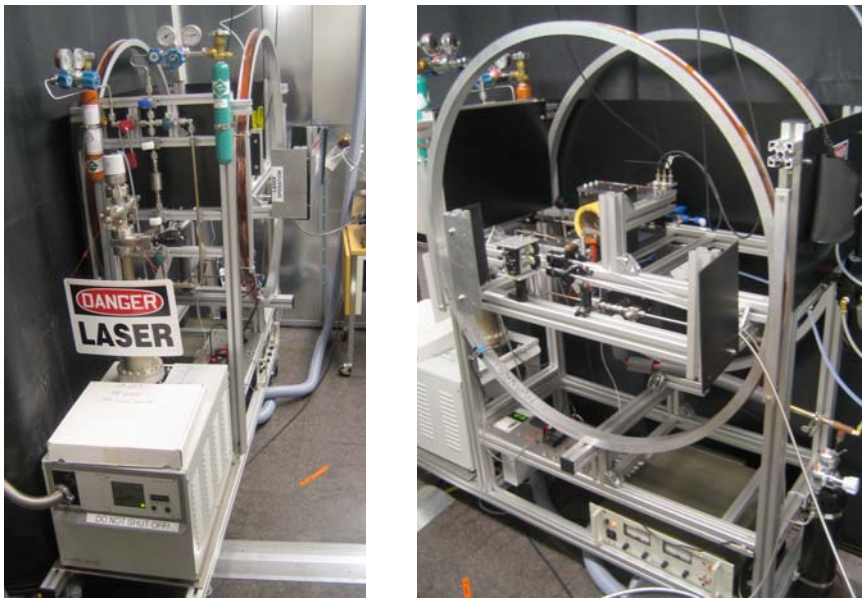

Figure 2.2: Two views of the ^{3}He polarizer. Some laser guards have been removed so that the B_0 coils and ^{3}He cell can be more easily seen.

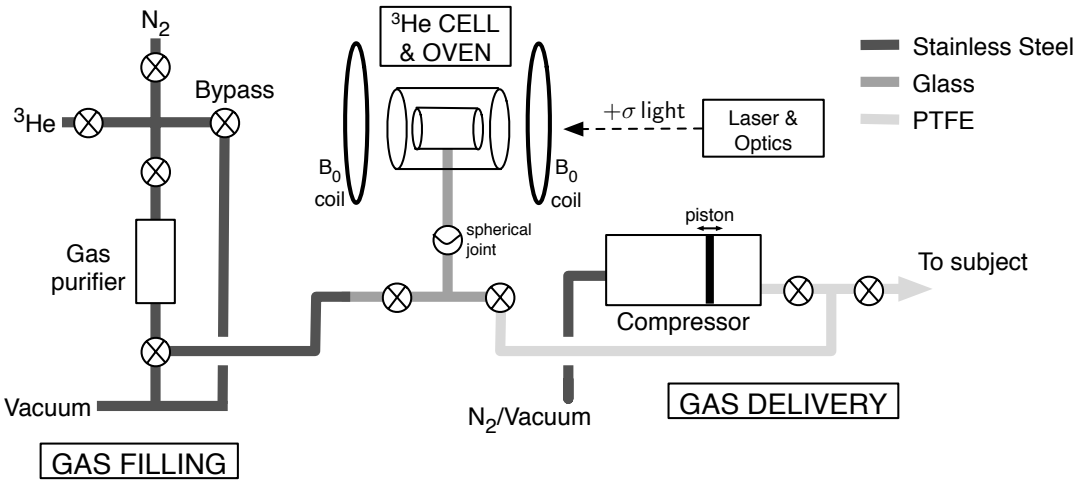

Figure 2.3: A schematic diagram of the ^{3}He polarizer, roughly separated into gas-filling, cell and B_0, and gas delivery sections. A map of the different tubing materials is also included. A more detailed schematic of the polarizer optics can be seen in Figure fig:polarizeroptics.

2.3.1 B_0 Coils

The polarizer B_0 coils consist of two one-meter coils separated by ~ 0.5 meters, in a Helmholtz configuration. This arrangement produces a highly homogeneous field at the center, where the ^{3}He cell rests. To determine if this coil arrangement was theoretically homogeneous enough for SEOP we estimated the ∇B contribution to T_1 using Equation 2.10. The magnetic field B_z along the axis of a Helmholtz coil is:

$$B_z = \frac{\mu_0 i}{2r}\left[\frac{1}{\left(\gamma^2+\gamma+\frac{5}{4}\right)^{3/2}}+\frac{1}{\left(\gamma^2-\gamma+\frac{5}{4}\right)^{3/2}}\right] \tag{2.12}$$

where r is the coil radius, γ is the ratio of the displacement from the center along the coil axis to r, i is the current through the coils, and μ_0 is the magnetic permeability constant. Using $r = 0.5$ m, $\gamma = 0.10$, and Equation 2.10, we calculate the $\frac{1}{T_1}$ contribution to be only 1.87×10^{-9} s for 5 atm of ^{3}He in the polarizer cell, far smaller than contributions from wall relaxation.

Each coil form consists of an extruded aluminum U-channel bent into a circular one-meter-diameter form with the two ends welded together. 10-AWG polyester-insulated copper magnet wire [MWS Wire Industries] was wound 66 times around each coil form (11×6 layers). The helmholtz geometry provides a relatively large region of homogeneity while providing an open-access environment for gas handling operation. The total resistance per coil is 0.7 Ω at room temperature (300 K). Both coils are wired in series to a Hewlett-Packard 6264B DC power supply. With this configuration we are able to obtain a sustained maximum center B_0 of 12.6 G at 11 A. The surface of the coils reach a steady-state temperature of approximately 50° C under this configuration and the total resistance of the coils rises to ~ 2.0 Ω. Under typical operating conditions we set $B_0 = 6.0$–6.5 G, where the resonant ^{3}He frequency is 19–22 kHz.

2.3.2 ^{3}He Cell and Oven

A variety of ^{3}He cells have been used; some of their relevant characteristics are summarized in Table 2.2. All cells were manufactured by Roy Wentz at the University of Michigan. Our first-generation cells (no longer in use) were made of GE-180 glass [Corning Industries], since then our cells have been made of Pyrex (borosilicate).

Cell	Material	Inner Volume (cc)	T_1 (h)
001	GE-180	90	< 2.0
002	GE-180	90	< 2.0
101	Pyrex	90	2.0
201	Pyrex	82	2.6
202	Pyrex	84	0.8
203	Pyrex	84	3.3
301	Pyrex	67	19.4
401	Pyrex	83	17.3

Table 2.2: Table of several ^{3}He cell characteristics. All T_1 measurements were performed using either the polarimeter system on the polarizer described below, or the low-field imager described in the following chapter. 3000–5000 Torr of ^{3}He was used for theses meaurements. Cell designs beginning with 301 were manufactured with a capillary tube connecting the main body of the cell to the valve. This reduced wall relaxation effects from the valve and significantly increased T_1.

In general, our ^{3}He cells are cylindrical with a diameter of 3–4 cm and a length of 9–12 cm. The ends either employ flat optical windows for the optimal passage of laser light, or are rounded blown ends extended from the main body of the cylinder. The inner volume ranges from 75–85 cubic centimeters (cc) depending on the cell design and window type. Since typical human lung experiments require approximately 400–500 cc of ^{3}He at 1 atm, the cell must be capable of withstanding at least 6 atm of pressure at 300 K and 10 atm at 500 K, the latter temperature being one typically used for SEOP on this system. To ensure that the cells can handle the large pressures, the cell wall is typically at least 3.5 mm thick.

Each cell is attached to a single glass valve that connects the cell to the the polarizer gas filling and delivery components. The valve stems are made of glass and

sealed with a single o-ring made of Viton rubber. A thin coating of vacuum grease is applied to the o-ring to ensure a proper airtight seal. We have recently used a thin capillary tube to connect the main cell cylinder to the valve; this greatly increases the diffusion time of ^{3}He from the cell body to the o-ring, where wall relaxation is greatly accelerated. As shown in Table 2.2, the inclusion of a $\sim$ 20 cm of 0.5 mm-diameter capillary increases the cell T_1 by at least one order of magnitude. A photograph of the most recent cell (Figure 2.4) shows the cell body as well as the capillary tube, which is coiled to allow for a long capillary length within a compact design.

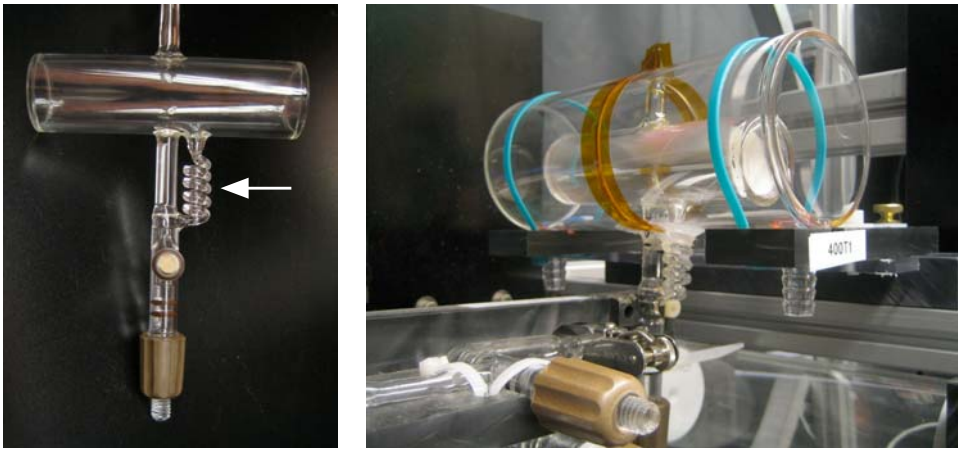

Figure 2.4: Left: Photograph of a ^{3}He cell prior to Rb filling. The arrow shows the coiled 0.5 mm-diameter capillary tube that connects the cell body to the valve below. The straight piece to the left of the capillary is a support beam of a solid glass. The stem at the top of the cell is used for Rb filling; following that procedure, the stem is pulled and sealed. Right: the same cell with its oven shell and mounting stage on the polarizer, with the fiberglass blanket removed. This entire unit can completely detach from the polarizer for NMR experiments that do not require gas delivery.

Each new cell is cleaned prior to the introduction of Rb. A pirhana solution (70% H_2SO_4, 30% H_2O_2 by volume) is typically used to clean the inner walls for cells that were not shipped immediately after the annealing process. All cells are then subject to three rinses with dIH_2O and three rinses with chromatography-grade methanol. The cell is then dried inside a vacuum oven at $\sim$ 420 K for 12 hours, then attached to

our cell filling station and baked for at least 48 hours at 520–550 K on a ultra-high-vacuum (UHV) system. When the cell is cooled back to room temperature the typical UHV pressure inside a clean cell is approximately 1×10^{-8} Torr. We then chase a few milligrams of Rb into the cell with a heat gun and flame-seal the cell interface to the UHV system and Rb ampule, leaving only the valve used for attachment to the polarizer.

A Pyrex cylinder surrounds the ^{3}He cell and serves as an oven (Figure 2.4). The bottom of the oven contains inlet and exhaust nozzles where heated air is passed through. A resistive temperature detector (RTD) is placed at the outlet nozzle and a Omron 3000 temperature control system activates a 1000 W ceramic air heater. Approximately 15 psi of air pressure drives filtered air through the heater and oven. A fiberglass blanket is wrapped around the oven to help maintain an even distribution of heat across the cell. Each cell is permanently attached to its own oven and mounting stage. We are typically able to reach an operating temperature of ~ 480 K in approximately 10 minutes. The ^{3}He cell valve interfaces with the rest of the polarizer via a single spherical glass joint with a Viton o-ring. This joint is held together with a stainless steel clamp, allowing safe operation at high pressures. The detachable joint allows the cell and its oven to be easily removed from the polarizer for NMR experiments that do not require delivery and loss of ^{3}He.

2.3.3 Laser and Optics

Two 30 W laser diode arrays (LDA) [Coherent Laser] provides the circularly-polarized 795 nm laser light. A pair of polarizing cubes splits each laser into separate beams with vertical and horizontal polarization. Four $\frac{1}{4}-\lambda$ waveplates are set with their fast axes $+45^\circ$ from the incident polarization axes so that all four beams are circularly polarized in the $+\sigma$ orientation.

The wavelength and output power of the LDAs are sensitive to the laser diode

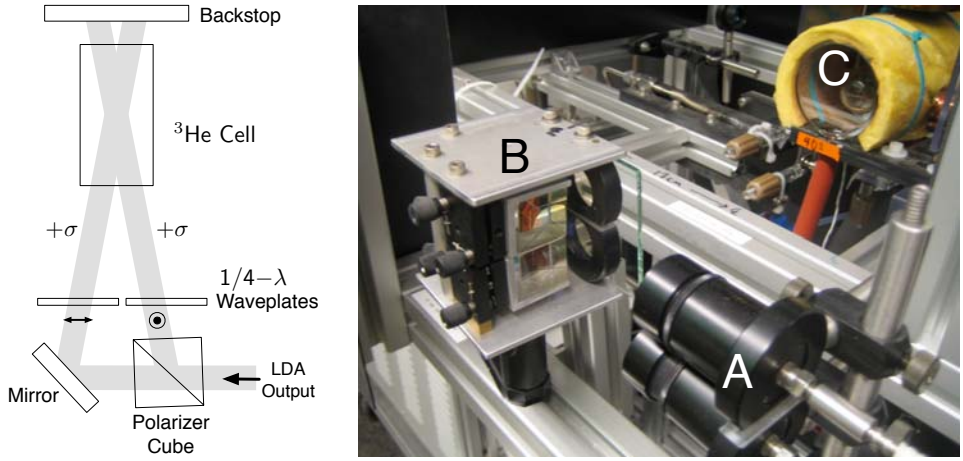

Figure 2.5: Left: A diagram of the polarizer optics guiding the output of the LDA and producing $+\sigma$ polarized light to the ^{3}He cell. The mirrors can be used to adjust the laser light path to the cell. The laser polarization is indicated just prior to the waveplates. Right: A photograph of the optics. Shown are the LDA fiber optic output (A), the unit containing the mirrors, polarizer cubes, and $\frac{1}{4}$-λ waveplates (B) and the ^{3}He cell (C).

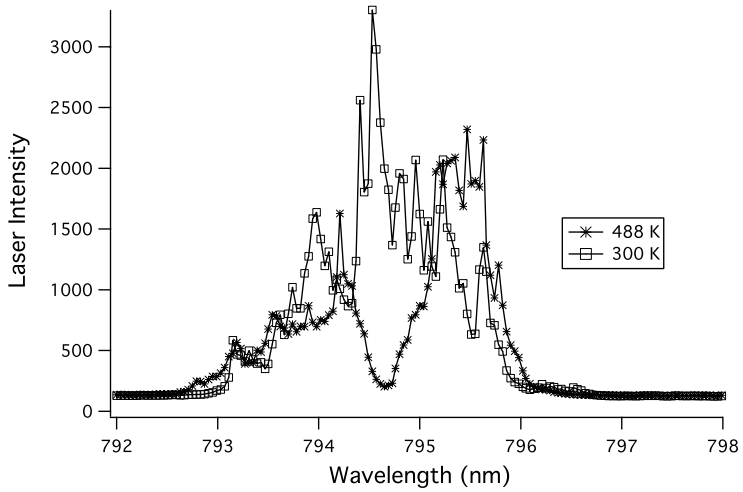

Figure 2.6: Typical LDA spectrum from unit 2017 [Coherent Laser] showing the intensity profile (arbitrary units) as a function of wavelength following passage through a ^{3}He cell at room temperature (300 K) and at a typical SEOP temperature (488 K). Although the Rb absorption line is temperature and pressure-broadened the LDA linewidth is still significantly wider.

temperature and the input current, and care must be taken to ensure that the lasers are tuned to the desired wavelength to maximize light absorption from Rb. We used a CCD-based spectrometer [Ocean Optics Inc.] to profile the LDA lineshapes from each of our lasers and to tune them to optimal diode temperature and current. SEOP parameters were determined by numerical simulations, given the polarizer cell geometry, operating pressure and temperature, and laser linewidth [68]. As shown in Figure 2.6, the LDA has a characteristically broad 2–3 nm linewidth that results in some laser power wasted during SEOP, as the Rb D1 line is less than 1 nm at 488 K.

2.3.4 Gas Filling and Delivery

We fill ^{3}He cells on the polarizer using a dedicated gas handling apparatus complete with an UHV system. A turbo vacuum pump [Pfiffer Inc] and a direct-drive mechanical roughing pump provides the vacuum. Lecture bottles containing ultra-pure ^{3}He and N_2 are located upstream of an inert gas purifier [Aeronex, Mykrolis Corp.] which reduces any traces of oxygen and water to below 1 ppb. All gas lines consist of electropolished stainless steel with VCR connectors and hand-operated UHV diaphragm valves. A cold cathode ionization gauge measures the turbo pump port pressure (1×10^{-9}–10 Torr), while a MKS Baritron sensor measures the gas filling pressure (1–10000 Torr). Before we fill a ^{3}He cell we evacuate it, leaving only the Rb metal inside. We then introduce 190 Torr of N_2 buffer gas, followed by 3000–5000 Torr of ^{3}He. To minimize the waste of ^{3}He we designed the gas filling station to have a minimal amount of dead space ($\sim$ 20 cc).

An all-glass manifold controls gas flow from the ^{3}He cell to either the gas filling area or the gas delivery apparatus. The latter section is located near the homogeneous region of B_0 and all gas delivery tubing consists of non-magnetic 1/4-inch perfluoroalkoxy (PFA) Teflon tubing with Teflon valves and Teflon-PFA Swagelok fittings to minimize T_1 wall-relaxation effects and dead space volume. To deliver ^{3}He from

the cell, we first evacuate a 1.0 L pneumatic piston-driven glass and teflon compressor, then open a connection between the two (Figure 2.3). The volume ratio is typically > 15 so nearly all of the ^{3}He diffuses into the compressor. We then close the cell and pressurize the gas to 1.1 atm by delivering pressurized N_2 from the other side of the piston. A valve connecting the compressor output to a delivery tube is then opened and ^{3}He flows out to the target. This pneumatically-driven delivery system is the first of its kind to be used on any polarizer.

2.4 ^{3}He Polarimeter System

To monitor the progress of ^{3}He laser-pumping in our polarizer we built a polarimeter system to be operated *in situ*. This essentially operates as a stand-alone pulsed-NMR system within the B_0 magnetic field of the polarizer. A schematic and photograph are shown in Figures 2.7 and 2.8. A single transmit coil and a pair of receive

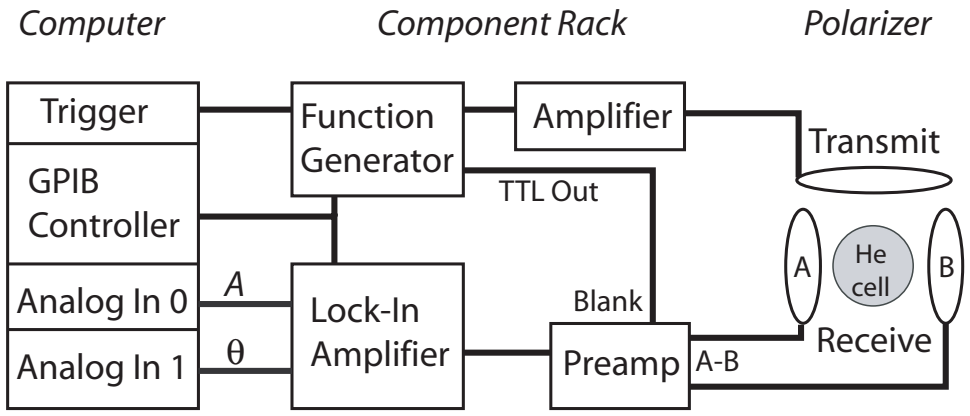

Figure 2.7: A schematic diagram of the polarimeter system. The data acquistion, triggering, and GPIB interfacing are controlled using a computer with Labview-controlled hardware. An adjoining component rack houses all other electronics.

coils surround the ^{3}He cell. A DS345 function generator [Stanford Research Systems, Inc], triggered by a data acquisition card on a computer, provides a sinusoidal RF pulse which is passed through a power audio amplifier that provides an additional 8 dB of gain.

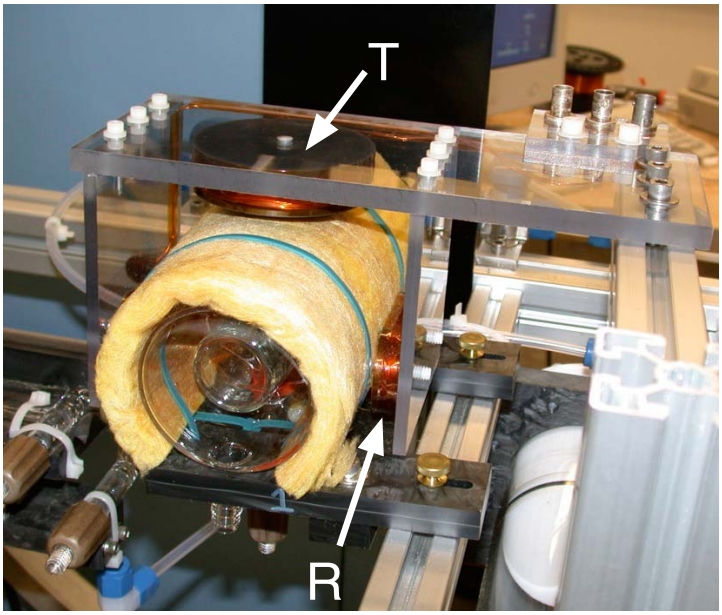

Figure 2.8: The B_1 transmit (T) and receive (R) coils mounted around the ^{3}He cell on the polarizer. A second receive coil (not shown) is mounted on the side of the cell opposite from the labeled one.

The output of the amplifier is coupled to the transmit coil via a standard 50 Ω BNC cable. The two receive coils are connected to a SR560 [Stanford Research Systems, Inc] preamplifier in a subtractive configuration to reduce pickup noise. Because we operate over a large bandwidth (20 kHz) and require an SNR suitable enough for pulsed-NMR, we did not use any tuning circuitry and the coils possess a Q of ~ 1. In addition the preamplifier input impedance is high (1 MΩ), which allows us to use 50 windings on each of the receive coils to increase their sensitivity.

The output from the preamplifier is connected to a SR560 lock-in amplifier [Stanford Research Systems, Inc] which provides quadrature amplitude and phase outputs, referenced to an internal clock. These are read by a data accquisition card on a computer running Labview software [National Instruments, Inc]. In addition, the lock-in amplifier and function generator are controlled via a GPIB interface with the computer using the same Labview program. Pulse width, amplitude, and frequency on

the function generator, as well as sampling rates, detection frequency, and digital filtering parameters on the lock-in amplifier, are set in this fashion. FID and FT spectra are displayed following each pulse. The system can be programmed to take multiple pulses with a user-specified time delay for spin-up and spin-down measurements. 1 ms RF pulses with flip angles of 10–20° are commonly used to monitor ^{3}He polarization. All data are stored in spreadsheet format and imported into MATLAB routines for flip angle calibrations, T_1, and T_2^* measurements. A sample FID and FT spectrum obtained with the polarimeter can be seen in Figure 2.9

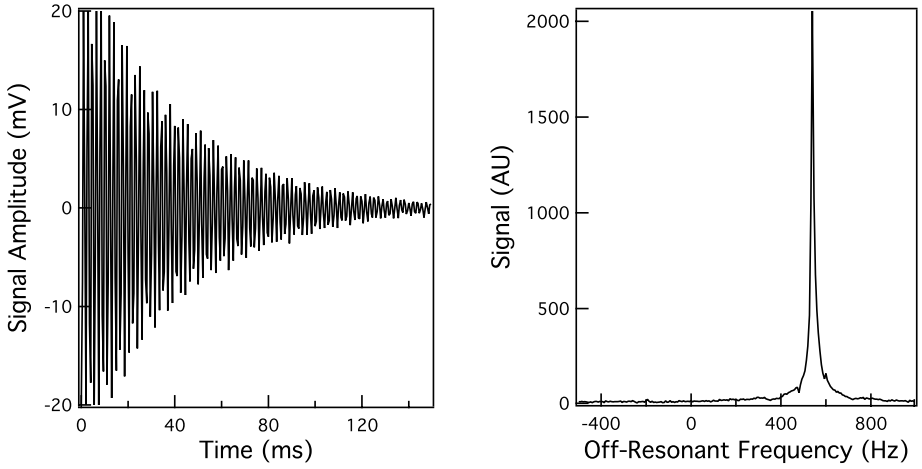

Figure 2.9: A sample FID and FT spectrum from the polarimeter, with $\theta = 14.1°$. T_2* $\sim$ 60 ms.

2.4.1 Flip Angle Calibration and T_1 Measurements

We use the polarimeter to assess polarizer and ^{3}He cell performance. Flip angle calibrations are performed to obtain an appropriate range of RF amplitude and pulse width settings. Once this is complete we can perform T_1 and spin-up measurements with the cell mounted on the polarizer.

As discussed in Section 2.1, at thermal equilibrium the ^{3}He magnetization and density are such that an NMR signal is undetectable at the magnetic fields that

we operate at (5–70 G). We can therefore effectively treat the thermal equilibrium magnetization as zero for all practical purposes. If we have a cell that is hyperpolarized with a bulk magnetization M_0, we expect the magnetization to decay to follow a T_1 exponential decay:

$$M(t) = M_0 e^{-\frac{t}{T_1}} \tag{2.13}$$

The magnetization is also affected every time an RF pulse is applied with a flip angle θ, because the bulk magnetization vector is rotated towards the transverse plane, leaving a fraction of the longitudinal component by a factor $\cos\theta$. Because the thermal equilibrium is effectively zero, the longitudinal component does not recover back to M_0 and the loss from the RF pulse is irreversible unless the ^{3}He is actively polarized again via SEOP.

If we apply several RF pulses with flip angle θ and an inter-pulse delay of τ, the longitudinal magnetization following the n$^{\text{th}}$ pulse is:

$$M_n = M_0 \cos^n(\theta) e^{-\frac{n\tau}{T_1}}. \tag{2.14}$$

The NMR signal detected by the receiver coil is proportional to the transverse component of the bulk magnetization ($M \sin\theta$), so we can rewrite Equation 2.14 as

$$S_n = kM_0 \sin\theta \, \cos^n(\theta) e^{-\frac{n\tau}{T_1}}. \tag{2.15}$$

k is the proportionality constant and is dependent on the RF coil resonance curve and the receive-channel amplification. Taking the natural log of both sides of this equation gives a linear relationship between S_n and n:

$$\ln(S_n) = \ln(kM_0 \sin\theta) + n\left[\ln(\cos\theta) - \frac{\tau}{T_1}\right], \tag{2.16}$$

where the slope b is dependent only on θ, T_1, and τ:

$$b = \ln(\cos\theta) - \frac{\tau}{T_1}, \tag{2.17}$$

We use this technique both for flip angle calibrations and T_1 measurements for our cells. To obtain a flip angle calibration we chose a τ that is relatively short compared to T_1; this is easily achieved since T_1 of ^{3}He is typically on the order of hours, and τ can be as short as a few hundred milliseconds. The slope is then:

$$b = \ln(\cos\theta). \tag{2.18}$$

We operate the polarimeter using a wide range of angles; as expected the flip angle depends linearly with RF amplitude (Figure 2.10). Once θ is known, a T_1 measurement

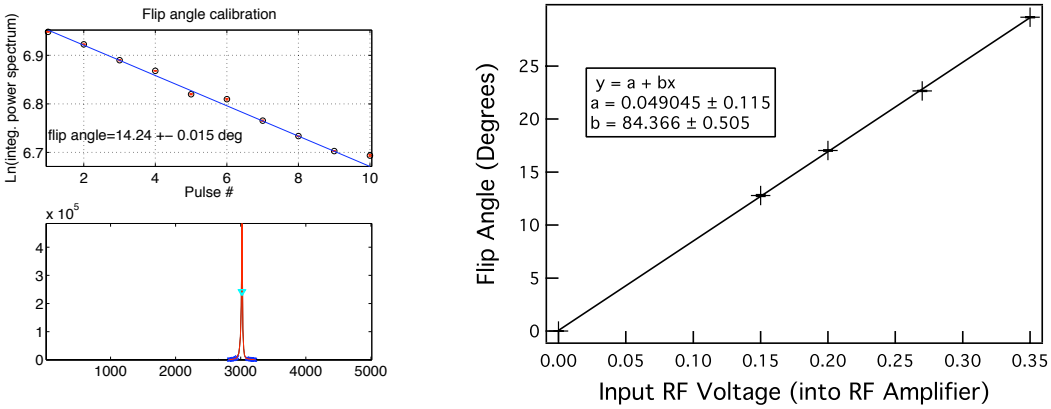

Figure 2.10: Left: An example flip angle calibration log plot and fit in MATLAB, with the first FT spectrum plot below. $\tau = 1$ s. Right: A plot of flip angles as a function of RF amplitude (peak-to-peak voltage set on the function generator).

can be performed using a similar pulse sequence and fitting routine as for flip angle calibrations. However, a larger value of τ is now used to make the T_1 component of the slope significant relative to $\ln\cos\theta$. We used this technique to measure T_1 of ^{3}He inside our polarizer cells (Table 2.2).

2.5 Polarizer Performance

We have successfully operated the ^{3}He polarizer at multiple sites in addition to our laboratory, including the University of New Hampshire (Durham, NH), the Brigham

and Women's Hospital (Boston, MA), and Millenium Pharmaceuticals (Cambridge, MA). We have performed ^{3}He cell NMR experiments and delivered polarized ^{3}He to phantom bag and cell systems as well as human and rat lungs. We typically filled the ^{3}He cells to 3000–5000 Torr, including 150 Torr N_2, at room temperature. Cells were heated to $\sim 215^\circ$ C with both lasers on, or $\sim 190^\circ$ C with one laser.

We use the polarimeter system to find an appropriate B_0 to operate in. This is especially important as the ^{3}He cell is not shielded from surrounding environmental noise. The largest noise sources often come from computer equipment, the LDA power supplies, and fluorescent light ballasts. The 18–24 kHz range is relatively quiet at most locations, however, and falls within the output range of the B_0 power supply (Figure 2.11). The B_0 homogeneity is adequate for SEOP but is sensitive to the

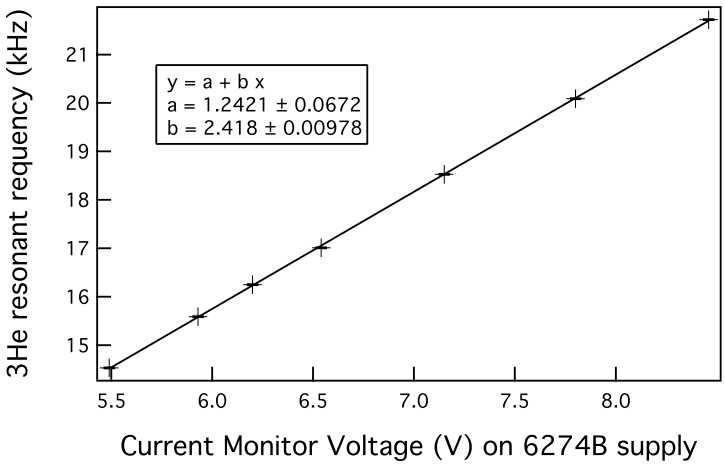

Figure 2.11: A plot of ^{3}He resonance frequency vs B_0 current monitor voltage on the HP 6264B power supply. We use this as a guide to set B_0 to the desired magnitude.

placement of the polarizer. Because the main coils are not magnetically shielded the presence of stray fields or nearby ferromagnetic substances can significantly effect the T_2* seen in the polarimeter FIDs. Typical T_2^* values range from 10–60 ms depending on the environment. We improve B_0 homogeneity by moving the polarizer away from the source of distortion (e.g., walls with steel framing) or the addition of small passive

steel shims.

We also use the polarimeter to monitor SEOP and relative ^{3}He hyperpolarization by pulsing every 10–30 minutes during the pumping process. The polarization rises in an monoexponential fashion:

$$P(t) = P_0 \left[1 - e^{-\frac{t}{\tau_{\text{spinup}}}}\right], \tag{2.19}$$

where P_0 is the starting polarization and τ_{spinup} is the spin-up time constant. Under typical operating conditions $\tau_{spinup} \sim$ 1.3–2.0 h (Figure 2.12). Thus to achieve near-maximum ^{3}He hyperpolarization we pump for at least six hours prior to each experiment.

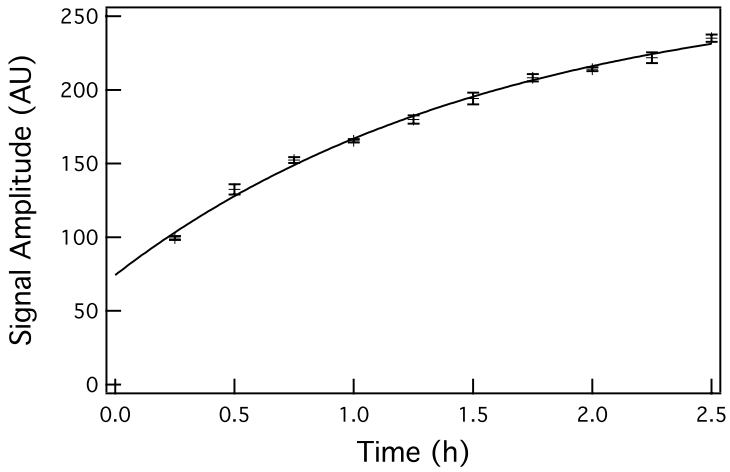

Figure 2.12: Example spin-up plot for a ^{3}He cell, taken with the polarimeter running during SEOP. The spin-up time constant is 1.58 ± 0.22 h for this cell (#201). A small flip angle ($\theta \sim 5°$) was used to allow for a simple mono-exponential fit. There is an appreciable signal amplitude at time zero because the cell was partially hyperpolarized when the polarimeter sequence was initiated.

A measurement of P requires a comparison between to a ^{3}He sample at thermal equilibrium to a hyperpolarized one. This is ideally performed by comparing the detected NMR signal from a ^{3}He sample at thermal equilibrium to the signal after undergoing SEOP, using the same sample, B_0, and RF and detector coils. In our case

this is impossible because we cannot detect a thermal ^{3}He signal at our magnetic field strengths. Instead we used two independent methods to estimate P. The first used a 7 T animal MRI system (at Millenium Pharmaceuticals, Cambridge MA) that could detect thermally polarized ^{3}He. We delivered hyperpolarized ^{3}He into a glass container and measured the NMR signal from an RF pulse. We then replaced the sample with a similar-sized glass container filled with 3 atm of ^{3}He, mixed with O_2 (used to shorten T_1). We then obtained a NMR spectrum at thermal equilibrium. We then compared the two NMR signals and obtained a rough estimate of $P \sim 15\%$ following 12 hours of hyperpolarization.

For the second scheme to measure P, we used our low-field MRI system, described in the following chapter, to compare a hyperpolarized ^{3}He NMR signal to a ^{1}H signal from a water sample of the same volume. We fixed the resonant frequency to 210 kHz to allow the use of the same RF coil, which required us to set B_0 to 50 G and 65 G for ^{1}H and ^{3}He, respectively, due to their different gyromagnetic ratios. The NMR signal from a single RF pulse can be expressed as a reduced form of Equation 2.15 (with $n = 0$):

$$S = kM_0 \sin\theta. \tag{2.20}$$

If we take the ratio of the ^{3}He to ^{1}H NMR signal and substitute M_0 with Equation 2.2, we obtain:

$$\frac{S_{\mathrm{He}}}{S_{\mathrm{H}}} = \frac{\sin\theta_{\mathrm{He}}\, N_{\mathrm{He}}\, \gamma_{\mathrm{He}}\, P_{\mathrm{He}}}{\sin\theta_{\mathrm{H}}\, N_{\mathrm{H}}\, \gamma_{\mathrm{H}}\, P_{\mathrm{H}}} \tag{2.21}$$

We used $\sin\theta_{\mathrm{H}} = 90^\circ$ to obtain as much ^{1}H signal as possible. From Equation 2.1 $P_{\mathrm{H}} = 1.70 \times 10^{-8}$ at 50 G. Using this method we calculated a maximum ^{3}He polarization of $P \sim 12$–15% under typical polarizer operating conditions described above, in agreement with the experiment performed using the 7 T MRI system.

Chapter 3

Design and Construction of the Low-Field Imager

3.1 Low-Field ^{3}He Imaging

Nearly all ^{3}He imaging studies have been performed using conventional clinical MRI magnets that typically employ > 1 T magnetic fields necessary for adequate SNR from thermally polarized ^{1}H. However there is no requirement to use such large magnetic fields for hyperpolarized noble gas imaging. This results in several advantages for ^{3}He lung imaging. First, open-access MRI magnets such as ours are now possible, allowing for better subject access and imaging at multiple subject orientations. Second, magnetic susceptibility-induced gradients are reduced at lower fields; this is especially convenient in lung imaging, where there is an abundance of tissue-air boundaries throughout pulmonary tissue. Lastly, low-field magnets permit the use of resistive or permanent magnets rather than bulkier and more expensive superconducting systems.

Low-field hyperpolarized noble gas MRI was first performed in our group in 1998 using a home-built solenoidal magnet that produced ^3Heimages of sealed cells and excised rat lungs at 2.1 mT [48] with an SNR comparable to high-field clinical systems.

We also demonstrated the reduced magnetic susceptibility-induced gradient artefacts by comparing T_2^* times in excised rat lungs at 2.1 mT ($\sim$ 100 ms) versus 1.5 T ($\sim$ 5 ms) [83]. Since then, ^{3}He lung spectroscopy and imaging has been performed by others at fields of 0.1 T [84,85], 15 mT [86], and 3 mT [87,88]. However, all of these studies have used conventional horizontal-bore MRI magnets or a vertically-oriented-only solenoidal magnet.

This chapter provides a detailed description of the design and construction of an open-access low-field MRI system built for human lung imaging in either upright or decubitus body postures at 6.5 mT. We previously constructed a prototype system with collaborators at the University of New Hampshire (UNH) and demonstrated preliminary human lung images at 3.8 mT [49]. Some details of that apparatus are provided in Appendix B. The electromagnet at UNH was originally built for nuclear physics experiments and was readapted for MRI; as a result the system was not optimized for human lung imaging. When we designed the current low-field imager (LFI) we addressed several key components that were problematic with the prototype system, in particular the B_0 homogeneity, gradient performance, noise filtering, and gradient coil heat dissipation.

A simplified schematic diagram of the LFI is shown in Figure 3.1. The requirements are similar to that of a conventional high-field system, but the lower operating frequency and the smaller B_0 places unusual physical and technical requirements and constraints for the individual components. In addition, we were constrained by practical resource limitations; many of our components, such as our power supplies and gradient amplifiers, were donated or obtained as surplus items to save cost. In the following sections we detail the design process and specification of each of these components, as well as tests and adjustments we performed to optimize the system for human lung studies. We also discuss the unique challenges and advantages associated with imaging at unconventionally low frequencies (200–300 kHz) with our apparatus.

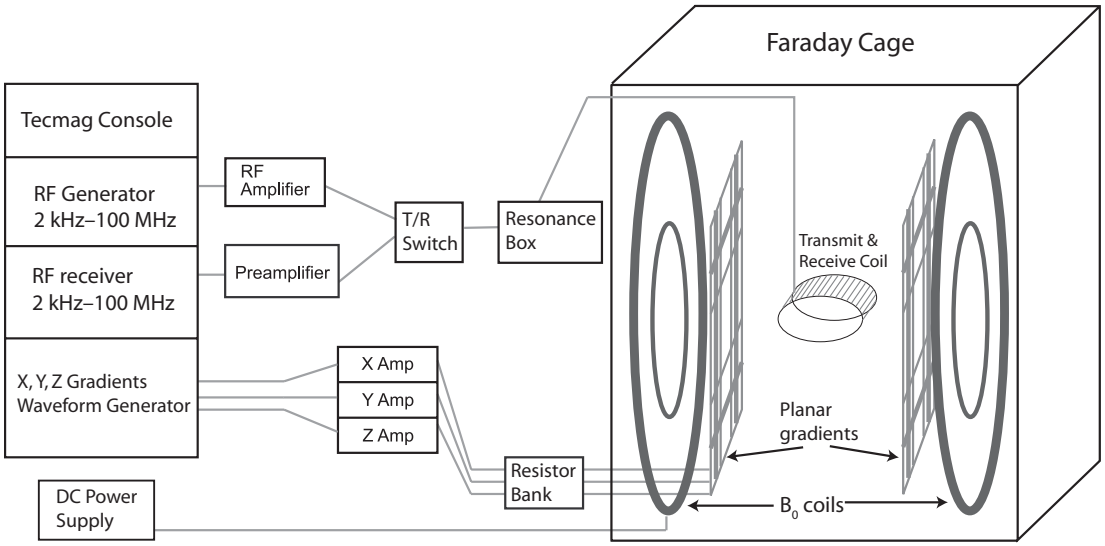

Figure 3.1: Simplified schematic diagram of the low-field, open-access, human MRI system. The major components include a commercial MRI research console (left), electronics components for RF and gradient pulse generation and B_0 control (center), and the B_0, field gradients and B_1 coils, located inside an RF-shielding Faraday cage (right).

3.2 Open-Access B_0 Electromagnet

MRI magnets are generally designed to produce a high B_0 to current ratio while allowing enough room for the subject. For conventional systems the former characteristic is often a greater priority because of SNR, and thus a solenoidal magnet is the optimal choice. This type of magnet is also advantageous because a highly homogeneous field is possible over a large region. However, the solenoidal form restricts body orientation along a single axis. It is theoretically possible to have a rotating solenoid or a large-diameter form that permits multiple body axes, but such designs are highly impractical.

A variety of open-access designs have been developed which consist of separate sets of ring-like coils, leaving an open space along two axes. The most well-known example is the Helmholtz pair, discussed in Section 2.3.1. The B_0 homogeneity

is excellent near the center region of this coil, which produces a 2^{nd}-order magnetic field. Human lung imaging, however, involves a region of interest that is 30–40 cm diameter-spherical-volume (DSV). A Helmholtz pair would be impractically large for an adequately homogeneous B_0 to be produced over such a relatively large volume. To overcome this barrier, more coils can be added to increase the magnetic field correction factor: four and six-coil magnets produce 8^{th} and 12^{th}-order fields.

A uniform spherical current shell produces a perfectly uniform magnetic field throughout its inner volume [89]. Many multi-coil magnets often approximate this; the Helmholtz pair is the lowest-order arrangement. Of the four-coil arrangements, the tetracoil, which employs four coils inscribing a sphere, is particularly popular because it produces a homogeneous field with a much larger area than the Helmholtz pair but with significantly smaller coils [90]. However, the tetracoil requires the inter-coil gap across the two middle coils to be relatively small; the only way to address this would be to increase the size of the coils. A theoretical study by Morgan et. al. found that reasonably-sized *bi-planar* magnets can have a large inter-coil separation and produce a homogeneous magnetic field over a large region, making them well-suited for multi-orientation imaging of humans [91]. In particular, this study favored four-coil bi-planar coils over six-coil versions, citing limits on inter-coil gap and coil size as the most critical determinants.

3.2.1 B_0 Coils

Our B_0 electromagnet is based on a four-coil bi-planar concept. This is the first experimental realization of this coil design for human MRI. The coil sizes and winding ratios were determined by Dr. Matthew Rosen. We used Biot Savart [Ripplon Software Inc.] to produce the theoretical B_0 field maps. Our imager requirements are for an inter-coil separation of ~ 90 cm, an imaging region of 40 cm DSV with a 100 ppm B_0 homogeneity, and the capability to generate a 10 mT B_0 field. Further discussion

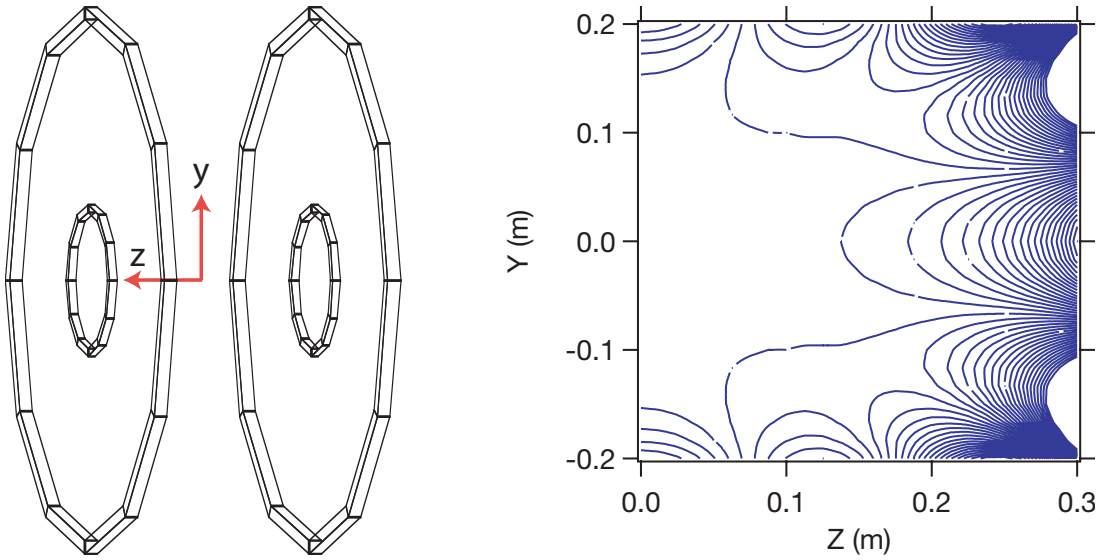

Figure 3.2: Left: A diagram of the biplanar, four-coil B_0 coil arrangement. The outer-inner coil winding ratio is 163/4. Right: A theoretical plot of B_0 homogeneity. The ordinance axis represents the y axis and intersects the center of the magnet at zero. The abscissa represents the distance from the central y axis, along z; thus, one half of the region of interest is shown. Each contour line is a 25 ppm B_z deviation from the center B_0. The design target DSV is 0.4 m.

of our B_0 homogeneity requirements can be found in Section 3.9.3. Figure 3.2 shows the coil form chosen and a theoretical plot of B_0 homogeneity. Our calculations also show that the B_0 homogeneity under this arrangement is significantly less sensitive to mechanical misalignment than other arrangements were. For example, we compared our coil arrangement to that of a tetracoil, which produces the best homogeneity for a four-coil arrangement with a similar footprint ($\sim$ 25 ppm over 40 cm DSV). However, if there is a 1 mm misalignment of the main coils along the coil axis, the B_0 homogeneity is worsened by a factor of 11. In contrast, the bi-planar arrangement suffers worse B_0 homogeneity within a 20 cm DSV under the same 1 mm misalignment, but the 40 DSV region does not lose its overall 100 ppm B_0 deviation (Figure 3.3).

The outer coils measure 2.10 m in diameter from the center of the wiring on one end to the other. Each coil contains 163 turns of square 6-AWG polyester-insulated

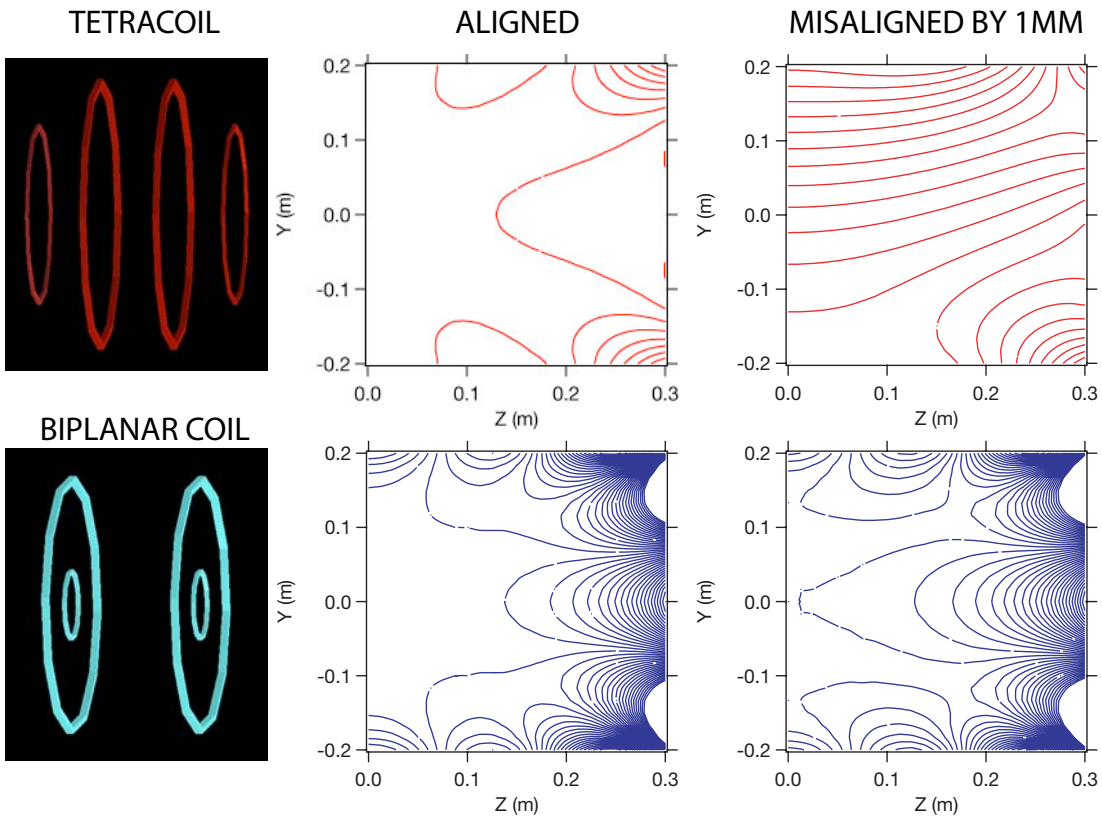

Figure 3.3: A comparison of bi-planar and tetracoil B_0 homogeneity and sensitivity to misalignment. The field plots show 25 ppm lines relative to the center magnetic field. Although a well-aligned tetracoil has superior B_0 homogeneity in comparison to the bi-planar coils, the tetracoil requires a much smaller inter-coil separation and is much more easily distorted by a 1 mm misalignment.

copper wire [MWS Wire Industries, Inc], wound in a 12 × 14-layer configuration, with seven windings across the final top layer. The position of this last layer was also numerically calculated to optimize B_0 homogeneity. We use a high-viscosity thermally-conductive epoxy [832TC, MG Chemicals] to bind the wiring onto two circularly-bent aluminum L-channels that are pre-mounted on a large 2.21-m circular aluminum flange. We measured the flange diameter at various points throughout the circumference of the flange and found that the deviation did not exceed 2 mm from the mean value. The coils possess a tight winding pattern; we took care to fill all wiring gaps with the epoxy

to ensure good thermal conductivity throughout the packed wiring. We wound the coils with the flanges in a horizontal position. After the epoxy set we used a pair of ceiling hoists to lift the flange into a vertical orientation for mounting. Each coil and flange set has a combined mass of $\sim$ 340 kg. The DC resistance for each coil is 1.1 Ω at 25° C.

The inner coils are in-plane with the outer ones. Each carries four windings using the same square copper wiring as the outer coils, and are bound with the same thermal epoxy to a Nylatron^{TM} circular disk. The disks are attached to the main aluminum flanges that hold the outer coils, via spring-loaded screws. This allows up to 10 mm adjustments to be made along the z axis for B_0 optimization. The DC resistance for each inner coil is < 0.01 Ω at 25° C.

3.2.2 LFI Frame

Each pair of inner and outer coils are mounted in-plane on a 2.21 m-diameter aluminum flange. The flange and coil sets are wound and arranged in a mirroring fashion and separated by $\sim$ 90 cm. The flanges themselves are mounted vertically on customized stands made from 90 mm $\times$ 90 mm extruded aluminum beams with mounting channels [Bosch-Rexroth]. We built an aluminum frame using the same materials, on which the flanges and their stands are mounted (Figure 3.4). The bottom of the frame serves as a rail; the stands slide over them on low-friction Delrin^{TM} plastic pads. This allows us to easily perform high-precision translational ($\pm$1 mm) and rotational ($\pm$1 mRad) alignment of the flanges simply by tapping the bottom of the stand along the desired direction with a rubber mallet. We lock down the coils into position by placing aluminum plates from the bottom rail to the stand and bolting them in place. Once secured, the entire structure is both stable and rigid, maintaining inter-coil separation to within 1 mm. The bottom of the LFI frame contains adjustable feet with up to 5 cm of travel. This allows leveling and height adjustment. In addition, the

Figure 3.4: A photograph showing the aluminum frame of the LFI and the two aluminum flanges. We wound the outer B_0 coil onto the frame prior to attaching the flange to the frame. The arrows at the bottom show the location of the Delrin pads on which the flange and its stand rests. We used detachable casters to transport the entire frame to its final location; they were later removed.

frame can be lowered on to custom-built plates with heavy-duty casters, as shown in Figure 3.4, allowing the entire LFI magnet and frame to be transported without any loss of coil alignment.

3.2.3 B_0 Power Supply

All four B_0 coils are connected in series to a single DC power supply [Alpha Power, Inc] capable of producing up to 45 A with a stability better than 15 ppm (Figure 3.5). To achieve this stability we modified the output stage to use a direct current-current transformer (DCCT) instead of a water-coiled resistive shunt as the

input to the current feedback loop. The B_0 coils output a magnetic field strength of 1.54 G/A, giving a maximum of 7.7 mT. All inter-coil and power supply connections are made with flexible 4-AWG multi-stranded copper wiring with rubber insulation. The power supply is constantly cooled by a recirculating water chiller [CFT-33, Neslabs, Inc.].

Figure 3.5: A photograph of the B_0 power supply. The small box at the top is the digital voltmeter we use to obtain a high-precision measurement of the output current (high-current resistor not shown).

The power supply has fine and coarse current control knobs and an analog current meter and built-in temperature alarm that shuts off the system automatically if it overheats. To monitor the output current more precisely we installed a high-precision, high-current 0.5 mΩ resistor in series with the B_0 line and measured the voltage across the terminals with a battery-powered voltmeter [Laskar Inc.].

3.2.4 B_0 Cooling

We typically operate the LFI with a B_0 current of 40 A. Under these conditions the total resistive heat dissipation—which is essentially all from the outer B_0 coils—is approximately 6000–7000 W. We use both active and passive techniques to cool the coils during operation.

The outer B_0 coils are wound against an aluminum L-channel as part of the mounting flange; thus two sides of the copper wiring are exposed to air and two are in contact with the flange. As mentioned previously the coils are bound to the channel by a thermally-conductive epoxy; in addition we applied a silver-based thermally-conductive paste between the L-channel and the flange as they were bolted together. This effectively allows the flange to act as a large heat sink for the outer B_0 coils. We use a 2000 W recirculating liquid chiller and pump [CFT-175, Neslabs Inc.] to provide active cooling of the flange and the aluminum L-channels. Two 0.5-inch copper tubes deliver the coolant—a mixture of ethylene glycol and water—in a counter-current fashion to maximize heat transfer efficiency. Aluminum brackets hold the copper tubing in place and a good thermal contact between the copper and the aluminum is made by filling air gaps with thermal paste. Figure 3.6 shows the arrangement of the cooling loops relative to the flange and the B_0 coil.

The coolant is run at 15° C and continuously pumped while the LFI is on. Although this removes a significant amount of heat during LFI operation, the bulk of heat removal comes from convective air flow. The heat transfer coefficient for dry air is approximately 10–100 W/m^2·K depending on the airflow characteristics. Although this is approximately one order of magnitude smaller than water, we exploit the large surface area of the coils and flange and the open-access design of the LFI to maximize the rate of heat removal through air. In addition, our LFI is housed inside a Faraday cage (detailed below) whose upper half is composed of copper mesh screens, allowing ample air exchange with the rest of the lab. There is also a large intake vent next to

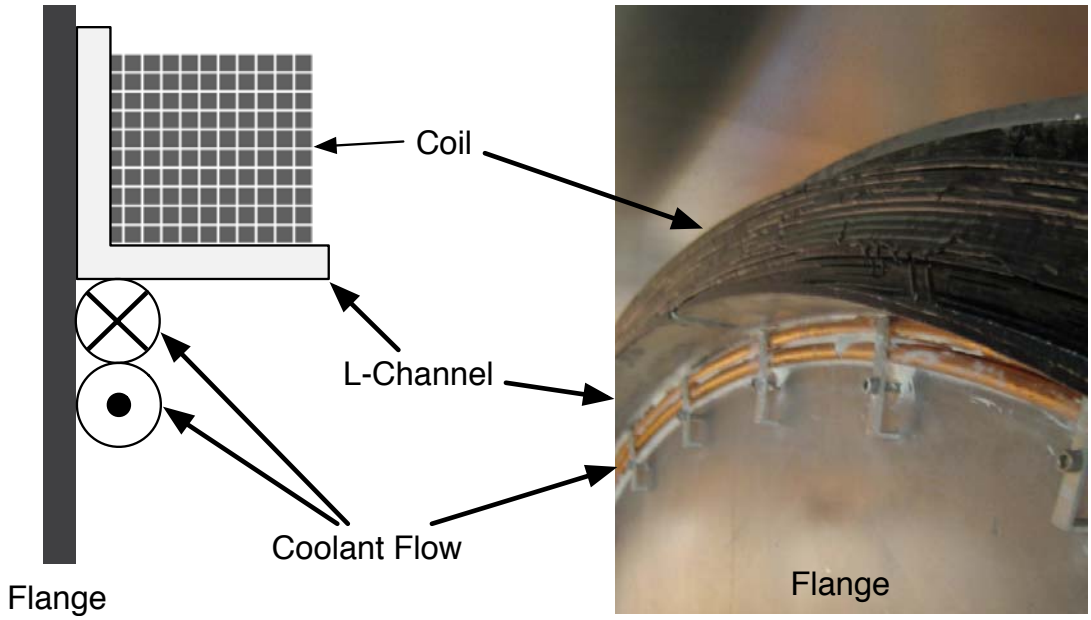

Figure 3.6: A diagram and photograph showing placement of the coolant tubes relative to the flange, L-channel, and outer B_0 coils. Thermal paste is applied at all contact points between the coolant tubes, L-channel, and the flange.

the LFI that continuously pumps air from the lab into a building-wide air conditioning system and actively promotes airflow through the copper mesh of the Faraday cage.

We performed several calculations to estimate equilibrium coil temperatures during operation to verify that we could operate under 200° C, the maximal thermal rating of the thermal epoxy and wire insulation. Ideally the surface of the B_0 coils should stay well below 100° out of general safety concerns. We estimated the surface temperature of the coils using a conservative maximum heat dissipation value of 3600 W for a single outer B_0 coil. The total exposed surface are of the coil is approximately 2 square meters, and the air temperature is roughly 30° C. Using a heat transfer coefficient of 50 W/m^2·K, we obtained a coil surface temperature of approximately 70° C.

We used the surface temperature estimate to calculate the approximate core temperature in the center of the B_0 coils, to see if it would approach near the safety ratings for the insulation and epoxy. To simplify our estimate we modeled our coil using

a circular cross-section instead of a square one and treated the system as a solid block of copper with an even distribution of heat production across the entire cross-sectional area.

Figure 3.7 summarizes this model. We define a total dissipated power, P_d that

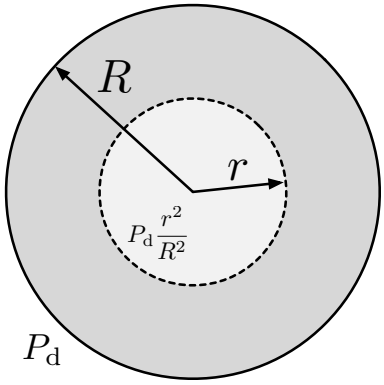

Figure 3.7: A diagram of a cylindrical model used to estimate the core temperature of the outer B_0 coils. We approximated the cylinder as a solid block of copper, with even heat production across the entire cross-section. The dotted line represents a shell with radius r; at thermal equilibrium the net heat transfer across that shell must be zero.

is evenly produced throughout the block, which has a radius R. The heat generated by the area enclosed by radius r, where $r < R$, is then $P_\mathrm{d}\frac{r^2}{R^2}$. At equilibrium the net heat exchange across this boundary shell must be zero, so the heat production from within the shell must equal the heat lost. The heat transfer equation is:

$$\frac{\mathrm{d}Q}{\mathrm{d}t} = k\,\frac{\mathrm{d}Q}{\mathrm{d}t}\,C, \tag{3.1}$$

where Q represents heat loss in units of energy, and C is the heat exchange surface, which, in this example, is the circumference of the shell. Thus, at equilibrium:

$$-P_\mathrm{d}\frac{r^2}{R^2} = k\,\frac{\mathrm{d}Q}{\mathrm{d}t}\,C. \tag{3.2}$$

From this relationship we can derive an expression relating the core temperature at $r = 0$, T_c, to the surface temperature T_s ($r = R$):

$$T_\mathrm{c} = T_\mathrm{s} + \frac{P_\mathrm{d}}{8\,\pi^2\,k\,R}, \tag{3.3}$$

where k is the thermal conductivity constant for copper, which is 401 W/m·K. For P_{d} = 3600 W, R = 5 cm, and $T_{\mathrm{s}} = 70°$, $T_{\mathrm{c}} = 92°$ C, well below the 200° C temperature limit.

Measurements of the B_0 coil surface temperatures show rough agreement with our predicted temperature values. We monitor the temperatures using surface RTD probes that attach directly on to the coil surface, and use a LABVIEW-equipped computer to record data during coil warmup and cool-down. For B_0 currents at 45 A the equillibrium coil surface temperature is approximately 70° C. We also measured the flange temperature near the cooling tubes and found that they never exceeded 40° C at maximum current, demonstrating effective cooling from the recirculating chiller. The

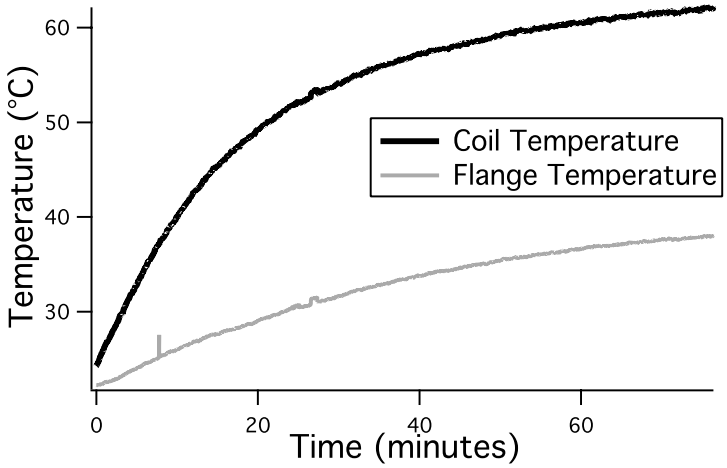

Figure 3.8: A plot of B_0 coil and flange temperatures during warmup. The B_0 current setting is 40 A in this example. The equilibrium outer B_0 coil surface temperature is $\sim 64°$ C and the rise time constant is 19 minutes. The flange RTD is placed right by the chiller loops and the outer B_0 coils, where the temperature is highest.

temperatures rise in a mono-exponential fashion with a time constant of 20–25 minutes (Figure 3.8). The room temperature is typically 20° C; after thermal equilibrium is established with B_0 at 40 A, the temperature inside the Faraday cage averages 30° C.

3.3 Open-Access Gradient Coils

To maintain the open-access environment of the LFI we designed and constructed a set of planar magnetic field gradient coils along the three cartesian axes. This differs from conventional MRI machines, which typically use cylindrical gradient coil forms that offer better efficiency (magnetic field output per unit of current) but less access. Our gradient designs were subjected to several constraints unique to our system. First, they needed to produce B_z magnetic field gradients over a 40 cm DSV with a linearity suitable for a 0.5 mm image resolution. Secondly, they needed to fit the mounting space on the aluminum flanges and maintain a similar inter-coil separation as the B_0 coils. Lastly, the coils needed to be inductive- and impedance-matched to current amplifiers originally designed for a conventional MRI system.

3.3.1 Gradient Coil Design

We designed bi-planar gradient sets to produce linear $\frac{\mathrm{d}B_z}{\mathrm{d}x}$, $\frac{\mathrm{d}B_z}{\mathrm{d}y}$, and $\frac{\mathrm{d}B_z}{\mathrm{d}z}$ magnetic field gradients[1] using an in-house optimization program written in MATLAB [Mathworks, Inc]. A vector-based method of drawing 3D current paths is defined within the program; we also added translation tools to export these paths to the CAD program Vectorworks [Nementschk Inc.] for coil mount designs, or to Biot Savart [Ripplon Software] for additional B field mapping and inductance calculations. The MATLAB routine reduces a current path to linear segments and applies the Biot Savart Law across all the segments to calculate a total B_z at a given point in 3D space. Using this subroutine we are able to produce magnetic field maps and plots for any given current path.

We subjected our coil designs to several physical constraints. To keep the designs practical, we restricted each gradient set to a single pair of coils only, with each coil along a single plane, and established a single current so they could be wired

[1] For simplicity we refer to these gradients as the x, y, and z gradients.

in series to a single power source. Since the gradient coils were to be mounted onto the aluminum flanges that also held the B_0 coils, the entire gradient coil set could not be wider than 1.9 m, nor could the coil pairs be separated by more than the 90 cm inter-flange gap. Finally, the different coil pairs needed to be separated at least 1 cm from each other to facilitate mounting and heat dissipation.

We set several variable coil parameters, such as coil loop number and inter-loop separation, to determine the coil form; these differed for the z gradient coils than for the transverse (x and y) coils, as discussed in detail below. We chose an initial set of values to start the optimization subroutine.

When executed, the program first calculates B_z across the central z axis ± 20 cm from the center, in 2 cm intervals (21 points total). A linear fit of B_z as a function of displacement along z is then performed. The slope of the fit, which we define as $G_{\rm p}$, thus represents a *perfect* linear gradient that best matches the coil output. The program then calculates B_z across a 20 cm $\times$ 20 cm grid that covers one quadrant of the 40 cm DSV along the yz plane, as shown in Figure 3.9. It is necessary to sample only one quadrant along one plane because of field symmetry. We define this grid of B_z values as a matrix $B_{j,k}$, where $\alpha\, j$ and $\alpha\, k$ correspond to position along y and z axes, respectively. α is typically set to 2 cm so the total number of sample points is 121. The program uses the first linear fit to create a perfect gradient across the grid:

$$B_{{\rm p}\,j,k} \equiv G_{\rm p}\, \alpha j. \tag{3.4}$$

We then define a difference value to use as a figure of merit:

$$\xi \equiv \sum_{j,k=0}^{j,k=20/\alpha} |B_{{\rm p}\,j,k} - B_{j,k}|. \tag{3.5}$$

The optimization routine then iteratively adjusts the coil parameter variables to minimize ξ. We ran this optimization scheme with different combinations of fixed and floating coil parameters. After a coil optimization routine was complete the software

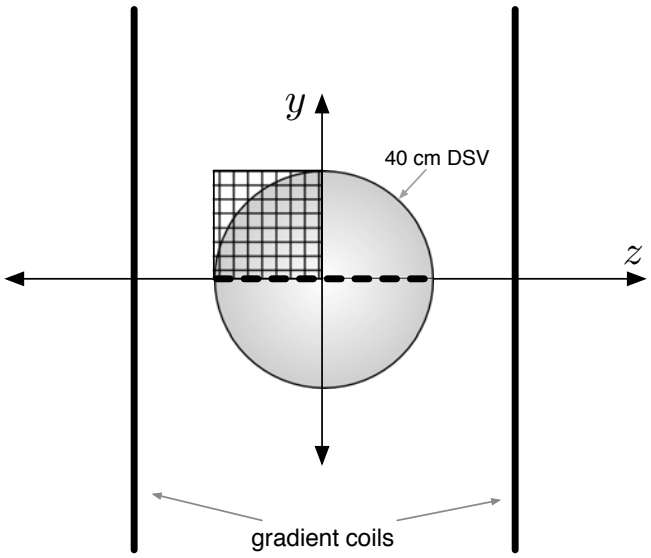

Figure 3.9: A diagram of the sampling regions for the gradient coil optimization scheme. The sphere shows the region of interest which we fix as 40 cm DSV. The dotted line represents the sampling region for the initial linear fit of B_z against displacement along z. The grid is the region over which $B_{j,k}$ is calculated.

produced B_z field maps across several slices of the 40 cm DSV region and a calculation of the magnetic field gradient strength in G/cm. We provided an input current of 180 A, near the 200 A maximum provided by the gradient amplifiers.

Our goal was to produce a gradient that would allow for 256-pixel-squared ^{3}He images across 40 cm with an imaging bandwidth of 10 kHz. This required a set of three criteria that each optimized coil form needed to pass. The first was a minimum magnetic field gradient strength. For ^{3}He ($\gamma = 3.24$ kHz/G), the minimum readout gradient field strength for our region of interest is:

$$10 \text{ kHz} \times \frac{1}{3.24 \text{ kHz/G}} \times \frac{1}{40 \text{ cm}} = 0.077 \text{ G/cm}. \tag{3.6}$$

Secondly, the gradient coil output also could not deviate from a perfect linear gradient by

$$\frac{1}{2} \times \frac{10 \text{ kHz}}{256 \text{ pixels}} = 19.5 \text{ Hz/pixel, or } 0.006 \text{ G}, \tag{3.7}$$

otherwise we would not be able to spatially resolve one pixel from its neighbor. Finally, the gradient coils could not possess too high an inductance because we needed to switch current settings across the coils on the scale of 500 μs to 1 ms during our imaging sequences. The maximum inductance is set by both the maximum voltage output across the gradient coils as well as the current slew rate:

$$L_{\max} = V_{\max} \left(\frac{\mathrm{d}I}{\mathrm{d}t} \right)^{-1}. \tag{3.8}$$

The gradient amplifiers (described in detail below) are capable of generating $V_{\max} = 100$ V across a 0.5 Ω resistor, yielding a maximum current of 200 A. We set a maximum slew rate of 0 to 200 A over 500 μs, or 4×10^5 A/s. Equation 3.8 yields $L_{\max} = 250$ μH.

The coil optimization program output consists of several components, seen in Figure 3.10. A coil form plot is generated, along with a linear fit across the central

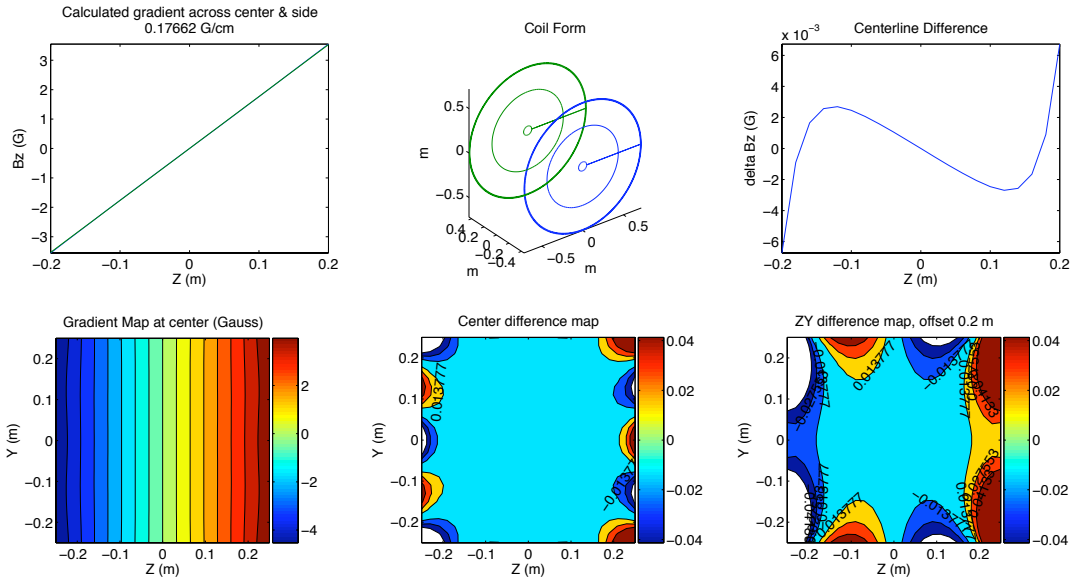

Figure 3.10: Sample output of the MATLAB gradient coil optimization software, in this case for a z gradient coil form. The program determines the magnetic field strength and produces difference plots and maps to help the user decide if the optimized form satisfies the performance requirements for imaging.

B_z axis, a calculation of gradient field strength at 180 A, and a gradient contour map. The program also creates a difference plot across the center line to show the deviation between the calculated gradient from a perfect linear fit, and two yz difference maps across the region of interest. The first map transects the field center, while the second map is displaced 10–20 cm—set by the user—in the $+x$ direction, towards the edge of the region of interest. The latter allows us to ensure that the appropriate level of gradient linearity exists off the central B_z axis. To facilitate the interpretation of these plots, we set the first contour line on the difference maps to the linearity limits imposed by Equation 3.7 (with appropriate scaling to account for the magnitude of the magnetic field gradient); thus the central contour must cover the 40 cm DSV region of interest for the coil design to be acceptable. For inductance calculations we export the coil form from our software to the Biot Savart program, which provides such a calculation as a standard option. Before we used this software we first verified that its B calculations matched the results from our MATLAB program.

3.3.2 z Gradients

The simplest z gradient consists of a Maxwell pair, with two separate current loops in a Helmholtz-like configuration but with opposing current directions. We extended this model by adding more loops to expand the region of gradient linearity to cover our region of interest. We fixed the number of loops and the coil separation, and allowed the optimization routine to adjust the various radii for each loop. The minimum inter-loop spacing allowed was 0.5 cm and the maximum loop diameter was 1.90 m.

Our chosen coil design consists of five loops total for each plane, with an inter-planar separation of 88.0 cm. The loops are arranged in three sections: an inner loop of radius 5.0 cm, a middle loop with radius 43.8 cm, and three outer loops wound together with radii 71.0 cm, 71.5 cm, and 72.0 cm, as seen in Figure 3.11. The coils are wound

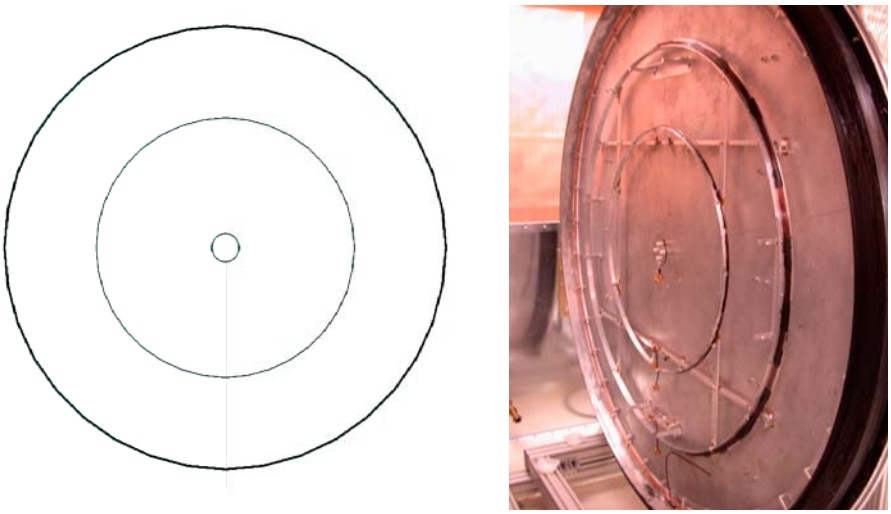

Figure 3.11: Left: A diagram of the z gradient loop pattern, showing the inner, middle, and outer sections. The current flow is in the same direction for all loops. Right: A photograph of the z gradient loops partially assembled and mounted on the main LFI flange. The large coil at the edge of the photograph is the outer B_0 coil.

using insulated round 5 AWG solid copper wire [MWS Wire Industries]. The coil forms for the middle and outer loops are made from 1/8-inch L-channel aluminum bent to semi-circular forms of the appropriate diameter. Custom-milled 1 cm-square aluminum beams and brackets are used to hold the L-channel to the correct configuration. The copper wire is wound around the L-channel and set using the same thermal epoxy used for the B_0 coils. The inner coils are wound about a 1/4 inch-thick piece of Lexan^{TM} polycarbonate plastic that we milled to a 10 cm-diameter form. The photograph in Figure 3.11 shows the coil framework. Connections between the coil loops are made in series using round 10 AWG insulated copper wire. The input and return wire, traveling in the opposite directions, are twisted around each other to reduce any stray B fields while the gradients are on. The entire planar coil is wired in series to its opposite pair by 4 AWG flexible multi-strand, rubber-insulated copper cable. The connection to the gradient amplifiers are made using twisted two-channel 6 AWG plastic-insulated copper

wiring. The total DC resistance of the entire z bi-planar gradient set is 0.08 Ω, with an inductance of ∼160 μH. These coils are capable of producing a magnetic field gradient strength of 1.0×10^{-3} G/cm/A.

3.3.3 x and y Gradients

The design for the transverse magnetic field gradient coils is more complex than for the z gradients because the desired B_z variation is now along an orthogonal axis. We approached this design by considering the more popular cylindrical coil forms. The simplest of these is the Golay pair, illustrated in Figure 3.12. Although there are four separate current loops in this arrangement, only four segments—the innermost turns— are responsible for generating the magnetic field gradient. As shown in the figure, we took this design concept and projected the coil pairs on to two planes as a first-order approximation.

We kept rectangular loops to simplify our calculations and coil construction methods. As done with the z gradients, we added more loops to include higher-order corrections for the gradient field linearity. For each plane we fixed the coil width and maximum height and mirrored the top and bottom current loops and separations from the center of the coil. We then use the optimization software to determine the ideal loop separations. Figure 3.13 shows one such coil arrangement.

The x gradient coil planes are separated by 81 cm. The optimal number of loops for each planar coil was 5 for each half (10 total). On the x gradient coils, the loop distances (as illustrated in Figure 3.13) are 8.55 cm, 26.4 cm, 47.5 cm, 48.0 cm, and 48.5 cm. The width and height of the entire plane are both 1.4 m. Each coil is wound about a custom-built Nylatron frame slotted to accomodate the x gradient coil plane on one side and a y gradient coil plane on the other (separated by 1.0 cm). The coil wire and epoxy are the same materials used for the z gradient coils. The y gradient coil planes are almost identical in form to the x coils, except they are oriented orthogonally,

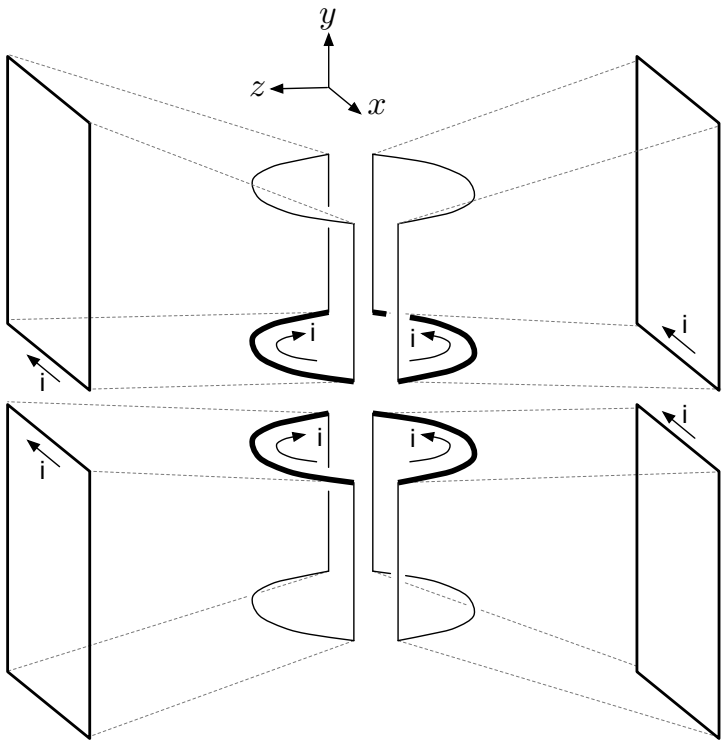

Figure 3.12: The Golay coil form and a projection onto a planar form. The Golay coil form is shown at the center. The direction of the current, i, is shown by the arrows. Only the inner coil segments (in bold) create the magnetic field gradient. We projected this coil form onto two planes (left and right) to produce a first-order planar gradient coil. This example shows the arrangement for a $\frac{\mathrm{d}B_z}{\mathrm{d}y}$ gradient.

separated by 79 cm, and possess slightly different coil loop distances: 8.05 cm, 24.75 cm, 45.9 cm, 46.4 cm, and 46.9 cm.

Both transverse gradient coils possess essentially the same circuit characteristics: the total DC resistance for each bi-planar pair is 0.09 Ω and the inductance is $\sim$ 90 μH. The x and y gradients produce a gradient field strength of 0.8×10^{-3} and 0.9×10^{-3} G/cm/A, respectively.

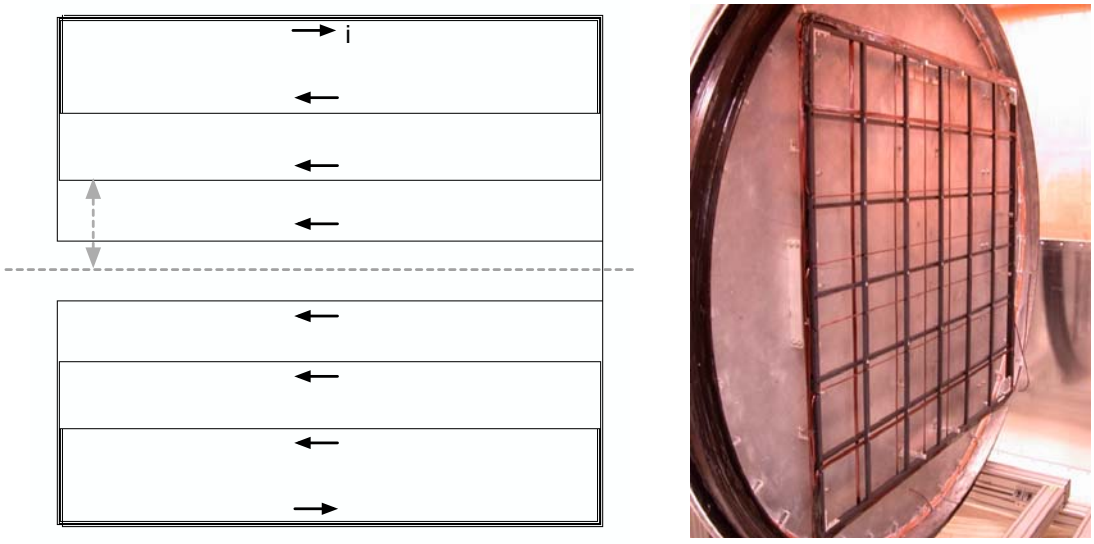

Figure 3.13: Left: A diagram of the y gradient loop pattern; the x gradient looks similar but is rotated 90°. The solid arrows show the current loop directions. The dotted line represents the coil center where the loop current and spacings above the line mirror those below. The loop distances are measured from the center line; the dotted arrow shows one such example. Right: A photograph of single x and y gradient coil planes wound on one of the two Nylatron frames. The large coil at the edge of the photograph is the outer B_0 coil.

3.3.4 Planar Gradient Coil Mounting

All three planar gradient sets are mounted on to the same aluminum flanges that support the B_0 coils. All mounting hardware are machined from aluminum bars and L-channels that are bolted on to threaded-holes in the flange, using 1/4"-20, 316-series non-magnetic steel screws. The mounts include slotted brackets that allow 4 cm of translational and 4° of rotational adjustment for each plane. The z gradient coils are mounted completely independently of the transverse gradients, so that the two sets can be adjusted separately. The 79-cm gap between the y gradients is virtually flush with the L-channel lip of the outer B_0 coils and represents the maximum spacing available for the imaging subject. Figure 3.14 shows the completed flange with all the gradient sets installed, as well as the imaging region in the middle.

Figure 3.14: Left: A photograph of the B_0 and gradient coils mounted on the aluminum flange. The arrows point to the outer and inner B_0 coils. The other circular coils are the z gradient coils, while the rectangular coils are the x and y gradient coils. Right: A view of the LFI imaging area with our defined imaging axes. The x axis points out of the page. The imaging area is approximately 79 cm wide.

Since the flanges and much of the mounting hardware are composed of aluminum we took care to reduce any potential eddy current effects that could arise during gradient pulsing. First we assembled the z gradient frame using plastic and teflon spacers that prevented electrical contact between the aluminum components; this prevented the formation of large electrical loops. The transverse gradient frames were fashioned entirely out of Nylatron and assembled using nylon screws. To limit eddy currents within the aluminum flanges we cut 50 μm slots in a sunburst pattern from the center out to the outer B_0 coils.

3.3.5 Gradient Amplifiers

Each planar gradient set is powered by a Techron 8607 Series gradient amplifier, capable of producing a peak current of 200 A across a 0.5 Ω load. We run these amplifiers in constant-current mode; the output is 20 A per 1 V input signal. These units were originally designed to drive cylindrical gradient coils in a conventional MRI system, and needed to be modified to mach our gradient coil inductance and impedance.

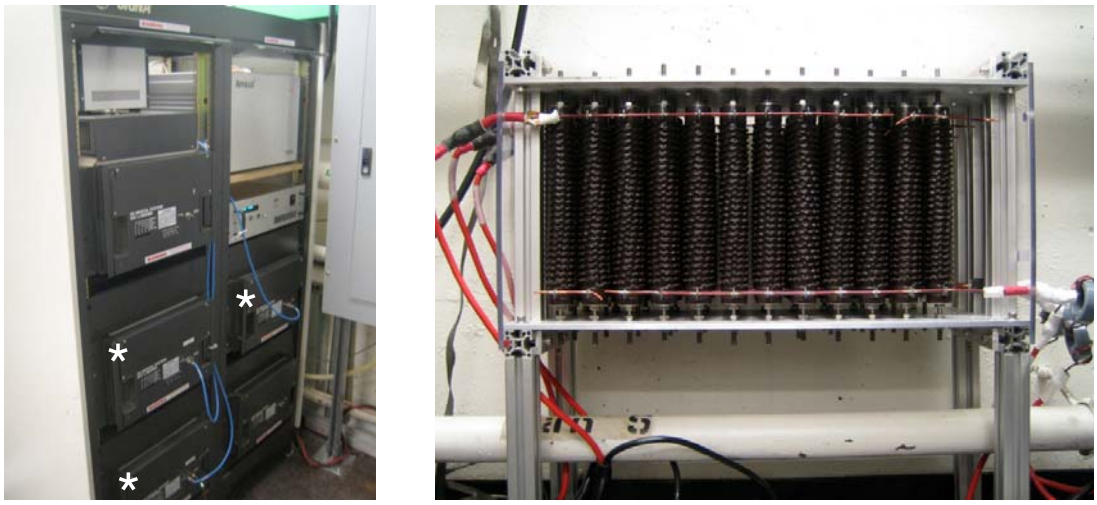

Figure 3.15: Left: A photograph of the gradient amplifier rack. Five amplifiers are mounted, with three in operation ($\star$) The spectrometer and RF amplifier are also mounted on to the same rack; they are discussed in detail in later sections. Right: A photograph of the coil resistor bank. The protective mesh cover has been removed to show the front row of power resistors.

The gradient coils are designed to have a very low DC resistance to avoid excessive heating; however the gradient amplifiers require a minimum load of 0.5 Ω for proper circuit stability and to protect the amplifiers from driving excessive currents. We built a resistor bank to increase the total circuit gradient loop resistance to 0.5 Ω and placed it downstream of the gradient amplifiers (Figure 3.15). The bank consists of three separate rows of 300 W, 5 Ω wire-wound power resistors [MultiComp]. Each row

consists of 12 of these resistors wired in parallel, yielding a net resistance of 0.41 Ω. The resistors are wired using 10 AWG solid copper wiring with direct solder connections to the resistor terminals. The connection ports contain insulated 4 AWG flexible copper tubing and copper lugs. A wire mesh protects the resistors and allows airflow through the bank to cool them during imaging. During a typical gradient echo imaging sequence the peak resistive dissipation can reach as high as 6–8 kW per channel over the course of 10–20 seconds. The resistor bank allows us to safely displace virtually all of this heat outside of the LFI Faraday cage and away from the imaging area.

The constant-current correction loop on the motherboard of the gradient amplifiers is typically set to match to a 1 mH inductive load. When connected to a circuit with a much smaller inductance the feedback loop overcompensates and produces large current oscillations through the coils. To correct this we reconfigured an RC integrator circuit in the compensation circuit to react more quickly to our gradient coils, which possessed inductances of $\sim$ 100–150 μH. We replaced the resistor element with a variable resistor and tuned the performance of the amplifiers by sending a square wave input and observing the current from a dedicated current monitor output channel on the gradient amplifier board. When optimized the gradients are capable of producing up to 180 A with rise times of $\sim$ 500–750 μs (Figure 3.16).

3.4 RF Coils

We built several RF coils for different tasks, including B_0 mapping, gradient field calibration, phantom NMR studies, and human lung imaging. These coils operated at $\sim$ 210 kHz for ^{3}He and $\sim$ 275 kHz for ^{1}H, corresponding to $B_0 = 6.5$ mT. These frequencies are roughly two to three orders of magnitude lower than those used in high-field MRI systems, making their design characteristics considerably different.

All RF coils use inductive loops to broadcast B_1, detect an NMR signal, or to

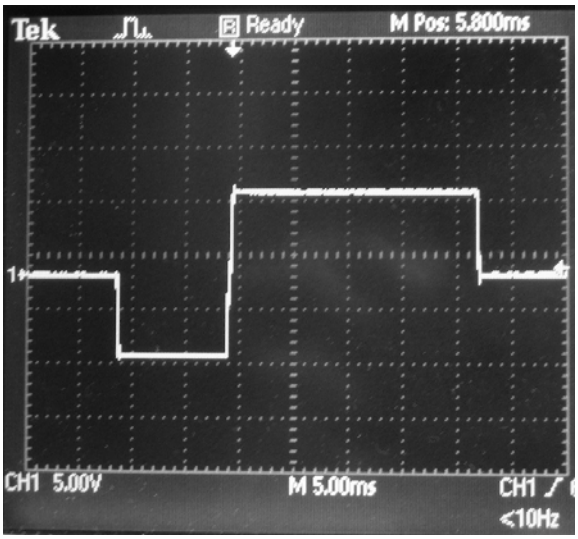

Figure 3.16: An example oscilloscope trace showing gradient current pulse across the z gradient coil. The input voltage is -7 V for 5 ms, followed by +7 V for 22.5 ms, with ramping times of 250 μs . The corresponding maximum current is 140 A. This pulse shape is typical for the read gradient in a gradient echo sequence.

do both. Capacitors are used to tune the circuit to the desired resonant frequency and to impedance match the coil to the rest of the electronics. We built all of our coils as simple solenoidal forms with multiple windings that spanned across the entire region of interest. For the case of large-volume designs, such as chest coils, a solenoid is only possible for low frequencies since a simple LC coil resonates at

$$\omega_0 = \frac{1}{\sqrt{L\,C}}, \tag{3.9}$$

so at high frequencies the inductance would become prohibitively large.

Conventional MRI RF coils typically operate from 50–200 MHz. At these frequencies the skin depth is only a few microns, and thus the conductor shape and the quality of wiring connections are especially critical in determining the overall performance of the coil. This is much less of a worry at the 200–300 kHz range; we exploit this by using simple winding patterns and connections, and placing the tuning and matching capacitors in a resonator box separate from the coil. The inductive load from a sample

is also significantly less at the lower frequencies. This has two important implications for our coils. First, sample loading imposes a relatively small shift in the resonant frequency such that we can simply fix our capacitor values when building a coil; in contrast, RF coils for high-field MRI systems typically require variable capacitors to retune the probe for every imaging subject because the resonance shift is usually greater than the operating bandwidth. Second, because sample inductive effects are minimal, the dominant source of detection noise at our frequencies is Johnson noise from the coil:

$$N = \sqrt{4\,R\,k\,T\,\Delta f}\ , \tag{3.10}$$

where R is the coil resistance, k is the Boltzmann constant, T is the coil temperature, and Δf is the operating bandwidth. Of these, R is the easiest factor to minimize, and we do so by using solid heavy-gauge copper wire in many of our designs.

We use our RF coils both for transmitting and receiving NMR signals. This has the advantage of reducing overall hardware components and eliminating the risk of cross-over noise that can occur if two separate coils are used. Figure 3.17 shows the typical coil arrangement for the LFI and the basic tuning and matching circuit we used. Although most of our coils are designed specifically for either ^{1}H or ^{3}He NMR, some can be tuned to either resonant frequency simply by switching the resonator box to another one with the appropriate tuning and matching capacitors. To simplify this operation we used standard RG-58 coaxial cables with BNC connectors to interface the coil with the different resonance boxes. For the most widely-used set of coils we constructed a single box with multiple resonant circuits, each with their own set of connectors.

3.4.1 Coil Tuning and Matching

In addition to tuning to ^{1}H and ^{3}He resonant frequencies we also needed to impedance match every coil to 50 Ω to maximize power transfer to and from the spectrometer electronics. We build each resonator circuit for a coil by first obtaining

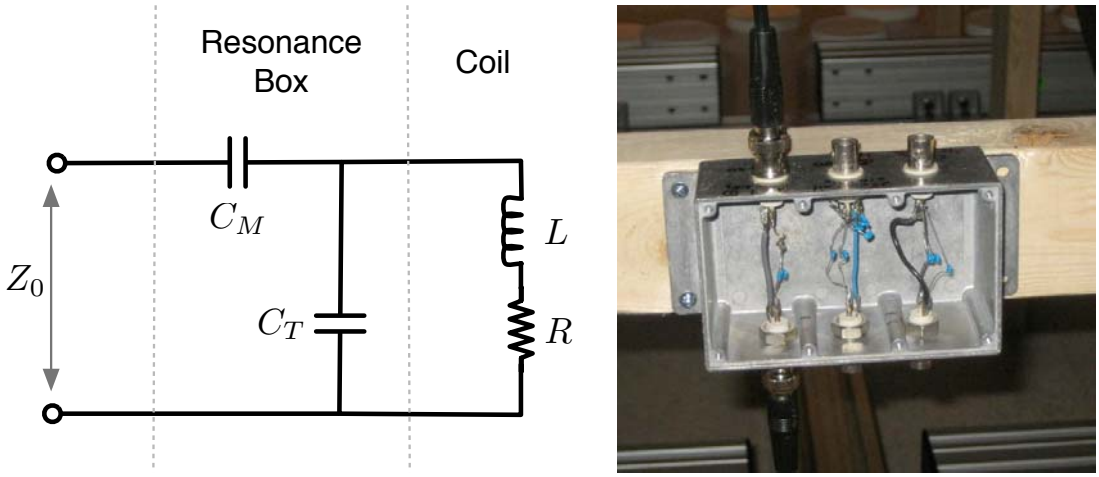

Figure 3.17: Left: A diagram of the basic tuning and matching circuit used for the RF coils. C_T and C_M are the tuning and matching capacitances, respectively, and Z_0 is the total coil impedance. The coil has a inductance L and a resistance R. The resonance box is separate from the RF coil and connected by an RG-58 coaxial cable. Right: a photograph of one of our multi-port resonance boxes with circuits for three different coils.

L with an inductance meter [LC53, Sencore], then using Equation 3.9 to obtain an estimate for the tuning capacitor. We insert this capacitor in parallel and measure the coil Q factor:

$$Q \equiv \frac{\omega_0 L}{R}, \tag{3.11}$$

where R is the effective resistance of the coil. We use a Bravo MRI impedance analyzer [AEA Technology Inc.] to obtain measurements of Q. From this we can determine estimates for the tuning and matching capacitors, based on the circuit configuration from Figure 3.17:

$$\frac{C_T}{C_M} = \sqrt{\frac{Z_0}{R}} - 1, \tag{3.12}$$

where C_T and C_M are the tuning and matching capacitances, respectively, and Z_0 is the total coil impedance, which we set to 50 Ω. As shown by Equation 3.12, this circuit form requires $Z_0 > R$ for impedance matching to be possible.

In practice Equation 3.9 is an oversimplification of the tuning circuit; R and

Z_0 influence the resonant frequency as well:

$$\omega_0^2 = \frac{1 \pm \sqrt{\frac{R}{Z_0}}}{L\,C_T}. \tag{3.13}$$

For most cases $R << Z_0$ so Equations 3.9 and 3.13 are similar. Once we obtain initial estimates for C_T and C_M we use the impedance analyzer to obtain both the resonance frequency and impedance profile. The initial resonance is typically 5–10 kHz lower than desired because the coaxial RG-58 cable that connects the coil to the resonator box carries a capacitance of ~ 0.95 pF cm^{-1} that adds to C_T; because of this effect we use the same set of coaxial cables (two ~ 30 cm cables) and BNC connectors for every coil configuration.

After the initial rough tuning we use the impedance analyzer as a guide to make adjustments to C_M and C_T to bring Z_0 and ω_0 closer to the desired values. However, in nearly all cases we are unable to raise the coil impedance to 50 Ω with capacitor elements alone. To address this we add resistors in series with C_M to raise the impedance. This lowers the coil Q factor, which is typically undesirable in NMR because the sensitivity of the coil is reduced. For our experiments, however, Q spoiling is *necessary* for proper bandwidth matching at our lower operating frequencies. The Q factor reflects the sharpness of the resonance:

$$Q = \frac{\omega_0}{\mathrm{BW}}, \tag{3.14}$$

where BW is the bandwidth of the coil. A high coil Q is detrimental to us because the resulting bandwidth may be much narrower than our operating one. For example, a 10 kHz bandwidth at 210 kHz limits coil Q to ~ 20. Thus the spoiler resistor provides us with a way to both match and broaden the response of the coil. For each coil we typically resort to making small adjustments in C_M, C_T, and the spoiler resistor R_s until we find the desired combination.

3.4.2 4-cm Field Mapping ^{1}H Coil

We use a small-volume ^{1}H coil for B_0 field mapping and gradient calibration at 275 kHz. This coil is made with 50-turns of insulated 23-AWG solid copper wire around a 4 cm-diameter polyethylene bottle. The coil length is 6 cm. A smaller 3 cm-diameter polyethylene bottle is placed inside the coil and filled with 50 cc of water. $L = 210$ μH, $C_T = 900$ pF and $C_M = 540$ pF, and $R_s = 15$ Ω. The coil Q is 60. The coil rests on a wooden mount and pegboard system that facilitates the production of field maps (Figure 3.18).

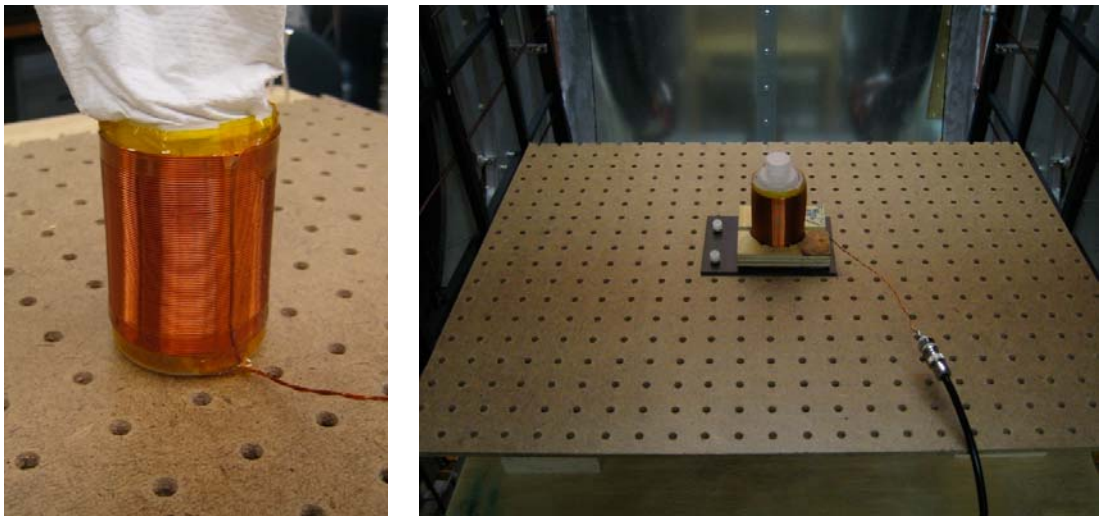

Figure 3.18: Left: A photograph of the ^{1}H field mapping coil. Right: the field mapping coil mounted on the pegboard at the center of the LFI magnet. We use this setup to generate B_0 and gradient maps. The pegboard grid has 1 inch spacings.

3.4.3 25 cm-Diameter ^{3}He/^{1}H Phantom and Head Coil

We built a medium-sized RF coil for a variety of NMR experiments both for the ^{3}He polarizer cells and ^{1}H samples such as water bottles. The main requirement was that the coil have the best filling factor available for our initial experiments with the ^{3}He cells, and for ^{1}H phantoms such as water bottles. A 25 cm diameter bore was

ideal for both tasks, and also allowed us to perform human head images as well.

The coil form is a cylindrical nylon plastic can with the ends removed. The coil is composed of 64-turns of insulated 5-AWG square copper wire, the same type used to wind the B_0 coils. The coil length is 30 cm and the inductance is 610 μH. Thermally-conductive epoxy was used to bind the wire to the plastic cylinder. The

Figure 3.19: Left: A photograph of the 25 cm-diameter general-purpose RF coil used in several ^{3}He and ^{1}H experiments, including human head imaging. Right: a photograph of the coil oriented along the y axis, with a ^{3}He cell inside.

tuning circuit at 275 kHz is: $C_T = 58$ pF, $C_M = 320$ pF, and $R_S = 23.5\ \Omega$. The coil Q is 30 under this configuration. The circuit at 210 kHz is $C_T = 350$ pF, $C_M = 320$ pF, and $R_s = 0$, with a Q of 100[2]. We built wooden stands to allow the 25 cm coil to be oriented along the x or the y axis in the LFI imaging region.

[2]We keep Q high at 210 kHz because the 25 cm coil can image only small ^{3}He samples such as the polarizer cells and thus does not require a large bandwidth. Furthermore, nearly all of our ^{3}He imaging studies, including cell imaging, are performed using the larger chest coil.

3.4.4 51-cm ^{3}He Human Chest Coil

Human lung imaging requires a chest coil large enough to cover the thoracic region; for comfort the subject's arms are kept within the coil. The coil form is a 52 cm-diameter Sonotube^{TM} cylinder made of compressed cardboard, typically used to make cement posts. We cut the tube to a length of 46 cm, enough to reach from the top of the subject's hips to the bottom of his or her chin, so that the subject can be imaged in a sitting position and still have access to the ^{3}He delivery tube.

We maximized the number of windings across the coil length to increase the overall sensitivity of the coil. We found that we were unable to tune the coil to 210 kHz if the coil possessed an inductance greater than 800 μH, corresponding to 44 turns. We wound the coil using insulated 19-AWG solid copper, with a winding separation of 1 cm. The wire is fixed to the cardboard tube with a fast-acting clear epoxy. For safety purposes we wrap the windings under a rubber insulating sheet (Figure 3.20). We also built several tables and beds to perform horizontal and upright imaging of

Figure 3.20: Left: A photograph of the human chest coil showing the winding pattern and cardboard cylinder form. Right: The completed human chest coil wrapped in rubber insulation and mounted on the subject table.

human subjects in a safe and comfortable manner as described in Section 3.7.

At this inductance, the capacitance of the coaxial cable is sufficient for tuning. The resonant circuit contains $C_T = 0$, $C_M = 488$ pF, and $R_s = 15\ \Omega$, resulting in a Q of 30. To test sample loading we used the impedance analyzer to obtain standing wave ratio (SWR) plots with the chest coil unloaded and with different human subjects. As expected the resonant frequency shifts downwards with increased inductive load (Figure 3.21). For imaging subjects weighing between 60–80 kg, the resonant frequency

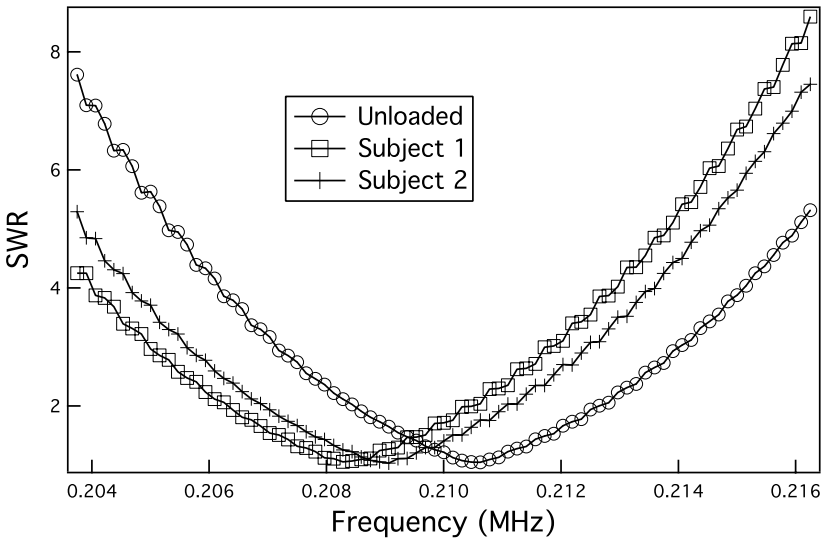

Figure 3.21: SWR plots showing the chest coil resonance profile as well as loading effects from two different human subjects inside the RF chest coil. Subjects weighing between 60–80 kg shift the resonance frequency by −2 kHz.

shift is −2 kHz. To compensate for this we shifted the unloaded coil resonance by +2 kHz by decreasing the length of the coaxial cable between the resonance box and the coil by 4 cm, so that the coil resonance would be centered at 210 kHz when loaded with a human subject.

Quantitative MRI techniques such as pO_2 mapping require careful knowledge of the pulse flip angle throughout the imaging region. The B field along the central

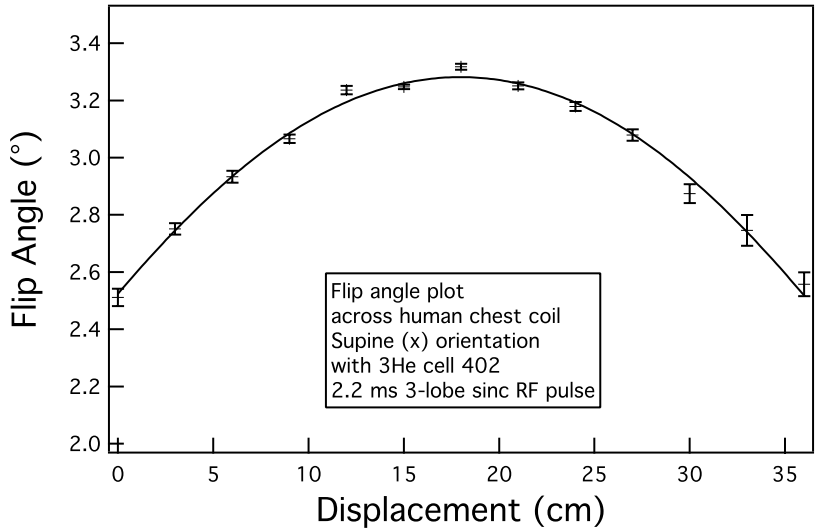

Figure 3.22: A plot of flip angle versus position across the chest coil. Flip angle calibrations were performed on ^{3}He cell #402 using a central flip angle of $\sim 3°$. The displacement is along the x axis in 3 cm increments, starting at one end of the coil. The fit curve comes from Equation 3.15.

axis of a finite solenoid is:

$$B(x) \propto \left[\frac{x}{(R^2 + x^2)^{\frac{1}{2}}} + \frac{L - x}{(R^2 + (L - x)^2)^{\frac{1}{2}}} \right], \tag{3.15}$$

where R is the coil radius and L is the coil length [92]. We performed ^{3}He flip angle calibration measurements to see if the B_1 profile of the human chest coil matched this description. We placed the coil at the center of the LFI system oriented along the x axis. We then placed ^{3}He polarizer cell #402, measuring 11 cm long and 3 cm wide, lengthwise along the z axis and centered about y axes. We measured a series of flip angles with the cell at different positions along the length of the coil (x). For each flip angle measurement we used 100 2.2 ms RF pulses with an inter-pulse time delay of 1 second. We obtained our data the using the LFI spectrometer (described below) with B_0 set to 6.5 mT (210 kHz). As expected, flip angles follow the B profile for a solenoid (Figure 3.22), with a$\sim$ 5% flip angle variation across the center 30 cm region.

3.5 Spectrometer Electronics

Our spectrometer consists of an Apollo commercial MR research console [Tecmag, Inc.] for RF and gradient pulse control and signal reception for the LFI. These consoles are commonly used for control of novel MR imaging systems used in fluid mechanics, geological and biological studies. They contain the same capabilities of RF and gradient pulse control and signal reception as a clinical MRI scanner but possess much greater flexibility and operator control over MR sequence manipulation. The Tecmag system can perform standard MRI pulse sequences and methods at kHz frequencies without requiring hardware modification and offers a graphically-driven MR pulse sequence programming and control environment. The user console is a PC workstation [Dell Computer, Inc.] that interfaces with the Apollo via a USB connection.

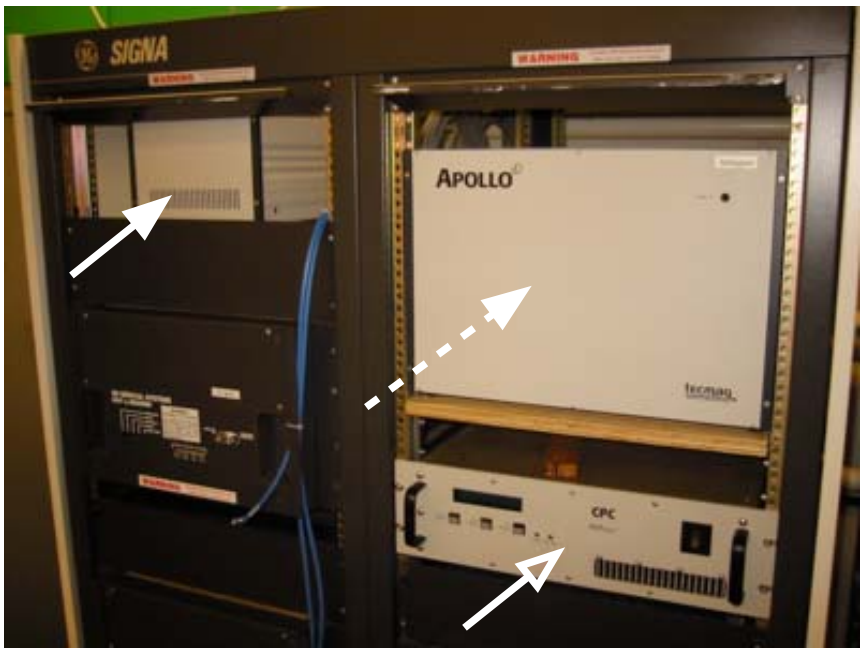

Figure 3.23: Photograph of the spectrometer and RF amplifier. These units are mounted on the same rack as the gradient amplifiers. Dotted arrow: the Apollo spectrometer unit that interfaces with the workstation computer. Solid arrow: The external gradient box that drives the gradient amplifiers. Open arrow: the CPC RF amplifier.

The Apollo includes a 2 kHz to 100 MHz RF transmitter with 0.02° phase shifts, absolute phase reset, 96 dB amplitude control and 1×10^{-6} Hz resolution. The digital receiver of the system provides digital over-sampling, $>$ 85 dB gain above 0.5 MHz, digital filtering, and a minimum dwell time of 300 ns per complex point. The system can deliver a minimum pulse width of 100 ns and up to 300,000 sequence events. In addition, the Apollo includes an external Gradient Control System with three DSP waveform generators and can perform digital pre-emphasis on the fly, gradient rotation for oblique imaging, and provide offsets for x, y and z shimming (Figure 3.23).

The transmit output of the spectrometer is connected to a NMR Plus 5LF300S [Communications Power Corp], a specially designed commercial amplifier unit that delivers 300 W of RF power across the range of 100 kHz to 1 MHz. This amplifier includes blanking circuitry that can be driven by the spectrometer, so that the unit is quiescent during NMR detection. The front panel of the amplifier also contains a power meter that can display either forward or reflected power during operation.

The amplifier connects directly with a Transcoupler II probe interface [Tecmag], a directional coupler with a 1/4-λ element optimized for 200 kHz operation. This coupler, also known as a T/R switch, allows us to use our RF coils both for high-power RF transmission as well as a high-sensitivity detection. All electronics, cables, and RF coils carry a 50 Ω impedance. The NMR signal coming out of the receive side of the Transcoupler (the coupled port) is amplified by an AU-1583-9421 pre-amplifier [Miteq, Inc.] which provides $\sim$ 36 dB gain above 200 kHz. This low-noise preamplifier is powered either via two 9 V batteries or using a filtered +15 V DC power source. The preamplifier output is sent directly to the spectrometer.

3.6 Noise Filtering and Suppression

Although much effort is made to increase our NMR signal sensitivity, we place an equal emphasis in minimizing noise levels in our detection scheme. There are many environmental noise signals within the 200–300 kHz frequency range in which we operate. Most electronic devices are designed not to interfere with radio signals and other wireless systems, which typically operate from 50 MHz up to 10 GHz, while little attention is given to the < 1 MHz regime. We used a spectral analyzer and a broadband pickup coil to detect sources of environmental noise in the LFI area. Several large signals exist from 200–250 kHz. The largest single source comes from fluorescent light ballasts located directly above the LFI magnet, which broadcasts a large peak at $\sim$ 215–225 kHz. Other large noise sources include AC/DC power adapters for our workstation monitor and for nearby laptops, and the power supplies for the two polarizer lasers.

3.6.1 Faraday Cage

The LFI magnet, gradient coils, and RF coil are housed inside of a 4 feet wide $\times$ 8 feet long $\times$ 7.5 feet tall Faraday cage [82 Series, Lindgren Inc.]. This room is designed to attenuate RF interference in the range of 10 kHz to 10 MHz by up to 100 dB. The lower half of the room is composed of steel-lined particle board panels. The upper half is constructed using copper mesh, allowing for adequate air flow for B_0 cooling. All electrical connections from outside are passed into the room using passive filtering boxes that shield out noise above 10 kHz [Lindgren Inc]. These include a 110V, 60 Hz power supply for electronics inside the room and power lines for the B_0 coils and the preamplifier. The LFI magnet is oriented so that the z axis is across the width of the Faraday cage and the doorway entrance is on the $+x$ side (Figure 3.24).

We grounded the Faraday cage to a large building ground strip located along

Figure 3.24: A photograph of the Faraday cage with the entrance door open. The -z and $+x$ corner of the LFI magnet is closest to the doorway. Axes are labeled.

the wall of the laboratory. We also grounded the entire LFI frame, including the coil flanges, to the Faraday cage. The rest of the LFI elements, including the spectrometer, gradient and RF amplifiers, and the B_0 power supply, connect to the same grounding strip. We added a 1:1 RF transformer (10 kHz to 125 MHz) upstream of the receive channel on the spectrometer to eliminate any ground loops along the spectrometer circuit. Finally, a 1 MHz low-pass filter is placed upstream of the receive channel of the spectrometer to filter out any high frequency noise.

The Faraday cage effectively filters out external environmental noise within the 200–300 kHz range. The degree of noise suppression is highly dependent on having proper conductive seals along all the walls, and having the door fully closed and locked (Figure 3.25). In addition, we tested all electronic equipment prior to their use inside the Faraday cage, and removed any items that generated any noise within our frequencies of interest (Figure 3.26).

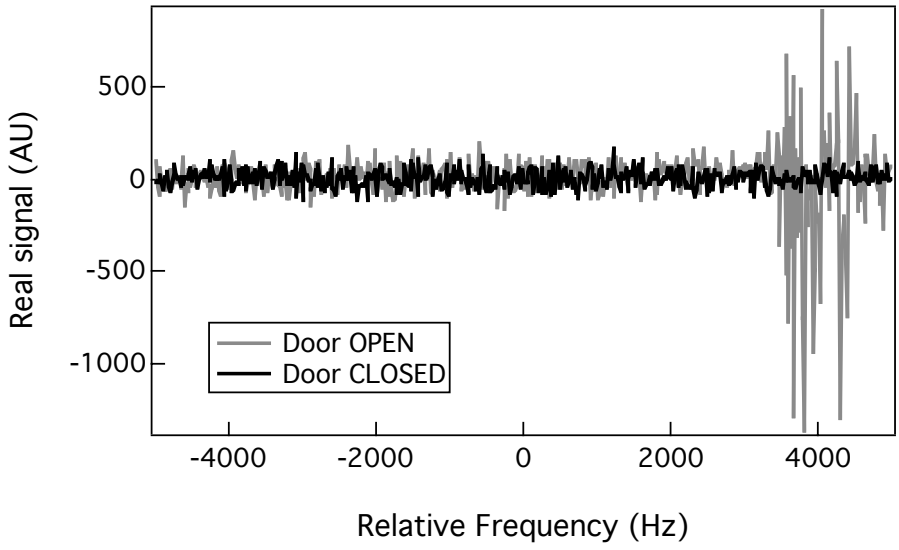

Figure 3.25: A comparison of background noise with the Faraday cage door fully closed and locked, and partially opened (in the unlocked position). The center frequency (indicated as 0 Hz) is 210 kHz. The bright signals at $\sim$ 214 kHz are primarily from overhead florescent light ballasts.

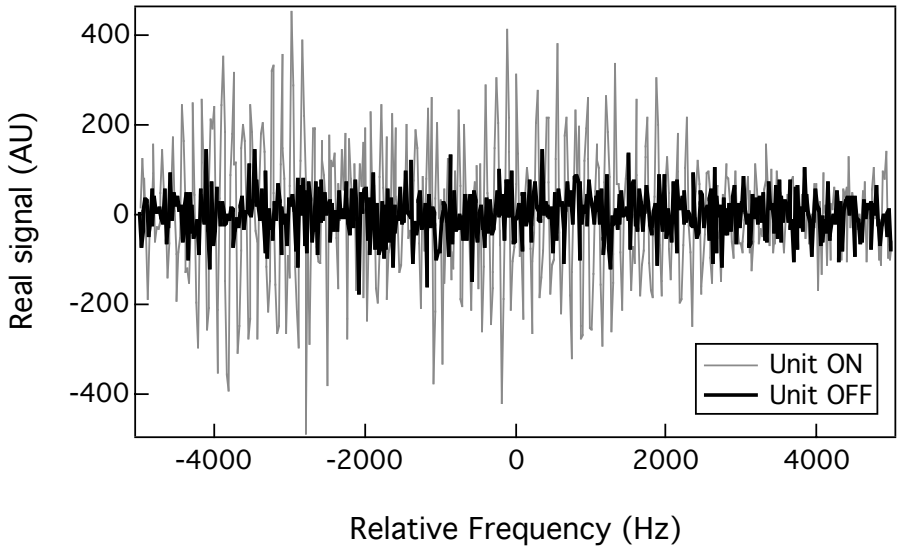

Figure 3.26: A comparison of background noise with a spO_2 monitor on versus off, inside the Faraday cage (with the door closed). The center frequency is 210 kHz. The LCD backlight on the unit was the primary source of the additional noise.

3.6.2 Gradient Line Noise

The gradient amplifiers were originally designed to be compatible with high-field systems operating between 50–150 MHz. The three gradient power lines are introduced into the Faraday cage via three sets of custom high-current feed-through passive line filters that produce ~ 25 dB attenuation at ~ 100 kHz [Schaffner, Inc]. These units have 400 nF capacitors integrated into a quick-release power connector.

We first optimized gradient performance by tuning the current feedback loop circuit to match our coil inductances and raising the coil resistances to 0.5 Ω (Section 3.3.5). To test the noise contribution from the gradient amplifiers we ran NMR sequences without any sample and compared data with the gradients pulsing against the same sequences with the gradients turned off. An overall noise floor increase of 3–5$\times$ was seen with all three gradient amplifiers on with maximum current. This represented more than an order of magnitude improvement over the filtering schemes used for the prototype low-field system. However, certain gradient amplitude settings caused small current glitches to be sent through the gradient coils while a current was applied. These glitches would occur 1–4 ms after a gradient had settled to a constant current (Figure 3.27), resulting in large broadband signals within our frequencies that would have made any NMR impractical. We were able to reproduce this glitch with different gradient amplifiers and verify that they would occur only within a certain range of output currents. This glitch disappeared, however when the gradients were run in constant-voltage mode, suggesting that the source originated from the current feedback loop. We successfully eliminated this glitch in most settings by raising the total coil resistance to ~ 0.6 Ω. To achieve this we disconnected two of the power resistors on the gradient resistor bank. We focused especially on the readout gradient (z), since these glitches only occurred when the gradients were on, while glitches outside of the acquisition window did not affect the receive signal. We also marginally improved the gradient stability by adding inductive chokes on all three circuits; doing so had a negligible effect

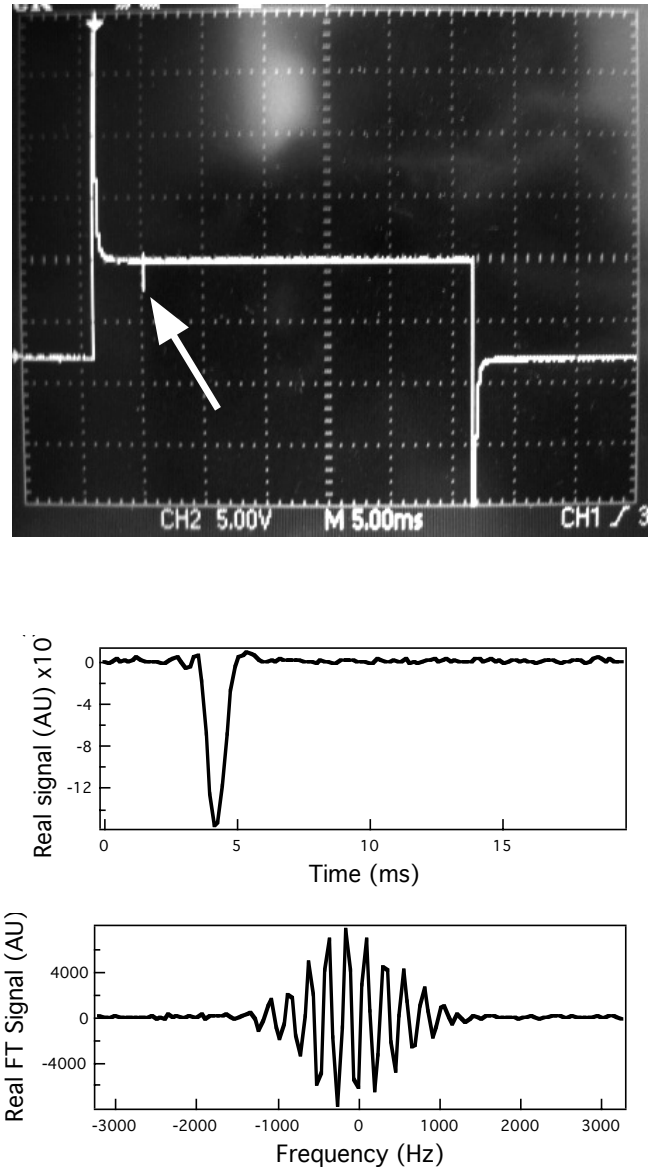

Figure 3.27: Top: An oscilloscope trace showing gradient amplifier glitching (arrow). The glitch is best seen by directly measuring the voltage across the output of the gradient amplifiers. The large peaks at the pulse ends are normal inductive spikes from the initial change in current. Bottom: The real part of the raw detection signal (top) and the corresponding FT spectrum (bottom) during the same gradient pulse. Signal acquisition started at the same time as the gradient pulse; the glitch time matches that seen on the oscilloscope. The glitch SNR against the background noise floor exceeds 1000.

on the gradient slew rates.

3.7 Phantom and Subject Positioning

NMR tables and subject beds are constructed out of plywood and pine lumber. We use wood epoxy to bind all joints to avoid the use of any metal connectors or nails near the imaging region. The tables and stands are modular so they can be reconfigured for phantom studies or human imaging.

We constructed two 24 inch $\times$ 24 inch $\times$ 40 inch-tall tables to be used either as standalone phantom table or as the weight-bearing sections for the supine human subject table. Several views of the tables are shown in Figure 3.28. For supine human imaging we constructed a 50 inch coil table that holds the chest RF coil. A second platform is suspended through the coil so that the subject can lie down on it without touching the coil. The coil itself is attached to an independent platform that slides along a rail on the bottom table. This allows the subject to lie down on to the top platform, followed by the operator sliding the RF coil into place. The human subject lies along the x axis of the magnet with his or her feet oriented towards the $+x$ side (closer to the door).

For upright human imaging, the center tables are removed and the coil table is moved towards the rear of the magnet. The RF coil and its mount are rotated to the upright orientation and held by a wooden frame that can be pivoted upwards to allow easy positioning of the subject (Figure 3.29). A wooden chair is placed in front of the table for the subject to sit on. The back of the chair is secured to the front of the coil table. The subject is instructed to lean against the back of the chair to minimize motion-related image artefacts.

Figure 3.28: Clockwise from upper left: A wooden stand for NMR phantom studies. Fully assembled subject table with the human chest coil installed viewed from the -x side. Supine subject with chest coil in place, viewed from +x side. Same subject with chest coil in place, viewed from the +x side.

Figure 3.29: Left: The arrangement for upright imaging, with the RF coil locked in the upper position for subject access. Right: The RF coil in place with a subject in the upright orientation.

3.8 LFI Safety and IRB Approval

Because the LFI is built for human imaging it must be compliant with general safety guidelines concerning medical equipment. For the LFI, the most relevant issues pertain to electrical safety. The LFI design places all high-voltage and high-current connections at the bottom and rear of the LFI magnet, well beneath the subject. These connections are themselves insulated in shrink wrap or high-temperature epoxy. The subject table also fills the entire gap between the two flanges to eliminate any possibility for the subject to touch the gradient or B_0 connections.

Clinical MRI scanners are required by the FDA to limit total RF exposure to subjects based on the Specific Adsorption Ratio (SAR), which measures the total RF power dissipated into a human body. Because SAR scales as the square of the RF frequency or applied magnetic field strength, our SAR values for typical gradient echo

imaging sequences are $\sim$ 40,000 times lower than those experienced in a clinical imager, and 10,000,000 lower than FDA limits. Therefore, the SAR values of the LFI system do not pose a risk to human subjects.

Exposure to rapidly time varying magnetic field gradients ($\mathrm{d}B/\mathrm{d}t$) can cause peripheral nerve stimulation, which at extreme values may result in severe discomfort or painful stimulation. Due to the planar design of the gradient sets on the very-low-field MRI system, typical values of magnetic field gradient, and the resulting slew rates, are smaller as compared to current clinical MRI scanners. The maximum $\mathrm{d}B/\mathrm{d}t$ values that can be generated in the LFI are lower than the FDA limiting value of 20 T/s by at least a factor of four. Therefore our gradient slewing rates do not pose any risk to human subjects.

Rapidly-varying magnetic gradient fields interact with B_0, producing Lorentz forces. These forces can cause significant mechanical stresses in the magnetic field gradient coils of clinical MRI scanners where B_0 is large, inducing significant acoustic noise, which is amplified by the cylindrical metal bore of the MRI magnet. On the LFI, however, gradient coils have been tested at their maximum currents and slew rates, without any noticeable generation of acoustic noise that could be detected with the human ear. This is expected, as the B_0 of the LFI is roughly two to three orders of magnitude smaller than that of clinical systems. A similar result was observed in the prototype MRI system, where the subject could not detect acoustic noise generated by the gradients [49]. Therefore there is no risk of any harm to human subjects from acoustical noise generated by the LFI gradient coils.

All human experiments are performed according protocols approved by either the Institutional Review Board at Brigham and Women's Hospital (^{3}He imaging) or the Faculty of Arts and Sciences at Harvard University (^{1}H imaging).

3.9 SNR and Image Resolution Limits for the LFI

As discussed previously, the LFI is well-suited for hyperpolarized ^{3}He imaging because the polarization of the ^{3}He is not dependent on the strength of the magnetic field B_0, thus allowing us to perform low-field MRI. Nevertheless B_0 magnitude and homogeneity are very important in determining and limiting SNR and imaging resolution. As discussed below, these and other factors such as susceptibility-induced magnetic field gradients can play critical roles when comparing theoretical image quality between low and high-field MRI. Our calculations serve as a necessary guide when optimizing LFI performance.

3.9.1 SNR and B_0

The voltage NMR signal detected by an RF coil can be expressed as:

$$\xi_s = (B_r/i_r)\, V_s\, \omega_0\, M_0, \tag{3.16}$$

where (B_r/i_r) is the magnetic field strength per unit current for the coil, V_s is the sample volume, ω_0 is the Larmor frequency, and M_0 is the total magnetization of the sample [93]. We substitute M_0 with Equation 2.2 and ω_0 with $\gamma\, B_0$ to obtain:

$$\xi_s = \frac{1}{2}(B_r/i_r)\, V_s\, N\, P\, \gamma^2\, B_0. \tag{3.17}$$

As previously discussed, at low magnetic fields the NMR detection noise is dominated by the coil. Therefore the SNR, using the Johnson coil noise expression from Equation 3.10, is:

$$\mathrm{SNR} = \frac{(B_r/i_r)\, V_s\, N\, P\, \gamma^2\, B_0}{2\sqrt{4\, R\, k\, T\, \Delta f}}. \tag{3.18}$$

For the case of thermally polarized spins, SNR $\propto B_0^2$, as the polarization P itself is linearly dependent on B_0. For hyperpolarized ^{3}He, however, P is determined externally by the SEOP process, so SNR $\propto B_0$.

We operate the B_0 power supply at ~ 40 A, near its maximum voltage output, to achieve $B_0 \sim 6.5$ mT (65 G). We choose this field not only to maximize SNR but because the corresponding ^{3}He and ^{1}H resonant frequencies, 210 kHz and 275 kHz, respectively, are both conveniently near the 250 kHz optimal operating frequency of both the T/R switch and the preamplifier.

3.9.2 T_2^* and Imaging Resolution

A sufficiently long T_2^* is vital for both SNR and image resolution in MRI. As discussed in Appendix A, the in-phase component of an FID takes the form of a Lorentzian following a Fourier Transform:

$$\mathrm{Re}\{\mathcal{F}\{S_0\,\cos(\omega t)\,e^{-\frac{t}{T_2^*}}\}\} \Longrightarrow \frac{S_0\,T_2^*}{1+T_2^{*2}\,(\Delta\omega)^2}. \tag{3.19}$$

The greater the T_2^*, the larger the peak signal. The frequency full-width-half-max (FWHM) of the FT spectrum is inversely proportional to T_2^*:

$$\mathrm{FWHM} = \frac{1}{\pi\,T_2^*}. \tag{3.20}$$

Thus the spectral line is sharper with increasing T_2^*. This linewidth sets fundamental limits on resolution for any imaging system. To achieve a spatial resolution of N pixels across this sample, the imaging system must operate at a bandwidth of $N \times$ FWHM. This places a limit based on the magnetic field gradient strength G [94]:

$$\Delta x_{T_2^*} = \frac{2}{\gamma\,G\,T_2^*}, \tag{3.21}$$

where $\Delta x_{T_2^*}$ represents the T_2^*-limited resolution along the readout gradient direction. For $G \sim 0.1$ G/cm and $T_2^* \sim 15$ ms, both typical values on the LFI, $\Delta x_{T_2^*} \sim 1$ mm.

There are several major contributors to T_2^* of importance in lung imaging:

$$\frac{1}{T_2^*} = \frac{1}{T_2} + \frac{1}{T_{2,\mathrm{in}}} + \frac{1}{T_{2,\mathrm{sus}}} + \frac{1}{T_{2,\mathrm{diff}}}, \tag{3.22}$$

where B_0 inhomogeneity (in), susceptibility-induced magnetic gradients (sus), and nuclei diffusion (diff) are the most significant. The intrinsic T_2 of ^{3}He is typically on the order of T_1; Darrasse et al. measured $T_2 \sim 9$ s in the lungs [95]. T_2^*, however is typically much shorter in the lung, on the order of milliseconds, both at low [48, 49, 88] and high [96] fields.

3.9.3 T_2^*: B_0 Homogeneity and Susceptibility-Induced Gradient Effects

Magnetic field gradients across an inhomogeneous B_0 typically contribute significantly to T_2^* broadening:

$$\frac{1}{T_{2,\text{in}}} = \frac{\gamma \Delta B_0}{2}. \tag{3.23}$$

This relationship stresses the importance of having good absolute B_0 homogeneity since the magnitude of $T_{2\text{in}}$ scales inversely with local field gradients. In cases such as ours where T_2^* is dominated by local main field inhomogeneity, any improvement of ΔB_0 will increase the maximum resolution allowed by the same proportional amount.

Although it is popular to express field homogeneity as a fraction, i.e., ppm, this method is misleading because the absolute field homogeneity is what determines T_2^*. For example, a 3.2 ms T_2^* from a ^{3}He FID corresponds to a 100 Hz linewidth. At 1 T, this represents a fractional B_0 homogeneity of 3.1 ppm, while the same T_2^* and linewidth at 65 G yields a fractional homogeneity of 480 ppm. The ideal theoretical B_0 homogeneity for our bi-planar magnet design is $\sim$ 100 ppm over a 40 cm DSV; this translates to $\frac{1}{T_{2,\text{in}}} = 21$ s^{-1} at 6.5 mT for ^{3}He.

The magnetic field seen by a sample has an additional contribution from its own magnetic suceptibility, χ:

$$B = B_0\,(1 + \chi), \tag{3.24}$$

where χ typically possesses a value of $\pm 10^{-6}$–10^{-7} for most tissues. In a sample with variations in magnetic susceptibility, the local magnetic field can possess substantial

gradients. This effect is particularly strong in the lung because of a high density of air-tissue boundaries. The susceptibility difference $\Delta\chi$ across this boundary is approximately 9×10^{-6} [97], and its contribution to T_2^* broadening follows a similar form as Equation 3.23:

$$\frac{1}{T_{2,\text{sus}}} = \frac{\gamma\,\Delta\chi\,B_0}{2}. \tag{3.25}$$

Thus the susceptibility-induced T_2^* broadening increases proportionally with B_0. At 1.5 T, $\frac{1}{T_{2\text{sus}}} = 217\ \text{s}^{-1}$; this is typically the dominant transverse relaxation factor for ^{3}He lung imaging on conventional high-field MRI scanners, a characteristic that cannot be improved upon. In contrast, at 6.5 mT, $\frac{1}{T_{2,\text{sus}}} = 0.91\ \text{s}^{-1}$, resulting in a small contribution to T_2^* relative to B_0 magnet inhomogeneity.

So far only stationary nuclei have been considered. In practice ^{3}He undergoes random walk diffusion across a region with varying χ. This also contributes to T_2^* broadening:

$$\frac{1}{T_{2,\text{diff}}} = (\gamma\,\Delta\chi\,B_0)^2\,\frac{l^2}{D}. \tag{3.26}$$

where D is the diffusion constant for the nuclei and l is the characteristic diffusion length over which χ varies. This equation is valid when the characteristic diffusion time of the nuclei is small in comparison to the frequency shifts across $\Delta\chi$; we operate in this "fast-diffusion" regime [48, 98]. In the lungs, $l \sim$ 10–50 μm [97]. The restricted diffusion constant for ^{3}He inside the lungs and mixed with 37° C dry air is $D = 0.15$ cm^2/s. If we use Equation 3.26 with these values and calculate the T_2^* contribution at 1.5 T, we obtain $\frac{1}{T_{2,\text{diff}}} = 31.9\ \text{s}^{-1}$, a significant factor. However, this scales with B_0^2, so at 6.5 mT, $\frac{1}{T_{2,\text{diff}}} = 5.98 \times 10^{-4}\ \text{s}^{-1}$, leading to a negligible diffusion effect.

Table 3.1 summarizes the ^{3}He T_2^* contributions at low and high fields based on the calculations above.

T_2 Component	Value at 1.5 T (s^{-1})	Value at 6.5 mT (s^{-1})
$[T_2]^{-1}$	0.11	0.11
$[T_{2,\text{in}}]^{-1}$	7	21
$[T_{2,\text{sus}}]^{-1}$	217	0.91
$[T_{2,\text{diff}}]^{-1}$	31.9	5.98×10^{-4}

Table 3.1: A comparison of T_2^* contributors at 1.5 T and 6.5 mT. We use $T_2 = 9$ s for both cases [95], and $[T_{2,\text{in}}]^{-1} \sim 7\ s^{-1}$ for the high field case [98]. At low fields we avoid T_2^* broadening from magnetic susceptibility and diffusion contributions.

3.9.4 SNR and Resolution Limits for ^{3}He Human Lung Imaging on the LFI

Table 3.2 summarizes some relevant typical ^{3}He relaxation values discussed above and performance characteristics of the LFI discussed in the following section. From this information we can determine the limit on lung image spatial resolution on

Parameter	Symbol	Value
^{3}He gyromagnetic ratio	γ	3.24 kHz/G
^{3}He restricted diffusion in the lung	D	0.15 cm^2/s
Polarization of ^{3}He	P	~ 0.15
Susceptibility difference at tissue-gas boundary	$\Delta\chi$	9×10^{-6}
Longitudinal relaxation times in the lung	T_1	10–20 s
Transverse relaxation times in the lung (LFI)	T_2^*	5–30 ms
LFI main magnetic field strength	B_0	65 G
Maximum gradient field strength on LFI	G	~ 0.2 G/cm

Table 3.2: Table of various LFI performance characteristics and ^{3}He properties in the lung, useful for calculating limits on resolution and SNR. As discussed below, T_2^* varies considerably with subject size due to non-uniform B_0; we use $T_2^* \sim 15$ ms as an estimate for our SNR/resolution calculations.

the LFI, Δx. This is dependent on a combination of both T_2^* and the diffusive properties of ^{3}He, as shown in the following expression [48, 94]:

$$\Delta x = 1.34 \left[\Delta x_{\text{diff}} \left(\Delta x_{T_2^*}\right)^2\right]^{\frac{1}{3}}. \tag{3.27}$$

Δx_{diff} is the ^{3}He diffusion-based resolution limit, which is set by the characteristic diffusion length traveled by the ^{3}He nuclei during the sampling acquisition time t_{acq}

$$\Delta x_{\text{diff}} = \sqrt{2Dt_{\text{acq}}}. \tag{3.28}$$

$\Delta x_{T_2^*}$ is the T_2^*-limited resolution factor introduced in Equation 3.21.

Given $t_{\text{acq}} = \pi\, T_2^* \sim 47$ ms (matched filter conditions), $\Delta x_{\text{diff}} \sim 1.2$ mm. $\Delta x_{T_2^*}$ depends on both T_2^* as well as the applied magnetic field gradient strength. Using $G \sim 0.2$ G/cm and a T_2^* of 15 ms, $\Delta x_{T_2^*} \sim 2.1$ mm. Thus, the overall resolution limit for the low-field imager under typical conditions mentioned above is $\Delta x \sim 2.3$ mm. This resolution is similar to ^{3}He MRI images obtained at 1.5 T ($2 \times 2 \times 20$ mm) [43,44,99]. As mentioned below, further improvements on the LFI should allow the resolution to be increased beyond the 2 mm limit.

Assuming a ^{3}He polarization P of 15%, our chest RF coil at room temperature, and with a 500 cm^3 sample of ^{3}He diluted into a 6 L total gas volume to represent a lung sample, Equation 3.18 yields SNR $\sim$ 25,000. The pixel SNR can then be calculated using the relationship [94]:

$$\text{SNR}_{\text{pixel}} = \frac{4}{\pi}\,\frac{N}{N_0^2}\,(\text{SNR})\, e^{-\frac{t_{\text{acq}}}{T_2^*}}\, \sin\theta, \tag{3.29}$$

where N is the number of pixels in an $N \times N$ image, N_0 is the number pixels encompassing the object, and θ is the flip angle. For 2 cm slice selection, $N = 256$ and $N_0 = 150$ (obtained by estimating for a maximum 2 mm resolution 256×256 image of a 30 cm $\times$ 30 cm lung sample), matched filter condition ($t_{\text{acq}}/T_2^* = \pi/2$), and a flip angle of 10°, we find $\text{SNR}_{\text{pixel}} \sim 5$.

Recently, detailed calculations have predicted that $B_0 \sim 0.15$ T yields optimal SNR for hyperpolarized ^{3}He MRI of an object approximating the size and gas density of human lungs, roughly corresponding to the onset of the coil-noise dominance regime [98]. These calculations confirm our SNR estimations for 6.5 mT and show that

the SNR obtained at 6.5 mT is only $\sim$ two to four times lower than the ^{3}He image SNR realized on a 1.5 T system, after adjusting the low-field values to match $T_2^* \sim 15$ ms as determined above for our system. Therefore, we are capable of obtaining image SNR with the LFI similar to that obtained on a clinical 1.5 T MRI system at similar resolutions, with the added benefit of our open-access design.

3.10 LFI Optimization

We obtained our first NMR signal from the LFI by moving a hyperpolarized ^{3}He cell inside the LFI Faraday cage and using the polarimeter system (Section 2.4), which was already operational at the time. We operated up to 3.0 mT, which corresponded to the upper frequency limit of the SRS lock-in amplifiers ($\sim$ 100 kHz). We first verified that the B_0 output corresponded to the current output from the Alpha power supply, then verified the stability of that power supply. Once these tests were complete we switched to single RF coils and used the Apollo spectrometer to allow the LFI to operate at higher B_0. Although we designed the B_0 coils to produce 10 mT we were limited by the output of the power supply to $\sim$ 7.0 mT, so we chose to operate at 6.5 mT.

Given the ease at which we could change B_0 on the LFI we originally intended to operate at two fields: at 6.5 mT for ^{3}He NMR and at 5.0 mT for ^{1}H. This would have allowed us to use the same RF coils tuned to 210 kHz for all of our experiments. Although our first images were produced at 5.0 mT using ^{1}H coils and samples, the B_0 homogeneity varied considerably with the main field strength, as discussed below. This led us to fix and optimize B_0 at 6.5 mT for all ^{1}H and ^{3}He experiments. We first optimized B_0 homogeneity to improve T_2^* through coil repositioning and passive shimming. Once the B_0 coils and flanges were in place and locked down, we then optimized the magnetic field gradient linearity.

3.10.1 LFI B_0 Homogeneity

Initial NMR spectra with ^{1}H and ^{3}He on the LFI revealed $T_2^* < 2$ ms with small samples located at the center of the magnet. We used a hall probe gaussmeter [F.W. Bell] to measure the local magnetic field at various points around the LFI electromagnet. We detected a significant degree of magnetization of the Faraday cage steel panels that comprised the lower half of the room. B_0 varied by as much as 0.1 G across 40 cm along the y axis. This level of distortion was approximately one order of magnitude greater than across the other two axes, which had more symmetrical arrangements of steel and copper mesh. The steel possesses a magnetic shielding effect which contains the B_0 field lines within the room, and thus higher B_0 values were measured near the lower portion of the room. Field lines near the bottom and the top of the Faraday cage are also drawn to the steel floor and ceiling panels. This reduced B_z at the $\pm y$ ends of the imaging region while simultaneously increasing B_y.

We first adjusted the spacing between the B_0 coils by moving the flanges and adjusting their angles such that we had equal inter-coil spacing. We used a prototype ^{1}H coil with 500 cc of water to obtain NMR spectra at the center of the magnet. We obtained FIDs following a $\pi/2$ pulse and used FT spectral linewidths to measure T_2^* broadening. We were able to achieve marginal improvements by moving the flanges to the spacing specified in the original magnet design and by moving the entire LFI frame closer to the center of the Faraday cage.

The most significant B_0 distortions came from the lower steel side panels along the main (z) axis of the electromagnet. To address this we added 0.006 inch-thick steel sheets over the upper-half copper mesh panels at the $\pm z$ sides of the Faraday cage. This immediately improved the B_0 inhomogeneity along the y axis by nearly five-fold and increased T_2^* from our water bottle sample to $\sim$ 10 ms. Before proceeding with more adjustments, B_0 was run for 5–8 hours a day for three days to determine how B_0 homogeneity was affected by the changing magnetization of the surrounding steel. This

manifested itself in two ways. First, the T_2^* fluctuated as much as 50% over the course of the tests, and did not correlate with the magnetic field strength. Second, B_0 itself, as determined from ω_0 on the NMR spectra, fluctuated as much as 1 G (2.0% relative to 50 G) at the same point within the magnet, at the same current settings (adjusted to within 0.1%). This was due to the steel panels exhibiting strong hysteresis while being cycled between different B_0 settings. This result prompted us to use one fixed B_0 for all our experiments. After several days of cycling only between 0 and 6.5 mT, the center magnetic field settled to within 0.03 G at 65 G (0.05%) every time we set the electromagnet to the same current using only the vernier knobs on the power supply.

Once B_0 was stabilized, we obtained B_0 field maps using the 4 cm-diameter ^{1}H coil and coil mapping pegboard described in Section 3.4.2. The NNR measurement consisted of a simple FID following a $\pi/2$ pulse. We recorded both the resonant frequency at that point as well as the measured linewidth. We began each field map with the bottle at the magnet center. We measured B_0 across a grid with 5.08 cm (2 inch) spacings, and mapped a 40 cm (16 inch) diameter circle. On average the B_0 would shift a few tens of Hz during the course of the measurement (approximately 10 minutes) due to slow current shifts and changing magnetization from nearby ferromagnetic materials. To minimize any spatially-dependent bias in our measurements from these B_0 shifts we performed measurements closest to the center first, in a mirroring pattern across the center. A typical mapping pattern is (0,0), (2, 0), (-2, 0), (0, 2), (0, -2), (4, 2), (-4, -2), etc., with the coordinates expressed as inches from the center.

Multiple horizontal xz field maps were obtained at several points along the vertical y axis. These maps are displayed as resonant frequency maps with the center frequency defined as zero. Initial field maps show strong positive distortions near the $\pm z$ regions (Figure 3.30). We attribute this to the steel panels at the $\pm z$ side of the electromagnet, which contain the magnetic field lines within the Faraday cage and increase the overall B field at the sides. There is also a distortion at the $-x$ region

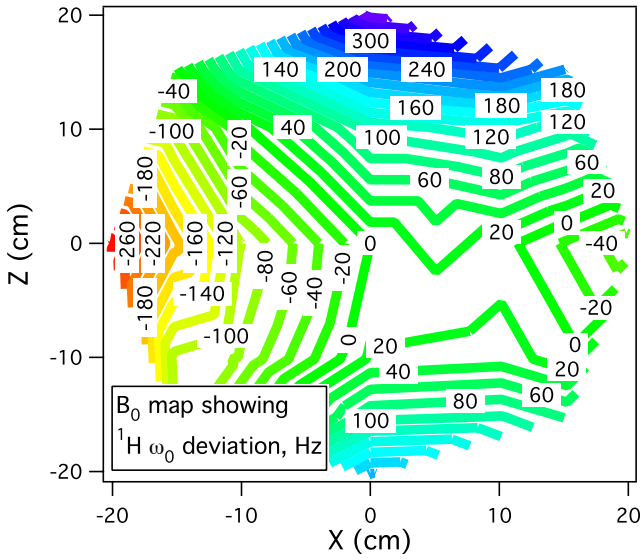

Figure 3.30: B_0 map following initial B_0 coil adjustments on the LFI frame. The center frequency is 210 kHz; the plot shows deviation from this frequency as measured using a 50 cc water sample. Strong positive distortions are evident in the $\pm z$ sides as well as the $+x$ side.

because the LFI is located closer to the $-x$ wall of the Faraday cage and the steel panels there are more magnetized than the ones near the $+x$ side.

To improve B_0 homogeneity we added passive ferromagnetic shims to the electromagnet. We began by positioning two 4 ft $\times$ 1 ft 0.006 inch-thick steel test panels near the outer B_0 coils at the $+x$ side. This produced gross changes in B_0 by containing field lines at the $+x$ side. To influence B_0 with greater precision we used 6 inch^2 pieces of the steel sheets and placed them along the back of the aluminum flanges, just behind the outer B_0 coils. We took a new B_0 field map with every new arrangement and used it to guide the following adjustments. As the homogeneity improved we left each new shim arrangement with the B_0 on for at least a half hour to allow the steel magnetization to settle. This was especially important with the shims near the warm B_0 coils because the magnetic susceptibility of galvanized steel is highly temperature dependent.

After several iterations we arrived at an eight-shim arrangement which produced excellent B_0 homogeneity at the center of the magnet (Figure 3.31). Frequency

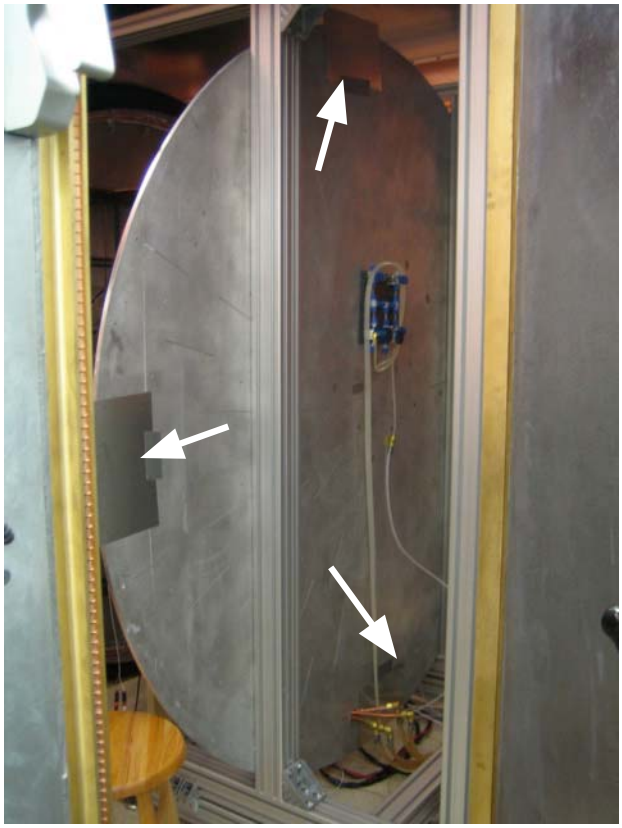

Figure 3.31: Photograph of the coil flange showing shim placements (arrows). Two shims are placed at the $+x$ end. A second set of shims is placed in mirroring fashion on the back of the opposite flange.

and linewidth maps of this optimized B_0 are shown in Figure 3.32. Excellent B_0 homogeneity exists across a 25 cm-diameter region at the center, where the resonant frequency shifts by no more than 80 Hz. The human lungs are approximately 25 cm wide $\times$ 25–30 cm long, and our subjects oriented such that the lung width is always across the z axis. This orientation is well suited for this B_0 because the field distortions at $\pm z$ are more severe than across the x or y axes. To assess B_0 characteristics for upright imaging we obtained several B_0 measurements at various points across the yz

plane and discovered that the level of magnetic field inhomogeneity across 30 cm was similar to that along the x axis.

In addition to B_0 mapping, we used the 25 cm-diameter coil (Section 3.4.3) with a 3.8 L (one gallon) jug of water and observed the ^{1}H linewidth in both horizontal and upright orientations. We used this phantom since it provided a crude representation of partially-filled human lungs. With the optimized configuration we obtained linewidths of $\sim$ 25 Hz for both orientations. For ^{3}He this linewidth is reduced to $\sim$ 20 Hz because the gyromagnetic ratio of ^{3}He is 0.76 that of ^{1}H. This corresponds to a T_2^* of $\sim$ 15 ms.

The region near the center of the LFI magnet contains an especially homogeneous region that is well suited for small ^{1}H bottle and ^{3}He cell NMR. In one experiment we obtained a $T_2^* > 3$ s with a ^{3}He cell near the magnet center (Figure 3.33). This makes the LFI potentially useful for other physics experiments that require a highly homogeneous B_0 with an open-access environment.

3.10.2 Optimizing LFI Gradient Performance

Once B_0 was optimized and the aluminum flanges were locked into place, we optimized the planar gradient coil separation to achieve an acceptable level of magnetic field gradient linearity. We used the same ^{1}H field mapping coil and pegboard to calibrate the z and x gradients, and a series of wooden spacers and a plumb line to map the y gradient.

For each NMR measurement we use two $\pi/2$–π spin echo sequences (Section A.7) to measure the B_z contribution from the gradient coil. We obtained the first echo with the gradient on. The gradient produces a 1D projection profile of the bottle in the FT spectrum; we choose the center of that profile to be the center resonant frequency with the gradient on, ω_g. The second spin echo is obtained five seconds after the first to allow nearly full T_1 recovery of the ^{1}H nuclei. This spectrum is obtained with

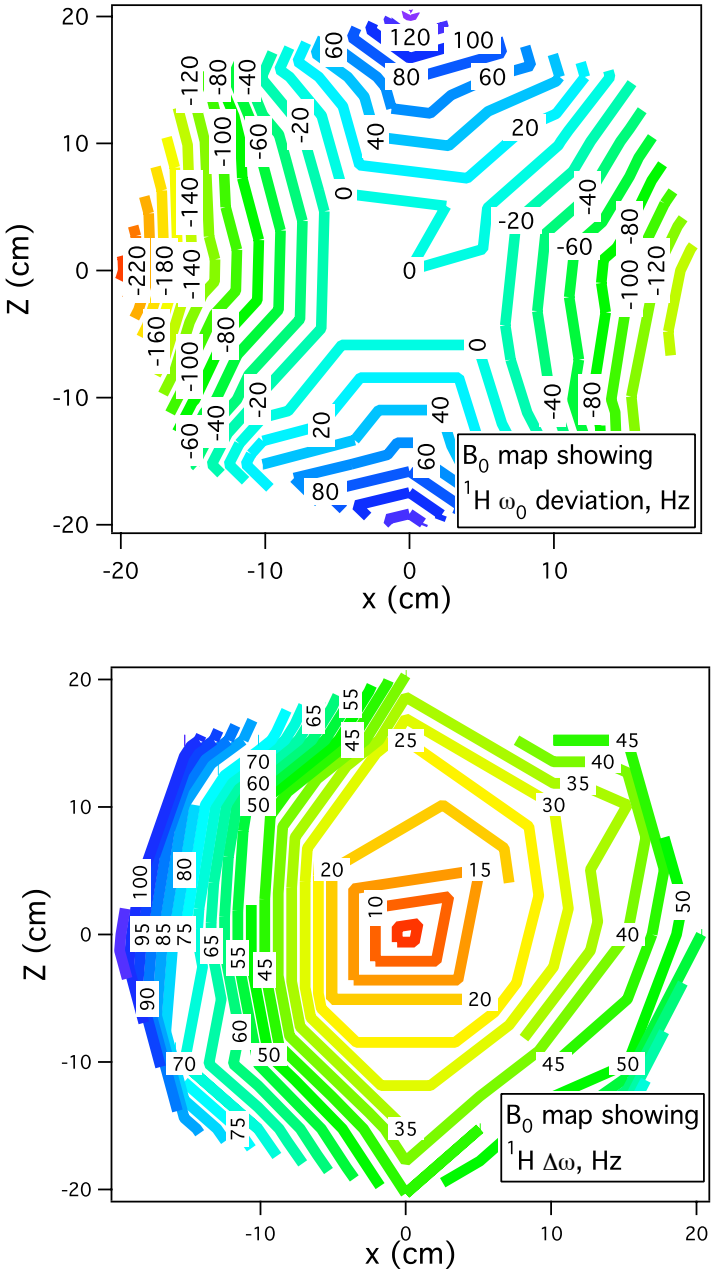

Figure 3.32: Optimized B_0 maps following shim placement. The top map is a plot of ω_0, where the zero-center frequency is 210 kHz. The bottom map is a plot of measured linewidths, $\Delta\omega_0$ for the 50 cc sample.

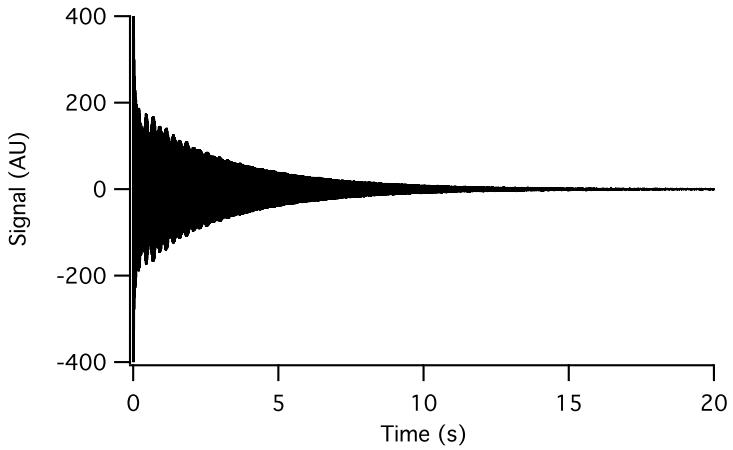

Figure 3.33: An example ^{3}He cell NMR FID showing $T_2^* > 3s$, obtained roughly near the center of the magnet. The cell volume is $\sim$ 80 cc. A more rapidly decaying component of the FID can be seen at the beginning of the plot; we attributed this to increased dephasing at Rb metal sites, which can generate local magnetic field distortions.

the gradients off, thus the center frequency is simply due to B_0 at the measurement point, ω_0. The frequency shift due to the gradients is thus $\Delta\omega = \omega_g - \omega_0$. This method corrects for the main field inhomogeneity by subtracting the background B_0 resonance altogether. Since each pair of data are collected within seconds of each other, there is virtually no systematic error arising from B_0 current instability or changes in shim magnetization.

For the gradient calibrations we chose typical gradient field strengths used in our imaging studies. The spectrometer controls the total current output using two parameters. The first is the amplitude setting used in the pulse sequence program *gr_amp*, which ranges from 0 to 100%. The second parameter, $A0$, is a global parameter that sets the maximum absolute amplitude as a percentage of the total current allowed by the gradient amplifiers, which is 200 A. The total current output from the gradient amplifier is thus $gr\_amp \times A0 \times 200$ A. Our calibration plots were made with $gr\_amp = 70$, $A0 = 70$ for the transverse gradients and $gr\_amp = 80$, $A0 = 70$ for the z gradients. This corresponds to current settings of 100 A and 112 A, respectively.

We calculate a linear fit for each gradient field plot and add a deviation plot to see how far the magnetic field gradients deviate from perfect linearity. Figure 3.34 shows the optimized plots for all three gradients. The optimal inter-coil spacings for all three planar gradients were within 2 mm of the specifications of the original design, so very little adjustment was needed. The deviation plots for all three gradients follows an odd-function behavior strongly suggesting that additional optimization is still possible. However, the resonant deviations are no more than 40 Hz for the y and z gradients and 60 Hz for the x gradients across a 40 cm span. These deviations are smaller than those from B_0 inhomogeneity; thus there is nothing to be gained by improving the linearity of these gradients any further.

The fits from the gradient plots were used to calculate the total gradient output from the coils using the gradient current amplitudes above. The calculated x, y, and z gradient coil strengths are 4.8×10^{-4}, 5.2×10^{-4}, and 5.3×10^{-4} G·cm^{-1}·A^{-1}. This is approximately a factor of two lower than our theoretical predictions. Upon further examination we determined that the current output from the gradient amplifiers corresponded to a maximum of $\sim$ 140 A rather than 200 A. We attribute this to the relatively high resistance of the gradient coils and the resistor bank, which we had increased to address gradient noise from the amplifiers. We will be able to compensate for this in later experiments by adding additional gradient amplifiers and driving each gradient coil with a pair of gradients, to double the total current output.

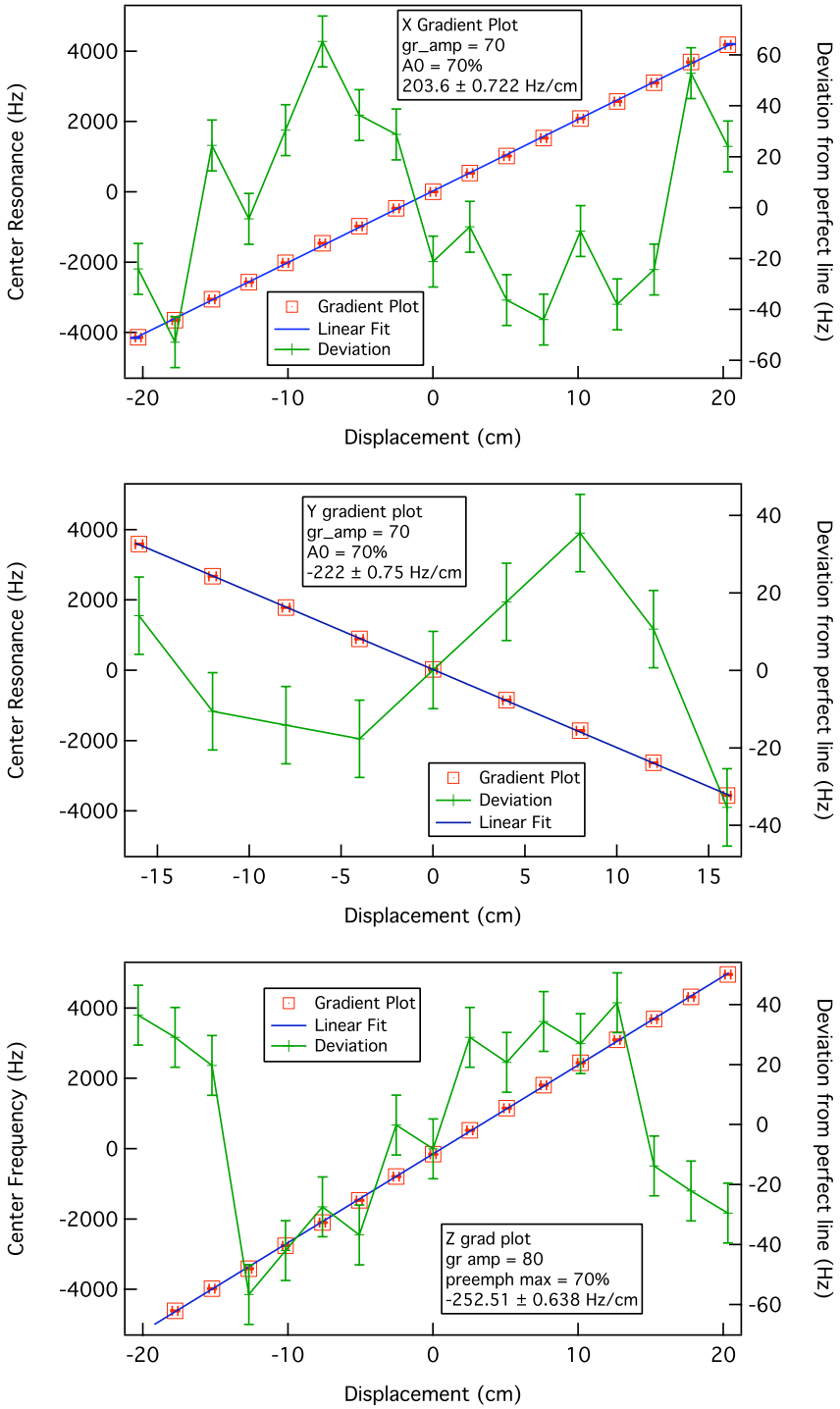

Figure 3.34: Gradient field plots for all three axes, obtained using a dual spin-echo sequence. Each plot shows the gradient measurement, a linear fit, as well as a deviation plot. These plots were made using the 4 cm-diameter ^{1}H probe with a 50 cc water sample.

Chapter 4

^{1}H and ^{3}He Imaging

The LFI was capable of providing enough SNR to allow ^{1}H imaging of water samples, so we performed our first imaging studies using ^{1}H phantom models, which were easier to use as they required no hyperpolarization. We used the ^{1}H studies to optimize gradient and RF coil performance, and to test imaging methods such as slice selection. Prior to human lung imaging we used ^{3}He phantoms—in sealed cells or delivered to plastic bags—to help us refine our imaging protocols and to test quantitative measurement schemes such as pO_2 mapping. These studies were necessary to allow us to understand the performance characteristics of the LFI and our pulse sequences.

We use the z gradients as the read gradient in all of our imaging. This has two advantages for the LFI. First, the z gradients are the strongest of the three and thus provides the best potential resolution along the read direction. Second, the same gradient can be used as the read gradient for both supine and upright imaging, allowing us to set up pulse sequences more easily and to compare images more reliably.

In this chapter we provide an overview of past and current ^{1}H and ^{3}He imaging studies performed on the LFI. This includes discussion of pO_2 measurement techniques using ^{3}He on phantoms. We conclude with recently-obtained initial human lung ^{3}He images obtained on the LFI.

4.1 ^{1}H Phantom Studies

The SNR on the LFI is roughly 1–1.5 orders of magnitude better than that of the prototype imager [49], mainly because of better performance from the Faraday cage and more effective filtering of the gradient lines. This allowed us to perform our initial imaging studies using ^{1}H phantoms, which initially consisted of a variety of containers that held ordinary tap water. This was much easier because ^{1}H imaging requires no hyperpolarization process nor the use of costly ^{3}He.

It was necessary for us to maximize the NMR signal from the ^{1}H nuclei because we relied on thermal polarization at 6.5 mT; this magnetic field is approximately 230 times smaller than 1.5 T. This necessitated the use of $\pi/2$ pulses and multiple signal averages to maximize the NMR signal amplitude from the ^{1}H nuclei.

We used spin echo imaging for all ^{1}H MRI (Section A.7). We initially tested 1D profiles across water bottles along all three axes to evaluate the performance of the planar gradient coils. Our initial images consisted of 2D projection images along the yz or xz plane. We used the 25 cm-diameter RF coil oriented along the y or x axes and place water samples inside.

We typically obtained 128×64 images and zero-filled them to 128×128 during post-processing. We also usually applied sine-bell apodization across the frequency encode direction as a noise filter. Figures 4.1 and 4.2 show some of the initial ^{1}H images acquired on the LFI at 210 kHz, prior to our optimizing B_0 at 65 G. We used these initial images to optimize pulse sequences, test RF coil performance, and calibrate our gradients. We used image profiles to determine how well we could quantify relative spin density across an image. We initially determined that quantitative spin-density imaging was highly dependent on the resonant profile of the RF coil, B_1 inhomogeneity, and B_0 inhomogeneity; this compelled us to broaden our coil Q and improve B_0 shimming.

After we optimized the B_0 at 65 G and Q-spoiled the RF coils, we repeated ^{1}H

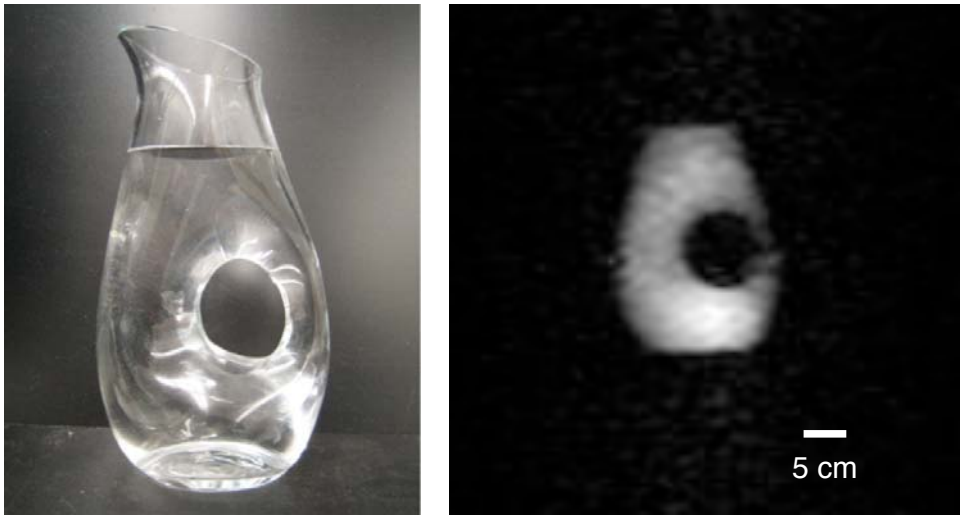

Figure 4.1: Left: a photograph of a glass pitcher partially filled with water. Right: ^{1}H image of the pitcher obtained with the LFI, using the 25 cm-diameter coil. Both the coil and the pitcher are oriented vertically (y). Imaging parameters: $B_0 = 50$ G, $\omega_0 = 210$ kHz, 128×64 (z, y) zero-filled to 128×128, FOV = 50 cm, 9 signal averages, $T_R = 3$ s, $T_E = 10$ ms, total scan time ~ 32 minutes. The maximum SNR ~ 50 for this projection image.

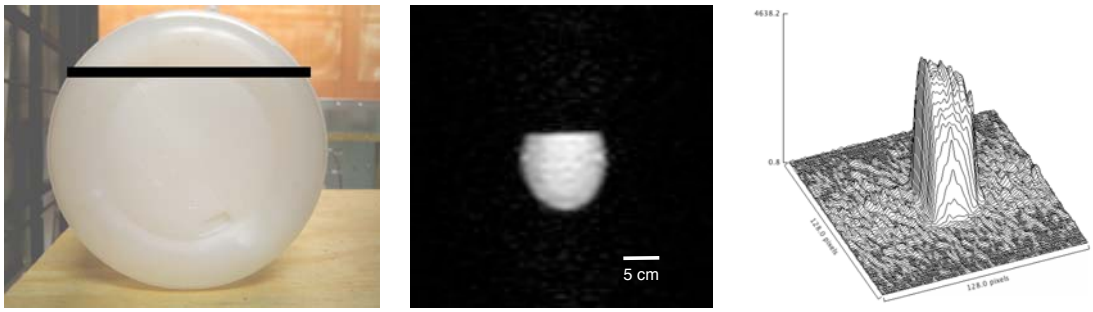

Figure 4.2: Left: a photograph of a 12.5 cm-diameter plastic water bottle. The black line indicates the water level. Middle: ^{1}H projection image of the bottle obtained with the LFI, using the 25 cm-diameter coil. Both the RF coil and water bottle are oriented along the x axis. Imaging parameters: $B_0 = 50$ G, $\omega_0 = 210$ kHz, 128×64 (z, y) zero-filled to 128×128, FOV = 38 cm, 8 signal averages, $T_R = 3$ s, $T_E = 10$ ms, total scan time ~ 26 minutes. The image resolution is 3 mm. Right: Profile plots across the image, rotated to show the sharp boundary at the top of the water level (left side). The profiles across the bottle are not flat due to sloping edges at the bottle ends.

Figure 4.3: Photograph and corresponding projection MRI of a 3.8 L water jug. Imaging parameters: $B_0 = 65$ G, $\omega_0 = 275$ kHz, 128×64 (z, y) zero-filled to 128×128, FOV = 60 cm, 8 signal averages, $T_R = 3$ s, $T_E = 10$ ms, total scan time $\sim$ 26 minutes. The image shows both the thin water-filled handle of the jug as well as the dimple across the bottom of the container. The image resolution is 4.7 mm.

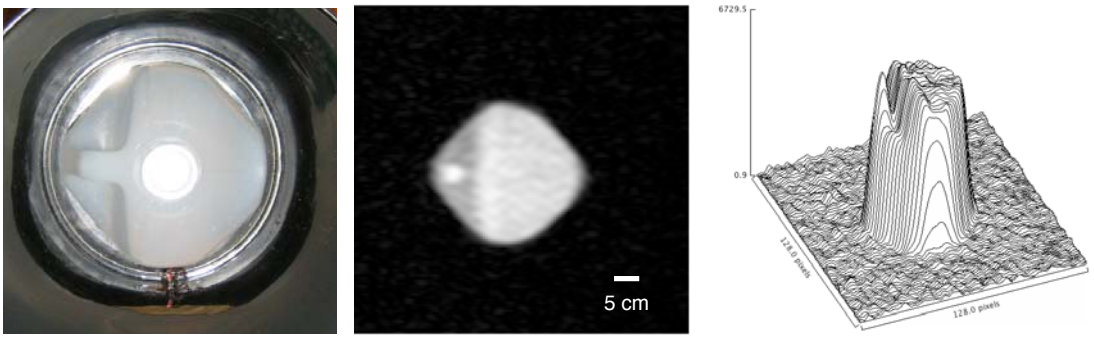

Figure 4.4: Left: a photograph of the water jug as viewed from the top, placed inside the 25 cm coil. Middle: ^{1}H projection image of the water jug obtained with the LFI. Both the RF coil and water bottle are oriented along the y axis. Imaging parameters: $B_0 = 65$ G, $\omega_0 = 275$ kHz, 128×64 (z, x) zero-filled to 128×128, FOV = 43 cm, 8 signal averages, $T_R = 3$ s, $T_E = 10$ ms, total scan time $\sim$ 26 minutes. The image resolution is 3.4 mm. Right: Profile plots across the image, showing the peak where the handle resides, as well as a flat profile across the water level.

imaging experiments using larger phantoms. We used a 3.8 L (one gallon) jug of water measuring $\sim 17 \times 17 \times 27$ cm tall. We chose this phantom model because it was a rough approximation of the dimensions of the human lung. The container has a rounded-square footprint, a 1.5 cm-thick handle filled with water, and a narrow dimple across its bottom. We obtained both xz and yz projection images with the 25 cm-diameter RF coil and the jug oriented vertically (y). The MRI images (Figures 4.3 and 4.4) show greatly improved SNR and image profiles. We were able to obtain image resolutions up to ~ 3 mm by increasing the gradient output and decreasing the operating bandwidth. Ultimately we were SNR-limited by the intrinsically weak thermal ^{1}H polarization at our magnetic field as well as the current output from the gradient amplifiers.

4.1.1 ^{1}H MRI with Slice Selection

We tested slice selection using a variety of phantoms, including water containers, fruits, and meats. Our slice selection RF pulse consisted of a 2.2 ms 3-lobe sinc pulse. This gave an excitation bandwidth of $\Delta f \sim 450$ Hz. We calibrated our slice selection gradient to 225–300 Hz/cm so that we were able to obtain 1.5–2.0 cm-thick slices.

Our initial tests were performed using the water jug to allow the highest ^{1}H density possible. We were able to successfully obtain a 1.5 cm-thick slice across the top of the jug, with a true imaging resolution of 3.9 mm $\times$ 7.8 mm $\times$ 15 mm (Figure 4.5). We used a slice selection along the y axis to obtain an image across the xz plane. As expected the SNR is considerably less than with projection imaging due to relatively small fraction of excited ^{1}H nuclei from the slice selection. This required us to lower the overall resolution of our image to increase SNR per pixel. We ran a similar imaging sequence with a honeydew melon, measuring ~ 20 cm in diameter. The ^{1}H density was less, requiring us to increase the number of signal averages, but we could still obtain an adequate SNR at the same resolution as the water jug image. The image resolves some

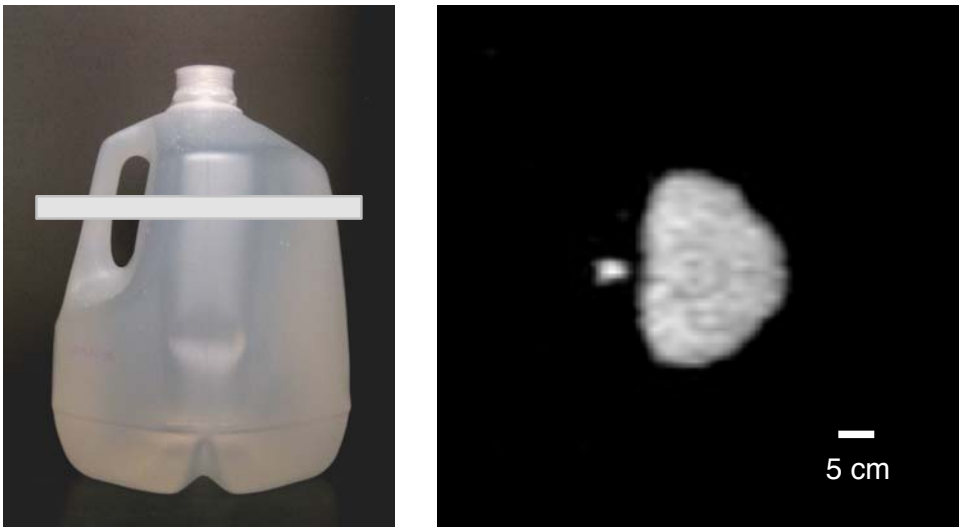

Figure 4.5: Left: a photograph of the water jug; the white line marks the image slice. Right: corresponding ^{1}H image. Both the RF coil and water bottle are oriented along the y axis. Imaging parameters: $B_0 = 65$ G, $\omega_0 = 275$ kHz, 128×64 (z, y), zero-filled to 128×128, FOV = 50 cm, 16 signal averages, $T_R = 3$ s, $T_E = 10$ ms, total scan time ~ 52 minutes. The processed image resolution is 3.9 mm $\times$ 3.9 mm $\times$ 15 mm. Peak SNR ~ 20.

Figure 4.6: Left: a photograph of a honeydew melon cut in half, showing the imaging slice plane. Right: The ^{1}H MRI of a melon obtained by the LFI with a 1.5 cm central slice. The RF coil is oriented along the x axis. Imaging parameters: $B_0 = 65$ G, $\omega_0 =$ 275 kHz, 128×64 (z, y) zero-filled to 128×128, FOV = 43 cm, 16 signal averages, T_R = 3 s, $T_E = 10$ ms, total scan time ~ 52 minutes. The processed image resolution is 3.9 mm $\times$ 3.9 mm $\times$ 15 mm. Peak SNR ~ 35.

fine structure of the melon including the central areas with slightly lower ^{1}H density, where the seeds are located (Figure 4.6).

4.1.2 Human ^{1}H Imaging

We obtained several human head ^{1}H images using the 25 cm-diameter coil. The subject was a healthy 29 year-old male. We reconfigured the imaging table to position a human subject with his head placed at the center of the LFI magnet. The subject lay supine on the table and his head was secured inside the RF coil (oriented along the x axis) with rubber mats and cotton sheets.

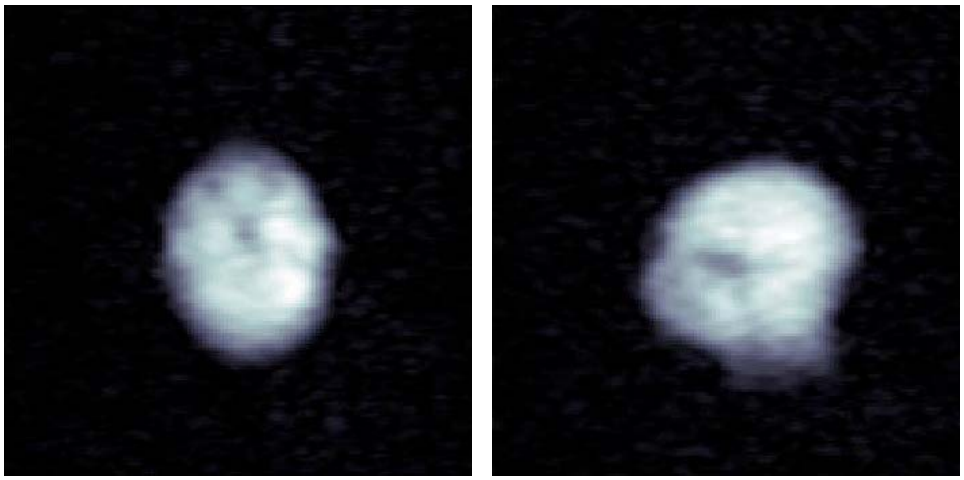

Figure 4.7: Left to right: Axial and sagittal slices of a human head, taken with the LFI. Various sinus passages can be seen in both images. The oral cavity and trachea can be seen in the sagittal slice. Imaging parameters: $B_0 = 65$ G, $\omega_0 = 275$ kHz, 128×64 (z, x slices), zero-filled to 128×128, FOV = 50 cm, 16 signal averages, $T_R = 3$ s, $T_E = 10$ ms, total scan time ~ 52 minutes. The processed image resolution is 3.9 mm $\times$ 3.9 mm $\times$ 15 mm. Peak SNR ~ 15.

We obtained both axial and sagittal slices by positioning the subject's head either supine or on its side, and obtaining slices across the xz plane. We used imaging protocols similar to those for the melon slice experiment, giving a true resolution of 3.9 mm $\times$ 7.8 mm $\times$ 15 mm (Figure 4.7). Our imaging quality was limited not only by

SNR but also by involuntary motion by the subject, who was required to hold his head in a fixed position for nearly one hour. Nevertheless the images can resolve some gross anatomical structures, such as the sinuses, oral cavity, and trachea.

4.2 ^{3}He Imaging

We obtained our first ^{3}He images using the ^{3}He polarizer cells, which could be easily removed and reattached to the polarizer. This allowed us to perform multiple imaging experiments without any loss of ^{3}He gas. We first performed NMR-based flip angle calibrations (Section 2.4.1) to determine the appropriate θ for our sequences. Once we obtained a range of flip angle settings for our spectrometer, we used gradient recall echo (GRE) sequences for all our ^{3}He images (Section A.8).

We used the human chest coil for all ^{3}He imaging. This allowed us to use and optimize a single coil for all imaging, from sealed glass cells to human lungs. We typically hyperpolarized ^{3}He cells to 10–15% by performing SEOP on the polarizer for 6–20 hours. Using $\theta \sim$ 2-3° we obtained images of polarizer cell with SNR $>$ 400. We tested imaging with the RF coil oriented along the y or x axes, with the cells oriented in multiple directions (Figure 4.8). Our tests showed no differences in imaging quality with the RF coil in either orientation. We were able to obtain imaging resolutions up to 2.8 mm using the maximum current output from the gradient amplifiers and an imaging bandwidth of $\sim$ 6 kHz. Profiles across the cell images are uniform but show increased signal amplitude at the middle and edges of the cell (Figure 4.9). This is due to restricted diffusion of ^{3}He at the edges and the cell pull-off, as well as the extra $\sim$ 0.5–1 cc volume at the pulloff.

We see significant imaging distortions at edges of our imaging region of interest which we attributed to B_0 inhomogeneity. Our optimal imaging region is approximately 33 cm across the z axis and 35 cm across the x and y axes. This is smaller than the

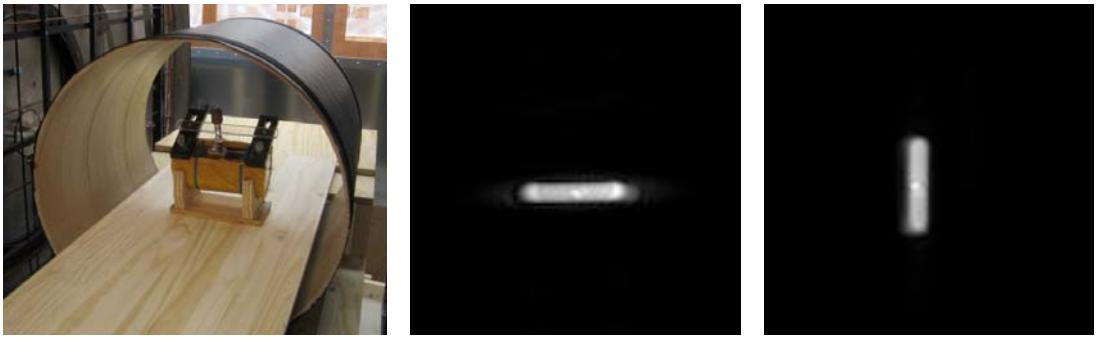

Figure 4.8: Sample ^{3}He cell images obtained using the human chest RF coil. The RF coil is oriented along the x axis, as shown in the photograph, and the images are xz projections. The left and and right images were taken with the cell oriented along the z and x axes, respectively. Imaging parameters: $B_0 = 65$ G, $\omega_0 = 210$ kHz, 128×128 resolution, FOV = 36 cm, no signal averaging, $\theta = 3°$, $T_R = 60$ ms, $T_E = 7$ ms, total scan time ~ 7.7 s. SNR $\sim$ 500–600.

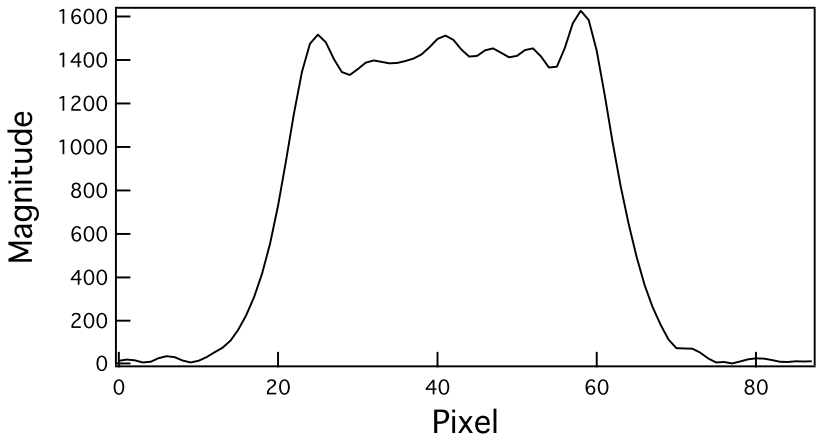

Figure 4.9: A 1D profile across the center of a ^{3}He cell image. This profile was taken lengthwise across the x-oriented cell image shown in Figure 4.8. The signal amplitude is increased at the cell edges and at a pulloff near the center. The edges of the cell profile are not sharp because the cell contains round windows.

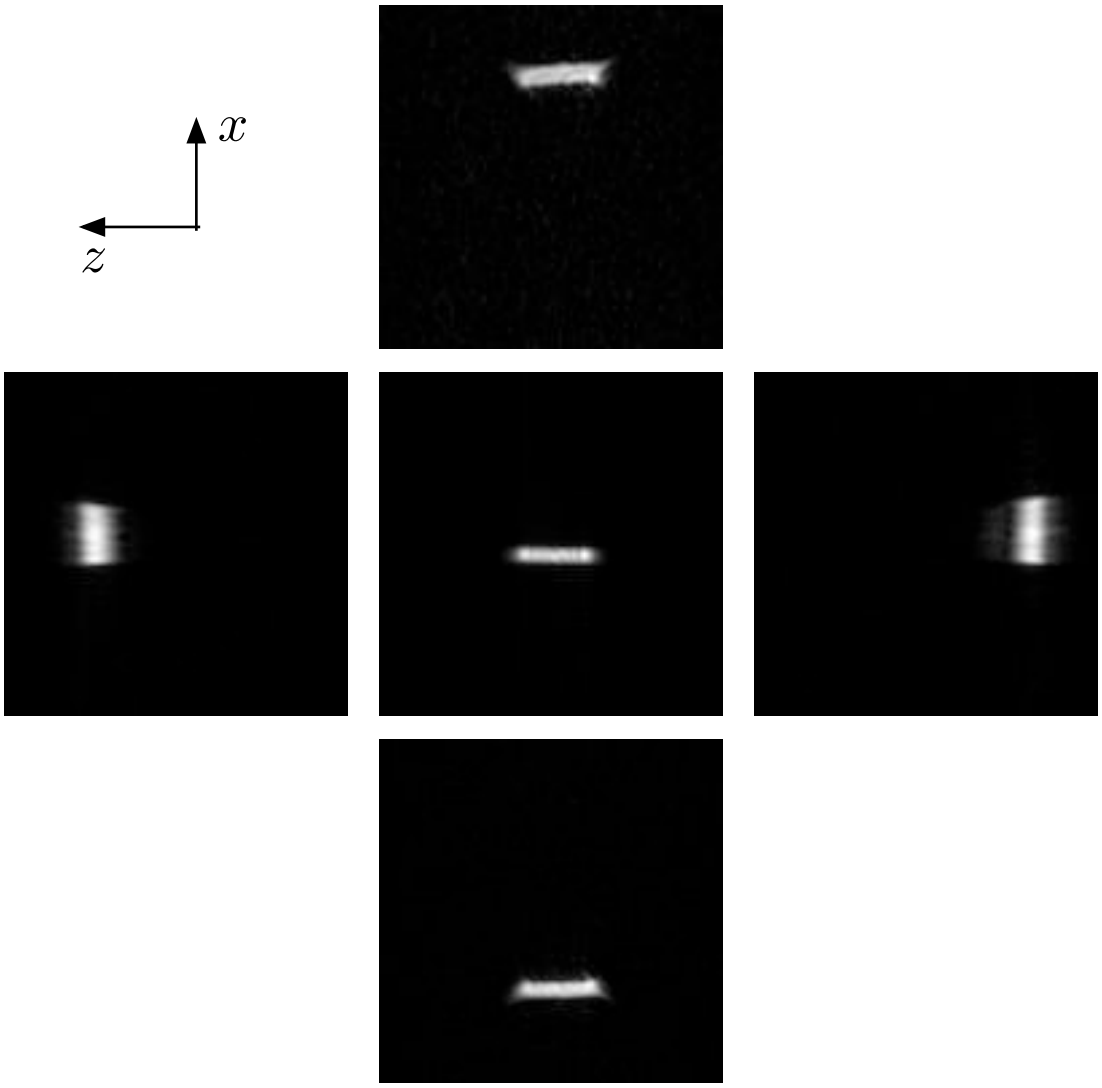

Figure 4.10: Five MRI scans obtained with a ^{3}He cell placed $\sim$ 16.5 cm from the center along the $\pm x$ and $\pm z$ directions, showing distortions at the edge of our imaging region of interest. Images are arranged showing the displacement direction, as defined by the axes. The RF coil was fixed at the center of the magnet, and all images were obtained using the same ^{3}He polarizer cell. Imaging parameters: B_0 = 65 G, ω_0 = 210 kHz, 128 $\times$ 64 image zero-filled to 128 $\times$ 128, FOV = 60 cm, no signal averaging, $\theta = 3°$, T_R = 60 ms, T_E = 7 ms, total scan time $\sim$ 3.3 s. SNR $\sim$ 400–600.

40 cm DSV region from the original B_0 designs, but adequate for human lung imaging. The distortions are most severe at the $\pm z$ sides (Figure 4.10). T_2^* broadening also resulted in decreased signal amplitude for regions further from the magnet center; in the worst case the image SNR at the $+z$ edges is approximately 0.75 in comparison to the center image. We found that the lowest distortions were along the y axis, which we attributed to the more symmetrical placement of the steel panels of the Faraday cage.

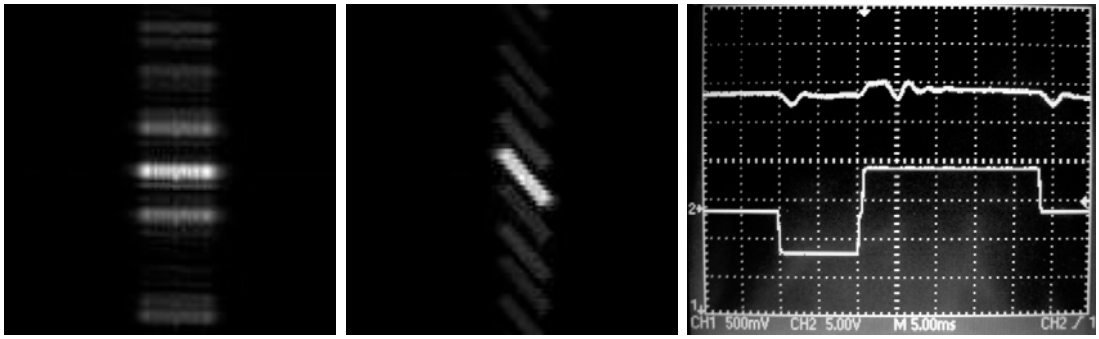

Figure 4.11: Left and middle: Sample ^{3}He cell projection images showing phase encoding artefacts seen during the first 30 minutes while the B_0 power supply is turned on. We attribute these artefacts to current compensation circuit instabilities in the power supply, triggered by small B_0 currents induced by pulsing gradients. The x axis is the phase encoding direction for these images. Similar artefacts have been seen using y phase encoding. Imaging parameters: $B_0 = 65$ G, $\omega_0 = 210$ kHz, 128×64, FOV = 50 cm, no signal averaging, $\theta = 3°$, $T_R = 60$ ms, $T_E = 7$ ms, total scan time ~ 7.7 s. Right: An oscilloscope trace showing B_0 current glitches (top trace) in response to z gradient slewing (bottom trace). The ghosting artefacts occur only when these glitches are present.

Our GRE images also occasionally suffered from ghosting artefacts (Figure 4.11). This caused smearing of the image across the phase encode direction, usually in some periodic pattern across the entire length of the image. We traced this effect back to inductive coupling between the magnetic field gradient and the B_0 coils. We disconnected the B_0 power supply and measured the inductively coupled current across the B_0 and were able to detect a signal during gradient slewing, but at levels more than two orders of magnitude smaller than what was seen with the B_0 power supply on. Oscillo-

scope traces of the B_0 current show voltage glitches occuring during gradient slewing, as shown in Figure 4.11; these voltages were as great as 1% of total voltage despite the B_0 coils possessing a self-inductance of 0.1 H. This suggested that the larger current spikes originated from the power supply. As expected, the glitching effect was greatest from the z gradients, which were much more inductively coupled to the B_0 coils than either the x or y gradient coils. We discovered that the current feedback loop on the B_0 power supply was the likely source of the glitching. After repeated testing we found that the noise decreases over time and becomes negligible approximately 30 minutes after the B_0 supply is turned on. This effect is not related to the B_0 temperature (and therefore coil resistance); if the B_0 supply is turned off for a few minutes, then turned back on, the glitch returns. Although we have largely solved this problem by making specific adjustments to our particular power supply, the general problem of inter-coil inductive coupling is one of particular importance for open-access, low-field coil designs such as ours, where the B_0 and gradient coils are all aligned nearly along the same plane.

Once the B_0 current is stable the magnetic field shifts no more than 20 Hz over an hour. The manual current control settings on the B_0 power supply are highly precise; when we first turn on the current we can dial in the LFI to within 100–200 Hz of the ^{3}He 210 kHz resonance at 65 G without the use of any high-precision current meters.

4.3 3D Imaging

We tested 3D sequences with a ^{3}He polarizer cell. The pulse sequence was identical to our 2D GRE sequences with the exception of a second phase encode gradient. We typically ran a $128 \times 32 \times 8$ scan, using either sequential or centric phase encoding schemes. We used eight phase encodes along the third dimension and cali-

brated the corresponding y gradient to produce $\sim$ 1–1.5 cm slices, for a total of 8–12 cm. We chose this setting to approximately match the postero-anterior dimension of the lung, in order to obtain as high a resolution as possible without requiring more time-consuming phase encode steps. We tailored the 3D scans to be performed in under 20 seconds to allow comfortable imaging under a single breath hold. Our resolution was approximately $0.5 \times 2 \times 1.5$ cm. We have used volume rendering subroutines in MATLAB to produce a 3D reconstruction of a ^{3}He cell with rounded windows, measuring $\sim$ 3.5 cm $\times$ 12 cm (Figure 4.12). We are continuing to optimize the 3D sequences for lung imaging. Our goal is to be able to obtain 1–4 cm^3-voxel 3D data sets of the lung in the supine versus upright postures, so that we can detect gross changes in lung shape as a function of subject orientation.

4.4 ^{3}He Tedlar Bag Imaging

We use Tedlar^{TM} plastic bags as a ^{3}He phantom for 2D imaging tests as well as pO_2 experiments discussed below. These bags are airtight with a plastic valve that can be modified for use with non-metallic Swagelok fittings and the PFA gas delivery tubes used by the polarizer. Their plastic walls are also highly compliant up to their maximum filling volume. The wall relaxation rate with ^{3}He is also relatively low; we measured $T_1 \sim$ 20–24 minutes for ^{3}He and ^{3}He-N_2 mixtures inside these bags.

We use the polarizer to deliver ^{3}He gas directly from the polarizer cell, as discussed in Section 2.3. We typically polarize the ^{3}He for at least six hours before commencing any experiments. Prior to gas delivery we flush the Tedlar bag three times with dry N_2 and evacuate any remaining gases using a plastic airtight syringe connected to the gas delivery lines. We then deliver 250–320 cc of ^{3}He directly into the bags, close the delivery valve, and start the imaging sequences.

We typically use 500 cc Tedlar bags measuring 15 cm $\times$ 15 cm. We are able

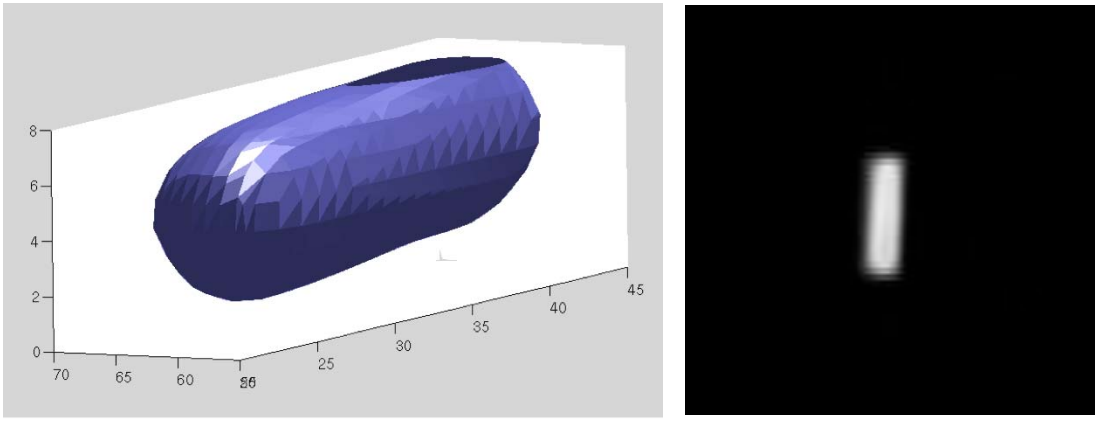

Figure 4.12: Left: A volume rendering of a 3D data set of a ^{3}He cell, performed in MATLAB. Imaging parameters: $B_0 = 65$ G, $\omega_0 = 210$ kHz, $128 \times 32 \times 8$, FOV = 36 cm, no signal averaging, $\theta = 3°$, $T_R = 60$ ms, $T_E = 7$ ms, total scan time ~ 16 s. SNR $\sim$ 400. The volume rendering includes inter-voxel interpolation to smooth the cell surface. The cell was oriented along the x axis, with the z axis as the readout direction. Right: A central slice through the cell taken from the 3D data set, showing a homogeneous signal across the cell. This data set was zero-filled to 128 $\times$ 128.

Figure 4.13: Left: a photograph of the 500 cc Tedlar bag with gas delivery tubes in place. Middle and Right: Two sample xz projection images of the Tedlar bag with the bag oriented along the yz and xz planes, respectively. Imaging parameters: $B_0 = 65$ G, $\omega_0 = 210$ kHz, 128×64, zero-filled to 128×128, FOV = 50 cm, no signal averaging, $\theta = 3°$, $T_R = 120$ ms, $T_E = 10$ ms, total scan time ~ 7.7 s. SNR $\sim$ 30–60.

to achieve SNR up to 35 with $\theta = 3°$ for projection images through the depth of the bag, which inflates to no more than 1.5–2.0 cm thick (Figure 4.13).

4.5 Quantitative Measurement of pO_2

Oxygen greatly reduces ^{3}He T_1—via a intermolecular dipolar relaxation process—when the two species are mixed together. This occurs during isolated binary collisions between ^{3}He and O_2, the latter being paramagnetic. The O_2 relaxation constant has been measured to be linearly dependent on the partial pressure of oxygen, pO_2 [41]:

$$\frac{1}{T_1} = \frac{pO_2}{1800\,\text{Torr}\cdot\text{s}}, \tag{4.1}$$

where the pressure is expressed in Torr. This relationship is valid for pO_2 as high as 10 atm. In the lungs, the total T_1 of ^{3}He can be expressed as:

$$\frac{1}{T_1} = \frac{1}{T_{1,\text{sl}}} + \frac{1}{T_{1,\text{wall}}} + \frac{1}{T_{1,\text{oxy}}}, \tag{4.2}$$

where spin-lattice (sl), wall interactions (wall), and oxygen concentration (oxy) terms are relevant. The spin-lattice contribution is on the order of hundreds of hours and can essentially be ignored. Wall relaxation often dominates when ^{3}He is contained by itself, or with an inert gas such as N_2. This contribution can vary considerably; for example we have measured T_1 of ^{3}He to be tens of hours in our polarizer cells, but only $\sim$ 20 minutes inside of a Tedlar bag. Deninger et al. measured $T_{1,\text{wall}}$ to be $\sim$ 260 s inside oxygen-depleted porcine lungs [42].

The typical alveolar oxygen partial pressure, p_AO_2, falls within 90–150 Torr in the human lungs; using Equation 4.1, we calculate $T_{1,\text{oxy}} \sim$ 10–15 s. Thus the total T_1 of ^{3}He in the lung is dominated by oxygen relaxation. Conveniently, the $\sim$ 13 s time constant is long enough to allow multiple data points to be taken, yet short enough to see substantial oxygen-dependent relaxation within a single breath hold.

4.5.1 NMR-based Measurement of pO_2

An NMR-based measurement of pO_2 is similar to that for T_1 on hyperpolarized ^{3}He, as discussed in Section 2.4.1. We revisit the relationship between the NMR signal from the n$^{\text{th}}$ pulse, $\ln(S_n)$, with the pulse flip angle θ, and inter-pulse time τ, from Equation 2.16:

$$\ln(S_n) = \ln(kM_0 \sin\theta) + n\left[\ln(\cos\theta) - \frac{\tau}{T_{1,\text{sl,wall}}} - \frac{\tau}{T_{1,\text{O}_2}}\right], \tag{4.3}$$

where we now add an additional T_1 term for pO_2 contributions. The slope, b, is now:

$$b = \ln(\cos\theta) - \frac{\tau}{T_{1,\text{sl,wall}}} - \frac{\tau}{T_{1,\text{O}_2}}. \tag{4.4}$$

We can solve for pO_2 by obtaining two sequences with and without oxygen present, and subtracting the two corresponding slopes from each other:

$$\Delta b = \frac{\tau}{T_{1,\text{O}_2}}. \tag{4.5}$$

Substituting in Equation 4.1, we obtain:

$$pO_2 = \frac{1800}{\tau}\,\Delta b. \tag{4.6}$$

We tested this method of measurement by performing pulsed NMR on a Tedlar bag filled with a mixture of ^{3}He and O_2. We ran an NMR pulse sequence similar to an angle calibration experiment. Midway through this sequence, we injected 50–60 cc of pure O_2 from a plastic syringe attached to the gas delivery tube. We drew and re-injected $\sim$ 50 cc of the mixture three times over $\sim$ 2 seconds to ensure adequate gas mixing. Figure 4.14 shows the log plot as a function of pulse number before and after the injection of oxygen into the bag. As expected, the presence of oxygen inside the bag increases the relaxation rate of the ^{3}He.

To check our results we measured the total gas volume in the Tedlar bag following each NMR experiment. We calculated pO_2 by taking the ratio of injected

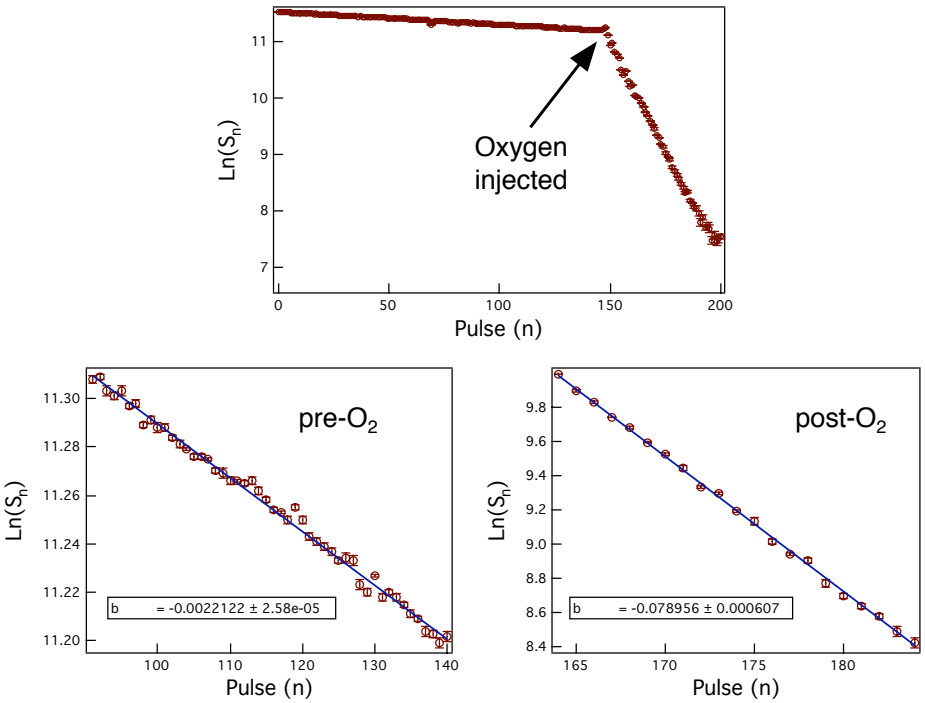

Figure 4.14: An NMR-based pO_2 experiment. The top graph shows the full plot of $\ln(S_n)$ showing the point of injection of oxygen into the Tedlar bag. The bottom graphs are data points taken before and after O_2 injection, which we fit linearly. The slopes are then used to calculate pO_2. The NMR pulse sequence used $\tau = 1.06$ s and $\theta = 2.5°$. We measured $pO_2 = 130 \pm 3$ Torr for this case, in agreement with our gas volume result of 136 ±5 Torr. We determined the total gas volume in the Tedlar bag to be 333 cc.

O_2 to the total gas volume, and multiplying by the room pressure ($\sim$ 755 Torr). Our NMR-based pO_2 measurements agree with our volume-based measurements to within 5–7%, for values ranging from 90–160 Torr. All of our NMR-based measurements have been 5–10 Torr less than our volume-based measurements. We attribute this to several systematic errors in our gas delivery methods. We typically fill the plastic syringe with pure O_2 from a separate Tedlar bag and reattach it to our delivery tubing prior to injection. Although we minimize the time the syringe tip is exposed to atmospheric air, there can be some loss of oxygen that occurs. We also suspect that some gas leakage can occur during the injection of oxygen. In earlier studies we pushed the O_2 into the

bag as quickly as possible and found up to a 20% underestimation of pO_2 from our NMR results; this error was largely eliminated simply by injecting and remixing the oxygen at a slower pace.

4.5.2 Regional Measurements of pO_2 using MRI

The basic principles behind image-based pO_2 measurements are essentially identical to the pulsed-NMR case. Instead of acquiring a series of FIDs we obtain a series of images with an inter-*image* time τ_i. We then fit for pO_2 for each pixel or a group of pixels in a region of interest (ROI) containing ^{3}He. We readapt Equations 4.3 and 4.4 for the case of image-based pO_2 mapping:

$$\ln(S_n) = \ln(S_0) + n\left[m\ln(\cos\theta) - \frac{\tau_i}{T_{1,\mathrm{sl,wall}}} - \frac{\tau_i}{T_{1,\mathrm{O_2}}}\right], \tag{4.7}$$

$$b = m\ln(\cos\theta) - \frac{\tau_i}{T_{1,\mathrm{sl,wall}}} - \frac{\tau_i}{T_{1,\mathrm{O_2}}}, \tag{4.8}$$

where m is the number of RF pulses per image and n is the image number. If we substitute Equation 4.1 into 4.8 we obtain:

$$b = m\ln(\cos\theta) - \frac{\tau_i}{T_{1,\mathrm{sl,wall}}} - \frac{\tau_i\, pO_2}{1800\,\mathrm{Torr}\cdot\mathrm{s}}. \tag{4.9}$$

Image-Based Flip Angle Calibration

We performed image-based flip angle calibrations prior to image-based pO_2 measurements. We took up to eight images of the ^{3}He polarizer cell in succession with the same pulse sequence parameters for each image (Figure 4.15). Under these conditions the T_1 relaxation time is of order 20 hours, so all signal decay is assumed to be only from the RF pulsing. Thus Equation 4.9 reduces to:

$$b = m\ln(\cos\theta) \tag{4.10}$$

for each corresponding ROI. Following our image-based experiment we performed an NMR-based pulsed flip angle calibration with the same RF pulse settings for comparisons between the two methods. We uploaded the images to the software program

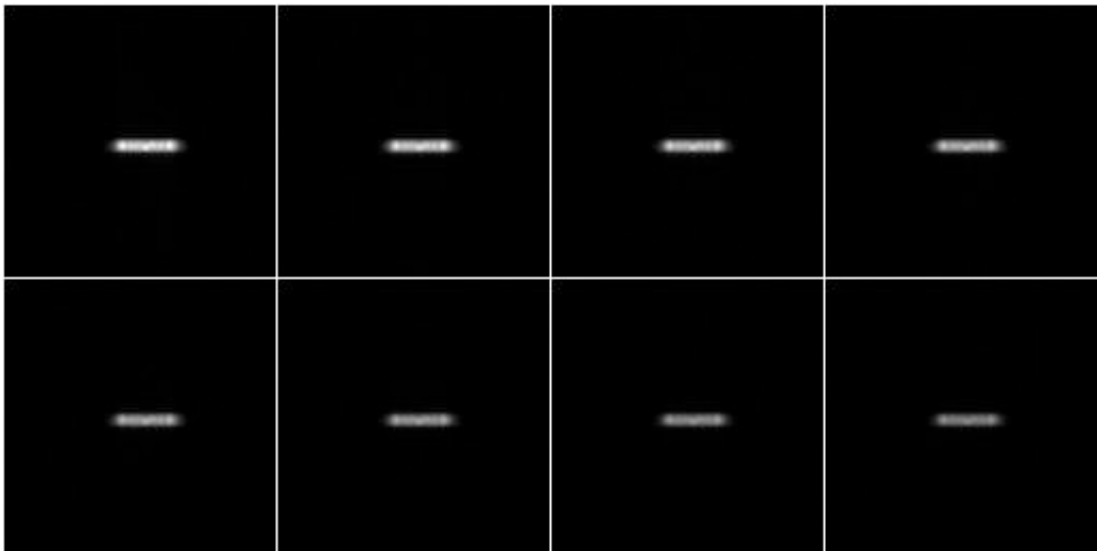

Figure 4.15: Sequence showing 8 successive GRE images of a ^{3}He polarizer cell (left to right, top to bottom). The average signal amplitude from the last image is approximately half that of the first image. Imaging parameters: $B_0 = 65$ G, $\omega_0 = 210$ kHz, 128×32, FOV = 55 cm, no signal averaging, $\theta = 3.3°$, $T_R = 60$ ms, $T_E = 7$ ms. Scan time =1.9 s per image, 15.4 s total.

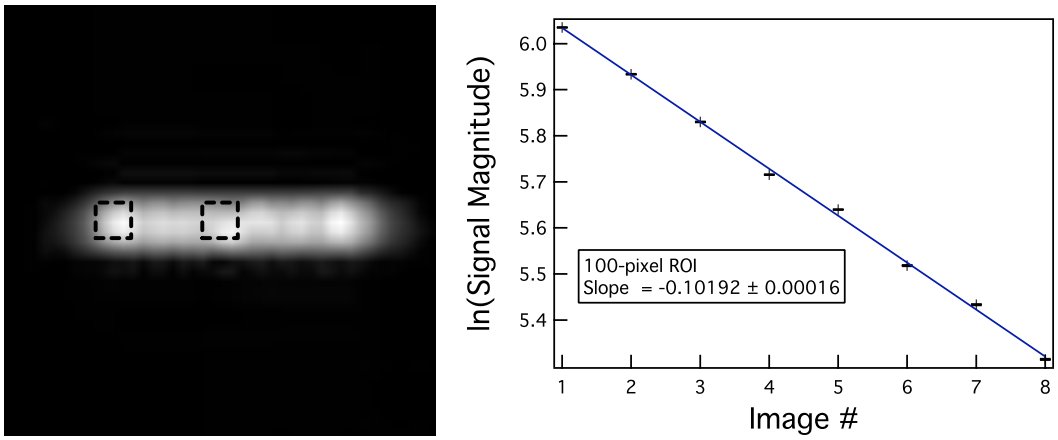

Figure 4.16: Left: A closeup of a cell image showing typical ROIs sampled (dotted boxes). Right: $\ln(S_n)$ plot and fit from the ROI at the $+z$ edge of the cell. This fit yielded $\theta = 3.23° \pm 0.02°$. The NMR-based experiment yielded $\theta = 3.27° \pm 0.02°$.

ImageJ [National Institutes of Health] where we drew regions of interest ranging from 20–100 pixels. For each ROI we obtained a mean density value M. We corrected for the baseline noise σ, which follows a Rician distribution in the FT spectrum; the adjusted intensity I_{adj} is [100, 101]:

$$I_{\text{adj}} = \sqrt{M^2 - \frac{2}{\pi}\sigma^2}. \tag{4.11}$$

We obtained σ from ROIs across the four edges of our images where there was only background noise. To obtain error bars for each M we used the standard deviation of M and divided it by the square root of the number of pixels in the ROI. Figure 4.16 shows a sample ROI and $\ln(S_n)$ plot for a typical image-based calibration.

We tested ROI sizes from 20–200 and across different portions of the cell. As expected we obtained similar calculations for θ, with variations no more than 5%. However, we also found that flip angles from image-based calibrations were typically lower than our NMR-based measurements by 2–8%. The noise background correction in our image-based studies tend to bias our results slightly downward in comparison to the simple background subtraction we use for the NMR spectra. Furthermore, we typically see a 1.5–2 $\times$ increase in the noise floor in data lines along the phase encode direction that transect the image. This is possibly related to the ghosting artefact discussed above, although this noise is present even after the B_0 supply has stabilized. Any possible current glitches are beyond the resolution of our probes. Lastly, our 2D reconstructions typically employ noise corrections such as sine-bell apodization; we find that these decrease the background noise as desired, but also result in an upward bias in I_{adj} following baseline correction.

All quantitative MRI data are highly dependent on the response characteristics of the amplification circuit. Ideally we expect the preamplifier and spectrometer receive amplifier to respond linearly to signal intensity. In practice we need to be careful not to saturate the amplifiers or to acquire signals in regimes where the response linearity has changed. We ran both NMR and image-based flip angle calibrations to

determine if the discrepancies in those two methods were related to the response of our detection electronics. We found that our flip angle responses were independent of the receiver gain settings on our spectrometer. However, there was a strong non-linear response from the preamplifier for large signals, which we confirmed by adding 10 dB and 20 dB attenuators [Minicircuits] upstream of the preampifier. If the NMR signal was too high and the attenuation too low, the flip angle calibrations were biased downward (Figure 4.17). We never saw clipping of FID data that would suggest complete

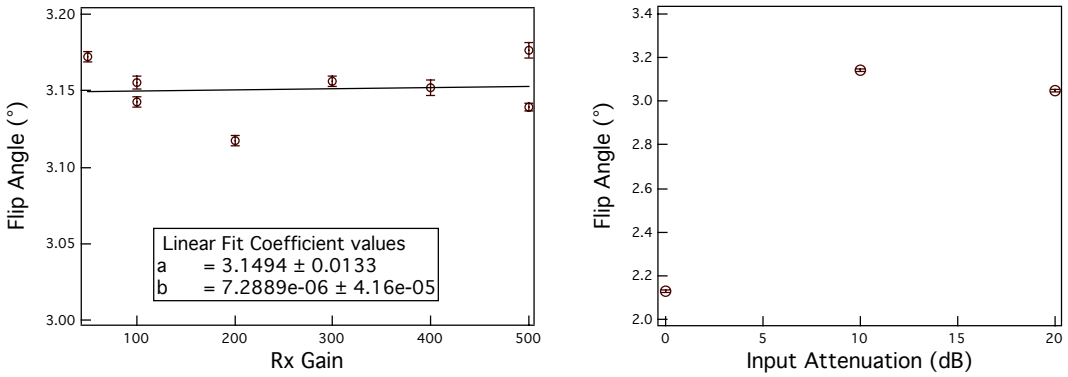

Figure 4.17: Left: A sample plot showing a series of NMR-based flip angle calibrations performed on a ^{3}He cell with different receiver gain settings on the spectrometer. We see no correlation between the gain setting and the flip angle. Right: Three flip angle calibrations performed on the same cell with differing degrees of attenuation upstream of the preamplifier. We see a significant decrease in calculated flip angle where there is no attenuation even though FIDs show now saturation clipping; we attribute this to a near-saturation, non-linear response of the preamplifier when the input signal is too high.

saturation of the preamplifier, but this effect occurred consistently only when the NMR signal was above a certain level. The NMR-based flip angle calibrations were more susceptible to this, so we used the attenuators for such experiments. A similar but much smaller effect was also seen for our image-based measurements, but we attribute this to relative differences in the noise floor affecting calculations of I_{adj}.

4.5.3 MRI-based pO_2 Measurements in Tedlar Bags

We tested image-based pO_2 measurements on Tedlar bags with known mixtures of ^{3}He and O_2. Our experimental setup and gas delivery are similar to the NMR-based pO_2 bag experiments (Section 4.5.1). However, we processed our data fits differently. First we obtained flip angle calibrations for θ—performed on ^{3}He cells—prior to the bag experiment. We then obtained our images with the ^{3}He-O_2 mixture only, without performing a similar run with ^{3}He only, and used the θ from the external calibration to obtain pO_2, using Equation 4.8. We used this method for two reasons. First, imaging required us to use a larger number of total RF pulses, and there was insufficient SNR to allow a ^{3}He-only measurement followed by a ^{3}He-O_2 measurement. Secondly, this method more accurately simulates *in vivo* imaging conditions, where a ^{3}He-only measurement is impossible.

The number of RF pulses per image can range from 16–128 depending on the imaging sequence used; this results in a 1–2 order-of-magnitude increase in the flip angle term of Equation 4.8, placing much greater importance on accurate knowledge of θ. For example, given $\theta = 5°$, $m = 64$, $\tau_i = 5s$, and $T_1 = 13$ s, and assuming negligible wall or spin-lattice T_1 contribution, a 20% uncertainty in θ contributes to a 14% error in calculated pO_2. To obtain an accurate fit for pO_2 we wish to maximize the contribution of $T_{1,\mathrm{pO_2}}$ in Equation 4.8. We use a small θ, a minimum number of phase encodes in our images ($m = 32$), and a τ_i of 7–9 s. This allows us to obtain between 3–4 images within 25 s. By reducing the number of phase encodes and acquisition points we decrease the overall resolution of our image but boost the SNR, which is critical for later images that have undergone significant T_1 decay. This gives us projection images with pixel dimensions of ~ 2 cm^2 which is adequate for initial regional mapping of the lung and for detection of gross changes in pO_2 distribution as a function of posture.

We tested our image-based pO_2 protocol on single Tedlar bags with pO_2 ranging from 50–160 Torr (Figures 4.18 and 4.19). We used θ obtained from our image-based

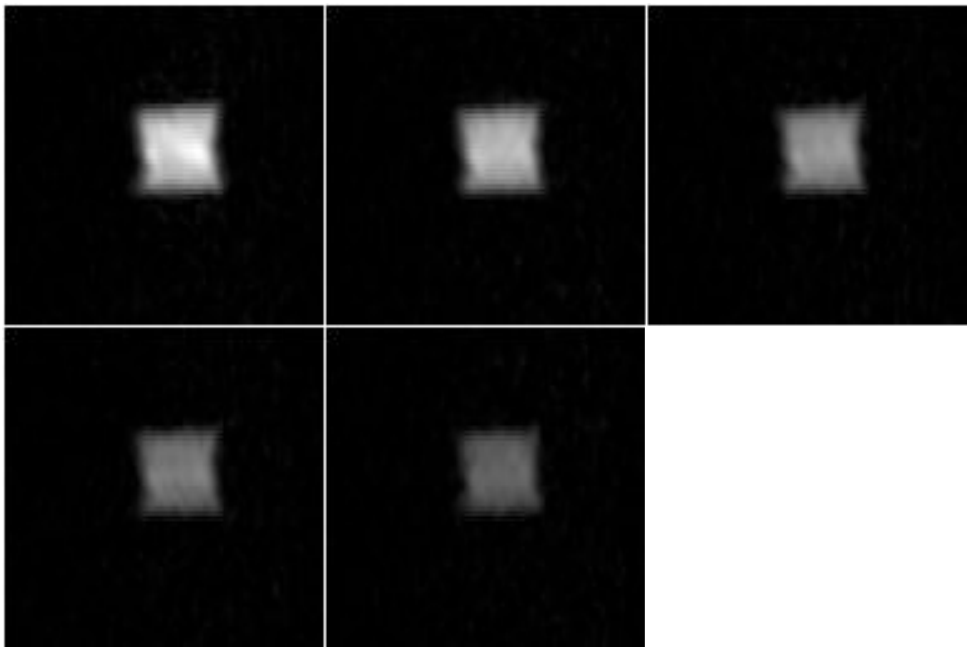

Figure 4.18: Sequence showing 5 successive GRE images of a Tedlar bag pO_2 experiment (left to right, top to bottom). The average signal amplitude from the last image is approximately one-fourth that of the first image. Imaging parameters: $B_0 = 65$ G, $\omega_0 = 210$ kHz, 64×32, no slice selection, FOV = 55 cm, no signal averaging, $\theta = 2.3°$, $T_R = 60$ ms, $T_E = 7$ ms, $\tau_i = 7$ s. Scan time =1.9 s per image, 30 s total.

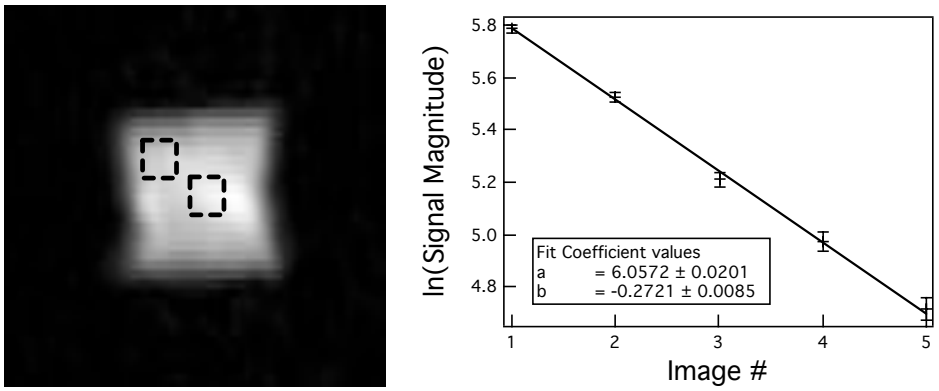

Figure 4.19: Left: A closeup of a Tedlar bag image from the experiment shown in Figure 4.18, showing typical ROIs sampled (dotted boxes). Right: $\ln(S_n)$ plot and fit from the ROI at the central region of the bag. This fit yielded $pO_2 = 60 \pm 3$ Torr. We calculated $pO_2 = 68 \pm 5$ Torr from gas volume measurements.

flip angle calibrations to limit systematic errors arising from differences between analyzing NMR and MRI data. Our measurements are similar to the NMR-based results in that the calculated pO_2 is always underestimated relative to the predicted value from our gas volume measurements, albeit to a greater degree, typically $\sim$ 7–10%. Curiously, we find that ratios between different image-based pO_2 measurements agree very well with ratios between their corresponding bag volume-based measurements (1–5%). This is also true when we look at ratios from our NMR-based measurements. This suggests that we may be able to calibrate our MRI data to a known standard (based on gas volume measurements) and adjust all of our calculations by the some standard correction factor. Further data are required before any conclusions can be drawn.

4.5.4 Use of the LFI for pO_2 Measurements in Human Lungs

Regional ^{3}He pO_2 measurements were first demonstrated at high field in animal models in 1999 [102]. Since then, oxygen influence on ^{3}He T_1 has been well characterized in the lung [103] and image-based pO_2 studies have been performed on human subjects [42, 104, 105]. All image-based pO_2 measurements have been acquired using conventional high-field instruments.

The most significant challenge for accurate pO_2 mapping involves accurate calibration of θ. In early studies the B_1 homogeneity was a significant culprit; θ varied by as much as 50% across the lungs [42]. This can be addressed at high fields by using resonator coil designs. However, coil loading at high frequencies remains a global problem that can lead to similar-size variations in θ; thus flip angle calibration must be performed as part of the imaging sequence with the subject in place. Earlier studies used two separate series of images whereby either inter-image time [42] or RF pulse amplitude [106] was changed. However, this requires two separate breath holds using two boluses of ^{3}He, making this method subject to errors from re-breathing maneuvers. Single-acquisition measurements of pO_2 have been developed using a combination of

inter-scan time and variable flip angles [107] but half the data are used for flip angle calibration purposes, limiting the accuracy of the measurement.

As discussed earlier the LFI RF coils do not suffer from significant loading effects at our frequencies, and the B_1 profile of our solenoidal coils are easy to characterize. We can thus calibrate our flip angles using NMR or image-based methods separately from our pO_2 experiment. To provide an upper bound for the effect of coil loading on θ in our system, we ran two NMR-based flip angle calibrations with a ^{3}He cell inside the RF chest coil, followed by the same sequence with 10 bottles (35 kg total) of isotonic saline (0.9% NaCl) surrounding the cell, to approximate the human thoracic region inside the coil. This resulted in a change in θ of only 2%. If we take a typical human lung experiment, where $\theta = 3°$, $m = 32$, $\tau_i = 5$ s, and $T_1 = 13$ s, and assume negligible wall or spin-lattice T_1 contribution, a 2.0% uncertainty in θ contributes only to a 0.9% error in calculated pO_2. Thus we can accurately measure regional pO_2 in the lung using pre-determined flip angles.

In practice the *in vivo* p_AO_2 changes over time, due to consumption of the oxygen by the pulmonary vasculature; in regions with adequate perfusion the local alveolar oxygen pressure will continue to fall until it equilibrates with the oxygen tension of deoxygenated blood. This consumption rate has been estimated to be roughly constant and linear, between 1.5–2.0 Torr/s [42]. If we now assume pO_2 to have a linear dependence with time:

$$pO_2 = p_0 - R\,t, \tag{4.12}$$

where p_0 is the initial pO_2 and R is the oxygen depletion rate, the expression for $\ln(S_n)$ (Equation 4.8) now becomes:

$$\ln(S_n) = \ln(S_0) + n\,m\ln(\cos\theta) - \frac{n\,\tau_i}{T_{1,\mathrm{sl,wall}}} - n\,\tau_i\,\frac{pO_2}{1800\,\mathrm{Torr}\cdot\mathrm{s}} - (\tau_i\,n)^2\,\frac{R}{1800\,\mathrm{Torr}\cdot\mathrm{s}}. \tag{4.13}$$

We now have a non-linear relationship with n which can be fit. A version of this technique was recently used in an NMR-based experiment to obtain R $\sim$ 0.001 bar/s

for the lung at 3.0 mT [88], but has never been implemented in an image-based form.

4.6 Initial ^{3}He MRI of Human Lungs

We have obtained initial human lung images with the LFI. Figures 4.20–4.21 show 2D and 3D MR images obtained with a female human volunteer subject in the supine orientation. We delivered 400–500 cc of hyperpolarized ^{3}He to the subject, who breathed in the gas from FRC. To facilitate the breath hold, the subject inhaled an additional 100–150 cc of room air. The subject held her breath for 35 s, long enough for one complete 3D data set to be obtained. The subject's blood pressure and spO_2 levels were monitored throughout the experiment, in compliance with IRB requirements.

The 2D projection image shows well-defined pleural boundaries with SNR $>$ 50 (Figure 4.20). The cardiac profile can be seen in the medial aspect of both right and left lungs, and both lateral and antero-posterior diaphragm curvature is evident. The image intensity is greatest nearer the middle-to-inferior and lateral aspects of the lung, where the anterio-posterior dimensions of the lung are thickest.

We optimized a 3D sequence to produce 1.5 cm slices across the antero-posterior dimension of the lungs. A total of six slices were obtained and zero-filled to eight. A 3D reconstruction of the data set clearly shows the region where the heart resides, with a larger groove on the medial aspect of the left lung than on the right, as expected (Figure 4.21). The 2D coronal slices show an even distribution of ^{3}He ventilation throughout the periphery of the lung. The regions exhibiting the greatest antero-posterior thickness correspond to the greatest intensity levels from the 2D projection image. Central slices also show a faint ^{3}He signal in the left bronchus, but not in the right one. We attribute this to residual ^{3}He remaining in the large airways even after the subject had taken a chaser breath of room air. This is consistent with anatomy; the left bronchus has a slightly sharper branching angle, and thus gas flow

through the region is lower in comparision to the right bronchus.

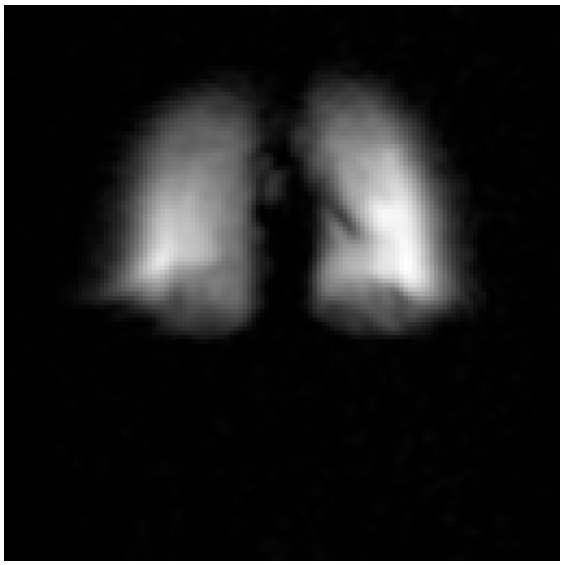

Figure 4.20: Coronal projection image of the human lungs, with the subject supine. Imaging parameters: $B_0 = 65$ G, $\omega_0 = 210$ kHz, FOV = 50 cm, 128×64, zero-filled to 128×128, no signal averaging, $\theta = 5.6°$, $T_R = 86$ ms, $T_E = 10$ ms, total scan time $\sim$ 5.5 s. SNR $\sim$ 50–60.

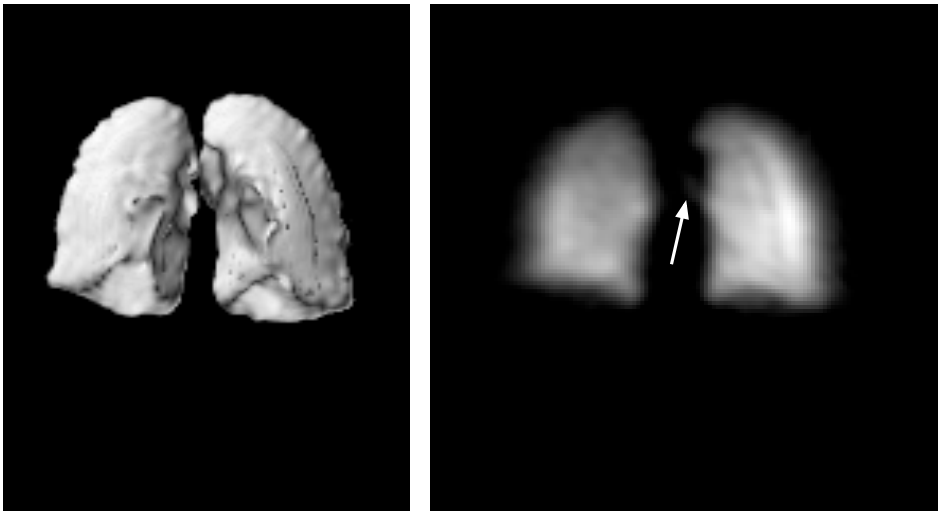

Figure 4.21: Left: A 3D reconstructed ^{3}He MR image of human lungs, with the subject supine. The anterior face of the lungs is shown, revealing the cardiac profile. Right: A central coronal slice from the 3D data set. The arrow shows a trace of ^{3}He gas remaining in the left bronchus. Imaging parameters: $B_0 = 65$ G, $\omega_0 = 210$ kHz, $128 \times 64 \times 6$, zero-filled to $128 \times 128 \times 8$, FOV = 50 cm, slice thickness = 1.5 cm, no signal averaging, $\theta = 4.1°$, $T_R = 86$ ms, $T_E = 10$ ms, total scan time $\sim$ 33 s.

Chapter 5

Conclusion

This thesis describes the design and construction of a low-field, open-access magnetic resonance imaging (MRI) system for *in vivo* ^{3}He imaging of the human lungs. Our system permits the study of lung function in both horizontal and upright postures, a subject with important implications in pulmonary physiology and clinical medicine. We constructed a custom polarizer that uses spin exchange optical pumping (SEOP) to hyperpolarize ^{3}He to 10–15%. This polarizer contains novel and cost-effective methods to store and deliver ^{3}He to our experiments. The LFI uses a bi-planar B_0 coil design that produces an optimized 65 G (6.5 mT) magnetic field for ^{3}He and ^{1}H MRI at 210 kHz and 275 kHz, respectively. The field homogeneity results in T_2^* broadening of $\sim$ 15–30 ms for a lung-sized region. Three custom-built bi-planar coils produce the x, y, and z magnetic field gradients and provide up to 79-cm inter-coil gap for the imaging subject. We use solenoidal Q-spoiled RF coil designs unique for operation at low frequencies, and are able to exploit the lack of significant sample loading effects to allow for pre-tuning/matching schemes and for accurate pre-calibration of flip angles.

We filter the B_0 and gradient current lines and modified several electronic components to be compatible at the 200–300 kHz frequency range. This allows sufficient SNR to perform thermal ^{1}H imaging at 65 G. We have produced images of water

phantoms as well as slice-selected images of a human head. We have also produced ^{3}He images of sealed glass cells and plastic bags at resolutions and SNR similar to those on conventional high-field systems. We show reproducible image quality for both horizontal and upright imaging configurations. We have also exploited a well-known ^{3}He relaxation dependency on oxygen concentration to obtain NMR and image-based measurements of pO_2 in known gas mixtures inside of plastic bags. Finally, we present initial ^{3}He MR images of human lungs obtained with the LFI.

5.1 Future Studies

Our first lung studies will involve a combination of qualitative imaging and quantitative measurements of pO_2. We plan to use 2D projection and slice-selection images to obtain high quality coronal images of the lung in the supine, prone, and upright postures. Preliminary results from the prototype imager shows elongation in lung shape in the upright posture [49], but more data are needed before any conclusions can be drawn. We also plan to use our 3D imaging techniques to more accurately detect changes in the pleural boundaries as a function of supine, prone, and upright postures.

pO_2 maps have been made on normal human subjects only in the supine position [42, 107]. We will obtain similar maps on the LFI with the subject in both supine and upright positions using the methods described in Chapter 4. The classical description of the upright lung shows gravity dependencies in both perfusion and ventilation, with a relatively greater perfusion gradient. The net effect is a higher V/Q at the top of the lungs versus the bottom [51]. We will use the LFI to provide upright pO_2 data in human lungs to directly measure this phenomenon. Our imaging technique will also allow measurement of O_2 consumption, which directly reflects V/Q. We will compare such results from our supine imaging to PET studies, which have so far provided the most reliable quantitative data on pulmonary gas exchange [17, 18].

Although our initial human subjects consist of healthy volunteers, the LFI is well-suited for studies of pulmonary pathophysiology. In particular, asthma involves air trapping easily visualized with ^{3}He MRI [108, 109]. Such trapping has never been visualized in the upright posture, which is more clinically relevant, as patients tend to exhibit better ventilation in that position. As mentioned in Chapter 1, the collapsing airways in an asthmatic attack has been shown to exhibit gravitational dependence in PET measurements on supine lungs [19], an effect that would be enhanced in the upright posture.

Diffusion measurements of ^{3}He in the lungs reflect local airway dimensions, and are significantly altered in diseases such as emphysema, where alveolar walls break down and form larger pockets with poor gas exchange surface area [43, 44]. Posture dependence in alveolar size has been demonstrated using ^{3}He diffusion techniques [110] but only in decubitus positions; we expect enhancement of this effect in the upright posture.

5.2 Future Improvements on the LFI

Although the LFI is currently optimized for lung imaging, there are several future improvements to the hardware and design that can further boost SNR and imaging speed, and allow newer quantitative sequences to be considered.

5.2.1 Continued ^{3}He Polarizer Development

We currently generate $\sim$ 500 cc of 10–15% polarized ^{3}He every 6–8 hours using the SEOP method. Recently, SEOP times have improved through use of K-Rb hybrid cells. This pumping technique is accelerated by the K-^{3}He spin exchange rate, which is up to 10 times greater than Rb-^{3}He [37,71]. These hybrid cells can achieve polarizations greater than 50% in under three hours [38, 111]. This would boost SNR by a factor of

4–6 on our system without requiring significantly new cell designs.

Another limitation to our polarization scheme is laser power. LDAs provide high laser power but suffer from broad spectra; as a result a significant portion of laser power is off-resonance during SEOP. External cavity diode arrays [112–116] and volume Bragg gratings [117,118] can narrow linewidths to < 0.5 nm while maintaining a total power output > 50 Watts, and are robust, cheap, and easy to assemble. This, in combination with hybrid cells, will boost our SNR by at least an order of magnitude for all of our experiments.

5.2.2 Continued LFI Development

Several aspects of our current setup can be changed to improve the performance of the LFI. The most significant gains in SNR will likely be made by improving B_0 homogeneity. Performance is most limited by the presence of ferromagnetic steel panels that form the bottom walls and floor of the Faraday cage. Despite our best efforts at shimming there remain significant distortions caused by the magnetization of the steel panels. Partial or full removal of these panels, particularly at the $\pm z$ sides along the B_0 coil axis, as well as the floor and ceiling panels closest to the outer B_0 coils ($\pm y$), will likely improve T_2^* significantly, albeit at the expense of total magnetic field strength.

LFI performance can also be enhanced by improving the total output from the magnetic field gradient coils. This would enable shorter echo times on GRE sequences and larger operating bandwidths, improving imaging time. Better gradient performance can also allow faster 3D sequences, which could be used for true 3D quantitative mapping of parameters such as pO_2 [119,120]. Increasing the magnetic gradient field strength in the LFI is most easily achieved by driving each planar gradient set with two gradient amplifiers run in master-slave configuration. This would produce up to twice the available current, and would not require any modification of the coil or re-

sistor banks, which are designed to withstand the extra power. However, special care needs to be taken to address gradient amplifier noise, as discussed earlier. An increase in the z gradient power may cause more severe inductive effects in B_0 during slewing, as mentioned in Section 4.2. If such a problem continues to exist, an actively-shielded coil design may be the best solution. Although these designs are considerably more complex in both design and construction, they would minimize inductive coupling with the B_0 coils and boost the overall output efficiency [121–123].

Appendix A

MRI Theory

This appendix provides a very brief overview of NMR and MRI theory. A basic quantum mechanical and semi-classical description of magnetic resonance phenomenon is presented, along with definitions of T_1 and T_2 relaxation times. A more thorough description of NMR and MRI can be found in several excellent sources [94, 124, 125].

A.1 Bulk Magnetization of Spin-$\frac{1}{2}$ Systems

An atom with a nuclear spin $\boldsymbol{I}$ will possess a net magnetic moment $\boldsymbol{\mu}$:

$$\boldsymbol{\mu} = \gamma \boldsymbol{I}, \tag{A.1}$$

where γ is the gyromagnetic ratio. If a magnetic field $B_0 \hat{\boldsymbol{z}}$ is applied to this system, the Hamiltonian operator describes the Zeeman interaction:

$$H = -\gamma \, \hbar \, B_0 \, I_z. \tag{A.2}$$

If we solve Schrödinger's equation:

$$\mathrm{i} \, \hbar \, \frac{\partial}{\partial t} |\boldsymbol{\Psi}(t)\rangle = H \, |\boldsymbol{\Psi}(t)\rangle, \tag{A.3}$$

where H is constant with time, we obtain an evolution operator $U(t)$:

$$|\mathbf{\Psi}(t)\rangle = U(t)\,|\mathbf{\Psi}(0)\rangle, \tag{A.4}$$

such that

$$U(t) = e^{\mathrm{i}\,\gamma\,B_0\,I_z\,t}. \tag{A.5}$$

This describes a precession about the z-axis at the Larmor frequency:

$$\omega_0 = \gamma\,B_0. \tag{A.6}$$

The simplest spin systems are for $I = \frac{1}{2}$, which pertains to ^{1}H and ^{3}He imaging, where there are only two energy states available, separated by $\Delta E = \hbar\,\omega_0$.

Although NMR can be completely described as a quantum mechanical problem, it is more easily visualized via a semi-classical description [94,124,125]. The motion of an ensemble of spins can be regarded as a bulk magnetization $\boldsymbol{M}$ where $\boldsymbol{M}/\gamma$ is the macroscopic angular momentum of the entire group. In the presence of a magnetic field $\boldsymbol{B}$ the magnetization feels a torque described by:

$$\frac{\mathrm{d}\boldsymbol{M}}{\mathrm{d}t} = \gamma \boldsymbol{M} \times \boldsymbol{B}. \tag{A.7}$$

with a net energy of

$$E = -\boldsymbol{M} \cdot \boldsymbol{B} = -M\,B\,\cos\phi, \tag{A.8}$$

where ϕ is the angle between $\boldsymbol{M}$ and $\boldsymbol{B}$. $\boldsymbol{M}$ precesses about the magnetic field (z) axis, at the same characteristic Larmor frequency ω_0 previously described for the single spin system (Figure A.1).

A.2 Resonance Behavior

NMR techniques involve the manipulation and detection of the bulk spin magnetization moment described above. To achieve this a transverse oscillating field B_1

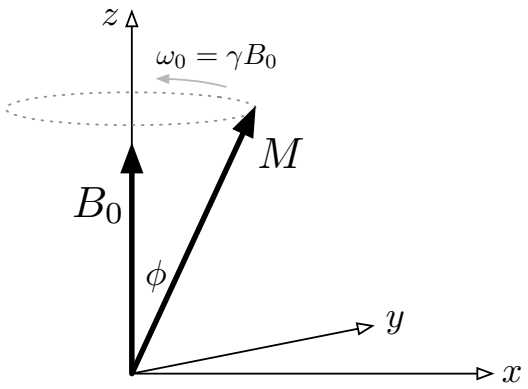

Figure A.1: Bulk Magnetization and Precession about B_0. The bulk magnetization M precesses about the z axis at the Larmor frequency ω_0.

is introduced along the plane transverse to B_0, with a frequency matching ω_0. NMR frequencies range from the 10 kHz to 1 GHz range and so B_1 is often referred to as a radiofrequency (RF) field. This field can be reduced to a combination of two circularly-polarized components, of which only one possesses the same rotational sense as $\boldsymbol{M}$:

$$\boldsymbol{B_1} = B_1 \cos(\omega_0 t)\, \hat{\boldsymbol{x}} + B_1 \sin(\omega_0 t)\, \hat{\boldsymbol{y}}. \tag{A.9}$$

The solution to Equation A.7 with the starting condition $\boldsymbol{M} = M_z$ and the addition of the co-rotating $\boldsymbol{B_1}$ is:

$$M_x = M_0 \sin\omega_1 t\, \sin\omega_0 t \tag{A.10}$$

$$M_y = M_0 \sin\omega_1 t\, \cos\omega_0 t \tag{A.11}$$

$$M_z = M_0 \cos\omega_1 t, \tag{A.12}$$

where $\omega_1 = \gamma B_1$, known as the Rabi frequency. To further simplify the mechanics of this interaction, a rotating frame of reference that follows B_1 is used. The result is simply a precession of M about B_1 (Figure A.2). B_1 is typically on for a finite "pulse" time τ. If the starting magnetization is along the z axis, M precesses about B_1 by the flip angle $\theta = \omega_1 \tau$ in the rotating frame.

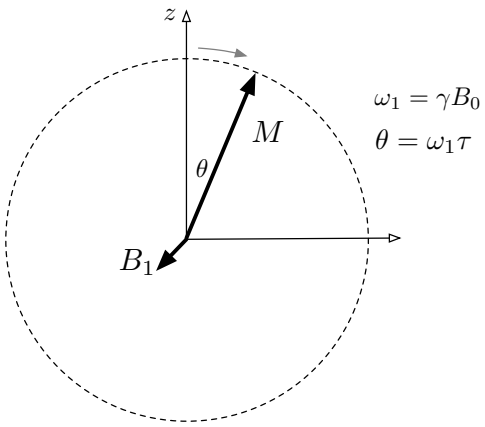

Figure A.2: The rotating frame follows B_1 at resonance, and results in M precessing around B_1 (pointing out of the page). The flip angle $\theta = \omega_1 \tau$ depends on the RF pulse amplitude and length.

A.3 Relaxation

If an RF pulse with $\theta \neq n180°$ (where n is any integer) is applied to an ensemble of spins originally aligned along the B_0 longitudinal direction ($M_0\,\hat{\boldsymbol{z}}$), the result is a bulk magnetization with both longitudinal M_z and transverse $M_{x,y}$ components. In the absence of any further interactions the system would continue to precess about the z axis at an angle θ. However, two relaxation mechanisms, T_1 and T_2, are present in real spin systems. If they are incorporated into the general form of Equation A.9 we obtain the Bloch Equations:

$$\frac{\mathrm{d}M_z}{\mathrm{d}t} = -(M_z - M_\circ)/T_1 + \gamma(\boldsymbol{M} \times \boldsymbol{B})_z \tag{A.13}$$

$$\frac{\mathrm{d}M_x}{\mathrm{d}t} = \gamma(\boldsymbol{M} \times \boldsymbol{B})_x - \frac{M_x}{T_2} \tag{A.14}$$

$$\frac{\mathrm{d}M_y}{\mathrm{d}t} = \gamma(\boldsymbol{M} \times \boldsymbol{B})_y - \frac{M_y}{T_2}. \tag{A.15}$$

T_1 is known as the spin-lattice, or longitudinal, relaxation time. This process involves energy exchange between the spin system and its surrounding thermal reservoir. In essence, the spin ensemble returns to its original thermal equilibrium M_{eq} along the

longitudinal axis (along B_0) via an exponential recovery:

$$M_z(t) = M_z(0)e^{-\frac{t}{T_1}} + M_{eq}(1 - e^{-\frac{t}{T_1}}) \tag{A.16}$$

T_1 times can range from milliseconds in solids to several seconds for ^{1}H in clean water, to hundreds of hours for ^{3}He inside a clean glass cell.

The transverse component of the magnetization also relaxes and contributes to dephasing across the spin ensemble as they precess about the longitudinal axis. This process is known as T_2, or spin-spin, relaxation. Spin-lattice energy interactions contributes to T_2, but so do other factors such as local energy exchanges between nearby spins; as a result $T_2 \leq T_1$. T_2 relaxation follows the form:

$$M_{x,y}(t) = M_{x,y}(0)\, e^{-\frac{t}{T_2}}, \tag{A.17}$$

where the decay of the transverse component $M_{x,y}$ is due to dephasing of the spins precessing about the longitudinal axis. The rate of dephasing can be worsened by local magnetic field inhomogeneities ΔB such that the total relaxation rate is greater than the spin-spin T_2:

$$\frac{1}{T_2^*} = \frac{1}{T_2} + \frac{\gamma \Delta B}{2}, \tag{A.18}$$

where T_2^* represents the total dephasing rate. Other factors such as susceptibility-induced magnetic gradients can also contribute to T_2^*.

A.4 Signal Detection and Measurement

NMR signal detection is performed using an inductive pickup coil orthogonal to the longitudinal axis. Precession of the bulk magnetization about the longitudinal axis induces a current in the detector coil, yielding a sinusoidal signal with a T_2^* decay. Heterodyne mixing is usually performed with two reference signals 90° out of phase, so that the detection scheme is phase sensitive. The mixed signal has a frequency $\Delta\omega$, the

difference between the reference and Larmor resonant frequency, and can be written in complex terms:

$$S(t) = S_0 e^{\mathrm{i}\,(\phi+\Delta\omega)\,t}\, e^{-\frac{1}{T_2^*}}, \tag{A.19}$$

where ϕ is the phase of the receiver, and S_0 is the initial signal amplitude, proportional to $M_z(0)$. This raw signal is known as the free induction decay (FID).

A Fourier transform (FT) of the FID gives a representation of the signal in frequency space, which is easier to interpret experimentally. ϕ is arbitrary and can be adjusted to zero during post-processing. The FT of the raw signal then yields both a real and imaginary components, corresponding to in-phase and out-of-phase components, respectively:

$$\mathrm{Re}\{\mathcal{F}(S(t)\} = \frac{S_0\, T_2^*}{1 + T_2^{*2}(\Delta\omega)^2} \tag{A.20}$$

$$\mathrm{Im}\{\mathcal{F}(S(t)\} = \frac{S_0\, T_2^{*2}\, \Delta\ \omega}{1 + T_{2*}^2\, (\Delta\omega)^2} \tag{A.21}$$

Figure A.3 shows plots of the real and imaginary components of the FID and corresponding FT spectra. The real FT spectrum follows a Lorentzian lineshape with the full-width-half-max of $\frac{1}{\pi T_2^*}$. This linewidth is often used in as a reflection of sample T_2^* or B_0 inhomogeneity.

A.5 Fourier Imaging and k-Space

Imaging in NMR is made possible through the use of longitudinal magnetic field gradients applied in addition to the original $B_0\hat{\boldsymbol{z}}$ magnetic field. If such a gradient field $\boldsymbol{G} = \nabla B_z$ is added, the resonant frequency of an ensemble of spins within the total magnetic field will be

$$\omega(\boldsymbol{r}) = \gamma\,(B_0 + \boldsymbol{G}\cdot\boldsymbol{r}), \tag{A.22}$$

where the resonant frequency is now a function of spin position $\boldsymbol{r}$. This is the basis for all spatial encoding techniques in MRI, as first exploited by Mansfield and Lauterbur [22,

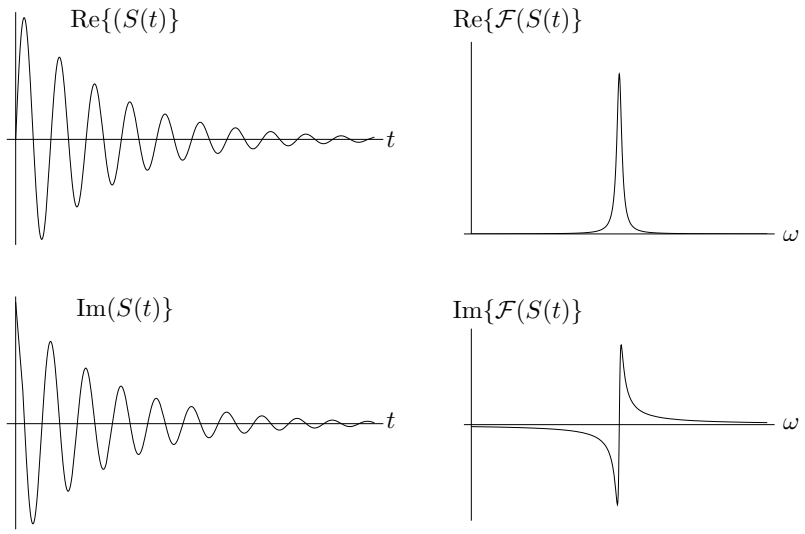

Figure A.3: Sample FID (left) and FT (right) plots corresponding to the real and imaginary components of a typical raw NMR signal. The FIDs have a characteristic T_2 decay from spin dephasing. The receiver phase ϕ has been adjusted to zero to yield Lorentzian and dispersion FT curves.

23]. Equation A.19 can be rewritten to include this gradient field:

$$S(t, \boldsymbol{G}) = S_0(\boldsymbol{\rho}) \int \rho(\boldsymbol{r}) e^{\mathrm{i}\,(\gamma\,\boldsymbol{G}\cdot\boldsymbol{r})\,t}\,\mathrm{d}r, \tag{A.23}$$

where $\rho(r)$ represents a spin density function that includes phase and frequency characteristics related to T_2 and B_0. This can be rewritten again into a more general form:

$$S(\boldsymbol{k}) = \int \rho(\boldsymbol{r}) e^{2\pi\mathrm{i}\,(\boldsymbol{k}(t)\cdot\boldsymbol{r})}\,\mathrm{d}r, \tag{A.24}$$

where $\boldsymbol{k}$ contains all the frequency and phase-encoded characteristics provided by the total magnetic field. From this expression $\rho(r)$ can be obtained from the raw signal function through a simple reverse Fourier transformation:

$$S(\boldsymbol{k}) = \int \rho(\boldsymbol{r}) e^{2\pi\mathrm{i}\,\boldsymbol{k}(t)\cdot\boldsymbol{r})}\,\mathrm{d}\boldsymbol{r} \iff \rho(\boldsymbol{r}) = \int S(\boldsymbol{k}) e^{-2\pi\mathrm{i}\,\boldsymbol{k}(t)\cdot\boldsymbol{r})}\,\mathrm{d}\boldsymbol{k} \tag{A.25}$$

This notation was used by Mansfield [23] and the term "k-space" has since been used to describe the 2D or 3D raw data space in $S(\boldsymbol{k})$.

A.6 Frequency and Phase Encoding

MRI typically employs three independent coils that provide a spatially dependent magnetic field gradient across each of the three cartesian axes. If these are defined as $G_x(t), G_y(t), G_z(t)$ and incorporated into Equation A.23, the resulting relationship becomes easier to implement experimentally:

$$S(t, \boldsymbol{\rho}) = S_0(\boldsymbol{\rho}) \iiint \rho(\boldsymbol{r}) e^{\mathrm{i}\,(\gamma\,(xG_x(t),+yG_y(t)+zG_z(t))\,t)}\,\mathrm{d}x\,\mathrm{d}y\,\mathrm{d}z \tag{A.26}$$

$S(t, \boldsymbol{\rho})$ represents a single FID. Typically only one gradient field (e.g., G_x) is activated during the detection period, and thus the spin density profile can be obtained across that single axis. The FT spectrum contains the 1D profile of the spins along the applied gradient axis; this is known as frequency encoding, and the associated gradient is often referred to as the readout gradient. In the simplest case of 2D imaging, a second gradient (e.g., G_y) is applied for a finite time prior to the acquisition period. Although that gradient is no longer on during the readout time, G_y has introduced an additional phase component to the evolution of the spin ensemble that is reflected in $S(t, \boldsymbol{\rho})$ during signal detection. This is known as phase encoding. In order to fully resolve the spin density profile, n FIDs must be acquired with varying G_y—usually by varying the amplitude of that magnetic field gradient— to achieve n points along that dimension in both k-space and in the final FT image.

3D information can be obtained using two common methods. The first is to employ a second phase-encode gradient along the third dimension. Thus for a m-by-n-by-k-pixel image where m represents the number of readout acquisition points, $m \times k$ FIDs must be acquired to produce the complete image. Another alternative is to excite only a slice of spins during the RF pulse, by employing a slice-selection gradient in conjunction with a sinc-shaped pulse. The latter excites a range of RF frequencies Δf, inversely proportional to the length of the pulse τ:

$$\Delta f = \frac{1}{\tau} \tag{A.27}$$

Only the spins possessing a Larmor frequency within Δf are excited. This slab is then subjected to the same frequency and phase-encoding scheme described above, and the result is a 2D slice across the subject. Multi-slice imaging schemes allow the stacking of multiple 2D slabs to construct a full 3D data set.

A.7 Spin Echo Imaging

The spin echo phenomenon was first described by Hahn in 1952 [126]. In its simplest form, an RF pulse with a flip angle θ is administered, followed by a π pulse a period τ later (Figure A.4). The first RF pulse results in a spin precession about the z axis and transverse relaxation associated with spin-spin dephasing. Following the π pulse, however, the phase decoherence process is reversed. At exactly one period τ following this pulse, the phase coherence is once again at a maximum, and an echo can be detected. The time from the first RF pulse to the maximum echo signal ($2\,\tau$) is known as the echo time, or T_E. A series of π pulses can also be utilized to obtain multiple echoes over a period of time, provided T_2 is sufficiently long.

Figure A.5 describes a pulse sequence diagram for typical spin echo sequences used in our experiments. We typically use $T_E \sim$ 10–40 ms, $\pi/2$ pulses on the LFI, with 8–16 signal averages for each image. On the LFI system the frequency encoding direction is along z.

A.8 Gradient Echo

We use gradient echo (GRE) sequences for all ^{3}He imaging. Here the transverse spin refocusing is performed by the magnetic field gradients rather than a $\pi/2$ pulse. This allows us to use only a single RF pulse per repetition time (T_R), and we can use a small flip angle θ to preserve the longitudinal magnetization of the hyperpolarized ^{3}He, which is irrecoverable. Figure A.6 shows a typical GRE pulse sequence. We typically

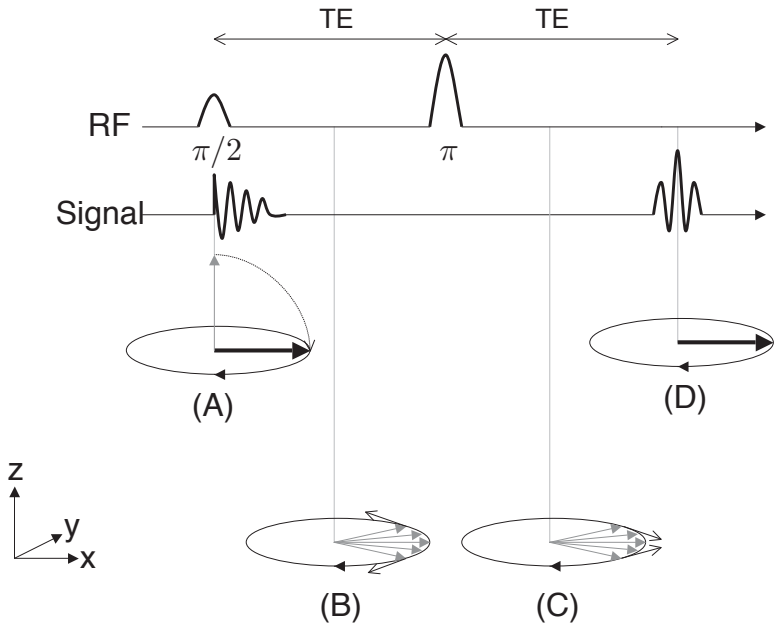

Figure A.4: A simple Hahn echo sequence, showing echo production following a π pulse. (A) In this example, a $\pi/2$ pulse flips the magnetization vector to the xy plane. An initial FID can be seen. (B) As time passes, the precession of the magnetization vector becomes gradually incoherent. (C) Following the π pulse, the decoherence process is reversed, and the signal is recovered in the form of an echo (D). For simplicity we ignore T_1 recovery.

use $\theta \sim 3$–7° and $T_R \sim 60$–100 ms for ^{3}He imaging. Because the rephasing gradient can be applied immediately following the phase encoding gradient, the GRE sequence can be much faster than spin echo.

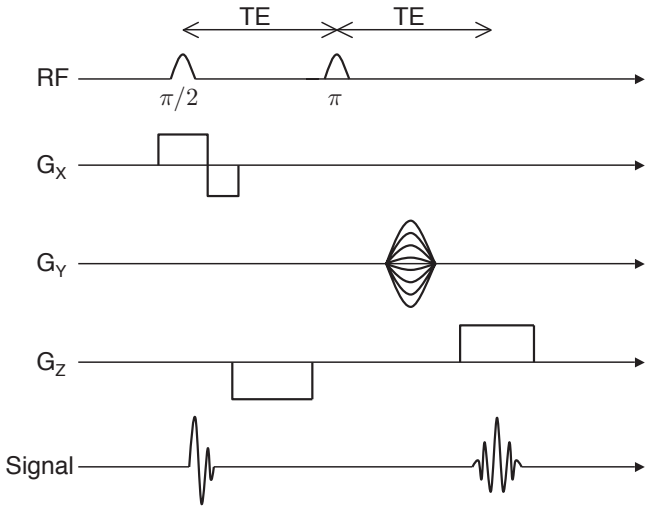

Figure A.5: Pulse sequence for spin echo imaging. The x, y, and z gradients are the slice selection, phase encoding, and readout gradients, respectively.

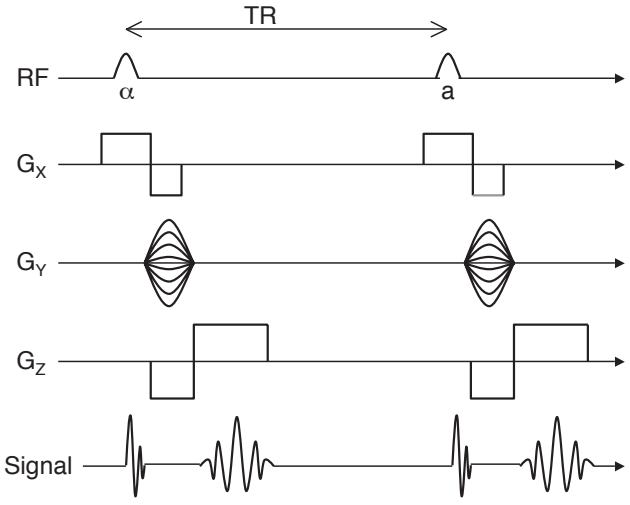

Figure A.6: Pulse sequence for gradient recovery echo imaging.

Appendix B

Description of the Prototype Low-Field ^{3}He MRI System

A short description of the prototype LFI system at UNH is presented here. We used this system to produce the first pair of ^{3}He human lung images in both the supine and upright postures. The ^{3}He polarizer used with this system is the same one described in Chapter 2. For a summary and discussion of our results from this system, see [49, 127].

B.1 Open-access electromagnet

The B_0 field was produced by two pairs of resistive coils. The larger pair consisted of 2 m diameter coils, each with 120 turns of copper wire (DC resistance = 0.91 Ω), and with the planes of the coils separated by 73.6 cm. The second pair—used for field correction and homogeneity optimization—consisted of two 86 cm diameter coils, each with 100 turns of copper wire (DC resistance = 0.11 Ω), and with planar separation of 120.0 cm. Both pairs were vertically mounted on large triangular aluminum brackets, and their coil positions and relative currents were optimized for field uniformity within

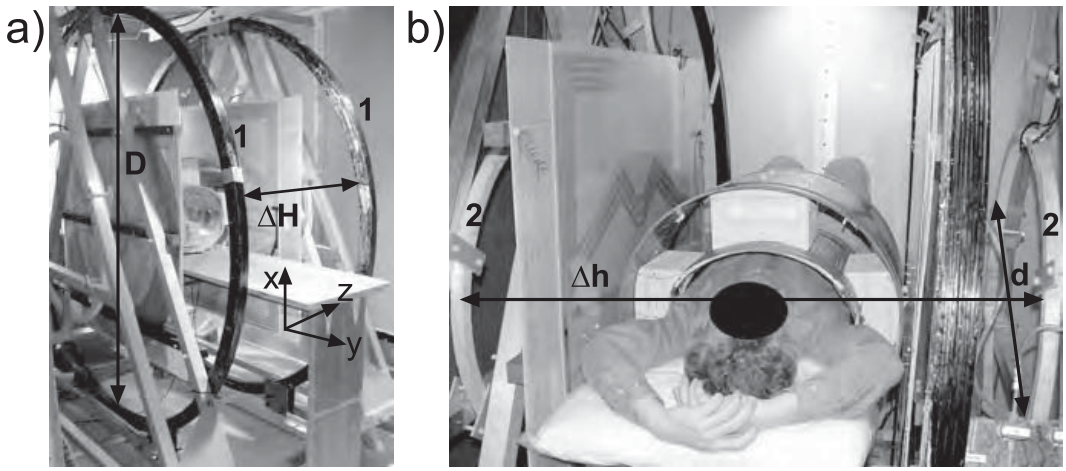

Figure B.1: Photographs of the prototype open-access human MRI magnet system showing the placement of the B_0 coils: a) Large B_0 coils, labeled "1," with diameter D = 2 m, separation ΔH = 0.74 m. Lab frame coordinates are included in this photograph. b) Small coils, labeled "2," with diameter d = 0.86 m, separation Δh = 1.2 m. Human subject is shown in the horizontal imaging position.

a 30 cm-diameter spherical region. Field calculations were made by applying the Biot-Savart equation to small segments of the coils. The assembly was positioned inside a large steel RF-shielded Faraday cage (8 ft wide x 12 ft long x 8 ft high) with the coil axis across the width of the Faraday cage. In Figure B.1, two photographs show the four coils with dimensions and axes indicated.

The two pairs of coils were powered by different current sources: the larger pair was driven by two Sorensen SRL 40-50 power supplies connected in series, and the smaller pair was supplied by a Hewlett-Packard 6012A. Laboratory electronics and other noise sources within the relevant range of NMR observational frequencies (50-200 kHz) required careful filtering of all power lines leading to the imager. The DC current feeds to the coils were filtered to prevent transmission of broadband kHz frequency noise, using large capacitors connected in parallel at the output of the power supplies and LC filters mounted on the feed-through panel of the Faraday cage. The B_0 field generated at the central imaging volume by this configuration was 1.34 G/A for the

large pair of coils and 0.68 G/A for the small pair. There was no active cooling method employed; the maximum resulting field was limited by the heat generated by the B_0 coils inside the Faraday cage to 7 mT (70 G). Due to the warm-up time of the power supplies and the coils, it was necessary to wait up to one hour before a stable B_0 coil temperature and current were achieved.

The optimum current ratio between the large and small coils was ~ 5 as determined by SNR measurements from low-flip angle single-pulse excitations of laser-polarized ^{3}He in small phantom glass cells, and by 90° pulses on water phantoms. In addition, B_0 shimming was possible via added current offsets to the gradient coils through the gradient amplifiers. A plot of the measured field uniformity in the horizontal yz plane of the system is shown in Figure B.2. The measured field uniformity differed from optimization calculations. The field was slightly greater on the negative z axis (see Figure B.1 for coordinate axes), due to the smaller diameter of the left large coil, and slightly greater along the negative y axis due to proximity of the Faraday cage steel wall.

B.2 Open-access gradient coils

Planar gradient coils were built on 3 mm thick G10 plastic sheets using three layers of 1.2 cm wide, 40 μm thick copper tape as the conductive material. The coil design was created using a procedure in which the 3D magnetic field distribution was calculated from the sum of fields created by small elements of the gradient coils, and the coil pattern was varied iteratively to maximize gradient strength and optimize linearity across a 60 cm diameter central imaging volume. The x and y gradients were wound on a 90 $\times$ 120 cm sheet, had a 0.78 Ω DC-resistance for each pair, an inductance of 92.2 μH, and an output field of 1.37×10^{-3} G/cm/A. The z gradient pair had a spiral form wound on a 120 $\times$ 120 cm sheet, a measured 1.29 Ω DC-resistance, an inductance

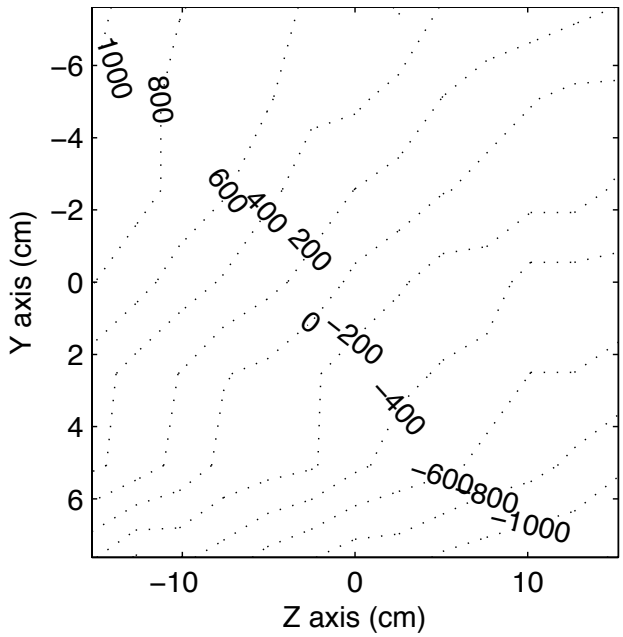

Figure B.2: Measured B_0 field deviation map (ppm). The plot was generated by moving a small water phantom along a 1 inch grid and recording the NMR frequency at each point.

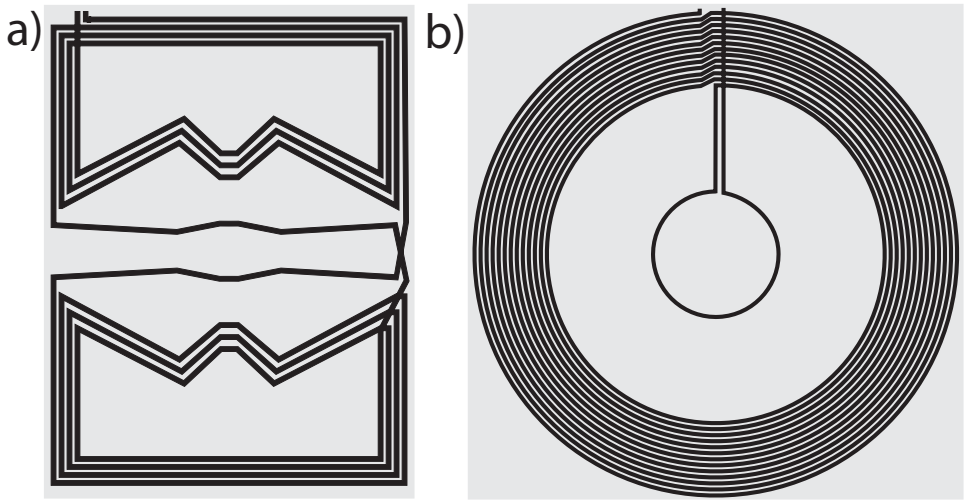

Figure B.3: Winding patterns for planar gradient coils designed for the open-access human MRI system. a) x and y-axis planar gradient design, on a 90 × 120 cm plane; b) z-axis planar gradient design, on a 120 × 120 cm plane.

of 368.8 μH , and an output of 4.82×10^{-3} G/cm/A. Both gradient designs are shown in Figure B.3.

The gradient sheets were attached to the same aluminum brackets as the main B_0 coils, leaving a gap of 71 cm for the placement of a subject table, B_1 coils, and the imaging subject. Figure B.4 shows the three planar gradients installed in the system. The gradients were powered using Techron 8606 amplifiers—the maximum current supplied by the amplifiers was limited by coil inductance to 130 A for the x and y gradients and 86 A for the z gradient. This resulted in maximum gradient fields of 0.18, 0.18, and 0.41 G/cm for the x, y, and z gradients, respectively. The magnetic field gradients deviated from linearity by no more than 0.4% across the central imaging region, easily exceeding the requirements for the imaging resolutions shown and discussed in later sections. Due to the poor thermal conductivity of the gradient plastic sheets, heating of the copper tape limited the pulsed gradient repetition time to at least 100 ms in imaging sequences.

Gradient line filtering was a special challenge, given the proximity of the desired band-pass frequencies (1-2 kHz) and those to be be filtered (50-200 kHz). Each of the three gradient coil power lines were filtered with simple passive inductors built with ferrite toroid cores [Ferroxcube TX63/28/25]. Both the output and sample common lines from each of the three Techron amplifiers were wound 20 times around these small toroids using a 10 gauge connection wire. These passive inductors blanked the gradient lines when the amplifier was not generating a pulse, effectively reducing their noise to quiescent levels. As these passive filters functioned effectively only when a gradient pulse was not applied and the ferrite core stayed unsaturated, the readout gradient required an additional filtering mechanism during the image acquisition. These filters consisted of two larger toroid ferrite cores (Ferroxcube T107/65/25), each double wound in a transformer configuration (2 $\times$ 9 windings). One side of windings contained one wire of the read-out gradient while the second winding was connected directly to a

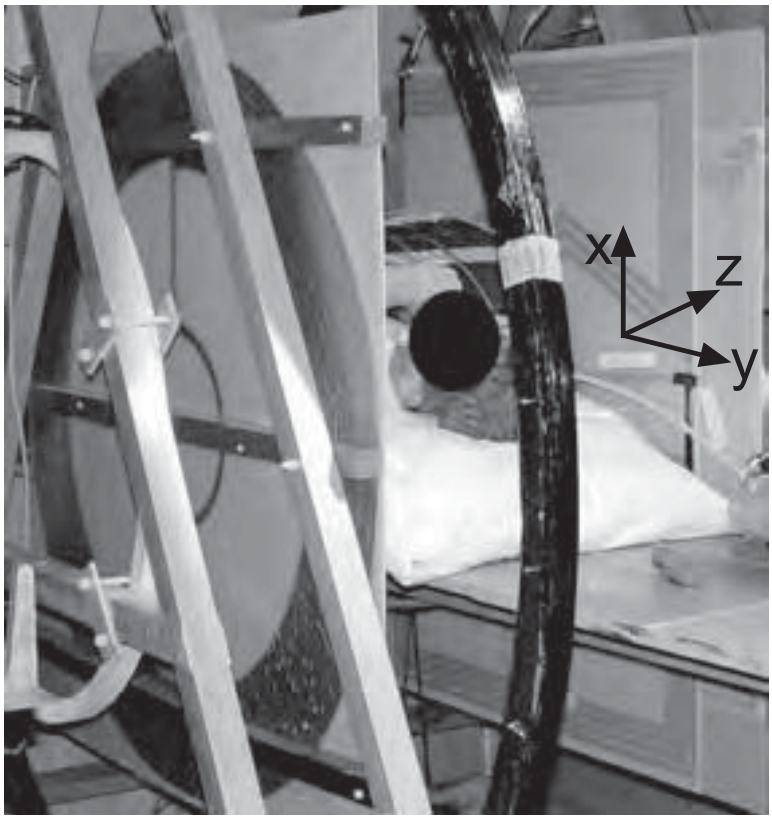

Figure B.4: The planar gradient sets mounted on the aluminum support frame of the open-access human MRI B_0 coil system. The x and y gradients are placed just inside of the z gradients, relative to the subject (seen in supine position). As such the z-axis gradient is visible on the subject's left, and the x-axis gradient is seen to his right.

Sorensen SRL 10-50 DC power supply that matched the read out gradient current during signal acquisition. This way the ferrite became unsaturated while the gradient was on during the image acquisition, reducing the baseline noise level to within a factor of 2 of that obtained when the gradient amplifier was off. To permit this filtering method, the Techron amplifier assigned for the read-out gradient was set to constant-voltage mode, mainly because the constant-current setting was unstable and noisy. Although this proved to be successful in reducing noise, the slew-rate of the read-out gradient amplifier was slower than the others because the attached z gradient coil possessed a greater inductance than the others, causing the shapes of each pulse to be slightly distorted on rise and fall.

B.3 RF Coils and System Control

A commercial MRI research console from Surrey Medical Imaging Systems (SMIS) was used for RF and gradient pulse control and signal reception. The console did not have the hardware to produce the kHz-range imaging frequencies required for the low B_0 field strengths used, so we implemented a heterodyne mix-down stage for the transmit signal and a mix-up for the receive signal using a reference signal of 20 MHz from the PTS-160 synthesizer in the SMIS console, and ZAD-3 mixers [Mini-Circuits, Brooklyn, NY]. Separate transmit and receive B_1 coils were used, which allowed straightforward impedance matching of the RF amplifier to the transmit coil and the preamplifier to the receive coil.

The transmit B_1 coil was built in a Helmholtz configuration with 5 windings on each side using 12 gauge copper wire on a 66 cm-diameter PVC pipe as a form. The RF transmit signal was fed into a two stage amplifying system: a home-built amplifier allowing a gate conditioning for the output, followed by one of the five channels of a 5×165 W audio amplifier [Outlaw Audio, Durham, NH]. A cross-diode box after the

RF amplifiers provided filtering for the transmit signal. Tuning of the transmit coil was achieved with high-voltage resonance capacitors that were connected in series with the coil to establish a low output impedance on the audio amplifier ($\sim 4\ \Omega$). The quality factor Q of the transmit coil resonance was ~ 10. The inductance of the B_1 transmit coil yielded a finite rise time from 10–50 μs, depending on the resonant frequency.

During system development, a variety of small, solenoidal RF coils, which could be easily tuned to 100-200 kHz, were used as receive coils. The human receive coil was designed to fit a medium sized human chest: the coil was wound in a cosine pattern with 4×80 turns on an ellipsoidal shape form 44 cm wide $\times$ 33 cm high $\times$ 38 cm long. The receive coil had a resonant output impedance of ~ 100 kΩ, which was well-matched to a Stanford Research Systems SR560 preamplifier in line between the coil and the mix-up stage prior to digitization by the SMIS. The receive coil was tuned from 54–200 kHz using "resonance boxes" with multiple capacitor configurations. The Q of this coil was $\sim$ 80–120, depending on the operating frequency. Such high Q values at frequencies ~ 100 kHz resulted in coil response bandwidths of $\sim$ 1–2 kHz, significantly less than typical imaging spectral widths of 10–20 kHz. As a result, all images acquired from this system required post-processing to remove the convolved effect of the frequency response of the coil.

Inductively-detected noise from living tissue is insignificant at low-RF frequencies. Thus the resonances of the B_1 coils were not affected by the presence of a human imaging subject. However, significant problems (noise and distortion of resonances) were caused by coupling between the transmit and receive coils and between the receive coil and the gradient coils during switching. Noise was significantly reduced by carefully aligning the transmit and receive coils orthogonally to each other, blanking the preamplifier during RF transmissions and adding a 3-4 ms dead-time employed after the transmit pulse. In addition, precise positioning of the receive coil in the magnetic center of the gradients greatly reduced the unwanted receive signal during gradient

Figure B.5: Photograph of the transmit and receive coils for the open-access human MRI system. The large Helmholtz transmit coil was bolted onto the subject imaging table, and the receive coil was attached using foam spacers and plastic bolts.

switching. The human coils were bolted together to maintain orthogonality and were fixed to the subject imaging table, as shown in Figure B.5.

The existence of several environmental noise signals within our operating frequencies necessitated the use of a steel Faraday cage that enclosed the electromagnet. This room was designed to attenuate RF interference in the range of 10 kHz to 10 MHz by up to 100 dB. A low-noise power transformer was used to deliver electrical power inside the room. A feed-through panel was made from thick aluminum and all the electrical connections were fed through using multiple passive filtering elements. Lower noise attenuation was detected at different points of the cage, mostly in the corners and in some places where the steel panels where jointed together. Where necessary, copper tape with conductive adhesive was added for a better electrical connection between cage panels, reducing the environmental noise level.

B.3.1 Subject Orientation

The human subject was imaged in two positions: supine and sitting upright. For supine imaging a wooden bed was constructed to fit within the imaging area for the subject to lie on top. The transmit coil was bolted to the bottom of the bed (Figure B.5) and the subject lay within the receive coil (Figure B.1b). To prevent deformation of the receive coil by the subject, a small weight-bearing bridge was placed just over the inside of the receive coil for the subject to lie upon.

For upright imaging, the wooden bed was replaced by a stool on which the subject sat. Horizontal plastic beams were mounted onto the aluminum frame to provide a secure mounting point for the transmit and receive coils. The subject was able to lean slightly against the receive coil to stabilize himself during the imaging session.

All human experiments were performed according to a protocol approved by the Institutional Review Board at the University of New Hampshire. The subject for lung imaging was a healthy 47-year-old male.

Appendix C

Measuring Pulmonary Vascular Compliance Using MRI

L.L. Tsai, G.P. Topulos, S. Patz, J.P. Butler, R.W. Mair, R.A. Rogers, M.S. Rosen, and R.L. Walsworth

MRI is a powerful method of mapping tissue components and structure, including the bloodstream. We report the use of MRI techniques for the first time to estimate pulmonary regional blood volume (RBV). In addition, we calculated vascular compliance after controlling vascular transmural pressure. Using a standard short-T_E gradient echo sequence and a clinically available intravascular contrast agent (Feridex^{TM}), spatially-resolved RBV measurements in freshly excised rabbit lungs were made.

This technique was tested using a renal dialysis unit as a phantom to simulate a bed of capillaries surrounded by an extravascular volume. The MR measurement determined the effective RBV to be 0.200 ± 0.003, in excellent agreement with a confocal microscopy measurement of 0.199 ± 0.001. Using the same MR technique a series of RBV measurements were performed on a series of excised rabbit lungs at different vascular and airway pressures. RBV values ranged from 0.1 to 0.2 for different conditions, with minimal variation throughout the lung in a single measurement. The results yielded vascular compliance values consistent with other techniques, correcting for complications from the *ex vivo* nature of the study. These results provide a basis for *in vivo* MR measurements of lung vascular compliance and RBV and the exploration of changes associated with pathology.

C.1 Introduction

The mechanical properties (pressure, volume, and compliance) of pulmonary capillaries (vessels < 20 micron diameter) affect the pattern of lung perfusion, matching of ventilation and perfusion and hence gas exchange, and leukocyte sequestration [128]. Normal mechanical properties are necessary for ideal lung function and can be significantly altered in a variety of pathologies, including acute respiratory distress syndrome, infection, and pulmonary hypertension. A better understanding of microvascular mechanics will aid our understanding of pulmonary physiology and pathophysiology, and may better inform clinical interventions.

Capillary compliance characterizes the change in capillary volume with capillary pressure. The former is particularly difficult to measure. Previous morphometric studies have used rapid freezing techniques [129] or relied on videomicroscopy of larger sub-pleural vessels for direct sampling. More recently, measurements have been performed via diffuse light scattering [130, 131]. This technique can potentially be used *in vivo*, but requires direct open access to the lung surface. Furthermore such measurements are limited to regions near the surface (1–2 cm) of the organ. These difficulties can be overcome by the use of MRI, which offers the advantages of noninvasive measurements in live tissue without limitations on penetration depth. However the lung has been a challenge to MR techniques because of its low proton density due to the presence of air, which results in a poor signal-to-noise ratio (SNR). This can be partially offset by implementing a higher main magnetic field, but T_2^* is shortened by increased susceptibility mismatches at the air-tissue interface [132, 133]. It is thus advantageous to employ an MR technique that combines use of a low field imaging system with a short T_E pulse sequence [134, 135].

Maps of the fractional regional blood volume (RBV) of *in vivo* brain, liver, heart, and kidney tissue have been made using a variety of MR methods [136–142], all

of which use a contrast agent to distinguish between intravascular and extravascular spaces. While pulmonary MR imaging with contrast agents has been evaluated [139], MR studies of pulmonary RBV and vascular compliance have not been performed. Here we demonstrate the ability of a short-T_E MR technique to measure RBV and vascular compliance measurements of rabbit lungs using a low-field clinical scanner and ferumoxides (Feridex), a commercially available contrast agent. In order to test the accuracy and precision of our measurements, we used a dialysis canister as a phantom to simulate a capillary bed immersed in an extravascular bath.

C.2 Theory

For a two compartment system, A and B, the NMR relaxation of the system can be easily treated for two cases, the fast exchange and the slow exchange limits. In the slow exchange limit, the proton exchange between the two compartments is slow relative to the NMR measurement or mixing time. In this limit, the total signal from the two compartments is simply the sum of the signals from each individually considered compartment. In the fast exchange limit, the average residence times for protons in the two compartments are small compared to the time allowed for relaxation. In this limit, assuming the proton density is equal in both compartments, the total signal decays with a single relaxation rate that is a volume fraction weighted sum of the individual compartment relaxation rates [136]. The general treatment of relaxation in a two component system where the exchange is neither fast or slow has been treated by Hazlewood et al. [143].

Donahue et al. [144, 145] argue that neither the fast nor slow exchange models are appropriate to describe physiological vascular/intravascular exchange because biological exchange rates Re (1–10 Hz) are the same order of magnitude as a typical $1/T_R$ (2.5–10 Hz). As a consequence, they have proposed exchange minimized methods,

i.e. fast gradient echo methods where $1/T_R >>$ Re. Thus, to minimize the effects of exchange, we used a short T_R, gradient echo sequence for the work described here to measure RBV in lungs. The equations for slow exchange can then be used to calculate RBV. When using a short T_R sequence, Donahue also shows that in experiments where perfusion is maintained, inflow effects can affect the vascular MR signal [145]. Thus, they have utilized a thick 3D slab such that inflow effects are only present at the edge of the slab, allowing the central portions of the slab to be used in RBV calculations. In our studies, we used an ex-vivo preparation and we deliberately stopped any blood flow during each data acquisition. Thus we interchangeably used both 2D and 3D techniques with similar results.

To obtain RBV using a short T_R gradient echo sequence where we assume that $1/T_R >>$ Re, one must acquire data both before the addition of contrast agent and again after the agent has been allowed to equilibrate within the intravascular space. To normalize our measurements, 5 cc vials containing blood both with and without contrast agent were placed within the image FOV. Thus RBV is estimated from four measurements of mean signal intensity (SI): the mean SI of voxels from a ROI in the lung before and after the contrast agent Feridex is used SI_{lung} and $SI_{\text{lung+Fe}}$ respectively, and the mean SI of voxels containing blood only both before and after contrast, SI_{blood} and $SI_{\text{blood+Fe}}$. The equations for slow exchange [145] are then used to derive a simple expression for the regional blood volume fraction:

$$\text{fractional RBV} = \frac{SI_{\text{lung+Fe}} - SI_{\text{lung}}}{SI_{\text{blood+Fe}} - SI_{\text{blood}}}. \tag{C.1}$$

C.3 Methods

All MRI procedures were performed using a General Electric Profile 0.2 T scanner in order to avoid severe magnetic susceptibility-related artifacts associated with high field imagers.

C.3.1 Contrast Agent

Feridex is a well-characterized [146] superparamagnetic nanoparticle MR contrast agent also known as ferumoxide. It is composed of a crystalline core of iron and oxygen surrounded by a dextran outer coating. At body temperature, the relaxivity of superparamagnetic particles is several times higher than that of gadolinium chelates. This allows use of relatively lower concentrations of ferumoxides during experimentation. Particles vary in size from 35 nm to 227 nm in diameter. The principle method of removal of Feridex from the vasculature is from liver macrophages, which are selective only for larger particles. The blood half-life of ferumoxide is approximately two hours in humans.

C.3.2 Dialysis Canister Phantom

A renal dialysis unit [Fresenius Medical Inc. model F8] was used as a phantom. The canister contains a series of parallel semi-permeable membrane fibers which serve as a capillary bed designed to carry a patients blood. Surrounding the fibers is a separate compartment which is normally filled with dialysate solution. During clinical use, blood waste products diffuse out of the blood within the fibers to the dialysate solution. Although there is free water exchange between the two compartments, Feridex cannot permeate through the fiber walls due to its size.

Both the fibers (intravascular space) and the dialysate space were first filled with saline. A 1 cm-thick MR image across the center of the cylinder was acquired using a 2D gradient echo sequence. The imaging matrix size was 256 $\times$ 256, with FOV = 400 mm, T_R=18 ms, and T_E=6 ms. The signal was averaged eight times, giving a total scan time of 37 s. A syringe filled with saline was simultaneously imaged beside the dialysis canister. The lumen of the dialysis fibers was then flushed and refilled with Feridex-doped saline at a concentration of 0.2 mM Fe. The canister was immediately imaged again, adjacent to both a pure sample of the Feridex-saline solution and the

syringe of undoped saline.

Three regions of interest (ROI) were selected from the MR images for data analysis: the syringes containing pure and Feridex-doped saline (representing the pure intravascular signal undiminished by partial volume effects), and the dialysis canister before or after addition of Feridex to the capillary bed. The signal intensity of each ROI was averaged and used to calculate a final value of the fractional internal volume, or effective RBV.

C.3.3 Microscopic Morphometry

Following the MR protocol, the dialysis canister was sectioned, dipped in blue dye for edge detection of the tube lumens, and oriented on a Leica DM IRBE inverted microscope, fitted with 5 × objective and charge-coupled device camera (JAI CV-M10, Glostrup, Denmark). 10 micrographs were examined, each containing approximately 10 tubes. Diameters were measured in pixels and converted to microns by a calibration image of a 21 line graticule with 10 micron spacing. Independently, the canister was placed on a Leica TCS NT confocal microscope configured for 488 nm excitation and reflected light imaging. The resulting images were analyzed for the number of tubes per unit area. These data were used to calculate the volume fraction of the "intravascular space" mimicked by the tube lumens.

C.3.4 Lung Imaging

RBV was measured in isolated perfused lungs harvested from three rabbits (following a protocol approved by the Institutional Review Board. Each rabbit (3-4 kg) was anesthetized, exsanguinated, and the heart and lungs were excised *en bloc*. The pulmonary artery (PA) and vein (PV) were cannulated via the right ventricle and left atrial appendage respectively. The PA and PV cannulae were each connected to separate reservoir bags filled with the collected heparinized autologous blood. The

height of the reservoir bags could be adjusted to control the PA pressure (Ppa) and PV pressure (Ppv), which were measured using a Sorenson Abbott Transpac 2 pressure meter, connected to a Marquette Solar 8000 monitor kept outside the MR room. The entire preparation was then placed in a 20 cm surface extremity MR coil, along with a syringe-filled sample of pure blood.

The tracheal cannula was connected to an adjustable constant pressure source of 100% oxygen. Before each set of MR images, the lung was set to transpulmonary pressures of 3 or 20 cm H_2O to reflect functional residual capacity (FRC) and total lung capacities (TLC), respectively. During imaging the PV cannula was clamped and the intravascular pressure was controlled by adjusting the height of the PA reservoir. Before each set of images were obtained the lung and vasculature were exposed to standard volume histories, and then deflated from approximately 30 cm H_2O to their target pressures. When each combination of target vascular and transpulmonary pressures was reached, MR images were acquired. After the pre-Feridex images were completed, all the blood in the perfusion circuit was collected, and Feridex was added at a dose of 0.001 ml Feridex/ml blood. The lungs were then perfused with this doped blood, a sample of which was collected in a fresh syringe and placed next to the lungs. MR images were obtained of both the lungs and the doped blood sample for each *ex vivo* rabbit preparation.

The MR pulse sequence used was a 3D spoiled gradient echo (SPGR) with T_R = 25 ms, T_E=8 ms, flip angle=30. The imaging matrix size was 128 ×128 × 26, with FOV=170 mm and a voxel size of 1.5 mm × 1.5 mm × 5.0 mm. Only one scan was acquired per image, while 26 planes were acquired, yielding a total scan time of 46 s. The time required for all imaging, including the time to introduce the Feridex, was approximately 25–30 minutes. If the time for initial animal preparation is also considered, the total time the lungs were *ex vivo* was less than two hours.

C.3.5 Data Processing and Analysis

Data processing on ROIs was performed on the GE Profile console using the built-in image analysis tools. From each plane of the 3D data set that contained lung tissue, ROI's were chosen over the lung tissue, avoiding large vessels or airways. On average, five to six 2D planes were analyzed and three ROIs were chosen on each image slice, resulting in 15 ROIs per animal. Each ROI contained at least 200-250 voxels. Each pre-Feridex ROI graphical boundary was superimposed on the corresponding post-Feridex image to ensure sampling of identical regions before and after contrast. Care was taken not to disturb the position of the lungs so that even after cycling of the pulmonary airway pressure and contrast administration, the registration of pre- and post-contrast images was within a few voxels.

RBV values were calculated for each ROI using the methods described above (Equation C.1). Capillary specific compliance, at a given transpulmonary pressure (P_L), is the percentage change in RBV with changes in vascular Ptm (here $\Delta Ptm =$ 15 cm H_2O), normalized to the RBV at a reference vascular Ptm (in this case vascular $Ptm = 5$ cm H_2O):

$$\text{Vascular Specific Compliance} = 100\frac{(\text{RBV}_{Ptm=20} - \text{RBV}_{Ptm=5})/\text{RBV}_{Ptm=5}}{\Delta Ptm}, \quad \text{(C.2)}$$

where $\text{RBV}_{Ptm=20}$ and $\text{RBV}_{Ptm=5}$ refer to the fractional RBV values, at a given P_L , at vascular 10 $Ptm = 20$ cm H_2O and at vascular $Ptm = 5$ cm H_2O, respectively. All mean values and variances were computed weighted by the number of voxels present in each ROI. Standard errors were computed from the sum of the variance estimated for variation of individual signal intensities about their respective means and the variance associated with the SNR of each ROI. Standard errors of differences, e.g. at different Ptms, were also computed from respective additive variances, since those measurements are independent.

C.4 Results

C.4.1 Dialysis Canister Measurements

Using the method outline above, the fractional effective RBV of the dialysis canister was determined from the MRI measurements to be 0.200 ± 0.003. A complementary confocal microscopy image of a region of the canister is shown in Figure C.1. Confocal microscopy revealed 12,819 fibers present in the canister, with an average fiber inner diameter of 189 ± 0.5 μm (n = 133). These measurements were consistent with the estimates provided by the manufacturer. The inner diameter of the entire canister was 4.80 cm. Because of the cylindrical geometry of the cannister, the fractional RBV is equal to the total lumenal area divided by the total internal cross sectional area of the cannister, for which we thus obtain

$$\frac{12819 \times \pi(190.4 \times 10^{-6})^2}{\pi\left(\frac{4.80\times10^{-2}}{2}\right)^2} = 0.202 \pm 0.001 \tag{C.3}$$

C.4.2 Pulmonary Capillary RBV and Compliance

An example MR image of the excised rabbit lungs perfused with Feridex-doped blood is shown in Figure C.2. From a series of similar images, acquired both before and after addition of contrast agent to the blood, at each of two P_L (3 and 20 cm H_2O), and two vascular Ptm (5 and 20 cm H_2O) fractional RBV was calculated (Equation C.1). The results are shown in Table 1. Table 2 shows the ΔRBV with vascular Ptm at each P_L ($\mathrm{RBV}_{Ptm=20} - \mathrm{RBV}_{Ptm=5}$) as well as the calculated specific compliance (Equation C.2).

C.5 Discussion

The dialysis canister experiment verified the ability of the MR method to determine RBV with high accuracy and precision. The result, 0.200 ± 0.003, is in excellent

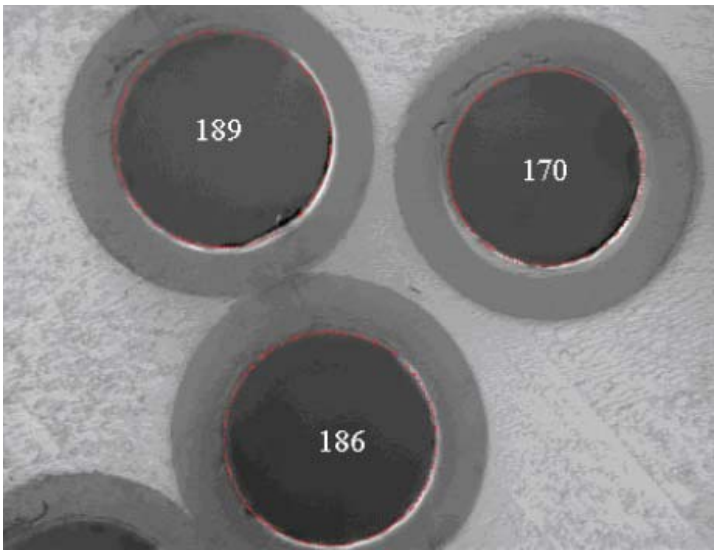

Figure C.1: Light micrograph image of a cross section of the dialysis canister, showing individual tubes. The numbers indicate the internal diameter of the tube lumen, in μm. The average (intravascular) internal diameter was 190 μm.

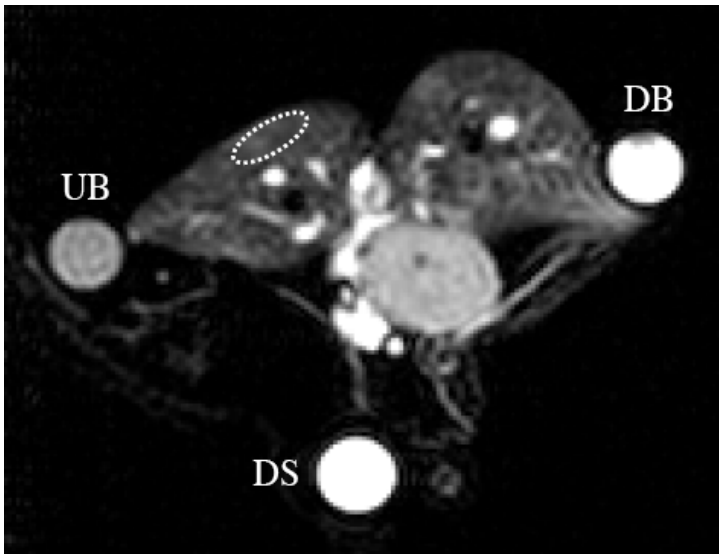

Figure C.2: MRI of rabbit lung with contrast. A typical ROI is outlined by the dashed line. Samples of contrast-doped blood (DB) and saline (DS) and undoped blood (UB) are also included.

Animal	$P_L = 3$ $Ptm = 5$	$P_L = 3$ $Ptm = 20$	$P_L = 20$ $Ptm = 5$	$P_L = 20$ $Ptm = 20$
1	0.205 ±.0041	0.276 ±.0053	0.183 ±.0037	0.197 ±.0041
2	0.152 ±.0025	0.192 ±.0027	0.126 ±.0017	0.157 ±.0016
3	0.160 ±.0024	0.218 ±.0031	0.101 ±.0014	0.105 ±.0014

Table C.1: Measured fractional RBV values for three rabbit lungs. Ptm and P_L are in cm H_2O.

Animal	ΔRBV $P_L = 3$, $\Delta Ptm = 15$	Compliance at $P_L = 3$ (%)	ΔRBV $P_L = 20$, $\Delta Ptm = 15$	Compliance at $P_L = 20$ (%)
1	0.071 ± 0.0067	2.3 ± 0.21	0.014 ± 0.0055	0.51 ± 0.20
2	0.040 ± 0.0037	1.8 ± 0.16	0.031 ± 0.0023	1.6 ± 0.12
3	0.058 ± 0.0039	2.4 ± 0.17	0.004 ± 0.002	0.26 ± 0.13
Average ΔRBV	0.056 ± 0.003	2.2 ± 0.14	0.016 ± 0.0021	0.78 ± 0.11
p value from single tailed T test	p <0.005		p < 0.025	

Table C.2: ΔRBV from vascular $Ptm = 5$ to 20 cm H_2O and calculated vascular specific compliance values, using Equation C.2, for lungs at $P_L = 3$ cm H_2O and 20 cm H_2O.

agreement with the direct morphometric measurement from confocal microscopy, 0.199 ± 0.001. The sensitivity of the MR technique allowed verification that Feridex was confined in the lumen of the fibers, and was not present in the membrane walls. Had contrast agent penetrated into the tube walls then the MR results would have been different; however this was not the case[1].

All the lung RBV measurements for the differing vascular Ptm and P_L correlated as expected for a given animal. At higher transpulmonary pressures the RBV fell, due to the increased volume occupied by air-filled alveolar spaces. At fixed transpulmonary pressures, RBV increased with higher vascular pressures as the capillary bed filled with blood. The results were comparable to those from a study by Brudin et al., which used positron emission tomography (PET) to obtain *in vivo* fractional RBV

[1]The wall thickness of the fibers was approximately 50 μm, as verified by confocal microscopy. Presence of Feridex in the inner 25 μm of the wall at similar concentrations to the intravascular space would have resulted in an MR RBV measurement 28% greater than the morphometric measurements, well above the 1.5% precision of the MR results.

values of 0.15–0.20 in human lungs [147]. However, the PET technique is prone to significant errors because RBV can be determined only by assuming a certain rate of exchange of the PET tracer between the capillary vessels and the alveolar air. Direct morphometric measurements in sectioned *ex vivo* lungs by Crapo et al. yielded RBV values of 0.075 ± 0.019 in alveolar regions and 0.38 ± 0.13 for non-alveolar compartments (including upper airways, trachea, and larger blood vessels) [148]. Our RBV values fall in between these extremes, suggesting that our ROIs contained a mix of both alveolar and non-alveolar compartments. Given the relatively small size of rabbit lungs, the 5 mm thickness of each image plane, and the multiple ROIs sampled to yield each RBV value, it is likely that a significant number of larger arterioles and bronchioles were sampled.

In addition to having a larger blood volume, larger vessels are also less compliant. Hillier et al. reported compliance values of 0.7–2.2% cmH_2O-1 for canine pulmonary arterioles and venules under 100 μm, and Al Tinawi et al. reported compliances of 1.5% cmH_2O-1 and 0.88% cmH_2O-1 in canine pulmonary arteries and veins with diameters from 100–1000 μm [130, 131]. These measurements were all performed at functional residual capacity. We previously measured pulmonary capillary compliance for vessels at the 10 μm-diameter level and obtained values of approximately 8% cm H_2O^{-1} and 2.7% cmH_2O^{-1} at FRC and TLC, respectively (5). These results are consistent with thinner-walled capillary vasculature being more pliable. Our compliance values of 2.2 ± 0.14% cmH_2O^{-1} at FRC and 0.78 ± 0.11% cmH_2O^{-1} at TLC fall reasonably in between values for large and small vessels, further supporting the suggestion that our MR measurements included a mixture of the two.

The ratio of compliances at FRC vs TLC was 2.8 from our results, nearly identical to the ratio of 3.0 in our earlier light scattering work [128]. Our current data also indicate that vascular compliance decreases at higher transpulmonary pressures. Glazier et al. found a similar trend in measurements of canine pulmonary capillaries

under 10 μm in diameter [129]. This is in contrast to the analysis of the red blood cell (RBC) number per capillary length, also performed by Glazier et al. in the same study, which suggests that compliance decreases with lung volume. However, RBC density does not necessarily reflect regional blood volume, particularly in the microvasculature, and at such small sampling regions. Furthermore, our MR technique is more similar to the diffuse light scattering used previously [149], i.e., both are from direct measurements of blood volume. This is unlike the capillary width and RBC density measurements, which need to be related to regional blood volume via a simplified model.

Our model has some technical limitations. The first is the relatively small size of the rabbit lungs, which made sampling of capillary regions difficult, as discussed above. The relatively large sample volumes were believed to be a contributor to the wide variation of RBV measurements between individual rabbits. The ROIs also contained variations in signal intensity that were dependent on image slice, providing further evidence that we were sampling across regions where the microvasculature was not uniform in size (nor compliance).

A second concern is leakage of contrast agent outside of the intravascular space. All organs are susceptible to vascular degradation during an *ex vivo* experiment, but the lungs are particularly delicate, and in this experiment they were subjected to additional physical wear via repeated volume cycling performed in between measurements. It was observed prior to the injection of Feridex that the blood in the pulmonary vein cannula had similar MR signal intensities as the blood in the pulmonary artery cannula. After the Feridex was mixed into the blood the MR signal intensities increased similarly in the two cannulae, as expected; but as the experiment continued, the venous cannula had relatively decreasing signal intensities. This signal loss suggests leakage of contrast agent into the tissue. Since Feridex does not easily cross the vessel wall, it is likely that the leakage is through physically damaged vessels. Thus we believe our RBV values to be an overestimation of the true RBV, as blood and Feridex were outside of the

intravascular space.

Contrast leakage is most easily addressed by performing *in vivo* experiments using animals or humans within normal tidal volumes. Other complications associated with *ex vivo* procedures, including thrombosis, emboli, cell death and leakage, and hypoxic vasoconstriction, would also be eliminated or minimized. *In vivo* human or canine MR imaging would also reduce the difficulty of sampling outside of the pulmonary capillary bed, since lung size would be significantly greater. Experiments *in vivo* will be complicated by subject motion, but such artifacts can be addressed by introducing ventilation gating, which is available on our MR system, or by performing breath holds during imaging, provided the pulse sequence is short enough. Furthermore, Feridex has been approved for humans and experimental dosages are within clinical range. Given the ease in applying MRI to live subjects and the results presented in this study, there is a clear potential for using MRI to study RBV dynamically in both normal and pathological animal systems, and in the clinical setting. Unfortunately, the determination of vascular compliance *in vivo* remains a challenge due to the technical difficulty of measuring vascular pressures within the live microvasculature.

C.6 Conclusion

Obtaining RBV and vascular compliance measurements of the lung is challenging, as it is difficult to measure capillary blood volume in such a dynamic and inaccessible organ. Here we demonstrate an MRI technique that provides such measurements with high accuracy. Although the low tissue density and air-filling of lung tissue present a problem for MR techniques, they can be overcome through use of low-field magnets and short T_E sequences. Employing a clinically available contrast agent, we measured RBV of a phantom, a dialysis canister, with a precision of 1.5%. We verified the accuracy of this measurement through direct morphometric measurement

using confocal microscopy. Next, we used MRI to measure RBV in a series of rabbit lungs and obtained RBV and compliance values that were consistent with previously published results. The data strongly suggest that our sampling regions contained a combination of both capillary vessels and larger, less compliant arterioles and venules. We also suspect a slight overestimation of RBV in our results due to leakage of the contrast agent outside of the vasculature. We believe these complications can largely be eliminated in future work with *in vivo* systems in larger animals and humans.

C.7 Acknowledgments

We thank Drs. Richard Rogers and Ben Fabry for assistance imaging the dialysis canister. We also thank Dan Kacher for help inthe use of the 0.2 T Profile scanner. We thank Paula Jacobs, Ph.D. at Advanced Magnetics for supplying us with Feridex, and Eric Stroup at Fresenius Medical for supplying the dialysis canisters (and their characteristics). This work was supported in part by NASA grant NA99-1166, NIH NHLBI 55569, NIH R21 RR14297, the Smithsonian Institution, and the Brigham and Womens Hospital.

Appendix D

Interstitial Gas and Density-Segregation in Vibrated Grains

M. Klein, L.L. Tsai, M.S. Rosen, T. Pavlin, D. Candela and R.L. Walsworth

We report experimental studies of the effect of interstitial gas on mass-density-segregation in a vertically-vibrated mixture of equal-sized bronze and glass spheres. Sufficiently strong vibration in the presence of interstitial gas induces vertical segregation into sharply separated bronze and glass layers. We find that the segregated steady state (*i.e.*, bronze or glass layer on top) is a sensitive function of gas pressure and viscosity, as well as vibration frequency and amplitude. In particular, we identify distinct regimes of behavior that characterize the change from bronze-on-top to glass-on-top steady-state.

Reprinted with permission from Physical Review E **74**, 010301 (2006). URL: <http://link.aps.org/abstract/PRE/v74/e010301>.

Vibrated granular media exhibit characteristics both similar to and distinct from solids, liquids, or gases, with important open questions about the applicability of hydrodynamic theories and the emergence of patterns and order [150–155]. Recent experiments have investigated the striking effects of interstitial gas on vibrated granular

media [156–162]. In particular, it was recently demonstrated [163–165] that interstitial gas (in contrast to vacuum) is necessary for spatial segregation (vertical layering) by particle *mass density* in a binary granular medium of equal-sized particles that is vertically vibrated in a sealed cell. In this paper we report an experimental study of such density-segregation as a function of interstitial gas pressure and viscosity, as well as vibration frequency and amplitude.

Our experimental setup was similar to that of [163,164]. The granular mixture consisted of equal-sized solid spheres of bronze (ACU Powder International) and soda lime glass (MO-SCI Corp.) with diameter $d = 98 \pm 8$ μm, where 90% of both types of particles fell within this range. The respective mass densities of the bronze and glass are 8.9 g/cm^3 and 2.5 g/cm^3. We used a volume mixing ratio of glass:bronze = 3:1, except where noted below. To reduce moisture, we heated each mixed granular sample for 3–5 minutes and used an electrically grounded brass pan to reduce static charge buildup. We used such freshly-prepared samples for each data-taking run, which we performed over times $\lesssim 3$ hours.

We placed each sample inside a sealed, rectangular borosilicate glass cell (Spectrocell, Inc.) of width 46 mm, height 50 mm, and depth 10 mm, mounted on a vibration platform (Fig. D.1). The height of the granular mixture at rest in the sample cell was approximately 20 mm for all data runs. We used an electromechanical shaker (Labworks, Inc. ET-126) driven by a sinusoidal waveform to vibrate the cell vertically, nominally with vertical (z) position $z(t) = A\sin(2\pi ft)$ and peak velocity $v = 2\pi Af = A\omega$. We characterized this vibration by the frequency f and dimensionless acceleration $\Gamma \equiv A\omega^2/g$, where g is the acceleration of gravity. We vibrated the cell over the range $f = 0$–200 Hz and $\Gamma = 0$–20. Over this range the particles did not interact with the top of the sample cell. A pair of accelerometers continuously monitored the vibration in three dimensions. We ensured that the dimensionless horizontal accelerations (Γ_x and Γ_y) were small (< 0.2, except as noted below), and limited variation in

the dimensionless vertical acceleration (Γ_z) to no more than 0.1 across the width of the platform. A gas-delivery system controlled the interstitial gas type and pressure inside the sample cell ($P = 1$–1000 Torr $\pm$ 3 Torr), without affecting the mechanical properties of the cell. We performed experiments with either N_2 or Ne gas, which have respective viscosities $\eta = 17.9$ and 32.1 μPa·s at room temperature (here η is independent of gas pressure for $P \gtrsim 25$ Torr).

For our range of experimental conditions, the vibrated grains moved relative to the interstitial gas with Reynolds number $Re \approx (\rho dv/\eta) \approx 0.01$–$1$, where ρ is the gas mass density. Hence viscous drag was usually larger than inertial drag. Importantly, there was no gas flow in and out of the sealed sample cell. Thus vertical gradients in the gas pressure were created across the vibrated particle bed inducing bulk gas flow through the granular medium (with gas flow velocity $v_g \sim \nabla P/\eta \sim P/\eta$ as given by application of Darcy's Law) [156]. To avoid hysteretic effects, we operated with the initial condition of a fully mixed, flat-topped sample, obtained by shaking under vacuum [156, 163, 164]. We then admitted the desired gas; observed visually and with video recording and digital photography (20 μm resolution) the steady-state reached for long-term vibration with constant Γ and f, as well as the behavior exhibited on the approach to the steady-state; removed the gas; and returned the sample to its initial mixed configuration before another run of the experiment.

Using this apparatus, we observed steady-state patterns of vibration-induced density-segregation such as "bronze-on-top" and "glass-on-top" (see Fig. D.2) consistent with the schematic results described in [163, 164]. We then studied the dependence of density-segregation and particle mobility on gas properties. We found that the heavier bronze particles are more mobile than the glass spheres when vertically vibrated in the presence of interstitial gas, which is consistent with particle deceleration due to gas-drag scaling inversely with particle mass. For example, we observed that vibrated bronze particles leave the sample surface and reach a noticeably greater height (about 3 times

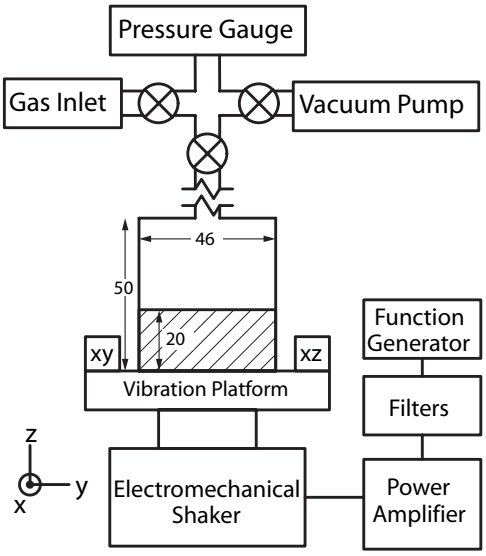

Figure D.1: Schematic of the apparatus, not to scale. Accelerometers are labeled by their sensitive axes (xy and xz). Dimensions are given in mm. The cell depth along the x-axis is 10 mm (not shown)

higher) than glass particles near the surface. Also, we determined the local expansion (dilation) of the granular bed under vibration to be greater for regions with higher bronze concentration: images showed these regions to have a greater total volume than given by the sample's glass:bronze mixing ratio. Consistent with previous experiment [164] and simulation [165], we found indirect evidence that the lighter glass particles are preferentially dragged along with bulk gas flow: *e.g.*, the glass-on-top state *never occurred* when bulk gas flow due to gas pressure gradients was inhibited by placing the sample in a cell with a gas-permeable bottom [1]. In addition, with this gas-permeable-bottom cell we found that overall particle mobility and bed expansion were diminished. Correspondingly, Γ had to be increased by about a factor of two (by increasing the amplitude A) to induce bronze-on-top segregation. Further, as described in [164] all forms of density segregation — including both bronze-on-top and glass-on-top — were suppressed for a cell with a gas-permeable bottom *and* top. These results are consistent

[1]The cell was made of Lexan^{TM} with a bottom of steel mesh. Sealing the bottom restored all segregation phenomena observed with the sealed glass cell

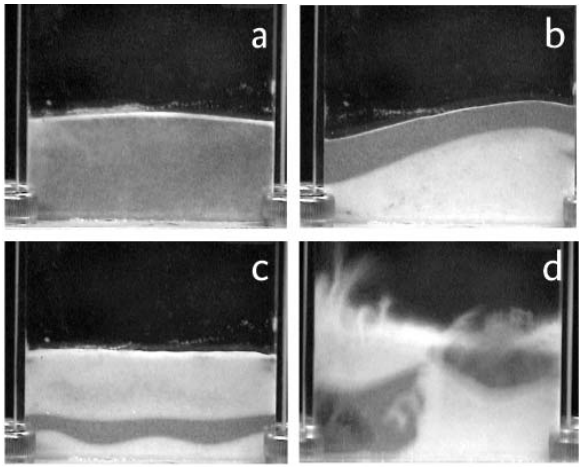

Figure D.2: Examples of steady-state behavior induced by vertical vibration. (a) The mixed state, which occurs under vacuum and was used as the initial condition for most experiments. (b) Bronze-on-top; N_2 interstitial gas at $P = 500$ Torr, $\Gamma = 8.7$, $f = 90$ Hz. Digital images show the boundary between the bronze and glass layers to be only one or two grain diameters thick. (c) Glass-on-top; same parameters as (b), except $\Gamma = 10.8$. Often a glass layer also forms below the bronze layer. (d) Unstable pattern formation characteristic of very large Γ; N_2 interstitial gas at $P = 800$ Torr, $\Gamma = 14$, $f = 50$ Hz.

with bed expansion and particle mobility being enhanced by bulk gas flow through the sample.

To characterize the competing effects of gas drag — *i.e.*, greater mobility of the heavier bronze particles and preferential dragging of the lighter glass particles with bulk gas flow — we used the sealed sample cell and performed experiments focusing on the typically sharp boundary in vibration-amplitude parameter space between the stable bronze- and glass-on-top states. In particular, we determined the critical value of the dimensionless acceleration (Γ_c) that delineates the change from bronze-on-top to glass-on-top steady states, as a function of gas pressure (P), vibration frequency (up to 200 Hz), and gas viscosity. Figure D.3 shows examples of the measured dependence of Γ_c on P for typical high and low vibration frequencies (90 and 50 Hz) and gases of differing viscosity (Ne and N_2). As discussed below, we observed a dramatic difference

in the dependence of segregation behavior on gas viscosity at $f = 50$ Hz, but little difference at $f = 90$ Hz. Specifically, the glass-on-top state does not occur at $f = 50$ Hz for Ne gas at any pressure.

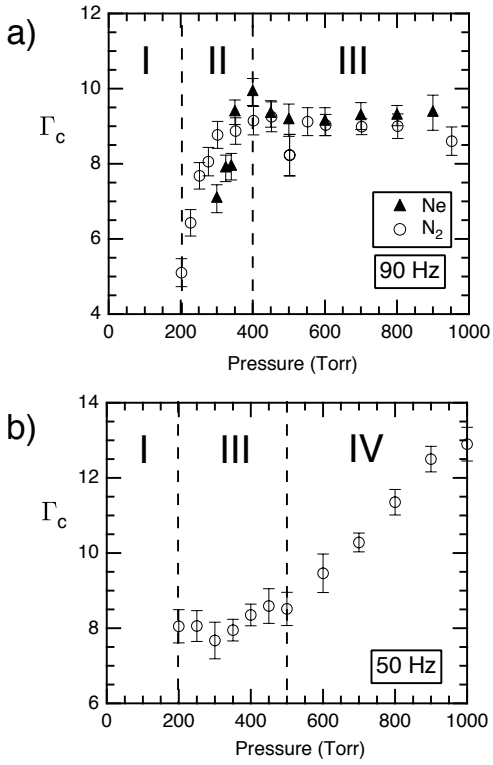

Figure D.3: Measured gas pressure dependence of the critical value of the dimensionless acceleration (Γ_c) delineating the change from the bronze-on-top to glass-on-top steady states. (a) $f = 90$ Hz vibration frequency, comparing N_2 and Ne interstitial gas. (b) $f = 50$ Hz, N_2 gas only; the glass-on-top state does not occur at this frequency for Ne. Four approximate pressure regimes of characteristic Γ_c behavior are indicated: (*I*) glass-on-top segregation does not occur at low gas pressure; (*II*) glass-on-top segregation occurs with the sample approximately flat on top; (*III*) glass-on-top segregation occurs via a pressure-independent spill-over mechanism; (*IV*) glass-on-top segregation occurs via pressure-dependent spill-over with inertial drag nominally comparable to viscous drag.

Each value of Γ_c, plotted in Fig. D.3, is an average between the highest Γ to yield bronze on top (Γ_{b-hi}) and the lowest Γ to yield glass-on-top (Γ_{g-lo}), as determined

by repeated sets of experimental runs. Uncertainty in the determination of Γ_c comes from several sources: irreproducibility of Γ_{b-hi} and Γ_{g-lo}, which contributed an uncertainty $\delta\Gamma_1 \approx 0.1$; spatial variation of Γ_{b-hi} and Γ_{g-lo} across the width of the platform, with associated uncertainty $\delta\Gamma_2 \approx 0.1$; and the systematic offset $\delta\Gamma_3 = \Gamma_{b-hi} - \Gamma_{g-lo}$, which varied from $\approx$ 0–0.5 for differing experimental conditions. The total uncertainty for each plotted value of Γ_c is $\Delta\Gamma_c = (\delta\Gamma_1 + \delta\Gamma_2)^{1/2} + \delta\Gamma_3$.

From the measurements of Γ_c vs. P and associated observations of bed dynamics we identify four characteristic regimes of steady-state behavior, as indicated in Fig. D.3 and summarized in the following.

Regime I (no glass-on-top steady state at low gas pressure) — The glass-on-top steady state does not occur at low gas pressure (below about 200 Torr for N_2 and 300 Torr for Ne), so Γ_c is undefined. In this low pressure regime we observed minimal bed dilation and low mobility of the glass particles, which is consistent with relatively small drag from bulk gas flow driven through the particle bed by vibration-induced pressure gradients (since the gas flow velocity scales as $v_g \sim \nabla P \sim P$). Note that at very low gas pressure ($\lesssim$ 50 Torr) we found that the bronze-on-top steady-state also does not occur.

Regime II (glass-on-top occurs with minimal sample heaping) — At moderate gas pressures and high vibration frequencies such as $f = 90$ Hz, both bronze-on-top and glass-on-top steady-states occur with the top of the vibrated particle bed remaining approximately flat; *i.e.*, with minimal heaping, see Fig. D.4(a). As P is increased, the observed bed dilation and particle mobility increase, the bronze-on-top steady-state is reached more quickly (for $\Gamma < \Gamma_c$), and Γ_c becomes larger. Similar dynamics, steady states, and values for Γ_c are found for N_2 and Ne interstitial gases. See Fig. D.3(a). This observed pressure-dependence and approximate viscosity-independence for Γ_c is consistent with viscous drag due to bulk gas flow through the particle bed playing a dominant role [165], which implies that the drag force on the particles scales as

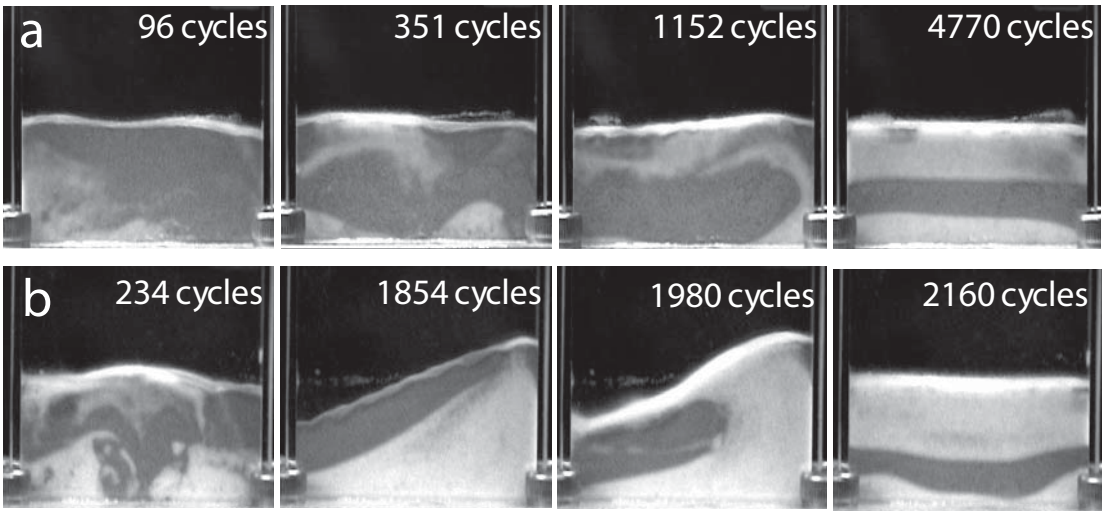

Figure D.4: Time-resolved images illustrating evolution from an initial mixed state [like Fig. D.2(a)] toward a glass-on-top steady-state. (a) Regime II: N_2 gas, $P = 250$ Torr, $\Gamma = 8.9$, $f = 90$ Hz. (b) Regime III: N_2 gas, $P = 500$ Torr, $\Gamma = 10.8$, $f = 90$ Hz.

$F_v \sim \eta v_g \sim P$ since application of Darcy's Law gives $v_g \sim \nabla P/\eta \sim P/\eta$ in a sealed sample cell [156]. At lower vibration frequencies such as $f = 50$ Hz, Regime II behavior does not occur, since for the relatively larger vibration and gas flow velocities ($\approx \Gamma g/\omega$) sample heaping already ensues in Regime I, *i.e.*, at gas pressures below that required for glass-on-top segregation.

Regime III (glass-on-top occurs via pressure-independent sample spill-over) — Above a gas pressure threshold, the glass-on-top state is reached via a "spill-over" mechanism in the presence of sample heaping, as illustrated in Fig. D.4(b). For $\Gamma \geq \Gamma_c$ the sample quickly forms a transient bronze-on-top layer, as heaping occurs across the width of the bed. The heaping builds until the bronze layer surpasses the angle of marginal stability [152]. Particles slide down the heap, with partial replenishment via convective upflow in the bronze layer. Glass particles then break through at the top of the heap and spill over, forming the glass-on-top steady-state. Particle-bed heaping is known to arise from vibration-induced pressure gradients and bulk gas flow, with a steepness that is largely pressure- and viscosity-independent for the pressures used

here [156]. Correspondingly, our measurements of Γ_c show little dependence on P and η in Regime III at higher vibration frequencies such as $f = 90$ Hz. For lower vibration frequencies, however, we observed that the spill-over mechanism is inhibited relative to the convective replenishment of the bronze layer. In particular, the glass-on-top state cannot be achieved for Ne gas and $f \lesssim 75$ Hz, nor for N_2 gas and $f \lesssim 40$ Hz, which is consistent with the opposite scaling of the viscous drag force with η and f: $F_v \sim \eta v_g \sim \Gamma_c \eta / f$, with Γ_c near the typical value for Regime III.

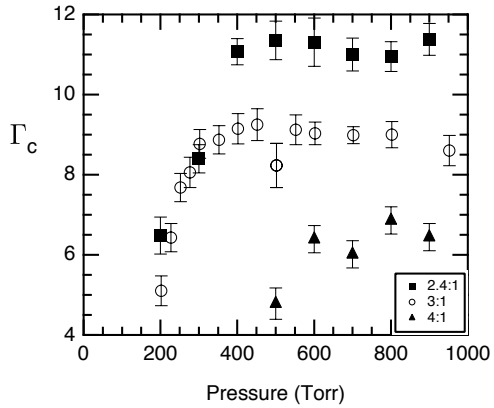

Figure D.5: Measured Γ_c variation with N_2 gas pressure at $f = 90$ Hz, for three glass:bronze mixing ratios, 2.4:1 (squares), 3:1 (circles), and 4:1 (triangles). As the bronze fraction grows, the thickness of the bronze-on-top layer increases, which suppresses the mobility of the underlying glass particles and increases Γ_c.

Regime IV (glass-on-top occurs with pressure-dependent sample spill-over) — At low vibration frequency and high gas pressure the observed difference in bronze and glass mobility grows with pressure, which inhibits the spill-over mechanism to the glass-on-top steady-state and yields an approximately linear dependence of Γ_c on P. See Fig. D.3(b). This pressure dependence may result from inertial gas drag on the particles, which according to a simple estimate ($Re \sim P/\eta f \sim 1$) becomes significant in this regime.

Further study will be needed to establish a full, quantitative understanding of the effect of interstitial gas on density-segregation in vertically-vibrated granular media. For example, density-segregation can depend in detail on system parameters such as the particle mixing ratio. In our experiments we found that a bronze-on-top layer greatly suppresses the mobility of the underlying glass particles; and the thicker the bronze layer the greater the suppression of glass mobility. One consequence of this bronze-on-top suppression is demonstrated in Fig. D.5: introducing more (less) bronze into the system requires a larger (smaller) Γ_c to bring glass to the top, as the glass-on-top steady-state is generally preceded by a transient bronze-on-top condition. In future work we plan to employ NMR/MRI techniques to map grain motion as well as gas pressure and flow dynamics, by using NMR-detectable grains [166] and hyperpolarized noble gas [167], respectively. We are also performing NMR investigations of fluidized beds and may extend these studies to segregation phenomena [168, 169].

This work was supported by NSF Grant No. CTS-031006.

Bibliography

[1] John B. West. *Respiratory physiology–the essentials*. Williams and Wilkins, Baltimore, 5th edition, 1995.

[2] Eric P. Widmaier, Hershel Raff, Kevin T. Strang, and Arthur J. Vander. *Vander, Sherman, and Luciano's human physiology : the mechanisms of body function*. McGraw-Hill Higher Education, Boston, 9th edition, 2004.

[3] P. D. Wagner, H. A. Saltzman, and J. B. West. Measurement of continuous distributions of ventilation-perfusion ratios: theory. *J Appl Physiol*, 36(5):588–599, 1974.

[4] S. M. Lewis. Emptying patterns of the lung studied by multiple-breath N_2 washout. *J Appl Physiol*, 44(3):424–30, 1978.

[5] C. J. Newth, P. Enright, and R. L. Johnson. Multiple-breath nitrogen washout techniques: including measurements with patients on ventilators. *Eur Respir J*, 10(9):2174–85, 1997.

[6] H. T. Robertson, R. W. Glenny, D. Stanford, L. M. McInnes, D. L. Luchtel, and D. Covert. High-resolution maps of regional ventilation utilizing inhaled fluorescent microspheres. *J Appl Physiol*, 82(3):943–53, 1997.

[7] H. W. Knipping, W. Bolt, H. Venrath, H. Valentin, H. Ludes, and P. Endler. A new method of heart and lung function testing, the regional functional analysis in the lung and heart clinic by the radioactive noble gas Xenon-133 (isotope thoracography). *Dtsch Med Wochenschr*, 80(31-32):1146–7, 1955.

[8] N. R. Anthonisen, M. B. Dolovich, and D. V. Bates. Steady state measurement of regional ventilation to perfusion ratios in normal man. *J Clin Invest*, 45(8):1349–56, 1966.

[9] J. B. West. Pulmonary function studies with radioactive gases. *Annu Rev Med*, 18:459–70, 1967.

[10] A. M. Cormack. Representation of a function by its line integrals with some radiological applications. *Journal of Applied Physics*, 34(9):2722, 1963.

[11] A. M. Cormack. Representation of function by its line integrals with some radiological applications .2. *Journal of Applied Physics*, 35(10):2908, 1964.

[12] A. M. Cormack. Reconstruction of densities from their projections, withapplications in radiological physics. *Physics in Medicine and Biology*, 18(2):195–207, 1973.

[13] G.N. Hounsfield. Computerized transverse axial scanning (tomography) .1. description of system. *British Journal of Radiology*, 46(552):1016–1022, 1973.

[14] N. L. Muller. Computed tomography and magnetic resonance imaging: past, present and future. *Eur Respir J Suppl*, 35:3s–12s, 2002.

[15] E. A. Hoffman and D. Chon. Computed tomography studies of lung ventilation and perfusion. *Proc Am Thorac Soc*, 2(6):492–8, 506, 2005.

[16] M. M. Terpogossian, M. E. Phelps, E. J. Hoffman, and N. A. Mullani. Positron-emission transaxial tomograph for nuclear imaging (PETT). *Radiology*, 114(1):89–98, 1975.

[17] S. Treppo, S. M. Mijailovich, and J. G. Venegas. Contributions of pulmonary perfusion and ventilation to heterogeneity in $V_A)/Q$ measured by PET. *J Appl Physiol*, 82(4):1163–1176, 1997.

[18] M. F. Vidal Melo, D. Layfield, R. S. Harris, K. O'Neill, G. Musch, T. Richter, T. Winkler, A. J. Fischman, and J. G. Venegas. Quantification of regional ventilation-perfusion ratios with PET. *J Nucl Med*, 44(12):1982–1991, 2003.

[19] J. G. Venegas, T. Winkler, G. Musch, M. F. Vidal Melo, D. Layfield, N. Tgavalekos, A. J. Fischman, R. J. Callahan, G. Bellani, and R. S. Harris. Self-organized patchiness in asthma as a prelude to catastrophic shifts. *Nature*, 434(7034):777–82, 2005.

[20] F. Bloch, W. W. Hansen, and M. Packard. The nuclear induction experiment. *Physical Review*, 70(7-8):474–485, 1946.

[21] E. M. Purcell, H. C. Torrey, and R. V. Pound. Resonance absorption by nuclear magnetic moments in a solid. *Physical Review*, 69(1-2):37–38, 1946.

[22] P.C. Lauterbur. Image formation by induced local interactions - examples employing nuclear magnetic-resonance. *Nature*, 242(5394):190–191, 1973.

[23] P. Mansfield and P. K. Grannell. "diffraction" and microscopy in solids and liquids by NMR. *Physical Review B*, 12(9):3618, 1975.

[24] R. R. Edelman, H. Hatabu, E. Tadamura, W. Li, and P. V. Prasad. Noninvasive assessment of regional ventilation in the human lung using oxygen-enhanced magnetic resonance imaging. *Nat Med*, 2(11):1236–9, 1996.

[25] Y. Ohno, Q. Chen, and H. Hatabu. Oxygen-enhanced magnetic resonance ventilation imaging of lung. *Eur J Radiol*, 37(3):164–71, 2001.

[26] H. Hatabu, E. Tadamura, Q. Chen, K. W. Stock, W. Li, P. V. Prasad, and R. R. Edelman. Pulmonary ventilation: dynamic MRI with inhalation of molecular oxygen. *Eur J Radiol*, 37(3):172–8, 2001.

[27] H. U. Kauczor and K. F. Kreitner. Contrast-enhanced MRI of the lung. *Eur J Radiol*, 34(3):196–207, 2000.

[28] H. Hatabu, J. Gaa, D. Kim, W. Li, P. V. Prasad, and R. R. Edelman. Pulmonary perfusion: qualitative assessment with dynamic contrast-enhanced MRI using ultra-short T_E and inversion recovery turbo flash. *Magn Reson Med*, 36(4):503–8, 1996.

[29] H. Hatabu, J. Gaa, D. Kim, W. Li, P. V. Prasad, and R. R. Edelman. Pulmonary perfusion and angiography: evaluation with breath-hold enhanced three-dimensional fast imaging steady-state precession MR imaging with short T_R and T_E. *AJR Am J Roentgenol*, 167(3):653–5, 1996.

[30] M. A. Bouchiat, T. R. Carver, and C. M. Varnum. Nuclear polarization in ^{3}He gas induced by optical pumping and dipolar exchange. *Physical Review Letters*, 5(8):373–375, 1960.

[31] G. K. Walters, F. D. Colegrove, and L. D. Schearer. Nuclear polarization of ^{3}He gas by metastability exchange with optically pumped metastable ^{3}He atoms. *Physical Review Letters*, 8(11):439, 1962.

[32] G. C. Phillips, R. R. Perry, F. D. Colegrove, L. D. Schearer, P. M. Windham, and G. K. Walters. Demonstration of a polarized ^{3}He target for nuclear reactions. *Physical Review Letters*, 9(12):502, 1962.

[33] D. Raftery, H. Long, T. Meersmann, P. J. Grandinetti, L. Reven, and A. Pines. High-field NMR of adsorbed xenon polarized by laser pumping. *Physical Review Letters*, 66(5):584, 1991.

[34] M. S. Albert, G. D. Cates, B. Driehuys, W. Happer, B. Saam, Jr. Springer, C. S., and A. Wishnia. Biological magnetic resonance imaging using laser-polarized ^{129}Xe. *Nature*, 370(6486):199–201, 1994.

[35] M. Leduc, P. J. Nacher, and G. Tastevin. Magnetic resonance imaging using polarized noble gases. *Laser Physics*, 8(3):799–802, 1998.

[36] T. G. Walker and W. Happer. Spin-exchange optical pumping of noble-gas nuclei. *Rev Mod Phys*, 69(2):629–642, 1997.

[37] E. Babcock, I. Nelson, S. Kadlecek, B. Driehuys, L. W. Anderson, F. W. Hersman, and T. G. Walker. Hybrid spin-exchange optical pumping of ^{3}He. *Phys Rev Lett*, 91(12):123003, 2003.

[38] E. Babcock, B. Chann, T. G. Walker, W. C. Chen, and T. R. Gentile. Limits to the polarization for spin-exchange optical pumping of ^{3}He. *Phys Rev Lett*, 96(8):083003, 2006.

[39] R. D. Black, H. L. Middleton, G. D. Cates, G. P. Cofer, B. Driehuys, W. Happer, L. W. Hedlund, G. A. Johnson, M. D. Shattuck, and J. C. Swartz. In vivo ^{3}He MR images of guinea pig lungs. *Radiology*, 199(3):867–70, 1996.

[40] G. H. Mills, J. M. Wild, B. Eberle, and E. J. Van Beek. Functional magnetic resonance imaging of the lung. *Br J Anaesth*, 91(1):16–30, 2003.

[41] B. Saam, W. Happer, and H. Middleton. Nuclear-relaxation of ^{3}He in the presence of O_2. *Physical Review A*, 52(1):862–865, 1995.

[42] A. J. Deninger, B. Eberle, M. Ebert, T. Grossmann, W. Heil, H. Kauczor, L. Lauer, K. Markstaller, E. Otten, J. Schmiedeskamp, W. Schreiber, R. Surkau, M. Thelen, and N. Weiler. Quantification of regional intrapulmonary oxygen partial pressure evolution during apnea by ^{3}He MRI. *J Magn Reson*, 141(2):207–216, 1999.

[43] M. Salerno, E. E. de Lange, T. A. Altes, J. D. Truwit, J. R. Brookeman, and 3rd Mugler, J. P. Emphysema: hyperpolarized ^{3}He diffusion MR imaging of the lungs compared with spirometric indexes–initial experience. *Radiology*, 222(1):252–260, 2002.

[44] B. T. Saam, D. A. Yablonskiy, V. D. Kodibagkar, J. C. Leawoods, D. S. Gierada, J. D. Cooper, S. S. Lefrak, and M. S. Conradi. MR imaging of diffusion of ^{3}He gas in healthy and diseased lungs. *Magnetic Resonance in Medicine*, 44(2):174–179, 2000.

[45] I. C. Ruset, S. Ketel, and F. W. Hersman. Optical pumping system design for large production of hyperpolarized ^{129}Xe. *Physical Review Letters*, 96(5), 2006.

[46] S. D. Swanson, M. S. Rosen, K. P. Coulter, R. C. Welsh, and T. E. Chupp. Distribution and dynamics of laser-polarized ^{129}Xe magnetization in vivo. *Magnetic Resonance in Medicine*, 42(6):1137–1145, 1999.

[47] M. Ferrigno, S. Patz, I. Muradian, M. Hrovat, J. Butler, G. Topulos, S. Ketel, I. Ruset, S. Covrig, and F. Hersman. Hyperpolarzied ^{129}Xe human gas exchange at 0.2t with xtc. In *14th Meeting of ISMRM*, page 1545, Seattle, WA, 2006.

[48] G. P. Wong, C. H. Tseng, V. R. Pomeroy, R. W. Mair, D. P. Hinton, D. Hoffmann, R. E. Stoner, F. W. Hersman, D. G. Cory, and R. L. Walsworth. A system for low field imaging of laser-polarized noble gas. *J Magn Reson*, 141(2):217–227, 1999.

[49] R. W. Mair, M. I. Hrovat, S. Patz, M. S. Rosen, I. C. Ruset, G. P. Topulos, L. L. Tsai, J. P. Butler, F. W. Hersman, and R. L. Walsworth. ^{3}He lung imaging in an open access, very-low-field human magnetic resonance imaging system. *Magn Reson Med*, 53(4):745–9, 2005.

[50] J. B. West, C. T. Dollery, and A. Naimark. Distribution of blood flow in isolated lung; relation to vascular and alveolar pressures. *J Appl Physiol*, 19:713–724, 1964.

[51] J. B. West, A. R. Elliott, H. J. Guy, and G. K. Prisk. Pulmonary function in space. *JAMA*, 277(24):1957–1961, 1997.

[52] R. W. Glenny, W. J. Lamm, R. K. Albert, and H. T. Robertson. Gravity is a minor determinant of pulmonary blood flow distribution. *J Appl Physiol*, 71(2):620–629, 1991.

[53] J. B. West. Importance of gravity in determining the distribution of pulmonary blood flow. *J Appl Physiol*, 93(5):1888–9; author reply 1889–91, 2002.

[54] W. A. Altemeier, S. McKinney, M. A. Krueger, and R. W. Glenny. Effect of posture on regional gas exchange in pigs. *J Appl Physiol*, 2004.

[55] M. Mure, S. Nyren, H. Jacobsson, S. A. Larsson, and S. G. Lindahl. High continuous positive airway pressure level induces ventilation/perfusion mismatch in the prone position. *Crit Care Med*, 29(5):959–964, 2001.

[56] M. Mure, K. B. Domino, S. G. Lindahl, M. P. Hlastala, W. A. Altemeier, and R. W. Glenny. Regional ventilation-perfusion distribution is more uniform in the prone position. *J Appl Physiol*, 88(3):1076–1083, 2000.

[57] G. Musch, J. D. Layfield, R. S. Harris, M. F. Melo, T. Winkler, R. J. Callahan, A. J. Fischman, and J. G. Venegas. Topographical distribution of pulmonary perfusion and ventilation, assessed by PET in supine and prone humans. *J Appl Physiol*, 93(5):1841–51, 2002.

[58] I. Frerichs, T. Dudykevych, J. Hinz, M. Bodenstein, G. Hahn, and G. Hellige. Gravity effects on regional lung ventilation determined by functional eit during parabolic flights. *J Appl Physiol*, 91(1):39–50, 2001.

[59] W. S. Druz and J. T. Sharp. Activity of respiratory muscles in upright and recumbent humans. *J Appl Physiol*, 51(6):1552–1561, 1981.

[60] P. K. Behrakis, A. Baydur, M. J. Jaeger, and J. Milic-Emili. Lung mechanics in sitting and horizontal body positions. *Chest*, 83(4):643–6, 1983.

[61] G. M. Barnas, M. D. Green, C. F. Mackenzie, S. J. Fletcher, D. N. Campbell, C. Runcie, and G. E. Broderick. Effect of posture on lung and regional chest wall mechanics. *Anesthesiology*, 78(2):251–9, 1993.

[62] J. C. Yap, R. A. Watson, S. Gilbey, and N. B. Pride. Effects of posture on respiratory mechanics in obesity. *J Appl Physiol*, 79(4):1199–1205, 1995.

[63] R. A. Watson and N. B. Pride. Postural changes in lung volumes and respiratory resistance in subjects with obesity. *J Appl Physiol*, 98(2):512–517, 2005.

[64] S. Appelt, A. Ben-Amar Baranga, C. J. Erickson, M. V. Romalis, A. R. Young, and W. Happer. Theory of spin-exchange optical pumping of ^{3}He and ^{129}Xe. *Physical Review A*, 58(2):1412, 1998.

[65] A. Kastler. Quelques suggestions concernant la production optique et la detection optique dune inegalite de population des niveaux de quantification spatiale des atomes - application a lexperience de stern et gerlach et a la resonance magnetique. *Journal De Physique Et Le Radium*, 11(6):255–265, 1950.

[66] William Happer. Optical pumping. *Reviews of Modern Physics*, 44(2):169, 1972.

[67] M. E. Wagshul and T. E. Chupp. Laser optical pumping of high-density Rb in polarized ^{3}He targets. *Physical Review A*, 49(5):3854, 1994.

[68] M. S. Rosen. *Laser-Polarized ^{129}Xe Magnetic Resonance Spectroscopy and Imaging; The Development of a Method for In Vivo Perfusion Measurement.* PhD thesis, University of Michigan, 2001.

[69] M. A. Bouchiat, J. Brossel, and L. C. Pottier. Evidence for Rb-rare-gas molecules from the relaxation of polarized Rb atoms in a rare gas. experimental results. *The Journal of Chemical Physics*, 56(7):3703–3714, 1972.

[70] B. Chann, E. Babcock, L. W. Anderson, and T. G. Walker. Measurements of ^{3}He spin-exchange rates. *Physical Review A*, 66(3):032703, 2002.

[71] A. Ben-Amar Baranga, S. Appelt, M. V. Romalis, C. J. Erickson, A. R. Young, G. D. Cates, and W. Happer. Polarization of ^{3}He by spin exchange with optically pumped Rb and K vapors. *Physical Review Letters*, 80(13):2801, 1998.

[72] J. C. Leawoods, D. A. Yablonskiy, B. Saam, D. S. Gierada, and M. S. Conradi. Hyperpolarized ^{3}He gas production and MR imaging of the lung. *Concepts in Magnetic Resonance*, 13(5):277–293, 2001.

[73] Thomas J. Killian. Thermionic phenomena caused by vapors of rubidium and potassium. *Physical Review*, 27(5):578, 1926.

[74] R. S. Timsit, J. M. Daniels, and A. D. May. Nuclear relaxation of ^{3}He gas on various solid surfaces. *Canadian Journal of Physics*, 49(5):560, 1971.

[75] R. E. Jacob, B. Driehuys, and B. Saam. Fundamental mechanisms of ^{3}He relaxation on glass. *Chemical Physics Letters*, 370(1-2):261–267, 2003.

[76] Ming F. Hsu, G. D. Cates, I. Kominis, I. A. Aksay, and D. M. Dabbs. Sol-gel coated glass cells for spin-exchange polarized ^{3}He. *Applied Physics Letters*, 77(13):2069–2071, 2000.

[77] Rodger L. Gamblin and Thomas R. Carver. Polarization and relaxation processes in ^{3}He gas. *Physical Review*, 138(4A):A946, 1965.

[78] L. D. Schearer and G. K. Walters. Nuclear spin-lattice relaxation in the presence of magnetic-field gradients. *Physical Review*, 139(5A):A1398, 1965.

[79] R. E. Jacob, J. Teter, B. Saam, W. C. Chen, and T. R. Gentile. Low-field orientation dependence of he relaxation in spin-exchange cells. *Physical Review A (Atomic, Molecular, and Optical Physics)*, 69(2):021401–4, 2004.

[80] R. Chapman and M. G. Richards. Longitudinal spin relaxation in ^{3}He gas at 4.2 K. *Physical Review Letters*, 33(1):18, 1974.

[81] N. R. Newbury, A. S. Barton, P. Bogorad, G. D. Cates, M. Gatzke, H. Mabuchi, and B. Saam. Polarization-dependent frequency shifts from Rb-^{3}He collisions. *Physical Review A*, 48(1):558, 1993.

[82] M. S. Rosen, T. E. Chupp, K. P. Coulter, R. C. Welsh, and S. D. Swanson. Polarized ^{129}Xe optical pumping/spin exchange and delivery system for magnetic resonance spectroscopy and imaging studies. *Review of Scientific Instruments*, 70(2):1546–1552, 1999.

[83] C. H. Tseng, G. P. Wong, V. R. Pomeroy, R. W. Mair, D. P. Hinton, D. Hoffmann, R. E. Stoner, F. W. Hersman, D. G. Cory, and R. L. Walsworth. Low-field MRI of laser polarized noble gas. *Phys Rev Lett*, 81(17):3785–3788, 1998.

[84] E. Durand, G. Guillot, L. Darrasse, G. Tastevin, P. J. Nacher, A. Vignaud, D. Vattolo, and J. Bittoun. CPMG measurements and ultrafast imaging in human lungs with hyperpolarized ^{3}He at low field (0.1 T). *Magnetic Resonance in Medicine*, 47(1):75–81, 2002.

[85] J. R. Owers-Bradley, S. Fichele, A. Bennattayalah, C. J. McGloin, R. W. Bowtell, P. S. Morgan, and A. R. Moody. MR tagging of human lungs using hyperpolarized ^{3}He gas. *J Magn Reson Imaging*, 17(1):142–146, 2003.

[86] A. K. Venkatesh, A. X. Zhang, J. Mansour, L. Kubatina, C. H. Oh, G. Blasche, M. Selim Unlu, D. Balamore, F. A. Jolesz, B. B. Goldberg, and M. S. Albert. MRI of the lung gas-space at very low-field using hyperpolarized noble gases. *Magn Reson Imaging*, 21(7):773–776, 2003.

[87] C. P. Bidinosti, J. Choukeife, G. Tastevin, A. Vignaud, and P. J. Nacher. MRI of the lung using hyperpolarized ^{3}He at very low magnetic field (3 mT). *Magma*, 16(6):255–258, 2004.

[88] C. P. Bidinosti, J. Choukeife, P. J. Nacher, and G. Tastevin. In vivo NMR of hyperpolarized ^{3}He in the human lung at very low magnetic fields. *J Magn Reson*, 162(1):122–132, 2003.

[89] J. E. Everett and J. E. Osemeikh. Spherical coils for uniform magnetic fields. *Journal of Scientific Instruments*, 43(7):470, 1966.

[90] G. Gottardi, P. Mesirca, C. Agostini, D. Remondini, and F. Bersani. A four coil exposure system (tetracoil) producing a highly uniform magnetic field. *Bioelectromagnetics*, 24(2):125–133, 2003.

[91] P. S. Morgan, S. Conolly, and A Mazovski. Design of uniform field biplanar magnets. In *5th Meeting of ISMRM*, page 1447, Toronto, Canada, 1997.

[92] Chih-Ta Chia and Ya-Fan Wang. The magnetic field along the axis of a long finite solenoid. *The Physics Teacher*, 40(5):288–289, 2002.

[93] D. I. Hoult and R. E. Richards. Signal-to-noise ratio of nuclear magnetic-resonance experiment. *Journal of Magnetic Resonance*, 24(1):71–85, 1976.

[94] Paul T. Callaghan. *Principles of nuclear magnetic resonance microscopy*. Clarendon Press ; Oxford University Press, Oxford [England] New York, 1991.

[95] L. Darrasse, G. Guillot, P. J. Nacher, and G. Tastevin. Low-field ^{3}He nuclear magnetic resonance in human lungs. *Comptes Rendus De L Academie Des Sciences Serie Ii Fascicule B-Mecanique Physique Chimie Astronomie*, 324(11):691–700, 1997.

[96] X. J. Chen, H. E. Moller, M. S. Chawla, G. P. Cofer, B. Driehuys, L. W. Hedlund, J. R. MacFall, and G. A. Johnson. Spatially resolved measurements of hyperpolarized gas properties in the lung in vivo. part II: T_2^*. *Magn Reson Med*, 42(4):729–37, 1999.

[97] A. Vignaud, X. Maitre, G. Guillot, E. Durand, L. de Rochefort, P. Robert, V. Vives, R. Santus, and L. Darrasse. Magnetic susceptibility matching at the air-tissue interface in rat lung by using a superparamagnetic intravascular contrast agent: Influence on transverse relaxation time of hyperpolarized ^{3}He. *Magnetic Resonance in Medicine*, 54(1):28–33, 2005.

[98] J. Parra-Robles, A. R. Cross, and G. E. Santyr. Theoretical signal-to-noise ratio and spatial resolution dependence on the magnetic field strength for hyperpolarized noble gas magnetic resonance imaging of human lungs. *Med Phys*, 32(1):221–9, 2005.

[99] R. R. Rizi, J. E. Baumgardner, M. Ishii, Z. Z. Spector, J. M. Edvinsson, A. Jalali, J. Yu, M. Itkin, D. A. Lipson, and W. Gefter. Determination of regional V_A/Q by hyperpolarized ^{3}He MRI. *Magn Reson Med*, 52(1):65–72, 2004.

[100] R. M. Henkelman. Measurement of signal intensities in the presence of noise in MR images. *Med Phys*, 12(2):232–3, 1985.

[101] H. Gudbjartsson and S. Patz. The Rician distribution of noisy MRI data. *Magn Reson Med*, 34(6):910–4, 1995.

[102] B. Eberle, N. Weiler, K. Markstaller, H. Kauczor, A. Deninger, M. Ebert, T. Grossmann, W. Heil, L. O. Lauer, T. P. Roberts, W. G. Schreiber, R. Surkau, W. F. Dick, E. W. Otten, and M. Thelen. Analysis of intrapulmonary O_2 concentration by MR imaging of inhaled hyperpolarized ^{3}He. *J Appl Physiol*, 87(6):2043–52, 1999.

[103] H. E. Moller, L. W. Hedlund, X. J. Chen, M. R. Carey, M. S. Chawla, C. T. Wheeler, and G. A. Johnson. Measurements of hyperpolarized gas properties in the lung. part III: ^{3}He T_1. *Magn Reson Med*, 45(3):421–430, 2001.

[104] A. J. Deninger, B. Eberle, M. Ebert, T. Grossmann, G. Hanisch, W. Heil, H. U. Kauczor, K. Markstaller, E. Otten, W. Schreiber, R. Surkau, and N. Weiler. ^{3}He-MRI-based measurements of intrapulmonary pO_2 and its time course during apnea in healthy volunteers: first results, reproducibility, and technical limitations. *NMR Biomed*, 13(4):194–201, 2000.

[105] A. J. Deninger, S. Mansson, J. S. PETersson, G. PETtersson, P. Magnusson, J. Svensson, B. Fridlund, G. Hansson, I. Erjefeldt, P. Wollmer, and K. Golman. Quantitative measurement of regional lung ventilation using ^{3}He MRI. *Magn Reson Med*, 48(2):223–232, 2002.

[106] K. Markstaller, B. Eberle, W. G. Schreiber, N. Weiler, M. Thelen, and H. U. Kauczor. Flip angle considerations in ^{3}He-MRI. *NMR Biomed*, 13(4):190–3, 2000.

[107] A. J. Deninger, B. Eberle, J. Bermuth, B. Escat, K. Markstaller, J. Schmiedeskamp, W. G. Schreiber, R. Surkau, E. Otten, and H. U. Kauczor. Assessment of a single-acquisition imaging sequence for oxygen-sensitive ^{3}He-MRI. *Magn Reson Med*, 47(1):105–114, 2002.

[108] T. A. Altes, P. L. Powers, J. Knight-Scott, G. Rakes, T. A. Platts-Mills, E. E. de Lange, B. A. Alford, 3rd Mugler, J. P., and J. R. Brookeman. Hyperpolarized ^{3}He MR lung ventilation imaging in asthmatics: preliminary findings. *J Magn Reson Imaging*, 13(3):378–84, 2001.

[109] T. A. Altes and E. E. de Lange. Applications of hyperpolarized ^{3}He gas magnetic resonance imaging in pediatric lung disease. *Top Magn Reson Imaging*, 14(3):231–236, 2003.

[110] S. Fichele, N. Woodhouse, A. J. Swift, Z. Said, M. N. J. Paley, L. Kasuboski, G. H. Mills, E. J. R. van Beek, and J. M. Wild. MRI of ^{3}He gas in healthy lungs: Posture related variations of alveolar size. *J Mag Res Imag*, 20(2):331–335, 2004.

[111] B. Saam, R. Jacob, B. Anger, and K. Minard. Rapid production of hyperpolarized ^{3}He gas for MRI. In *International Society for Magnetic Resonance in Medicine*, Seattle, WA, 2006.

[112] B. Chann, I. Nelson, and T. G. Walker. Frequency-narrowed external-cavity diode-laser-array bar. *Optics Letters*, 25(18):1352–1354, 2000.

[113] I. A. Nelson, B. Chann, and T. G. Walker. Spin-exchange optical pumping using a frequency-narrowed high power diode laser. *Applied Physics Letters*, 76(11):1356–1358, 2000.

[114] J. N. Zerger, M. J. Lim, K. P. Coulter, and T. E. Chupp. Polarization of ^{129}Xe with high power external-cavity laser diode arrays. *Applied Physics Letters*, 76(14):1798–1800, 2000.

[115] B. Chann, E. Babcock, L. W. Anderson, T. G. Walker, W. C. Chen, T. B. Smith, A. K. Thompson, and T. R. Gentile. Production of highly polarized ^{3}He using spectrally narrowed diode laser array bars. *Journal of Applied Physics*, 94(10):6908–6914, 2003.

[116] E. Babcock, B. Chann, I. A. Nelson, and T. G. Walker. Frequency-narrowed diode array bar. *Applied Optics*, 44(15):3098–3104, 2005.

[117] B. L. Volodin, S. V. Dolgy, E. D. Melnik, E. Downs, J. Shaw, and V. S. Ban. Wavelength stabilization and spectrum narrowing of high-power multimode laser diodes and arrays by use of volume bragg gratings. *Optics Letters*, 29(16):1891–1893, 2004.

[118] F. Havermeyer, W. H. Liu, C. Moser, D. Psaltis, and G. J. Steckman. Volume holographic grating-based continuously tunable optical filter. *Optical Engineering*, 43(9):2017–2021, 2004.

[119] J. M. Wild, M. N. Paley, L. Kasuboski, A. Swift, S. Fichele, N. Woodhouse, P. D. Griffiths, and E. J. van Beek. Dynamic radial projection MRI of inhaled hyperpolarized ^{3}He gas. *Magn Reson Med*, 49(6):991–997, 2003.

[120] J. M. Wild, S. Fichele, N. Woodhouse, M. N. Paley, L. Kasuboski, and E. J. van Beek. 3D volume-localized pO_2 measurement in the human lung with ^{3}He MRI. *Magn Reson Med*, 53(5):1055–64, 2005.

[121] K. Yoda. Analytical design method of self-shielded planar coils. *Journal of Applied Physics*, 67(9):4349–4353, 1990.

[122] E. D. Caparelli, D. Tomasi, and H. Panepucci. Shielded biplanar gradient coil design. *J Mag Res Imag*, 9(5):725–731, 1999.

[123] D. Tomasi, E. C. Caparelli, H. Panepucci, and B. Foerster. Fast optimization of a biplanar gradient coil set. *Journal of Magnetic Resonance*, 140(2):325–339, 1999.

[124] E. Mark Haacke. *Magnetic resonance imaging : physical principles and sequence design*. Wiley, New York, 1999.

[125] Z. H. Cho, Joie P. Jones, and Manbir Singh. *Foundations of medical imaging*. Wiley, New York, 1993.

[126] E. L. Hahn and D. E. Maxwell. Spin echo measurements of nuclear spin coupling in molecules. *Physical Review*, 88(5):1070, 1952.

[127] I.C. Ruset. *Hyperpolarized ^{129}Xe Production and Applications*. PhD thesis, University of New Hampshire, 2005.

[128] G. P. Topulos, R. E. Brown, and J. P. Butler. Influence of lung volume on pulmonary microvascular pressure-volume characteristics. *J Appl Physiol*, 89(4):1591–600, 2000.

[129] J. B. Glazier, J. M. Hughes, J. E. Maloney, and J. B. West. Measurements of capillary dimensions and blood volume in rapidly frozen lungs. *J Appl Physiol*, 26(1):65–76, 1969.

[130] A. Al-Tinawi, A. V. Clough, D. R. Harder, J. H. Linehan, D. A. Rickaby, and C. A. Dawson. Distensibility of small veins of the dog lung. *J Appl Physiol*, 73(5):2158–65, 1992.

[131] S. C. Hillier, P. S. Godbey, C. C. Hanger, J. A. Graham, Jr. Presson, R. G., O. Okada, J. H. Linehan, C. A. Dawson, and Jr. Wagner, W. W. Direct measurement of pulmonary microvascular distensibility. *J Appl Physiol*, 75(5):2106–11, 1993.

[132] A. G. Cutillo, K. Ganesan, D. C. Ailion, A. H. Morris, C. H. Durney, S. C. Symko, and R. A. Christman. Alveolar air-tissue interface and nuclear magnetic resonance behavior of lung. *J Appl Physiol*, 70(5):2145–54, 1991.

[133] C. J. Bergin, G. H. Glover, and J. M. Pauly. Lung parenchyma: magnetic susceptibility in mr imaging. *Radiology*, 180(3):845–8, 1991.

[134] J. R. Mayo, A. MacKay, and N. L. Muller. MR imaging of the lungs: value of short T_E spin-echo pulse sequences. *AJR Am J Roentgenol*, 159(5):951–6, 1992.

[135] C. J. Muller, R. Loffler, M. Deimling, M. Peller, and M. Reiser. MR lung imaging at 0.2 T with T_1-weighted true FISP: native and oxygen-enhanced. *J Magn Reson Imaging*, 14(2):164–8, 2001.

[136] C. Schwarzbauer, J. Syha, and A. Haase. Quantification of regional blood volumes by rapidT_1 mapping. *Magn Reson Med*, 29(5):709–12, 1993.

[137] H. C. Schwickert, T. P. Roberts, D. M. Shames, C. F. van Dijke, A. Disston, A. Muhler, J. S. Mann, and R. C. Brasch. Quantification of liver blood volume: comparison of ultra short T_1 inversion recovery echo planar imaging (ULSTIR-EPI), with dynamic 3D-gradient recalled echo imaging. *Magn Reson Med*, 34(6):845–52, 1995.

[138] R. Kuwatsuru, D. M. Shames, A. Muhler, J. Mintorovitch, V. Vexler, J. S. Mann, F. Cohn, D. Price, J. Huberty, and R. C. Brasch. Quantification of tissue plasma volume in the rat by contrast-enhanced magnetic resonance imaging. *Magn Reson Med*, 30(1):76–81, 1993.

[139] J. Blustajn, C. A. Cuenod, O. Clement, N. Siauve, V. Vuillemin-Bodaghi, and G. Frija. Measurement of liver blood volume using a macromolecular MRI contrast agent at equilibrium. *Magn Reson Imaging*, 15(4):415–21, 1997.

[140] W. Lin, R. P. Paczynski, K. Kuppusamy, C. Y. Hsu, and E. M. Haacke. Quantitative measurements of regional cerebral blood volume using MRI in rats: effects of arterial carbon dioxide tension and mannitol. *Magn Reson Med*, 38(3):420–8, 1997.

[141] E. Kahler, C. Waller, E. Rommel, K. H. Hiller, S. Voll, A. Broich, K. Hu, K. D. Schnackerz, W. R. Bauer, G. Ertl, and A. Haase. Quantitative regional blood volume studies in rat myocardium in vivo. *Magn Reson Med*, 40(4):517–25, 1998.

[142] K. M. Donahue, H. G. Krouwer, S. D. Rand, A. P. Pathak, C. S. Marszalkowski, S. C. Censky, and R. W. Prost. Utility of simultaneously acquired gradient-echo and spin-echo cerebral blood volume and morphology maps in brain tumor patients. *Magn Reson Med*, 43(6):845–53, 2000.

[143] C. F. Hazlewood, D. C. Chang, B. L. Nichols, and D. E. Woessner. Nuclear magnetic resonance transverse relaxation times of water protons in skeletal muscle. *Biophys J*, 14(8):583–606, 1974.

[144] K. M. Donahue, R. M. Weisskoff, D. A. Chesler, K. K. Kwong, Jr. Bogdanov, A. A., J. B. Mandeville, and B. R. Rosen. Improving mr quantification of regional blood volume with intravascular T_1 contrast agents: accuracy, precision, and water exchange. *Magn Reson Med*, 36(6):858–67, 1996.

[145] K. M. Donahue, R. M. Weisskoff, and D. Burstein. Water diffusion and exchange as they influence contrast enhancement. *J Magn Reson Imaging*, 7(1):102–10, 1997.

[146] O. Clement, N. Siauve, C. A. Cuenod, and G. Frija. Liver imaging with ferumoxides (feridex): fundamentals, controversies, and practical aspects. *Top Magn Reson Imaging*, 9(3):167–82, 1998.

[147] L. H. Brudin, C. G. Rhodes, S. O. Valind, T. Jones, B. Jonson, and J. M. Hughes. Relationships between regional ventilation and vascular and extravascular volume in supine humans. *J Appl Physiol*, 76(3):1195–204, 1994.

[148] R. O. Crapo, J. D. Crapo, and A. H. Morris. Lung tissue and capillary blood volumes by rebreathing and morphometric techniques. *Respir Physiol*, 49(2):175–86, 1982.

[149] G. P. Topulos, N. R. Lipsky, J. L. Lehr, R. A. Rogers, and J. P. Butler. Fractional changes in lung capillary blood volume and oxygen saturation during the cardiac cycle in rabbits. *J Appl Physiol*, 82(5):1668–76, 1997.

[150] H. M. Jaeger, S. R. Nagel, and R. P. Behringer. Granular solids, liquids, and gases. *Reviews of Modern Physics*, 68(4):1259–1273, 1996.

[151] Jacques Duran. *Sands, powders, and grains : an introduction to the physics of granular materials*. Partially ordered systems. Springer, New York, 2000.

[152] Gerald H. Ristow. *Pattern formation in granular materials*. Springer, Berlin ; New York, 2000.

[153] Sarath G. K. Tennakoon and R. P. Behringer. Vertical and horizontal vibration of granular materials: Coulomb friction and a novel switching state. *Physical Review Letters*, 81(4):794, 1998.

[154] D. Brone and F. J. Muzzio. Size segregation in vibrated granular systems: A reversible process. *Physical Review E*, 56(1):1059, 1997.

[155] P. M. Reis and T. Mullin. Granular segregation as a critical phenomenon. *Physical Review Letters*, 89(24):244301, 2002.

[156] H. K. Pak, E. Vandoorn, and R. P. Behringer. Effects of ambient gases on granular-materials under vertical vibration. *Physical Review Letters*, 74(23):4643–4646, 1995.

[157] M. E. Mobius, B. E. Lauderdale, S. R. Nagel, and H. M. Jaeger. Brazil-nut effect - size separation of granular particles. *Nature*, 414(6861):270–270, 2001.

[158] X. Yan, Q. Shi, M. Hou, K. Lu, and C. K. Chan. Effects of air on the segregation of particles in a shaken granular bed. *Physical Review Letters*, 91(1), 2003.

[159] M. A. Naylor, M. R. Swift, and P. J. King. Air-driven brazil nut effect. *Physical Review E*, 68(1), 2003.

[160] M. Rhodes, S. Takeuchi, K. Liffman, and K. Muniandy. The role of interstitial gas in the brazil nut effect. *Granular Matter*, 5(3):107–114, 2003.

[161] E. Mobius Matthias, Cheng Xiang, S. Karczmar Greg, R. Nagel Sidney, and M. Jaeger Heinrich. Intruders in the dust: Air-driven granular size separation. *Physical Review Letters*, 93(19):198001, 2004.

[162] E. Mobius Matthias, Cheng Xiang, Eshuis PETer, S. Karczmar Greg, R. Nagel Sidney, and M. Jaeger Heinrich. Effect of air on granular size separation in a vibrated granular bed. *Physical Review E (Statistical, Nonlinear, and Soft Matter Physics)*, 72(1):011304, 2005.

[163] N. Burtally, P. J. King, and M. R. Swift. Spontaneous air-driven separation in vertically vibrated fine granular mixtures. *Science*, 295(5561):1877–1879, 2002.

[164] N. Burtally, P. J. King, M. R. Swift, and M. Leaper. Dynamical behaviour of fine granular glass/bronze mixtures under vertical vibration. *Granular Matter*, 5(2):57–66, 2003.

[165] P. Biswas, P. Sanchez, M. R. Swift, and P. J. King. Numerical simulations of air-driven granular separation. *Physical Review E*, 68(5), 2003.

[166] Xiaoyu Yang, Chao Huan, D. Candela, R. W. Mair, and R. L. Walsworth. Measurements of grain motion in a dense, three-dimensional granular fluid. *Physical Review Letters*, 88(4):044301, 2002.

[167] Ruopeng Wang, Matthew Scott Rosen, Donald Candela, Ross William Mair, and Ronald Lee Walsworth. Study of gas-fluidization dynamics with laser-polarized ^{129}Xe. *Magnetic Resonance Imaging*, 23(2):203–207, 2005.

[168] M. A. Howley and B. J. Glasser. Hydrodynamics of a uniform liquid-fluidized bed containing a binary mixture of particles. *Chemical Engineering Science*, 57(19):4209–4226, 2002.

[169] M. C. Leaper, A. J. Smith, M. R. Swift, P. J. King, H. E. Webster, N. J. Miles, and S. W. Kingman. The behaviour of water-immersed glass-bronze particulate systems under vertical vibration. *Granular Matter*, 7(2-3):57–67, 2005.